SPECTROSCOPIC AND STRUCTURAL CHARACTERIZATION OF REACTIVE METAL NITRENOIDS

A Dissertation

by

GERARD PIERRE VAN TRIESTE III

Submitted to the Graduate and Professional School of
Texas A&M University
in partial fulfillment of the requirements for the degree of

DOCTOR OF PHILOSOPHY

Chair of Committee,	David C. Powers
Committee Members,	François P. Gabbaï
	Timothy R Hughbanks
	Cecilia Tommos
Head of Department,	Simon W. North

August 2022

Major Subject: Chemistry

ABSTRACT

C–H bonds are the most ubiquitous functional groups found in nature. While C–H bonds are abundant, they are oxidatively robust due to the lack of polarity about the C–H bond and resulting high bond dissociation energy. Classic methods to functionalize unactivated C–H bonds are based on free-radical processes, which typically proceed with preference for cleavage of the weakest available C–H bond but are not highly selective. Significant research effort has been pursued towards selective C–H functionalization using transition metal complexes. Terminal metal–ligand (M–L) multiply bonded species (L = CR^{3-}, CR_2^{2-}, O^{2-}, NR^{2-}, and N^{3-}) are now known to be ubiquitous intermediates in both biological. and metal-catalyzed synthetic C–H functionalization reactions.

This dissertation will present efforts to develop new platforms to characterize reactive terminal M–L multiply bonded species. The first three chapters discuss the relevant literature and associated challenges with designing appropriate photoprecursors to access M–L multiply bound species on Mn and Cu centers. We also discuss photoreduction, where the apical M–L bond is cleaved instead of generating a reactive intermediate, and how designing photolabile groups such as N–I moieties help bias L–X cleavage over M–L cleavage. The fourth chapter discusses the chemical non-innocence of supporting ligands, and how this affects the identity of the active catalyst. The last two chapters discuss methods to structurally characterize M–L multiply bound reactive intermediates. We demonstrate the affect changing anions bound in the primary

coordination sphere has on the selectivity of the intermediate produced and discuss the design of new photoprecursors to access novel reactive structures.

ACKNOWLEDGEMENTS

I would like to thank the chemistry department here at A&M for giving me the opportunity to pursue a PhD in chemistry.

I would like to thank Drs. Joseph Reibenspies and Yu-Sheng Chen for teaching me the ins and outs of crystallography and helping me troubleshoot the numerous problems I brought to them. I would also like to thank Drs. Greg Wylie and Doug Elliot for training me on the NMR instruments and specifically helping accommodate our cryogenic NMR experiments. Additionally, I would like to thank Dr. Vladmir Bakhmoutov for training me on EPR. I am also thankful to Yohannes Rezenom for running all our mass spectrometry and being extremely willing to try anything to get the data we needed. I would also like to thank Dr. Joshua Telser and Dr. Andrew Ozarowski for collecting HFEPR spectra and also helping to trouble shoot and simulate our X-band EPR spectra. Additionally, I would like to thank Dr. David Bergbreiter, Dr. Lei Fang, Dr. Sarbajit Banerjee, and Dr. Tamara Powers for letting me use their respective IR and UV-vis spectrometers. I would also like to thank the entire staff of the Rough Draught for providing a relaxing atmosphere for scholarly discussions.

I would also like to thank my fellow group members and friends for helping me develop into the scientist I am today. I would specifically like to thank Dr. Wenyang Gao, Dr. Anuvab Das, and Dr. Sung-Min Hyun for teaching me good experimental design and being great mentors when I started out. I would also like to specifically thank Andrew Ezazi, Mario Cosio, and Dr. Richard Thompson for being great friends and lab mates. I

would also like to thank the rest of the Powers Lab. We have a great work environment, and I don't think I'll ever work with such a great group of people again. I would also like the thank the two undergraduates I mentored, Madeline Hicks, and Hannah Goble, for helping me develop my mentorship skills and providing a fresh perspective.

I am incredibly grateful to my advisor, Dr. David Powers. Coming into graduate school I was not as prepared and up to speed as some of the other members of my cohort were. He was patient and allowed me the time to grow and learn, and to turn into the scientist I am today. I have also learned a great deal about how to communicate ideas in a direct and succinct manner, and also how to make pretty figures. He is a great educator and a good friend.

CONTRIBUTORS AND FUNDING SOURCES

Contributors

This work was supervised by a dissertation committee consisting of my advisor Professor David C. Powers, Professor François P. Gabbaï, and Professor Tim R. Hughbanks of the Department of Chemistry and Professor Cecilia Tommos of the Department of Biochemistry and Biophysics.

Anuvab Das contributed in conceiving the project in Chapter II. Madeline Hicks initially synthesized **II-13a**. Nattamai Bhuvanesh did the single-crystal refinement in Chapter II. Vladimir Bakhmoutov helped collect the X-band EPR spectra in Chapter II. William Seward built the sample holder used for cryogenic photolysis in Chapter II. Josh Telser helped analyze the X-band EPR in Chapter II. Andrew Ozarowski collected the HFEPR and simulated the X-band EPR in Chapter II. Kaleb Reid and Matthew Figgins helped with the calculations in Chapter II. Yohannes Rezenom collected the ESI-MS in Chapter II. Mario Cosio helped collect the Raman spectrum in Chapter II. Debabrata Sengupta helped conceive of the project and preformed the reactivity studies in Chapter III. Kaleb Reid helped collect the photocrystallography data and ran the computations in Chapter III. Yohannes Rezenom collected the ESI-MS and MALDI-MS data in Chapter III. Manuel Quiroz helped collect the GC data in Chapter III. Joseph Reibenspies helped refine the single-crystal X-ray data in Chapter III. Vladmir Bakhmoutov helped collect the X-band EPR spectra in Chapter IV. Yohannes Rezenom collected the ESI-MS data in Chapter IV. Mario Cosio helped collect the ^{1}H NMR data in Chapter IV. Nic Cool helped

collect the IR data in Chapter V. Hannah Goble helped preform the UV-vis reactivity studies in Chapter V. Arpan Paikar helped collect the photocrystallography data in Chapter V. Matthew Figgins preformed the calculations in Chapter V. Yu-Sheng Chen and Joseph Reibenspies helped with the refinement of X-ray data in Chapter V. Sven Schneider provided complexes **VI-8** and **VI-10** in Chapter VI. Kay Severin provided complex **VI-12** in Chapter VI. Yu-Sheng Chen and Joseph Reibenspies helped with the refinement of the single-crystal X-ray data in Chapter VI. Arpan Paikar and Kaleb Reid helped with the collection of the photocrystallography data in Chapter VI. Matthew Figgins ran the computational studies in Chapter VI. Computational portions of this research were conducted with the advanced computing resources provided by Texas A&M High Performance Research Computing.

Funding Sources

This work was funded by Texas A&M University, the Welch Foundation (A-1907), and the U.S. Department of Energy (DOE), Office of Science, Office of Basic Energy Sciences, Catalysis Program under Award Number DE-SC0018977. Single-crystal X-ray diffraction was collected at NSF′s ChemMatCARS Sector 15, which is principally supported by the Divisions of Chemistry (CHE) and Materials Research (DMR), NSF, under Grant NSF/CHE-1834750. Use of the Advanced Photon Source, an Office of Science User Facility operated for the U.S. DOE Office of Science by Argonne National Laboratory, was supported by the U.S. DOE under Contract DE-AC02-06CH11357. A portion of this work was performed at the National High Magnetic Field

Laboratory, which is supported by NSF Cooperative Agreement DMR-1644779 and the State of Florida.

TABLE OF CONTENTS

Page

LIST OF FIGURES

Page

LIST OF TABLES

CHAPTER I

INTRODUCTION: SPECTROSCOPIC CHARACTERIZATION OF METAL NITRENOIDS

I.1. Introduction

C–H bonds are the most ubiquitous functional groups found in nature. While C–H bonds are abundant, they are oxidatively robust due to the lack of polarity about the C–H bond and resulting high bond dissociation energy (BDE).[1] Classic methods to functionalize unactivated C–H bonds are based on free-radical processes, which typically proceed with preference for cleavage of the weakest available C–H bond but are not highly selective.[2, 3] Significant research effort has been pursued towards selective C–H functionalization using transition metal complexes.[4-12] Terminal metal–ligand (M–L) multiply bonded species (L = CR^{3-}, CR_2^{2-}, O^{2-}, NR^{2-}, and N^{3-}) are now known to be ubiquitous intermediates in both biological[13-15] and metal-catalyzed synthetic C–H functionalization reactions.[16-23] For example, C–H hydroxylation chemistry in cytochrome P450 enzymes proceeds at an active site-bound terminal Fe oxo species, generated by the combination of O_2 and NADH.[24-27] Similarly, a non-heme Fe_2 site housed at the core of soluble methane monooxygenase (sMMO) catalyzes the hydroxylation of methane via the intermediacy of an aerobically generated Fe oxo intermediate (both terminal and bridging oxo intermediates have been proposed).[28] Abiotically, cytochrome P450 mimics, metalloporphyrins, have been used to facilitate carbene,[29] nitrene,[30, 31] and oxo transfer,[21,

[29] all of which are hypothesized to pass through a transient M–L multiply bound species.[32-35]

This dissertation discusses the structures and reactivity of M–L multiply bound fragments, specifically M–NR fragments that are relevant to C–H functionalization. In this context, this chapter will introduce the electronic structure and reactivity of porphyrin-supported metal nitrenoids. In addition, photochemical methods to access reactive M–L multiply bound intermediates and the processes that complicate the photosynthesis of these species will be discussed.

I.2. Organic Nitrenes

Nitrenes are compounds that include monovalent nitrogen centers with six valence electrons about the nitrogen. The electron deficiency at nitrogen gives rise to highly electrophilic reactivity towards a diverse scope of substrates (Figure I-1). The parent nitrene, NH (**I-1**) which is also known as imidogen, features a nitrogen that is sp hybridized with a triplet ground state where the electrons reside in degenerate p_x and p_z orbitals. The triplet state of NH is 36 kcal/mol more stable than the corresponding singlet. The triplet-singlet energy gap is sensitive to the identity of the R group attached to the nitrene.[36]

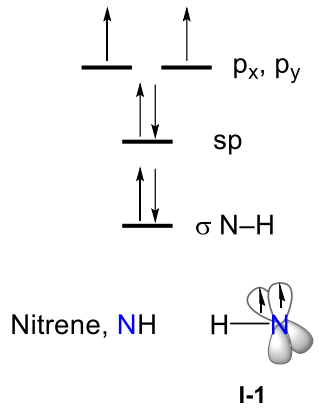

I-1

Figure I-1. The molecular orbital diagram of imidogen (NH, I-1), which highlights the triplet ground state.

The reactivity of nitrenes is tuned via π-donation from the R group, which lessens the triplet-to-singlet gap, and makes the singlet reaction manifold available. While the involvement of singlet nitrenes is debated in the Curtius rearrangement and the Schmidt reaction, singlet nitrenes are accessible and involved in other reaction schemes.[37, 38] A common strategy to access singlet nitrenes involves installation of an ester or benzoyl group next to the nitrene moiety.[39-43] This results in a nitrene with a singlet ground state due to donation from the lone pair of the oxygen into the empty 2p orbital on the nitrene nitrogen. Applying this strategy, Toscano and coworkers photolyzed benzoyl azide (**I-2**) with 254 nm light in an Ar matrix at 12 K, which yielded singlet benzoyl nitrene **I-3** which featured characteristic peaks in the IR and UV-vis spectra centered at 2270 cm^{-1} and 300 nm, respectively (Figure I-2).[44] These new features are well-matched to the computed spectra via DFT.

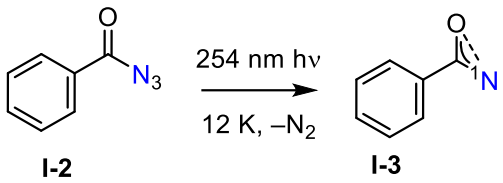

Figure I-2. Photolysis of I-2 at 12 K results in N_2 extrusion, generating nitrene I-3. Donation from the lone pair on the oxygen into the 2p orbital on the nitrene nitrogen results in the stabilization of the singlet state relative to the triplet state.

Tuning the singlet-to-triplet gap in nitrenes can result in a small energy difference between them, thus both the singlet and triplet states can be populated. In a seminal study by Lwowski, thermolysis of ethoxycarbonylazide (**I-4**) generates singlet nitrene **I-5**, which participates in stereospecific insertion with substituted olefins to give rise to a single aziridine diastereomer.[45, 46] Over the course of the reaction, **I-5** decays into the triplet ground state (**I-6**).[47] Triplet nitrene **I-6** reacts with olefins in a non-stereospecific process, originating from the asynchronous reaction mechanism generating a carbon radical which allows the C–C bond to rotate, depicted in Figure I-3c.[48, 49]

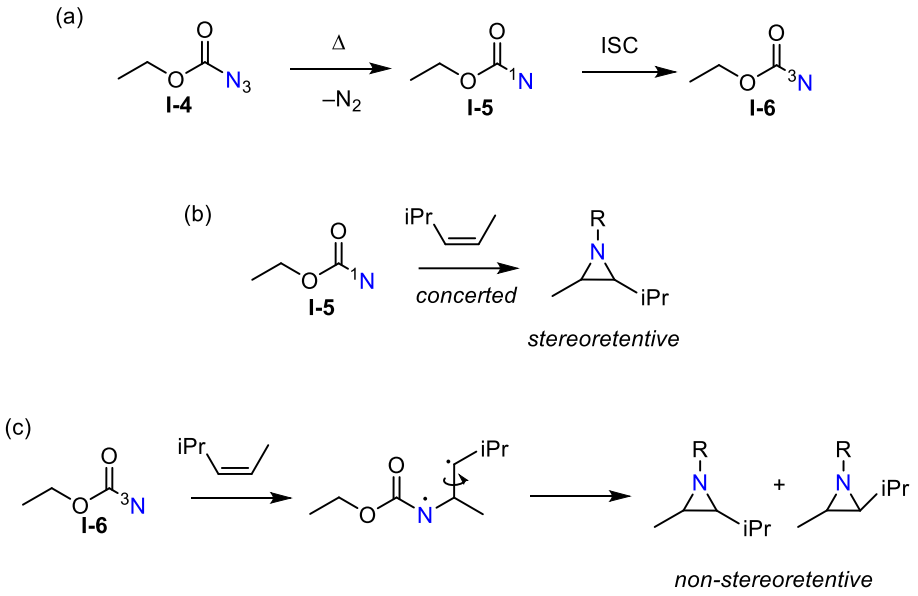

Figure I-3. Thermolysis of I-4 results in N_2 extrusion generating alkyl nitrenes. (a) Thermolysis of **I-4** results in singlet nitrene **I-5**, which then undergoes intersystem crossing (ISC) yielding triplet nitrene **I-6**. (b) Reaction of singlet nitrene **I-5** with substituted olefins in a concerted manner results in aziridination with maintained stereochemistry. (c) The reaction with triplet **I-6** occurs via an asynchronous mechanism, where rotation about the C–C bond results in a non-stereoretentive reaction.

In contrast to the photolysis of aryl and carboxyl azides such as **I-2** and **1-4**, photolysis of alkyl azides often results in imine formation via hydrogen atom transfer from a vicinal C–H bond (HAT), or isonitrile formation via carbon migration.[50-52] Imine formation is hypothesized to occur via a concerted rearrangement of a singlet excited state of the alkyl azide, rather than from an alkyl nitrene.[50, 53-55] With these challenges in mind, the Gudmundsdóttir group used azidoacetophenone **I-7** to access a triplet nitrene, via intramolecular triplet sensitization (Figure I-4a).[56] Photolysis of **I-7** in a deoxygenated toluene solution resulted in product **I-10**, which formed via combination of nitrene **I-8**, and acetophenone radical **I-9** (Figure I-4b). Verifying that product **I-10** was made via triplet nitrene **I-8**, azide **I-7** was thermalized, bypassing any triplet sensitization, yielding

product **I-12**. Thermolysis of **I-7** is hypothesized to form a singlet nitrene (**I-11)** and subsequently rearranges to **I-12 (**Figure I-4c). This strategy has also been applied to other alkyl azides such as adamantyl and benzyl azide, via intermolecular triplet sensitization with benzophenone and acetone.[57]

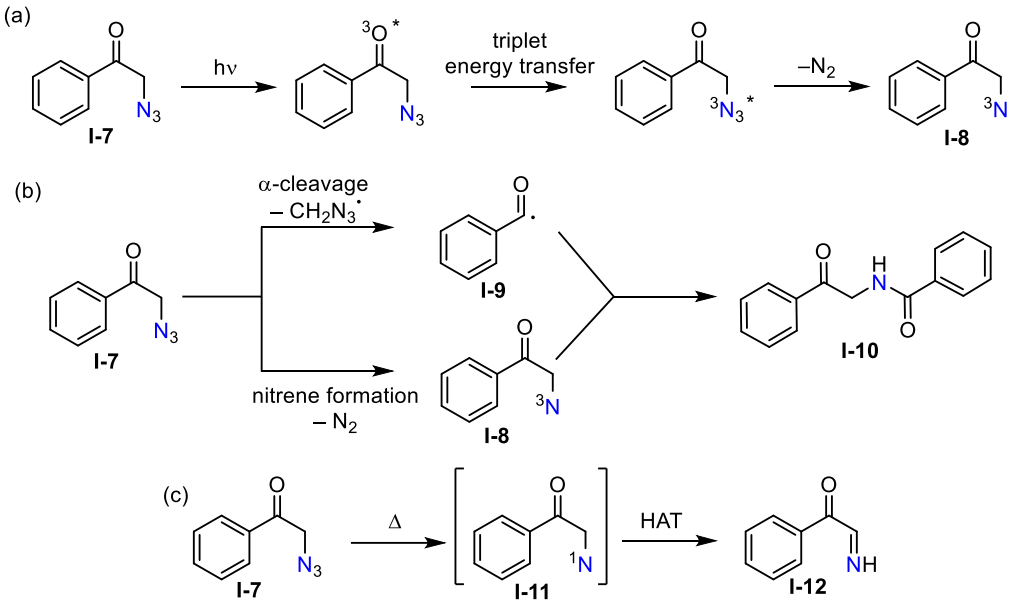

Figure I-4. Generation of triplet alkyl nitrenes via intramolecular triplet sensitization. (a) Photolysis of azidoacetophenone I-7 generates an excited state triplet, which then undergoes triplet energy transfer yielding a triplet alkyl azide. The triplet alkyl azide loses N_2 which furnishes triplet alkyl nitrene I-8. (b) Photolysis of I-7 results in both nitrene formation and α-cleavage of the C–C bond forming radical I-9. Radical I-9 can intercept nitrene I-8 in solution, forming product I-10. (c) Access to imine I-12 is facilitated via thermolysis of azide I-7, which circumvents any triplet sensitization. Singlet nitrene I-11 is hypothesized to be the intermediate.

I.3. Porphyrin Supported Metal Nitrenes

Since the seminal discovery of copper promoted sulfonyl azide decomposition in 1967 by Kwart and Khan, nitrene transfer catalysis has become an important technology

for the introduction of nitrogen-based functional groups in organic synthesis.[58, 59] A general nitrene insertion mechanism features a ligand supported metal center that reacts with a nitrene source, which are commonly iminoiodinanes, organic azides, hydroxylamines, and haloamides to form a terminal M–NR species which then insert into C–H bonds or C=C bonds, furnishing aminated or aziridinated products respectively (Figure I-5). While there are many ligand platforms that are available to support metal nitrenoids, the introduction of this thesis will mainly focus on 3*d* metal porphyrin supported nitrenoids.

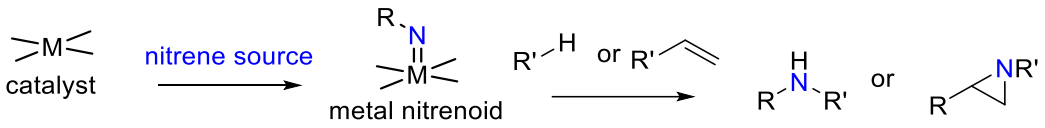

Figure I-5. General nitrene insertion mechanism for metal nitrenoids. Common nitrene sources are comprised of iminoiodinanes, organic azides, haloamides, and hydroxylamines. Metal nitrenoids will either insert into C–H bonds to form C–N bonds, or insert into C=C bonds to form aziridines.

The bonding picture for a transition metal center with a nitrene fragment depends on the relative orbital energies of the two fragments (Figure I-6).[60] The relatively high d-orbital energies of early transition metals results in highly polarized M–N bonding, where the electron density resides on the nitrogen center, resulting in observed nitrogen-centered nucleophilicity, and in which the nitrogen ligand can be considered as a –2 fragment and are called metal imido complexes. As the d-orbital energy of the metal fragment decreases, the M–N bond gains more covalent character, thus electron density is shared equally across the M–NR fragment, and in which the nitrogen ligand acting as a –1 donor.

Complexes that are described by this bonding picture are referred to as metal iminyl or metal nitrene radical complexes. For late-transition metals, the d-orbital energy is lower than the 2p nitrogen orbital energy, thus the HOMO of the M–NR complex is predominantly metal-centered. This resulting ligand field results in electron density being metal-centered, thus the nitrene fragment features only 6 valence electrons which results in an is electrophilic nitrogen fragment. These species are called metal nitrene complexes. Similar to free nitrenes, the nitrene fragment can bind as either singlet or triplet configuration. Because intimate knowledge of the bonding picture of specific complexes is not always available, this thesis will generically refer to M–NR complexes as metal nitrenoids.

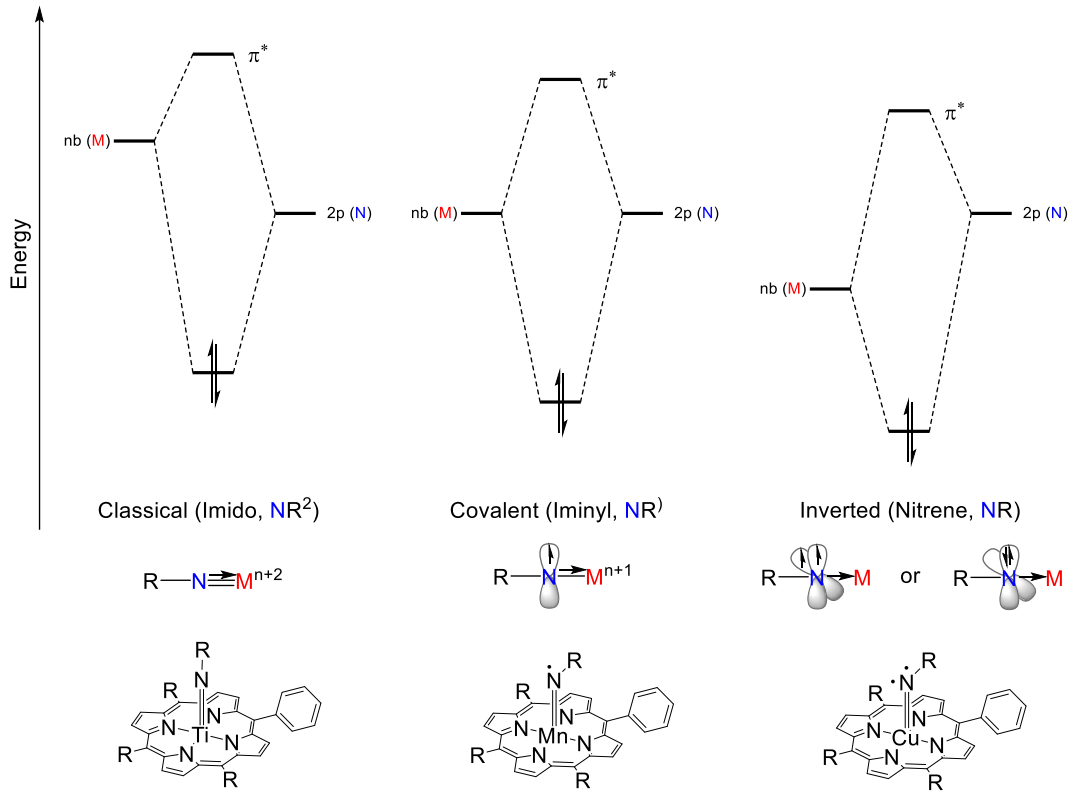

Figure I-6. Impact of frontier molecular orbital energies on the bonding between NR fragments and transition metals. In early transition metals, such as Ti, the high d-orbital energies yield a HOMO that is mainly nitrogen in character, thus the electron density residing on the nitrogen makes it highly nucleophilic and is an imido complex. As the metal d-orbital energies decreases across the periodic table, the resulting HOMO becomes more covalent and has equal metal and nitrogen character. Complexes that resemble this are called iminyl radicals. At the limit of the transition metals, the 3d orbital energy becomes lower than the 2p nitrogen orbital, resulting in an inverted ligand field. The resulting HOMO is mainly metal in character, resulting in a nitrogen fragment that has six valence electrons about the nitrogen. These species are called metal nitrenes and are exquisitely electrophilic due to the lack of electron density about the NR fragment.

Inspired by the ability of cytochrome P450 to insert into C–H bonds and forge C–O bonds,[24-27] Breslow and Gellman demonstrated the tosylamidation of unactivated C–H bonds using Mn (**I-13)** and Fe (**I-14**) porphyrin-supported catalysts.[61] They reported use of a nitrene transfer reagent, an iminoiodinane (PhINTs) to deliver *N*-tosyl fragments that

subsequently insert into the C–H bond of cyclohexane (Figure I-7a). Breslow and coworkers also demonstrated intramolecular reactivity from both Fe and Mn porphyrin complexes, aminating the appended sp^3 C–H bond on the iminoidodinane (Figure I-7b).[30] Furthermore, Mansuy and coworkers have shown that Mn porphyrins are competent at allylic amination, aminating *cis*- and *trans*-2-hexene.[62] Use of manganese tetraphenylporphyrin (**I-15**) resulted in almost total selectivity for allylic amination, where when a more electron poor porphyrin was used (**I-16**) the reaction yield was relatively unchanged however the selectivity for allylic amination was decreased by an order of magnitude. These latter examples highlight that varying both the use of nitrene precursor and porphyrin support will affect the overall selectivity and yield of the reaction.

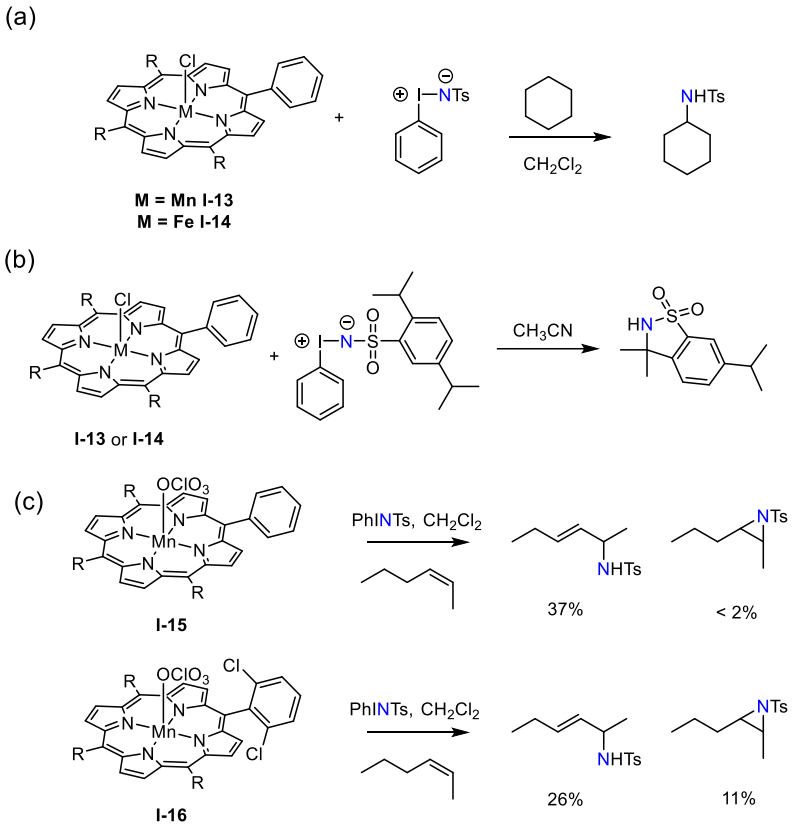

Figure I-7. Porphyrin-supported Mn(III) and Fe(III) complexes catalyze C–N bond formation. (a) Mn or Fe metalloporphyrin I-13 or I-14 catalyzed insertion of an tosyl nitrene fragment, from PhINTs, into the C–H bond of cyclohexane. (b) Similar to the reaction with cyclohexane, both I-13 and I-14 catalyzed the intramolecular insertion into the α-C–H bond of the appended isopropyl group. (c) Porphyrin I-15 showed a near complete preference towards intermolecular allylic amination, whereas use of a more electronegative porphyrin support in I-16 produced more aziridine product. This highlights that the electronic structure of the metalloporphyrin can affect the selectivity of the reaction.

In 2000 Breslow reported the first regio- and stereospecific amidation of a C–H bond from a Mn porphyrin.[63] Mn porphyrin **I-17** catalyzed the amidation of equilenin acetate **I-18** in 47% yield (Figure I-8a). Subsequently, the Che lab reported catalytic chiral Mn porphyrin amidation of C–H and C=C bonds.[64] Utilization of Mn catalyst **I-19** affords up to 57% *ee* and yields in the high 90% of amidated substrates (Figure I-8b). Additionally,

use of $PhI(OAc)_2$ and NH_2R produced the iminoiodinanes of interest *in situ*, circumventing the need to prepare and isolate the reagent beforehand.

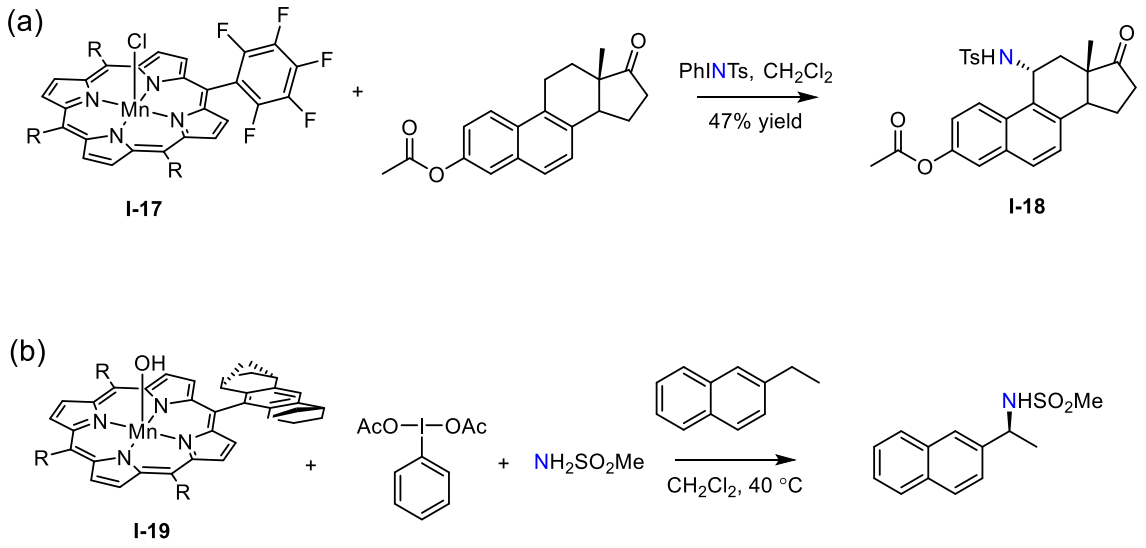

Figure I-8. Use of Mn porphyrins in chiral catalysis. (a) Mn(III) pentafluoroporphyrin catalyzes selective amidation of equilenin acetate, solely forming product I-18. (b) Chiral porphyrin I-19 was utilized to produce chiral products, such as a chiral napthyl sulfonamide.

The White lab has pioneered the use of phthalocyanines to support Mn nitrenoids in catalysis.[65] Perchlorinated phthalocyanine-supported Mn catalyst **I-20** catalyzes benzylic position of dozens of substrates with iminoiodinanes. Kinetic isotope effect (KIE) studies of **I-21** and d_2-**I-21** show that the KIE is 2.5(2), which was interpreted as consistent with a stepwise, hydrogen-atom abstraction (HAA)-and radical rebound (RR) mechanism. A similar HAA-RR mechanism has been proposed for metalloporphyrin-catalyzed reactions.

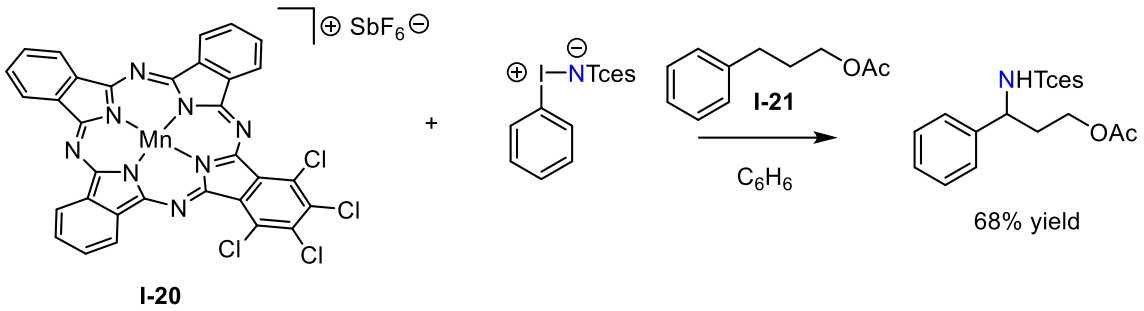

Figure I-9. Mn phthalocyanine I-20 was used in conjunction with iminoiodinanes to forge C–N bonds via insertion into benzylic C–H bonds.

Inspired by the seminal contributions that Breslow and Gellman shown with iron porphyrins,[30, 61] the Che group pioneered the use of iron porphyrins in combination with organic azides to forge C–N bonds.[29, 66] In their first report, perfluorinated tetraphenylporphyrin Fe(III) complex **I-22** was demonstrated to which catalyze benzylic and aliphatic C–H bond amination (Figure I-10a).[67] Moreover, this same system facilitates intramolecular C–H insertion to afford of indolines, tetrahydroquinolines, and quinazolinones (Figure I-10b).[68] Appending two NHC moieties to the apices of **I-23** facilitates the intramolecular reactivity of aliphatic azides, where amination of benzylic, allylic, tertiary, secondary, and primary C–H bonds was accomplished. (Figure I-10c).[69]

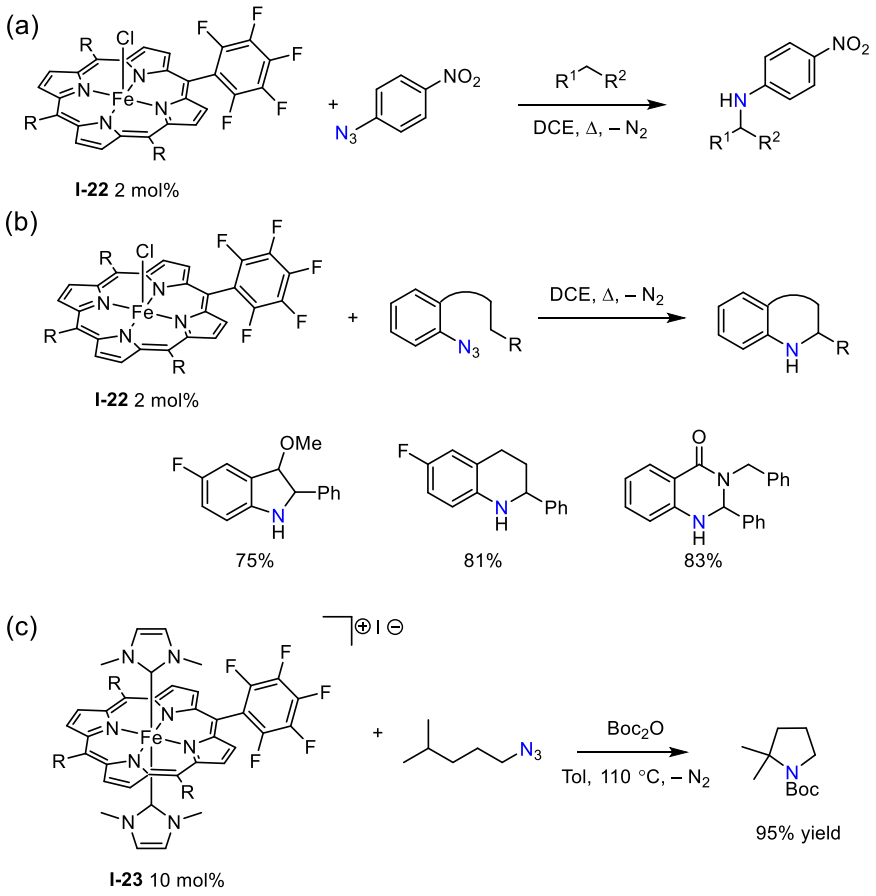

Figure I-10. Perflourinated Fe(III) porphyrins catalyze intra- and intermolecular C–N bond formation utilizing azide starting materials. (a) Fe porphyrin I-22 is used to generate an aryl nitrene, which will insert into intermolecular aliphatic and benzylic C–H bonds. (b) I-22 is utilized to catalyze the formation of heterocycles such as indolines, tetrahydroquinolines, and quinazolinones in high yields. (c) Implementation of a Fe perfluorinated porphyrin with two NHCs installed at the apices (I-23) allows for the use of alkyl azide substrates, which will undergo intramolecular insertion to form 5-membered rings, inserting into primary, secondary, and tertiary C–H bonds.

Cenini, de Bruin, and Zhang have advanced porphyrin-supported Co(II) catalysts for nitrene transfer to C–H and C=C bonds.[29, 66, 70] The first report of Co porphyrin-catalyzed intermolecular nitrene transfer was by Cenini and coworkers, who reported the use of Co(II) octaethylporphyrin to effect allylic amination of cyclohexene with aryl

azides.[71, 72] Similarly, Zhang reported a tosyl nitrene transfer reaction using bromamine-T and Co(II) porphyrins to promote nitrene transfer to C–H and C=C bonds.[73-75] Since Zhang's initial report, the combination of Co(II) porphyrins and organic azides has been established as efficient conditions for inter- and intramolecular amination of C(sp^3)–H bonds including benzylic, allylic, and aliphatic positions.[76-78] Moreover, Zhang and coworkers have developed new classes of porphyrin ligands that feature amide hydrogen bond doners that both enhance the catalytic activity of the Co(II) catalysts, but also achieve highly enantioselective C–H amination.[79-96]

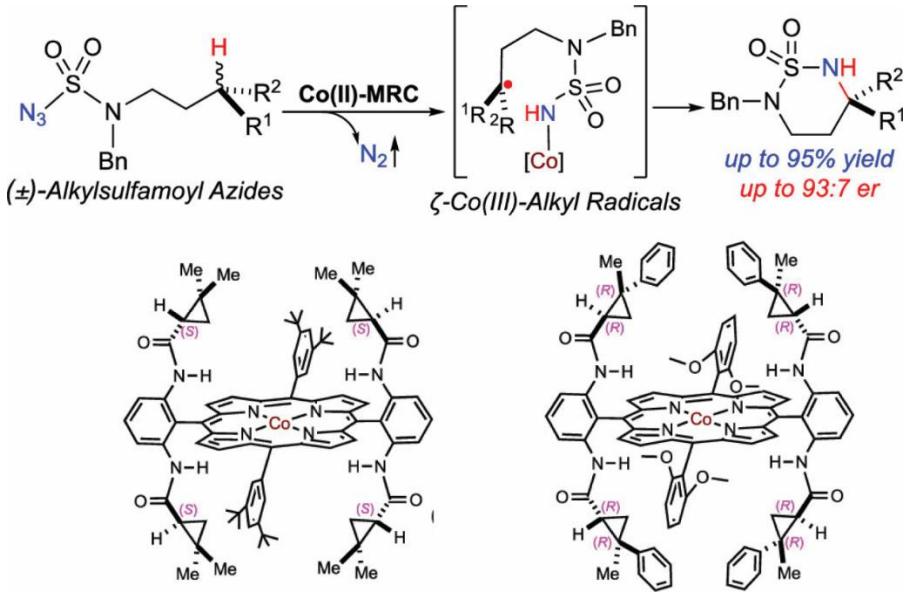

Figure I-11. Intramolecular amination reactions using sulfonyl azides. Top: Cyclization of alkylsulfamoyl azides is catalyzed via Co(II) porphyrin species, which is hypothesized to proceed via a HAA-RR mechanism, which is pictured here. Furthermore, use of chiral porphyrin scaffolds allows for enantioselective nitrene transfer. Bottom: The chiral porphyrin scaffolds that were designed and synthesized by Zhang and coworkers. Adapted with permission from reference 93. Copyright 2020 American Chemical Society.

The research in this thesis is motivated by the observed C–H insertion chemistry exhibited by these metalloporphyrin-supported nitrenoids. The central motivation in the

later chapters is to characterize the ligand-supported reactive intermediates at the heart of C–H cleavage and C–N construction in these reactions. Due to the kinetic lability of porphyrin supported Mn and Fe nitrenoids, both reactive intermediates are challenging to spectroscopically and structurally characterize. The following sections in this chapter focus on methods to characterize porphyrin supported reactive intermediates, both through steady-state spectroscopy and/or photosynthetic methods.

I.4. Steady-state Spectroscopic Characterization of Porphyrin Supported Metal Nitrenes

Due to the exquisite reactivity, and correspondingly fleeting lifetimes, observation of thermally generated metal nitrenoids that are capable of C–H functionalization is often not feasible. In the following section, select examples are discussed where the lifetime of the intermediate is compatible with steady-state spectroscopic methods. Techniques to characterize short lived intermediates include stop-flow spectroscopy, and transient absorption spectroscopy. These latter techniques will be discussed in section I.5.1.

Zhang, de Bruin, and coworkers fully characterized the Co(III) iminyl radical **I-25** using EPR, UV-vis, IR, VCD, ESI-MS, and XAS.[35] Exposure of **I-24** with a 100-fold excess of nosyl azide results in a stark change in the room temperature X-band EPR spectrum (Figure I-12). Signals corresponding to Co(II) vanished, and a new signal centered around $g = 2.005$ evolved, which was ascribed to Co(III) iminyl radical **I-25**. The experimentally observed EPR spectrum is well-matched to the calculated EPR spectrum via DFT. Compound **I-25** was also characterized with ESI-MS, where injection of a

C_6D_6/MeCN solution of Co(tpp) and nosyl azide yielded a signal at 872 *m/z*. Generation of intermediate **I-25** was monitored by UV-vis spectroscopy. Upon mixing **I-24** and nosyl azide, new UV-vis spectral features were observed at 420, 550, 650 and 780 nm. Well-anchored isosbestic points indicated the absence of steady-state intermediates between **I-24** and **I-25**. Finally, the oxidation state and coordination environment of the Co ion in **I-25** was investigated via XAS. First, a XANES spectrum of the Co K-edge was collected and featured a pre-edge transition at 7722.8 and 7710.2 eV, which is consistent with a cobalt (III) iminyl radical species. Moreover, the EXAFS analysis indicated that the coordination geometry about Co in **I-24** is C_{4v} with six ligands attached, with an average distance of all N/O scatters at 1.95 Å from the cobalt center. In addition to formation of complex **I-24**, a Co(III) *bis*-nitrenoid could also be accessed via the exposure of Co(tpp) to excess **I-26**. This *bis*-nitrenoid was also characterized via the same spectroscopy as **I-25**, which showed that *bis*-nitrene **I-27** was indeed a Co(III) bis iminyl radical, that oxidized the porphyrin ring via one electron (Figure I-12).

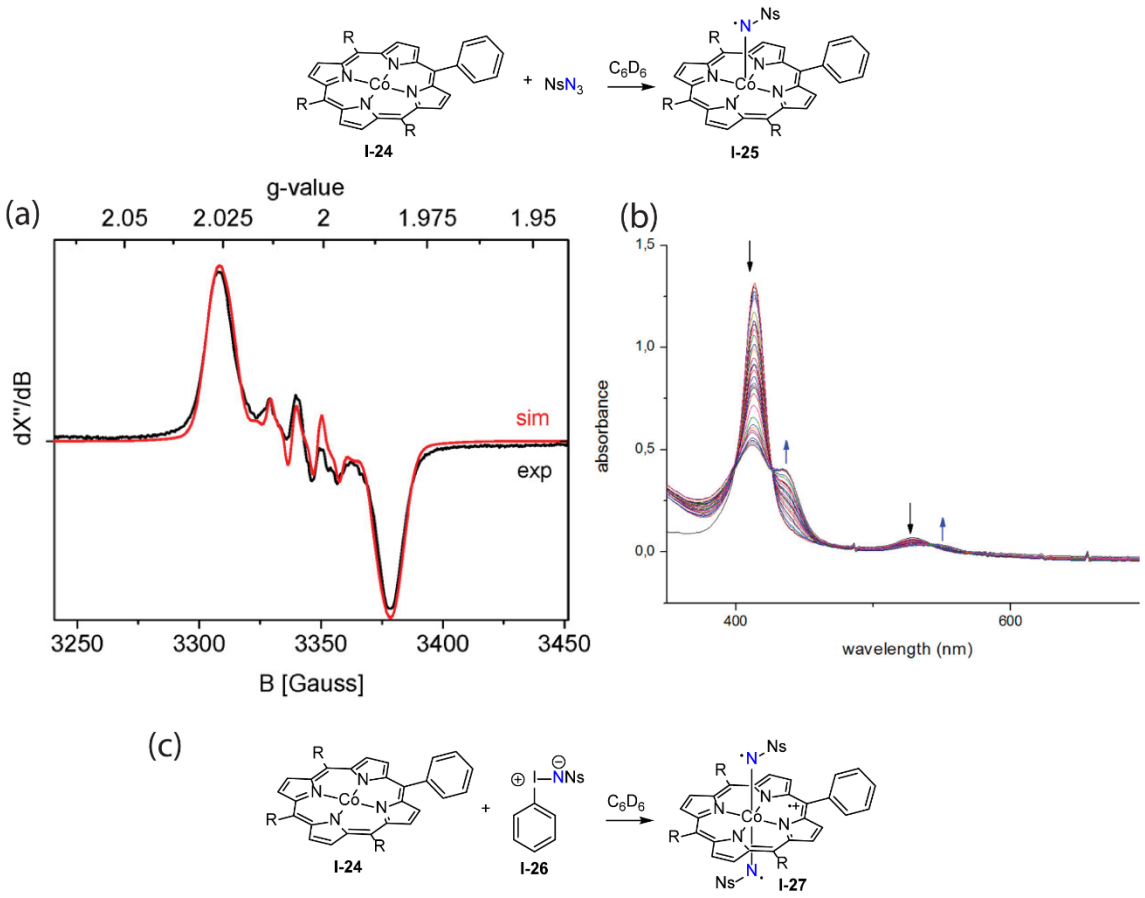

Figure I-12. Characterization of a reactive Co(III) iminyl radical via steady-state spectroscopy. (a) This X-band EPR spectrum is obtained with Co(II) porphyrin I-24 is exposed to an 100-fold excess of nosyl azide. The growth of the shown signal at g = 2.005, which comes from the S = ½ nitrogen center, is accompanied by the loss of the signal from I-24 at g = 6, suggesting complete conversion of I-24 to I-25. (b) Under identical conditions to the EPR, the formation of I-24 from I-25 is tracked via UV-vis spectroscopy. New peaks appear at 420, 550, 650 and 780 nm, which also accompanied by well-anchored isosbestic points, indicates the absence of any steady-state intermediate between formation of I-24 from I-25. (c) A bis-nitrenoid I-27 is accessed by exposing I-24 excess iminoiodinane I-26. Adapted with permission from reference 35. Copyright 2015 American Chemical Society.

In contrast to the characterized Co(III) iminyl radical **I-25**, which displays a relatively long lifetime, the lifetimes of porphyrin-supported Mn and Fe reactive intermediates, specifically nitrenoids and oxos, are often too short to observe via steady-

state spectroscopy. Modulation of the ancillary ligand field can stabilize these species and enable characterization. For instance, tris-anionic tetrapyrroles such as corroles and corrolazines have been used instead of porphyrins, which typically result in an isolable intermediate.[97-101] The Abu-Omar group isolated a terminal Mn(V) imido (**I-28**) via photolysis of Mn pentafluorocorrole and mesityl azide as shown in Figure I-13a.[102] Imido **I-28** was identified to be a low spin d^2 diamagnetic species via NMR, which was also supported by UV-vis measurements. In addition, the Goldberg group used a perarylated Mn corrolazine in the presence of mesityl azide to generate and isolate Mn(V) imido **I-29** (Figure I-13b).[103] Similarly to **I-28**, Mn(V) imido **I-29** is low spin d^2 diamagnetic species and is thoroughly characterized via ^{1}H NMR, UV-vis, MALDI-MS, EA, and single-crystal X-ray diffraction. Both **I-28** and **I-29** are unreactive towards substates that contain activated C–H bonds or olefins, which reflects the significant stabilization afforded by the corrole and corrozaline ligands. In 2006, Abu-Omar and coworkers reported the synthesis of **I-30**, which features the same corrole ligand as **I-28**, but with an *N*-tosyl group not an *N*-mesityl substituent.[104] **I-30** was not isolated as a solid but was stable in solution on the order of hours, which enabled spectroscopic characterization of **I-30** as a high spin d^2 paramagnetic complex. Similar to **I-28** and **I-29**, **I-30** does not insert an –NTs fragment into the olefin of styrene. However, when an excess of PhINTs is present with **I-30**, a –NTs fragment is transferred to styrene making the aziridine. Kinetic and stop-flow spectroscopic studies indicated that the active group transfer reagent is an adduct of **I-30** with PhINTs, depicted in Figure I-13c.

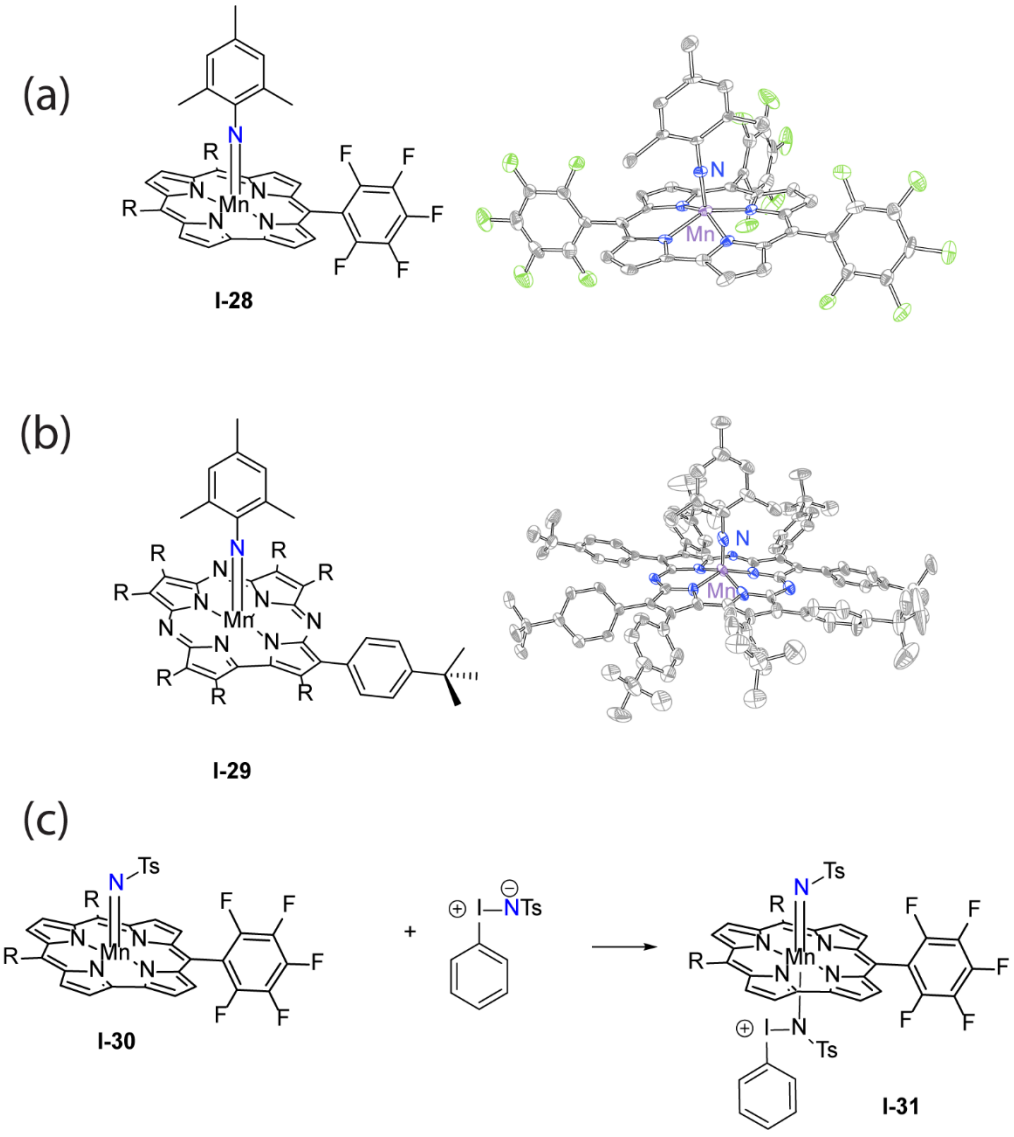

Figure I-13. Perturbation of the tetrapyrrole scaffold facilitates structural characterization of Mn(V) imidos. (a) Pentaphenylcorrole supports a Mn(V) imido, that is characterized via spectroscopy and single-crystal X-ray diffraction. (b) A perarylated corrazaline facilitated structural characterization of a Mn(V) imido. (c) Stabilized tetrapyrrole complexes are amenable towards steady-state spectroscopies, elucidating new reaction pathways, such as a Mn(V) imido iminoiodinane adduct which an active nitrene transfer reagent.

Perturbation of the porphyrin scaffold is not always required to spectroscopically characterize Mn nitrenoids; modulation of the *N*-substituent also impacts the lifetime of

the intermediate. Groves and coworkers demonstrated that Mn(V)N(tpp) (**I-32**), a stable and isolable terminal nitride, acts as a nucleophile towards trifluoroacetic anhydride (TFAA), resulting in nitrenoid **I-33** (Figure I-14a).[105] Upon reacting with TFAA, the d^2 low spin nitride **I-32** transforms into high spin d^2 Mn(V) nitrenoid (**I-33**), which is characterized by paramagnetic shifts in the ^{1}H NMR spectrum, a distinct UV-vis Soret band, and a stretch in the IR spectrum at 1745 cm^{-1} which corresponds to the carbonyl stretch of the newly formed *N*–trifluoroacyl moiety. **I-33** reacts with excess cyclooctene forming aziridine **I-34** as the sole product in 84% yield, with no trace of allylic amination. Bottomley and coworkers further explored this system, investigating the role of the identity of the porphyrin and R-group on the kinetics of the formation of the Mn nitrenoid.[106] Porphyrin rings that were more basic, such as **I-35** and **I-36**, had higher rate constants, which was rationalized due to the increased nucleophilic character of the Mn≡N fragment. Expectedly, the anhydrides that had most electron withdrawing substituents reacted faster than substituents without, such as TFAA versus acetic anhydride.

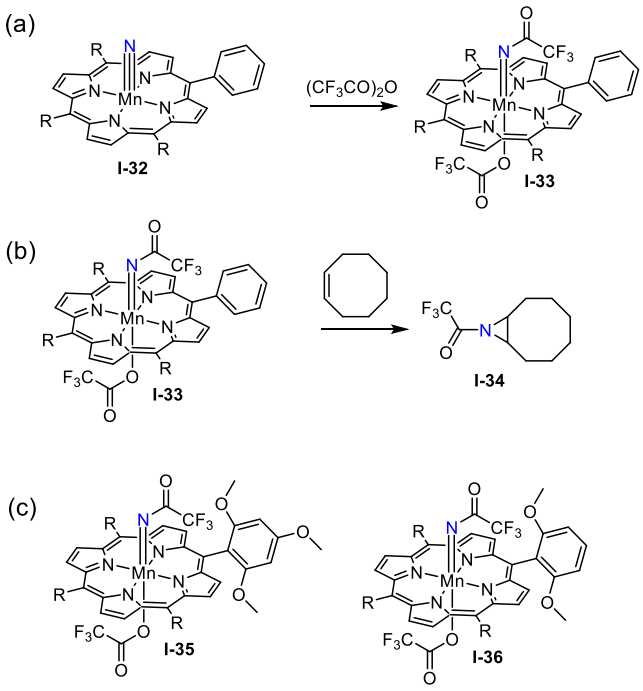

Figure I-14. Synthetic modification of Mn(V) nitrides to access group transfer reagents. (a) Mn(V) nitride I-32 acts as a nucleophile towards trifluoracetic acid anhydride generating imido I-33. (b) Imido I-33 will insert into a C=C bond, solely forming aziridine I-34, with no allylic amination detected. (c) Varying the donicity of the supporting porphyrin ligand affects the rate of imido formation.

I.5. Photochemistry

I.5.1 Synthetic Photochemistry

Synthetic photochemistry facilitates access to reactive species under conditions that allow for characterization by time-resolved or cryogenic methods without necessitating stabilization via synthetic derivatization. The following two examples in this thesis feature metalloporphyrin oxo complexes, and not metalloporphyrin nitrenoid complexes, due to a dearth of metal nitrenoid photoprecursors. Zhang and coworkers demonstrated application of time-resolved photochemistry towards the characterization of reactive and transient Fe porphyrin oxo complexexes.[107] Steady-state photolysis of a series

of meso substituted Fe(III) bromate porphyrin complexes resulted in heterolytic cleavage of the O–Br bond yielding either a Fe(IV) oxo with singly oxidized radical cation porphyrin ring, or a Fe(IV) neutral oxo (Figure I-15a). When photolyses were monitored by UV-vis spectroscopy, both tetraphenylporphyrin **I-37** and tetramesitylporphyrin **I-38** resulted in Fe(IV) radical cation complexes which was indicated via peaks at 404 and 656 nm (Figure I-15b). However, when the photolysis of perfluorinated tetraphenylporphyrin bromate complex **I-39** was monitored by UV-vis spectroscopy, new peaks were seen at 410 and 548 nm, which were interpreted as diagnostic of a neutral Fe(IV) oxo (**I-42**) (Figure I-15c).[108] All three compounds are competent OAT reagents, inserting into C–H and C=C bonds. Fe(IV) radical cation complexes **I-40** and **I-41** react with substrates with rates 3 orders of magnitudes larger than **I-42**. The hypothesized primary photoproduct from all three compounds is a Fe(V) oxo which is formed via heterolytic cleavage of the O–Br bond (Figure I-15a). Fe(V) oxos have been observed and are thermally accessible, and have been shown to isomerize to the Fe(IV) oxo radical cation, which occurs in compounds **I-40** and **I-41**.[109, 110] However, the Fe(V) oxo formed via photolysis of **I-39** comproportionates with another equivalent of **I-39** to form the neutral Fe(IV) oxo **I-42**. **I-42** does not undergo internal electron transfer due to how electron deficient the supporting porphyrin ring is, thus the unstable Fe(V) oxo comproportionates with **I-39** to yield **I-42**. Other studies have similar findings, where oxidation of perfluorinated Fe(III) porphyrins with iodosylbenzene results in **I-42**, which occurs through a similar mechanism.[111]

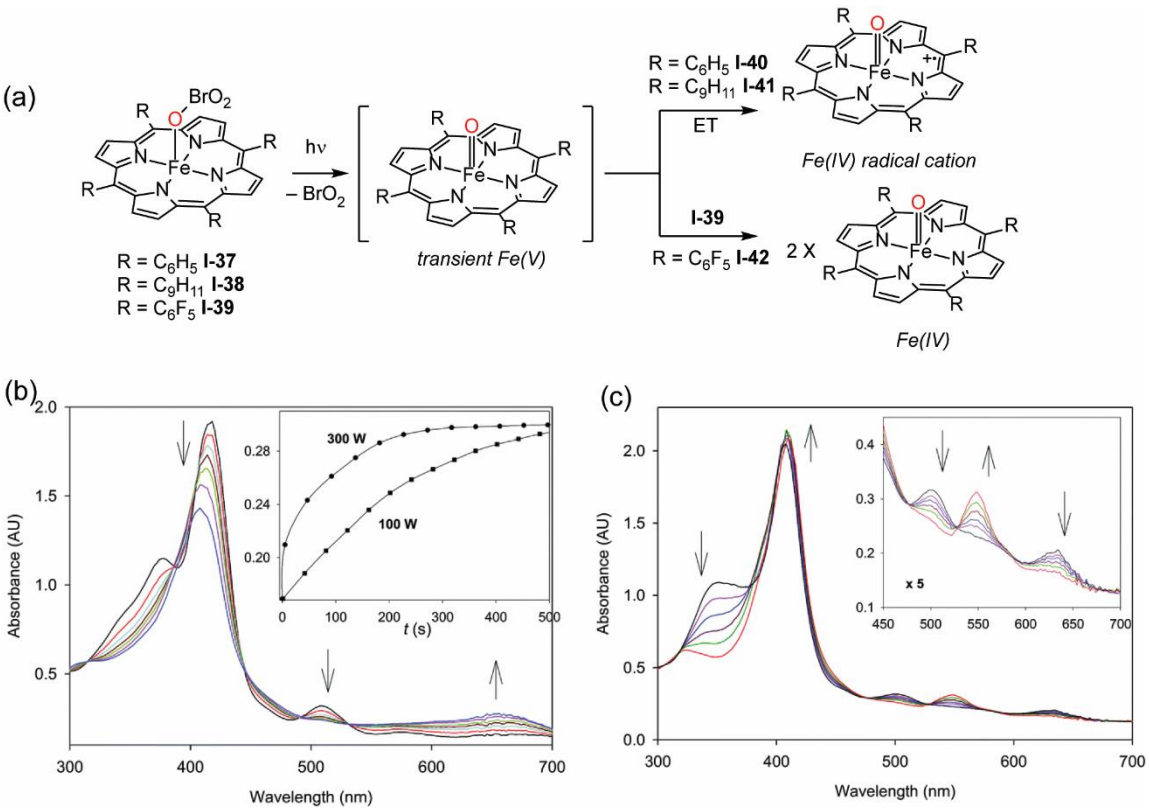

Figure I-15. Different Fe(OBrO$_2$) porphyrin photoprecursors are used to access high-valent Fe oxos. (a) Photolysis of all three Fe complexes is hypothesized to result in heterolytic cleavage of the O–Br bond, unveiling a Fe(V) oxo. Products of the photolysis of complexes I-37 and I-37 undergo internal electron transfer to yield a Fe(IV) oxo with a singly oxidized radical cation porphyrin. The Fe(V) generated from the photolysis of I-39 does not undergo electron transfer, but will comproportionate with unreacted I-39 forming a Fe(IV) oxo with a unperturbed porphyrin ring. (b) Tracking the photolysis of I-37 via UV-vis shows new peaks at 404 and 656 nm, which are indicative of Fe(IV) radical cation species. (c) Tracking the photolysis of I-39 via UV-vis shows new peaks at 410 and 548 nm, which is diagnostic of a neutral Fe(IV) oxo. Reproduced from reference 107 with permission from the Royal Society of Chemistry.

Further showcasing the utility of synthetic photochemistry, Newcomb and coworkers photochemically generated and characterized transient Fe(V) oxo species via laser flash photolysis (LFP).[112, 113] The transient Fe(V) oxos were found to react with substrate 4-5 orders of magnitude faster than Fe(IV) oxo radical cation species.[112, 113]

Exposure of Fe(III) porphyrin **I-43** to $Fe(ClO_4)_3$ initially results in Fe(IV) species **I-44** (half-lives of ca. 10 s) before ultimately generating Fe(III) complex **I-45** supported by a porphyrin radical cation ligand (Figure I-16a).[114-117] These relatively long lived Fe(IV) species were generated in a stop-flow setup, and then were subsequently photolyzed with 355 nm light via LFP. The combination of stop-flow and subsequent LFP results in homolytic cleavage of the O–Cl bond, yielding a Fe(V) oxo porphyrin **I-46** which was indicated by new peaks in the UV-vis at ~400 nm (Figure I-16b). Both the peak placement and the lifetimes of the species observed in the transient spectra differ from the spectra Fe(IV) oxo radical cation species, even when comparing species supported by identical porphyrins.[32, 33, 118, 119] Analysis of the rate constants for the oxidation of olefins also provide more evidence of Fe(V) oxo formation; the rate constant for epoxide formation from cyclooctene when Fe(V)O(tmp) is present is $1.6(2) \times 10^6$ vs 6.2×10 when $Fe(IV)O(tmp)^{+\bullet}$ is used.[119]

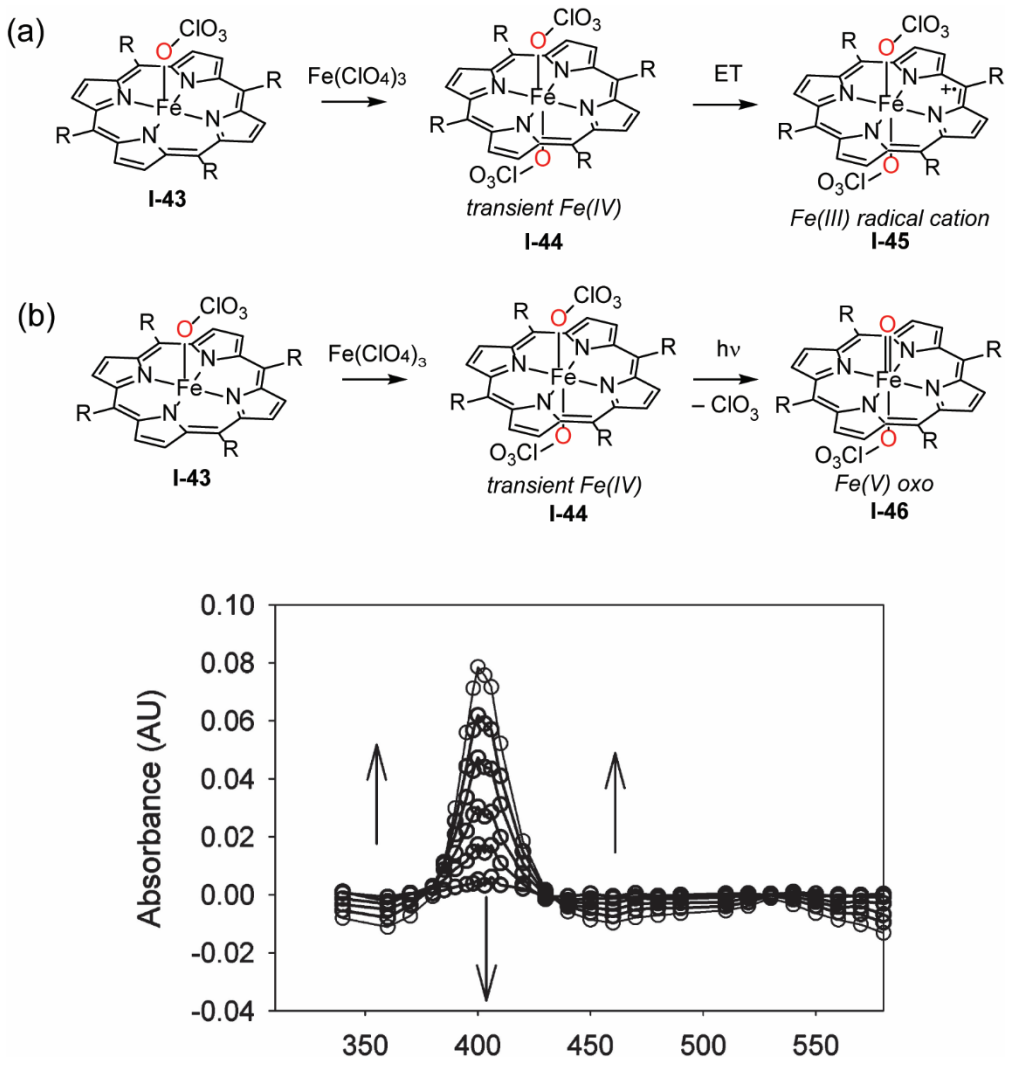

Figure I-16. Oxidation of Fe porphyrin oxyanion complexes and subsequent photolysis yields genuine Fe(V) oxo complexes. (a) Oxidation of Fe(III) porphyrin complex I-43 with $Fe(ClO_4)_3$ first yields a Fe(IV) complex, which then undergoes internal electron transfer to produce a Fe(III) complex with a singly oxidized porphyrin ring. The half-life of I-44 is on the order of seconds. (b) Photolysis of I-44, prior to internal electron transfer, homolytically cleaves the O–Cl bond yielding a genuine Fe(V) oxo species. (c) Transient absorption spectroscopy shows a peak centered in around ~400 nm which belongs to the Fe(V) intermediate I-46. Adapted with permission from reference 112. Copyright 2009 American Chemical Society.

I.5.2 Photoreduction

Photosynthetic access to specific complexes of interest is often complicated by the availability of other photochemical reaction pathways that generate undesired products. For example, Groves and Buchler separately reported that the photolysis of MnN_3(tpp) (**I-47**) in benzene or toluene at room temperature yielded Mn(V) nitride **I-32** upon extrusion of N_2.[105, 120] However, Imamura and Fujimoto have observed that room temperature photolysis of **I-47** in 2-Me-THF gives only the reduced porphyrin Mn(II) **I-48** via homolytic cleavage of the Mn–N bond, indicated by clean isosbestic points and new peaks in the UV-vis spectrum at 430, 560, and 640 nm (Figure I-17a).[121, 122] However, the photolysis of **I-47** in 2-Me-THF at –80 °C yields only Mn nitride **I-32**, indicated by the Soret band at 410 nm.[123] Raising the photolysis temperature from –80 °C to –51 °C yields a mixture of photoreduced **I-48** and photooxidized **I-32** (Figure I-17b). Thus, photolysis always results in homolytic cleavage of the M—N bond, resulting in **I-48** and $N_3^{\bullet}$. Room temperature photolysis of **I-47** produce $N_3^{\bullet}$ which is quickly scavenged by 2-Me-THF, yielding HN_3.[124] However at –51 °C the rate of scavenging via 2-Me-THF becomes similar to Mn nitride formation, thus both **I-48** and **I-32** are observed. However, in the absence of weak C–H bonds, e.g. toluene and benzene, $N_3^{\bullet}$ cannot be scavenged, and only nitride formation is observed.

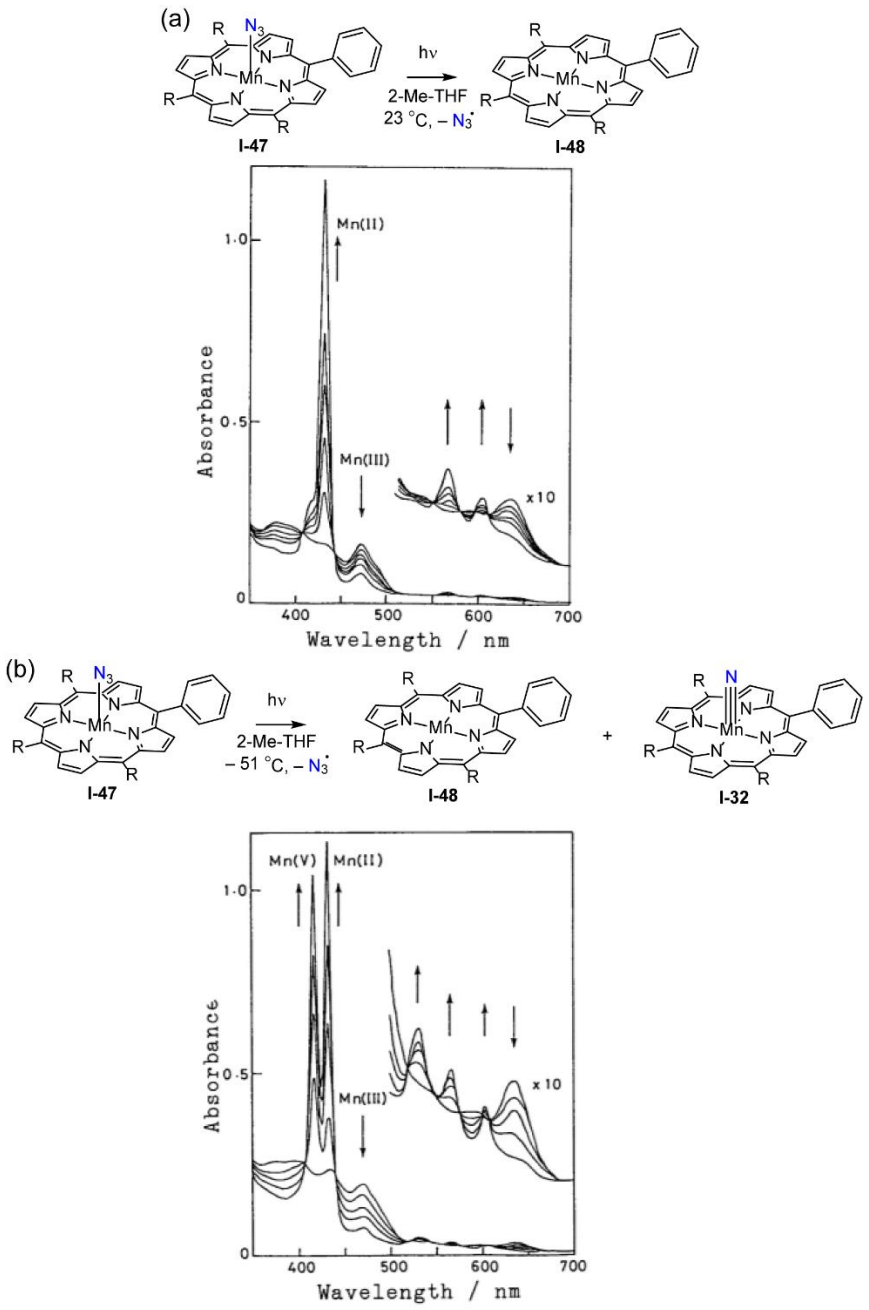

Figure I-17. The primary photo-event of Mn–N_3 complexes is cleavage of the Mn–N bond. (a) Photolysis of azide I-47 in 2-Me-THF at 23 °C selectively yields the photoreduced Mn(II) complex I-48 via homolytic cleavage of the Mn–N bond. (b) Photolysis of I-47 in 2-Me-THF at –51 °C yields both Mn(II) I-48 and Mn(V) nitride I-32. Mn(II) recombination with azide radical, forming I-32, is competitive with HAA of 2-Me-THF, thus both I-48 and I-32 are observed. Adapted with permission from reference 122. Copyright 1985 Chemical Society of Japan.

Photoreduction is also the primary photo-event in the photolysis of Mn porphyrin oxoanion complexes. Suslick and coworkers photolyzed both Mn nitrate and nitrite complexes **I-49** in benzene, which resulted in Mn(IV) oxo **I-50** (Figure I-18a).[125] Oxo **I-50** could transfer oxygen atoms to aryl phosphines, olefins, and activated C–H bonds such as toluene. To examine if photoreduction was the primary photo-event, and oxo **I-50** was produced via a thermal radical recombination, the Suslick lab isolated **I-49** in both polymer matrices and solvent glasses at 10 K.[126] Photolysis of **I-49** at 10 K shows only photoreduction, where the apical Mn–O bond is cleaved homolytically, yielding Mn(II) **I-32** and oxyanion radical (Figure 1-18b). Photolysis of other porphyrin species suspended in a rigid matrix such as Mn(tpp)ClO_4, Mn(tpp)Cl, Fe(tpp)NO_3, and Fe(tpp)Cl all resulted in photoreduction as shown in Table I-1. Thus it was suggested that the primary photo-event in Mn and Fe porphyrin complexes is always photoreduction, and subsequent thermal chemistry can occur depending on the matrix to yield metal oxos or nitrides.[124]

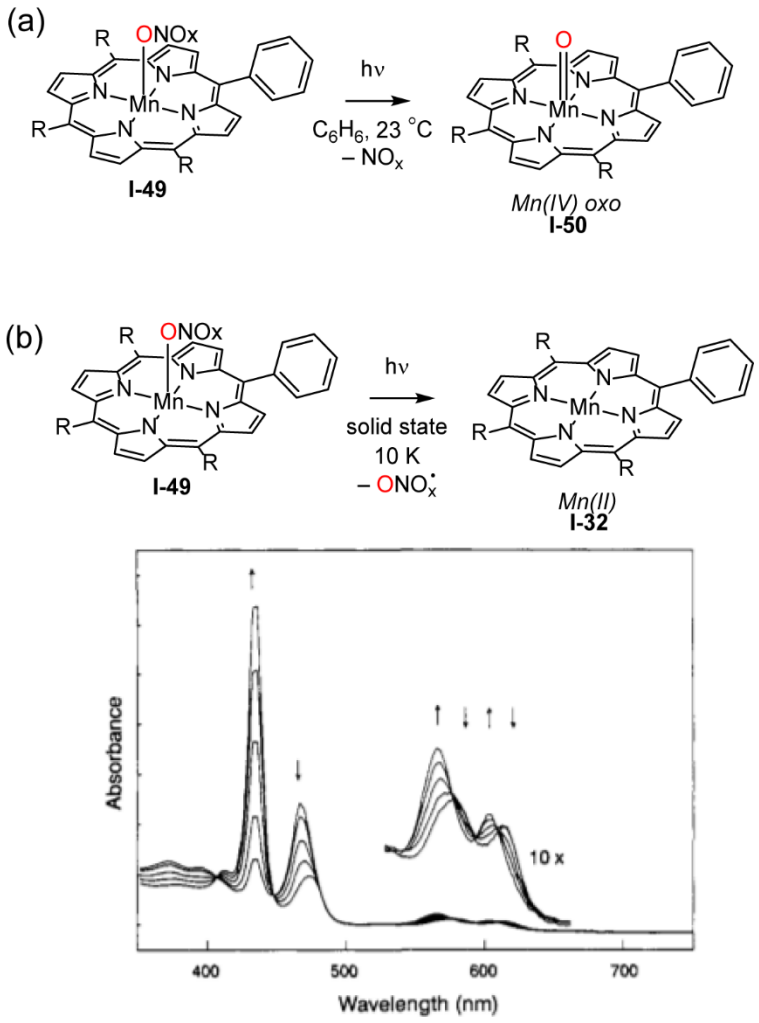

Figure I-18. Differing photochemical reaction conditions lead to different products. (a) Photolysis of complex I-49 in benzene at room temperature gives the formal product of O–N homolysis to make a Mn(IV) oxo. (b) Photolysis of complex I-49 in the solid-state at 77 K results in the cleavage of the Mn–O bond, which is highlight in the included UV-vis spectrum, where the Soret band of I-32 grows in at ~420 nm and the Soret of I-49 decreases in intensity. Thus, the primary photo-event of Mn oxyanions is hypothesized to be photoreduction, and access of Mn oxos comes from thermal recombination of expelled oxyanion radicals. Adapted with permission from reference 125. Copyright 1991 American Chemical Society.

Table I-1. Comparison of the photolysis products of different metalloporphyrins, in solutions or matrix isolated, shows that photoreduction is always prevalent.

Species	Solution	Matrix
$Mn(tpp)NO_3$	Mn(IV)(tpp)O	Mn(II)(tpp)
$Mn(tpp)NO_2$	Mn(IV)(tpp)O	Mn(II)(tpp)
$Mn(tpp)ClO_4$	Mn(III)(tpp)Cl	Mn(II)(tpp)
Mn(tpp)Cl	Mn(II)(tpp)	Mn(II)(tpp)
$Fe(tpp)NO_3$	Fe(II)(tpp)	Fe(II)(tpp)
Fe(tpp)Cl	Fe(II)(tpp)	Fe(II)(tpp)

Photoreduction has been observed in metalloporphyrin scaffolds with central metals other than Mn and Fe. Imamura and Fujimoto have found that photolysis of Mo(tpp)OCl (**I-51**) at 490 nm in 2-Me-THF proceeds with well-anchored isosbestic points to afford new UV-vis spectral features at 427 and 555 nm (Figure I-19).[122] This new species is Mo(tpp)O (**I-52**), which was confirmed by comparison to independently synthesized **I-52**. Additional conformation of the identity of **I-52** came from EPR studies, where the disappearance the signals of of $S = 1/2$ **I-51** was observed, resulting in EPR silent $S = 0$ **I-52**. Addition of phenyl-*N*-tert-butylnitrone (PBN) during photolysis resulted in a signal from PBN radical in the EPR spectrum, which the authors attribute to Cl mediated hydrogen-atom abstraction, further supporting photoreduction of **I-51** to **I-52**. Similar studies have been carried out with other Co(III),[122, 127] Fe(III),[122, 125, 128-155] Mn(III),[121, 122, 156, 157] Cr(III),[124] Mo(V),[122, 154, 158] and Rh(III)[159] porphyrin systems, showing that photoreduction is the primary photo-event in synthetic metalloporphyrin photochemistry and must be considered when using metalloporphyrins as photoprecursors.[160]

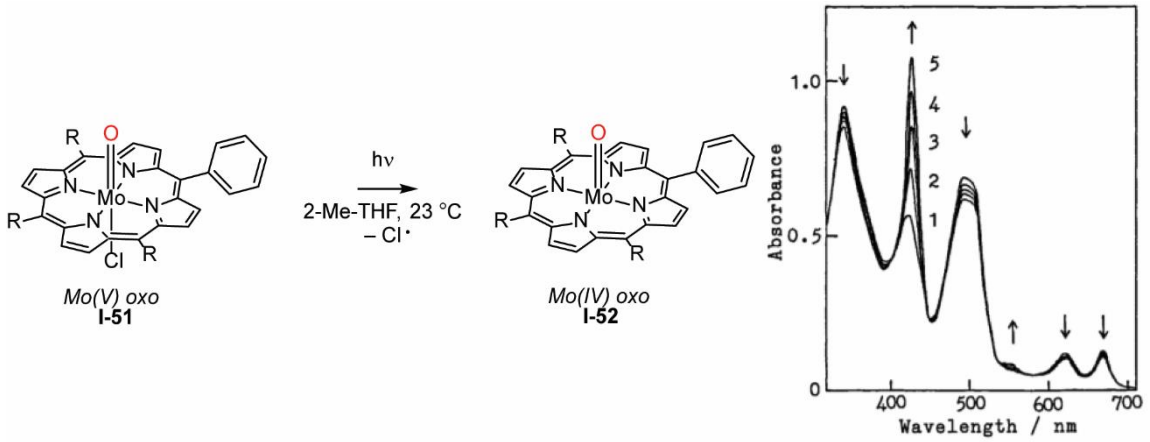

Figure I-19. Photolysis of Mo oxo complex I-51 in 2-Me-THF results in Mo–Cl cleavage, generating Mo(IV) oxo 1-52, which is indicated by new peaks growing in at 427 and 555 nm in the UV-visible spectrum. Adapted with permission from reference 122. Copyright 1985 Chemical Society of Japan.

I.5.3 Harnessing Photoreduction

Photoreduction of metalloporphyrins can be harnessed to catalyze various oxidation chemistries. Bartocci and coworkers found that photolysis of Fe(tdcpp)Cl **I-53** in an ethanol/CCl_4 solution with $\lambda > 350$ nm light yielded $CHCl_3$, acetaldehyde, and HCl as depicted in Figure I-20a.[130, 146] Substitution of the porphyrin ring has no effects on the quantum yield of the photoreduction of the *meso* phenyl group of porphyrins.[132, 147] Furthermore, photolysis of an oxygenated cyclohexane solution with **I-55** results in both cyclohexanone and cyclohexanol, but does not proceed through a Fe oxo intermediate.[131] Mansuy and Maldotti propose that the oxidation of cyclohexane occurs first via hydrogen atom abstraction from the photogenerated $OH^{\bullet}$, forming an alkyl radical (Figure I-20d). The generated alkyl radical forms a complex with the Fe(II) porphyrin and an equivalent of O_2, which then cleaves the O–O bond and abstracts another H-atom, generating cyclohexanone and regenerating **I-55** (Figure I-20b).[136] Formation of the alkyl radical was

verified using PBN as a spin trap, and no Fe(V) oxo species were observed via UV-vis. The Maldotti group further developed this reaction by heterogenizing the Fe porphyrin in a Nafion matrix, and then used sunlight as the photon source to oxidize cyclohexane and cyclohexene.[137]

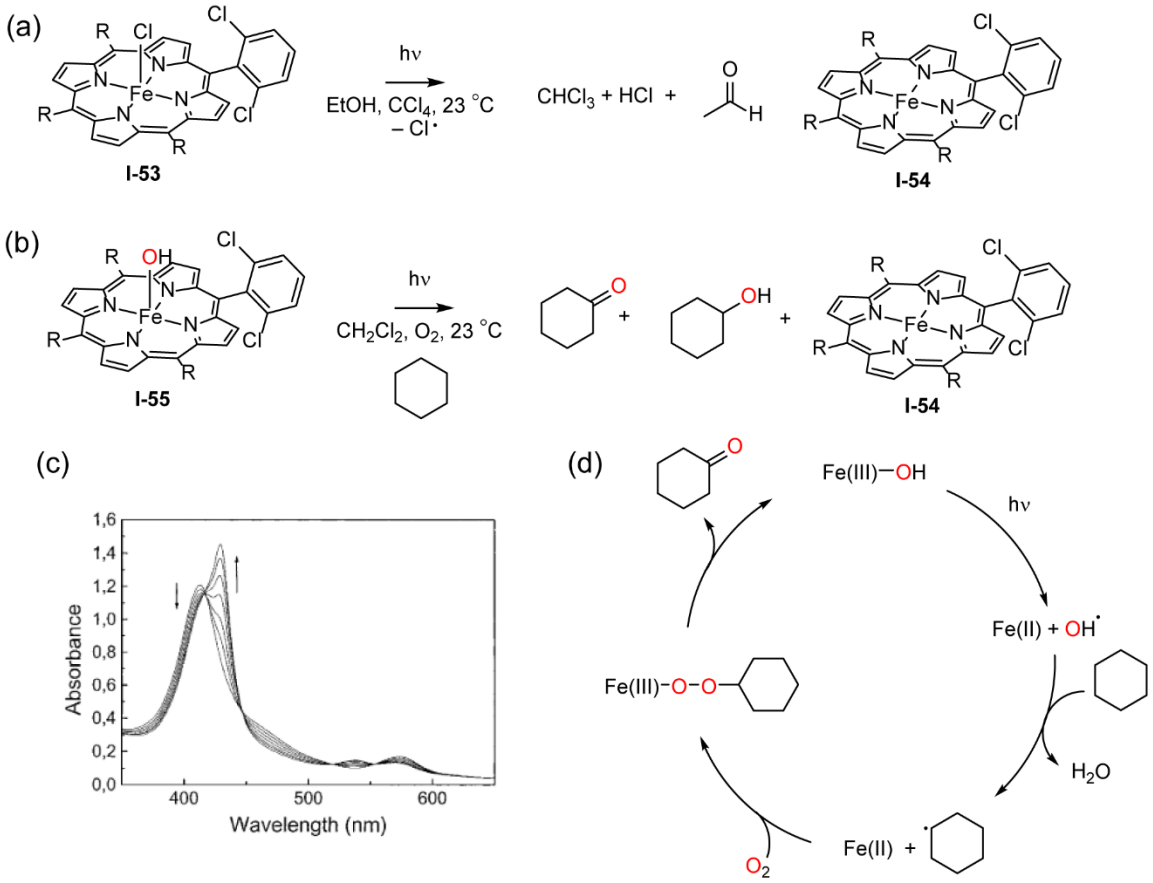

Figure I-20. Photoreduction of metalloporphyrins produces radical species which can be used to drive catalysis. (a) Photolysis of I-53 in EtOH and CCl_4 results in the formation of chloroform, HCl, acetaldehyde, and Fe(II) I-54. (b) Photolysis of hydroxy species I-55 in an oxygenated solution of DCM and cyclohexane yields cyclohexanone, cyclohexanol, and Fe(II) I-54. (c) Tracking the photolysis of I-55 via UV-vis spectroscopy shows the gradual formation of Fe(II) species I-54. (d) The hypothesized catalytic cycle to produce cyclohexanone begins with homolytic cleavage of the Fe–O bond to produce hydroxy radical. HAA of cyclohexane by the hydroxy radical results in a cyclohexyl radical, which then forms a peroxo species with Fe(II) I-54, and O_2. Cleavage of the O–O bond forms cyclohexanone and regenerates Fe(III) I-55. Figure I-20c was adapted with permission from reference 131. Copyright 1996 American Chemical Society.

Photoreduction has been observed and harnessed in systems other than metalloporphyrins. Recently, several studies have shown that Cl• produced via photoreduction can catalyze alkylation,[161-164] alkenylation,[165] arylation,[166-169] acylation,[166, 170] and amination[171, 172] of C–H bonds. In the following section, a few examples of catalytically relevant photoreduction from non-metalloporphyrin systems will be highlighted. For a more complete discussion of all relevant references that discuss photo-extrusion of radicals other than chlorine, see this relevant review.[173]

Nocera and coworkers structurally and spectroscopically characterized photoreduction of Cl• from Fe(III) pyridinediimine pincer complex **I-56** (Figure I-21a).[174] TA spectroscopy of **I-56** shows that photolysis with 355 nm light generates a new peak in the absorption spectrum at 430 nm, which is attributed to a transient Cl•–arene complex. Monitoring the photolysis via EPR shows a new spectrum growing in with features at g = 2.006. This spectrum was attributed to the formation of a carbon-centered radical, which forms after the Cl• abstracts a H-atom from the methyl of **I-57**. Further, the photoreduction was monitored via photocrystallograpy, where a single crystal of **I-56** was photolyzed and the reaction progress was monitored *in situ* with single-crystal X-ray diffraction (Figure I-21). The X-ray data showed that photolysis resulted in cleavage of the apical Fe–Cl bond, and the Cl atom migrates to two separate methyl groups of neighboring ligands. Thus, the TA spectroscopy indicates that the primary photo event is Fe–Cl cleavage and yields a Cl•–arene adduct, EPR spectroscopy showed that an H-atom is abstracted to afford a carbon-centered radical, and the photocrystallography data set supported selectrive extrusion of the apical Fe–Cl to yield Cl•, which then abstracts a H-atom from an adjacent

methyl group in the solid state. In the absence of pendant methyl groups on **I-56**, the photogenerated $Cl^{\bullet}$ will functionalize aliphatic C–H bonds such as 3-methylpentane.[175] Interestingly, due to the steric hinderance enforced by the bulky ligand of **I-59**, accessible primary and secondary C–H bonds were functionalized in favor over the weaker tertiary C–H bonds in 3-methylpentane.

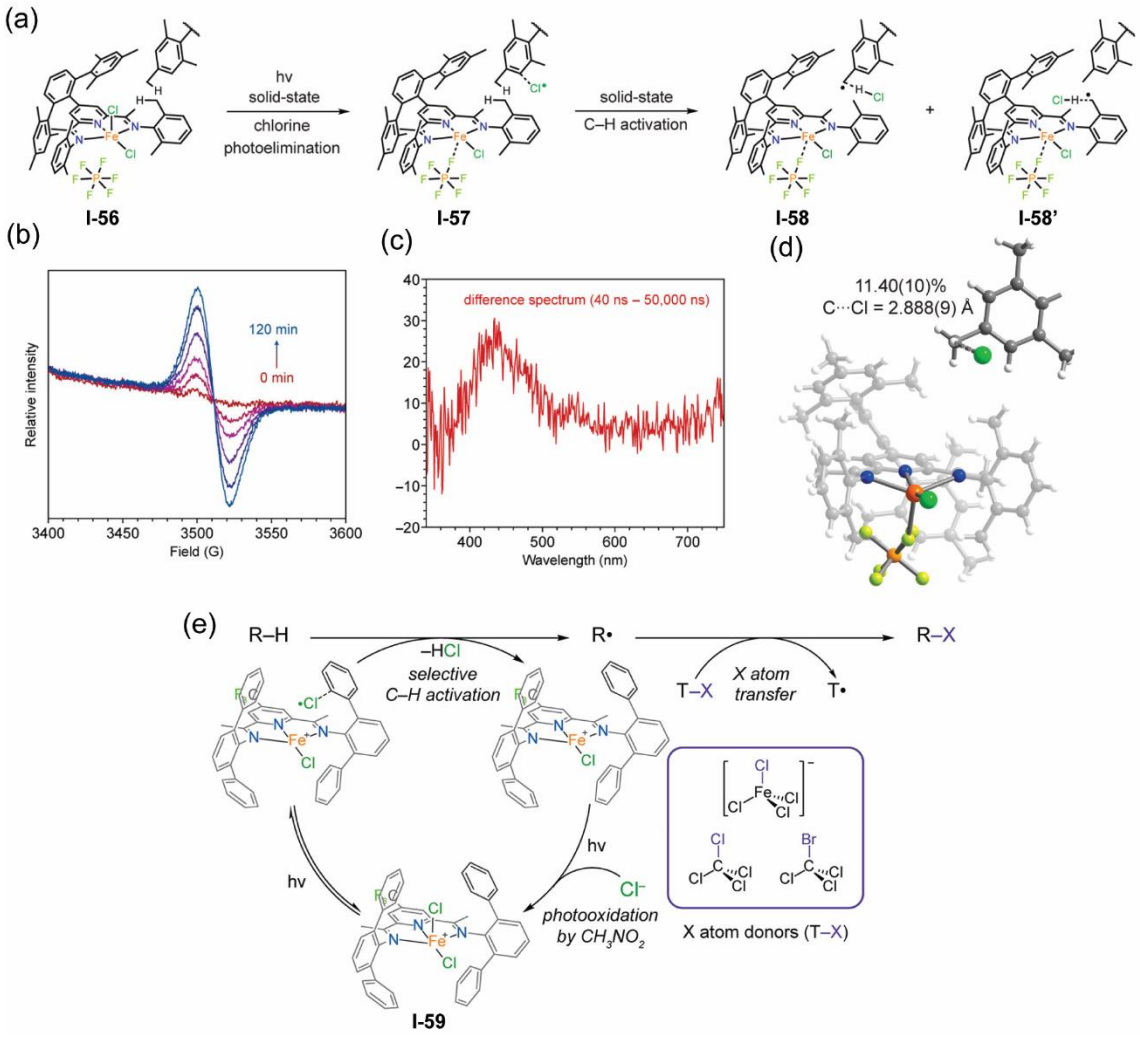

Figure I-21. Characterization of photoreduction from Fe(III) pyridinediimine pincer complex I-56. (a) Photolysis of I-56 results in cleavage of the apical Fe–Cl bond, which abstracts a H-atom from a adjacent methyl group. (b) Tracking the photolysis via X-band EPR shows a signal grow in at g = 2.006, which is attributed to a carbon centered radical, after HAA via Cl•. (c) Generation of the Cl• via TA spectroscopy shows a signal centered at 430 nm, which is attributed to a Cl•–arene complex. (d) Photolysis of I-56 in a single crystalline habit results in cleavage of the apical Fe–Cl bond, which is shown here via photocrystallography. (e) C–H functionalization from I-59 works via abstracting the H-atom via Cl• from I-59, which then forms a R–X bond from a variety of sources. Figure I-21a-d was adapted with permission from reference 174. Copyright 2021 American Chemical Society. Figure I-21e adapted with permission from reference 175. Copyright 2022 American Chemical Society.

Photoreduction of Cl• from a Ni(III) center has shown to be involved in cross-coupling catalysis. In 2015, Nocera and coworkers observed halogen extrusion upon photolysis of a bis-phosphine supported Ni(III) complex.[176, 177] Inspired by this, Doyle used Ni(II) complex **I-60** in conjunction with an Ir(II) photoredox catalyst to forge sp^3–sp^2 C–C bonds.[166] Ni catalyst **I-60** is oxidized via photoredox catalyst **I-61**, generating a Ni(III) species **I-62**. Species **I-62** cleaves the Ni–Cl bond via photoreduction, generating a Cl• which subsequently abstracts a H-atom from THF. Rebound of the carbon-centered radical resulted in Ni(III) species **I-63**, which subsequently underwent reductive elimination to yield the desired coupled product. Further reduction of Ni(I) species and oxidative addition of aryl chloride regenerated catalyst **I-60**. Confirming this mechanism, Stern–Volmer quenching studies revelated that Ni(II) **I-60** was the species responsible for quenching the Ir photocatalyst.[169] Furthermore, TD-DFT studies of Ni(III) **I-62** show that the Ni(III)–Cl BDE is 44 kcal/mol whereas the Ni(II)–Cl BDE is 77 kcal/mol, supporting facile photoreduction from a Ni(III) state. The fact that Ni(II) **I-60** does not exhibit any photoreduction highlights a significant fact commonly seen in photoreduction processes; the oxidation state of the metal prior to photoreduction should be in a relatively high oxidation state (Ce(IV), Mn(III), Fe(III), Co(III), Ni(III), Cu(II), etc.), thus the resulting reduced species is also stable.

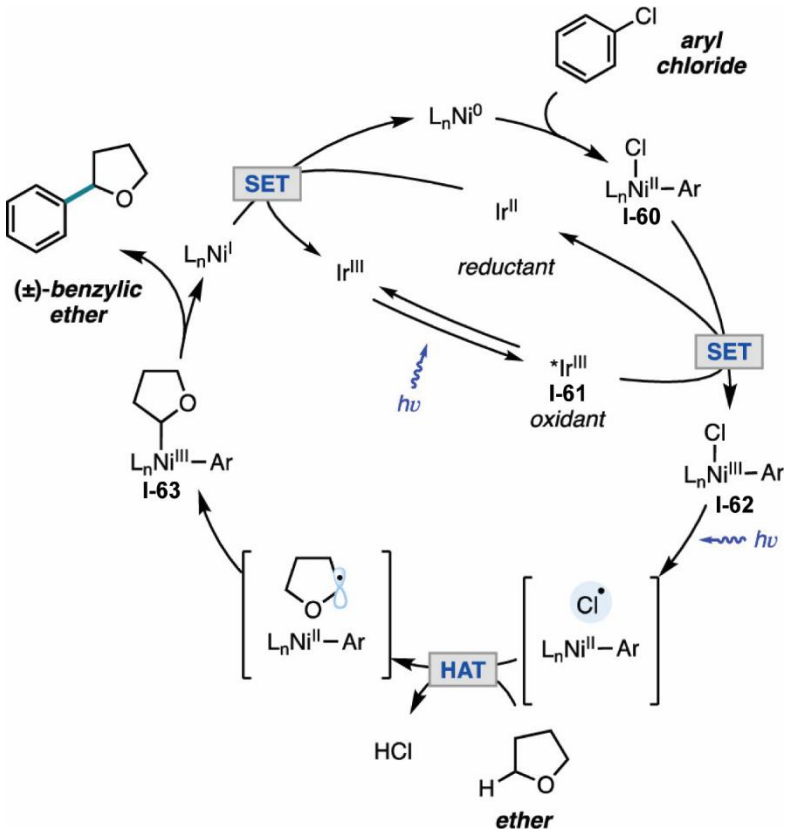

Figure I-22. Photocatalytic C–C bond formation from a Ni Ir coupled system. Ni(II) species I-60 is oxidized from the excited state Ir(III) photocatalyst I-61. The resulting Ni(III) species I-62 undergoes photoreduction to form Ni(II) and $Cl^{\bullet}$. $Cl^{\bullet}$ then abstracts a H-atom from THF, yielding HCl and a THF radical, which forms Ni(III) species I-63. I-63 then undergoes reductive elimination to form the benzylic ether and Ni(I). The Ni(I) species is reduced by the Ir(II) species, and then oxidatively adds with an aryl chloride to reform Ni(II) I-60. Adapted with permission from reference 169. Copyright 2021 American Chemical Society.

I.6. Conclusions

Thorough characterization of M–L multiply bonded complexes is challenging and often stymied by their innate reactivity. Therefore, obtaining any information about the chemical or electronic structure often relies exclusively on theory. This chapter reviewed strategies for the characterization of M–L multiply bonded species. Synthetic perturbation

to modify the ligand donicity of the supporting ligand on the metal ion or appended R-group on the M–L species, have been shown to stabilize the reactive intermediate. While these species are kinetically stable enough to probe via spectroscopy and single-crystal X-ray diffraction, these derivatized structures commonly do not participate in the reaction of interest. Thus, the reactive intermediate involved in these catalytic processes are still yet to be observed.

In a similar context, photochemical synthesis of reactive species from characterized isolable photoprecursors, provides an avenue to generate reactive M–L fragments, either under conditions compatible with steady-state or time-resolved spectroscopy. However, the primary photo-event in these studies has been shown to be photoreduction, cleaving the M–X bond leads to either; radical chemistry from X$^{\bullet}$ such as HAA from alkanes, or thermal recombination of X$^{\bullet}$ with the metal center to forge a M–L multiply bonded intermediate. The research in this thesis is predicated on the design of novel photoprecursors to generate metal nitrenoids relevant to C–H amination that facilitate photochemical synthesis of M–L multiply bound species in solution and the solid-state. The two outstanding challenges to this goal were: (1) design of a new class of photoprecursors to access metalloporphyrin nitrenoids and, (2) append photolabile bonds which will cleave instead of the apical M–N bond. Furthermore, photochemical synthesis of reactive intermediates lends itself towards generation and structural characterization of reactive intermediates in a single-crystalline habit. The research in the later chapters in this thesis demonstrate the design of solid-state photoprecursors, and the photocrystallographic characterization of M–L multiply bound reactive intermediates.

CHAPTER II

NITRENE CHEMISTRY OF MANGANESE *N*-HALOAMIDES[*]

II.1 Introduction

Since Breslow's seminal discovery of Mn porphyrin-catalyzed amination of cyclohexane, Mn tetrapyrroles have emerged as an important platform for nitrene transfer catalysis.[29-31, 61, 178-181] The combination of nitrene precursors, such as iminoiodinanes[29, 62-64, 182-184] or *N*-haloamides,[73, 185] and Mn(III) porphyrin catalysts enables nitrene transfer to C–H bonds and olefinic substrates to afford amines and aziridines, respectively (Figure II-1). Enantioselective nitrene transfer catalysis has been realized using D_4-symmetric chiral Mn porphyrin catalysts.[64, 186] More recently, White *et al.* have developed related Mn(III) phthalocyanines as highly active catalysts for aliphatic C–H amination.[65, 187] In analogy to metalloporphyrin-supported metal oxo intermediates in C–H hydroxylation catalysis, the developed nitrene transfer catalysis is proposed to proceed via the intermediacy of reactive high-valent Mn nitrenoids.[105, 188-190]

[*] Data, figures, and text in this chapter were adapted with permission from reference Van Trieste, G..P.; Reid, K..A.; Hicks, M..H.; Das, A.; Figgins, M..T.; Bhuvanesh, N.; Ozarowski, A.; Telser, J.; Powers, D.C. Nitrene Photochemistry of Manganese *N*-Haloamides *Angew. Chem. Int, Ed*. **2021**, *60*, 26647–26655.

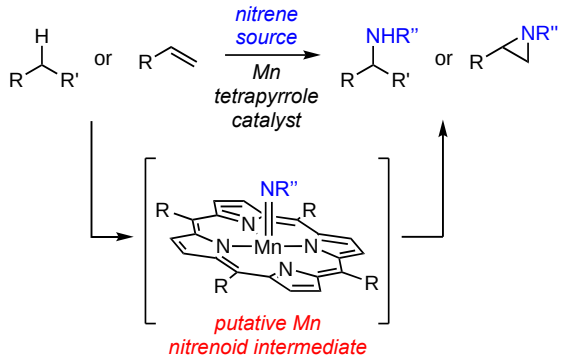

Figure II-1. Mn tetrapyrrole-catalyzed nitrene transfer catalysis has been applied to both C–H amination and olefin aziridination reactions. Electrophilic Mn nitrenoids are proposed to mediate this family of nitrene transfer reactions.

The reactivity of the Mn nitrenoids that are invoked as transient intermediates in nitrene transfer catalysis renders these species challenging to observe.[191] Stabilization of these intermediates via synthetic modification of the ancillary ligand set can attenuate the reactivity of the supported Mn nitrenoid and enable isolation. Abu-Omar and co-workers leveraged triply anionic corrole ligands to stabilize and isolate Mn(V) nitrenoid **II-1**, which was prepared by photolysis of a solution of mesityl azide and Mn(III) tris-pentafluorophenylcorrole (Figure II-2a).[102] Complex **II-1** was found to be unreactive towards alkenes and alkanes but did participate in reaction with PPh_3 to afford the corresponding iminophospine. Goldberg and co-workers reported the isolation of corrolazine-supported nitrenoid **II-2**, which was similarly found to be unreactive towards either olefins or C–H bonds (Figure II-2b).[103] Use of a tetraanionic tetraamido macrocyclic ligand (TAML) enabled the isolation of Mn(V) imido complex **II-3** (Figure II-2c).[192] Further oxidation to the corresponding Mn(VI) complex was necessary to engender nitrene transfer chemistry. In the context of porphyrin-supported nitrenoids, acylation of Mn(V) nitrido complex **II-4** with trifluoroacetic anhydride affords Mn(V) nitrenoid **II-5**,

which was characterized by ^{1}H NMR and UV-vis spectroscopies and displays olefin aziridination activity (Figure II-2d).[105, 106]

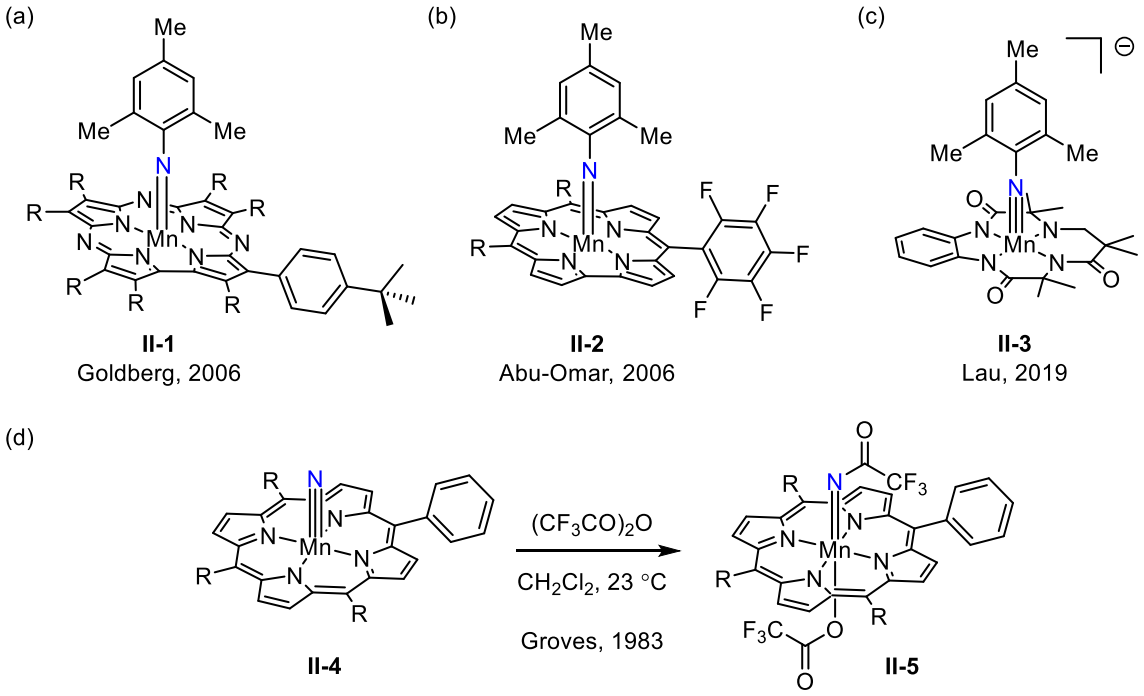

Figure II-2. A small family of Mn(V) nitrenoids has been characterized, including (a) corrole-supported II-1, (b) corrolazine-supported II-2, and (c) TAML-supported II-3. (d) Treatment of Mn(V) nitride II-4 with trifluoroacetic anhydride resulted in the observation of porphyrin-supported Mn(V) nitrenoid II-5.

Synthetic photochemistry provides opportunities to access reactive species under conditions that allow for characterization by time-resolved or cryogenic methods without necessitating stabilization via synthetic derivatization. The following examples feature photopromoted metal oxo generation. As discussed in Chapter I, we hypothesize that photoreduction is the primary photoevent and subsequent chemistry between the reduced metal center and the expelled radical afford the metal oxo complexes. In the context of Mn oxo chemistry, Newcomb and co-workers demonstrated that both Mn(IV) and Mn(V)

oxo complexes could be accessed by photolysis of Mn oxyanion complexes (Figure II-3).[97, 98, 193-195] Flash photolysis of Mn(III) chlorate complex **II-6a** resulted in Cl–O bond homolysis to generate a Mn(IV) oxo compound **II-7**; in contrast, flash photolysis of Mn(III) perchlorate complex **II-6b** resulted in Cl–O bond heterolysis to generate a Mn(V) oxo complex **II-8**. Similar photochemically promoted O–X cleavage to generate Mn oxo complexes was described by Suslick and co-workers in the context of porphyrin-supported Mn nitrite and nitrate complexes,[124-126, 196-198] and Zhang and co-workers have described photogeneration of Mn oxo complexes from μ-oxo dimanganese precursors.[199]

In contrast to metal oxo chemistry, photochemical strategies to generate the corresponding reactive metal nitrenoids are much less developed. While organic azide ligands can represent viable photoprecursors to metal nitrenes, the poor donicity of organic azides as ligands coupled with the thermal instability of these ligands towards N_2 loss results in a limited family of potential photoprecursors.[35, 68, 200-202] Conceptually, haloamide ligands, which are X-type donors, could serve as nitrene precursors via N–X photoactivation. In analogy to oxyanion photochemistry pictured in Figure II-3a, both N–X homolysis and heterolysis mechanisms are potentially available to haloamide complexes (Figure II-3b). In 2018, we demonstrated that photolysis of a Rh_2 complex with an *N*-chloroamide ligand afforded the corresponding Rh_2 nitrenoid via N–Cl homolysis.[203] Exploration of the generality of N–X photocleavage and the photoactivation modes available to a more diverse set of transition metal complexes is critical to generalizing *N*-haloamide photochemistry as an approach to catalytically relevant metal nitrenoids. At present, the synthetic chemistry of transition metal haloamide complexes is extremely

limited, with only three structures reported,[203, 204] and while significant work has been carried out on the photolysis of organic *N*-haloamines,[3, 205-207] the corresponding photochemistry of inorganic *N*-haloamides is almost completely unknown.

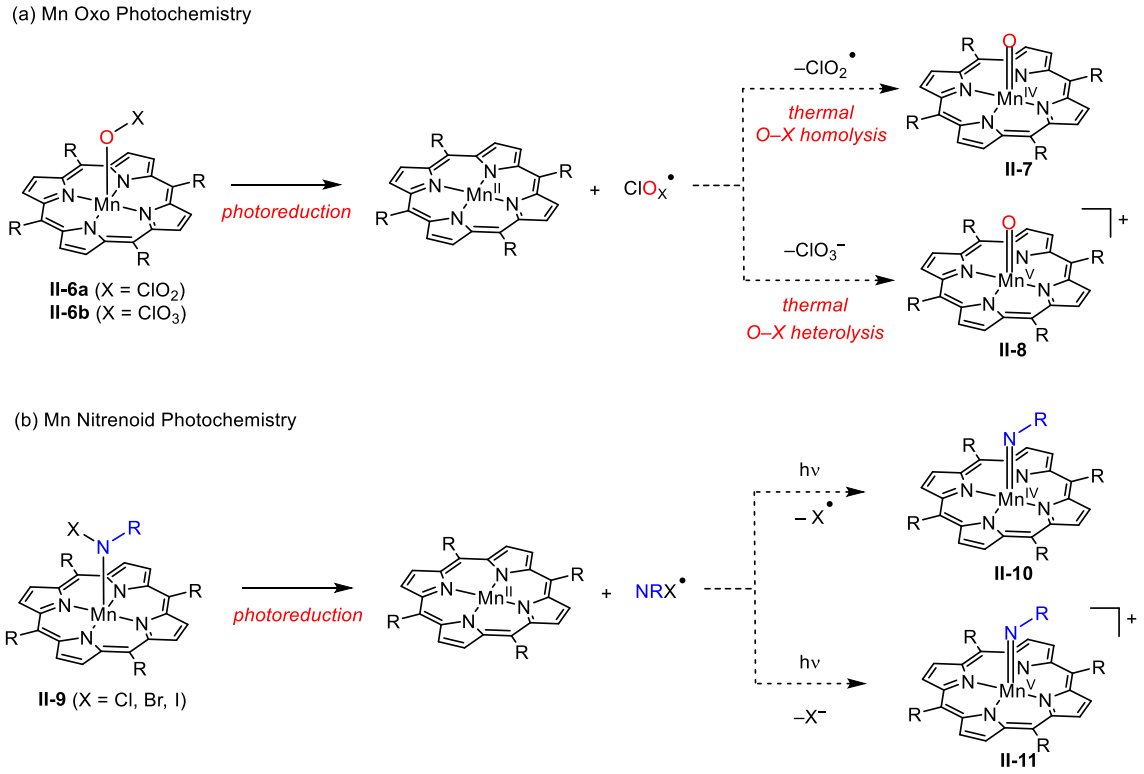

Figure II-3. (a) Photolysis of Mn chlorate II-6 affords photoreduced Mn(II) and the respective oxyradical. The reaction of chlorate radical and Mn(II) affords Mn(IV) oxo II-7 via Cl–O homolysis. In contrast, combination of perchlorate radical and Mn(II) affords Mn(V) oxo II-8 via Cl–O heterolysis. (b) Corresponding Mn nitrenoid photochemistry could also pass through a similar pathway as II-6, with subsequent reactions resulting in either hetero- or homolytic N–X cleavage to afford II-10 or II-11, respectively.

Here we report the synthesis and characterization of a family of Mn porphyrins featuring N-haloamide ligands. These complexes are S = 2 species and are fully characterized in both solution phase and the solid state. This family of complexes includes the first examples of *N*-bromoamide and *N*-iodoamide complexes of transition metals.

Photolysis of these complexes gives rise to the product of C–H amination and olefin aziridination. A combination of kinetic isotope effect analysis and low-temperature spectroscopy indicates that while the photolysis of Mn(III) *N*-chloroamides proceeds via initial cleavage of the Mn–N bond to generate Mn(II) and amidyl radical intermediates, photolysis of the corresponding *N*-iodoamide complexes proceeds via N–I cleavage to generate a Mn(IV) nitrenoid that participates in both C–H amination and olefin aziridination. These observations represent the first example of a porphyrin-supported Mn(IV) nitrenoid, highlight the impact of ligand design in the synthesis of novel photoprecursor ligands, and establish *N*-haloamides as a class of nitrene photoprecursor ligands.

II.2 Results

In this section, we describe the synthesis and characterization of a family of porphyrin-supported Mn(III) haloamide complexes (**II-13**) featuring variation of both the identity of the porphyrin meso-substituent and on the *N*-halogen. This suite of complexes provides the opportunity to investigate the halogen-dependent photochemistry of Mn(III) haloamides, which reveals the decisive impact of N–Cl (*i.e.*, **II-13a**) versus N–I (*i.e.*, **II-13e**) identity of differentiating Mn–N cleavage (*i.e.*, photoreduction) and N–X cleavage (*i.e.*, photooxidation) pathways.

II.2.1 Synthesis and Characterization

Sequential treatment of porphyrin-supported Mn(III) chlorides **II-12** with $AgBF_4$ and M[NTsX] (M = Na or K; i.e., haloamine-T) provided access to the corresponding Mn(III) haloamide complex **II-13** (Figure II-4; for characterization of the intermediate

[MnL]BF4 complexes, see section II.5.1). The spectroscopic data for iodoamide **II-13e** is representative of the family of haloamides and is described in detail here; for characterization details of the other haloamide complexes, see the section II.5.1. The ^{1}H NMR spectrum of **II-13e** displays three paramagnetically shifted peaks corresponding to the methyl group (13.0 ppm), the aryl C–H bonds of the tosyl group and the meso substituents (8.3 ppm), and the pyrrole protons (–22 ppm) (Figures II-5-II-6). The UV-vis spectrum of **II-13e** displays absorbances at 383 nm ($\varepsilon = 3.5 \times 10^4$ $M^{-1}cm^{-1}$), 479 nm ($\varepsilon = 5.2 \times 10^4$ $M^{-1}cm^{-1}$), 585 nm ($\varepsilon = 7.8 \times 10^3$ $M^{-1}cm^{-1}$), and 620 nm ($\varepsilon = 8.2 \times 10^3$ $M^{-1}cm^{-1}$), which we assign as ligand-to-metal charge-transfer (LMCT), Soret, and Q-bands respectively, based on comparison to other Mn(III) porphyins.[193] Based on the ratio of the molar absorptivities of the two Q-bands and the position of the Soret band, the ligand field strength of the *N*-iodoamide ligand is similar to that of chloride (*i.e.*, Mn(tpp)Cl) and the ligand field strength of the haloamide ligands examined here is not sensitive to the identity of the N-halogen (Table II-1).[208, 209] Consistent with previous reports of Mn(III) porphyrin complexes,[210] both ESI- and APCI-MS experiments provide signals that correspond to $[Mn(tpp)]^{+}$. Raman spectra of complexes **II-13a** and **II-13e** are collected in II-16.

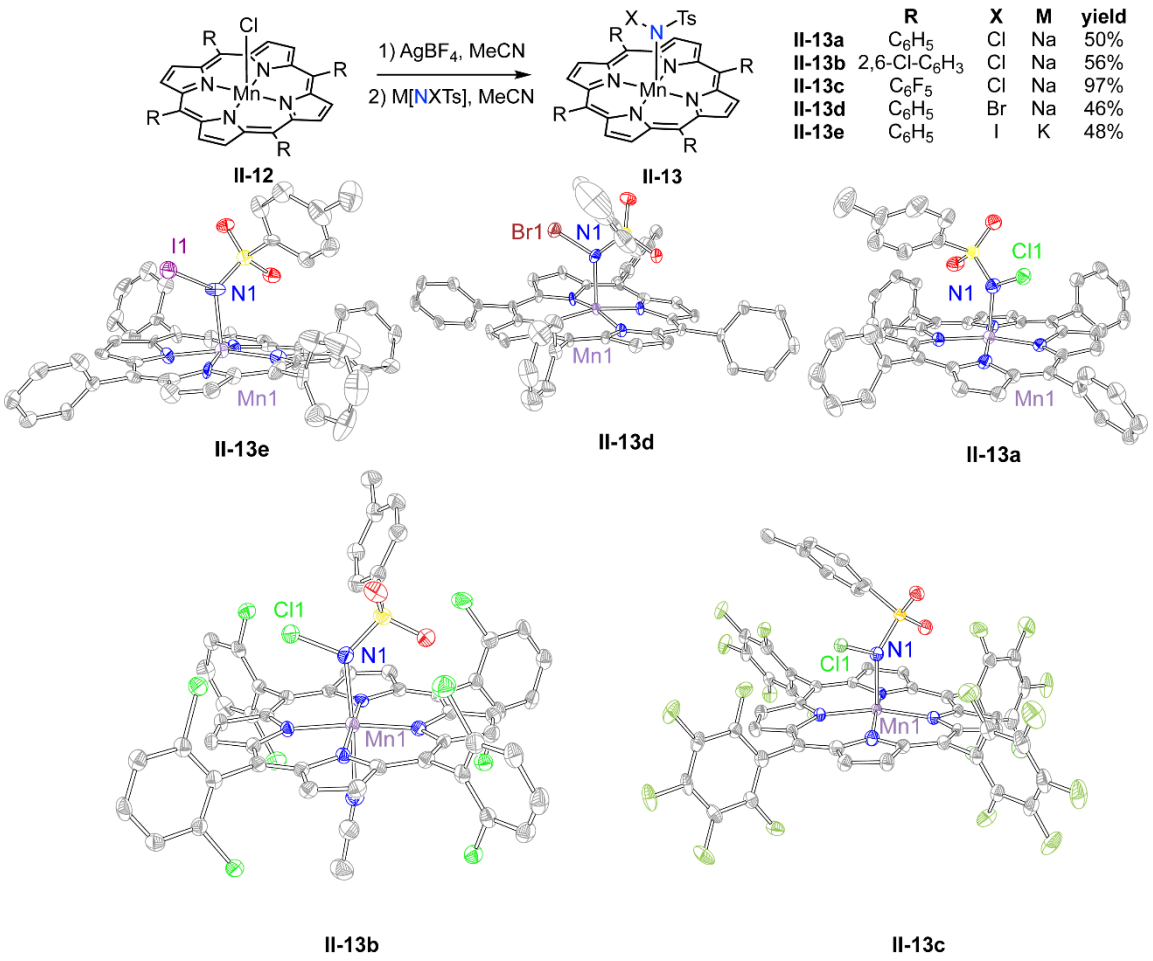

	R	X	M	yield
II-13a	C_6H_5	Cl	Na	50%
II-13b	2,6-Cl-C_6H_3	Cl	Na	56%
II-13c	C_6F_5	Cl	Na	97%
II-13d	C_6H_5	Br	Na	46%
II-13e	C_6H_5	I	K	48%

Figure II-4. Top: General synthetic strategy for the Mn(III) N-haloamide complexes II-13. Bottom: Displacement ellipsoid plots of the Mn N-haloamides II-13. H-atoms and solvent molecules have been omitted for clarity. Ellipsoids drawn at 50% probability. Selected bond distances (Å): II-13a, Mn–Cl = 1.745(3); II-13d, Mn–Br = 1.884(6); II-13e, Mn–I = 2.056(7).

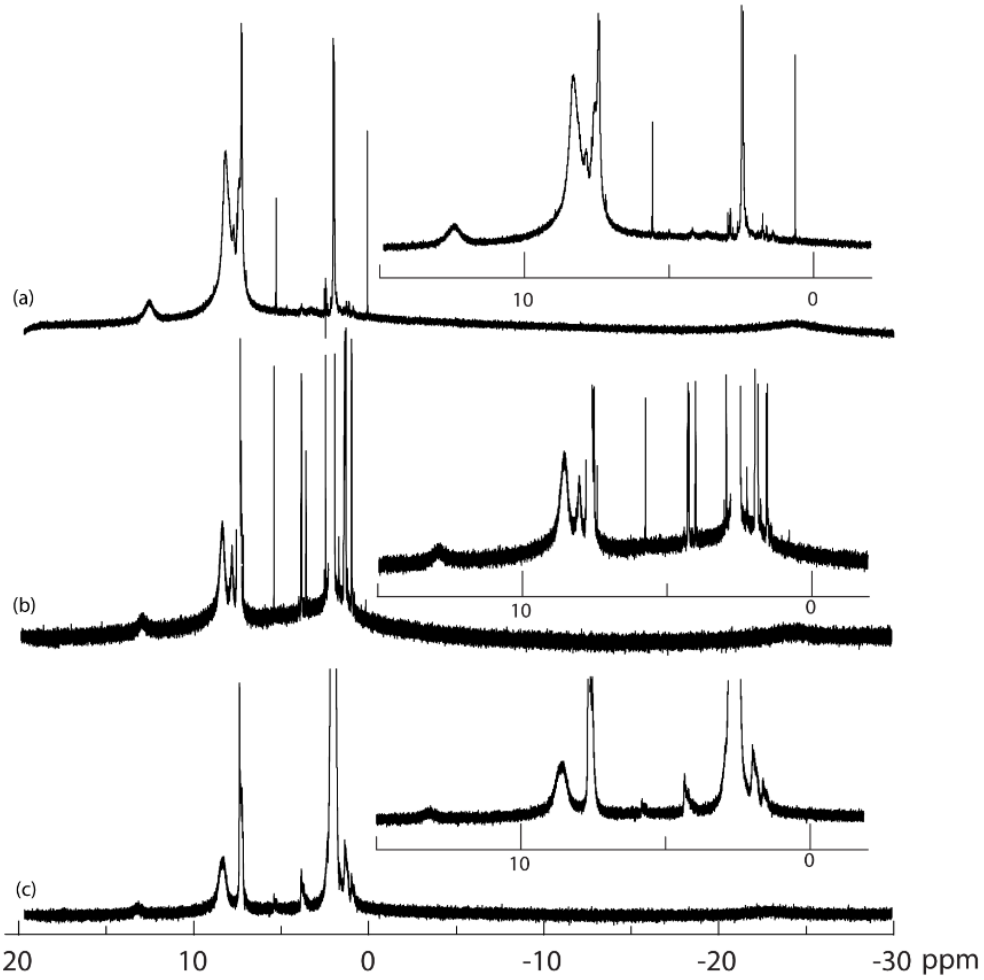

Figure II-5. ^{1}H NMR spectra of (a) II-13a, (b) II-13d, and (c) II-13e measured at 500 MHz in $CDCl_3$ at 23 °C with each inset magnified on the diamagnetic region.

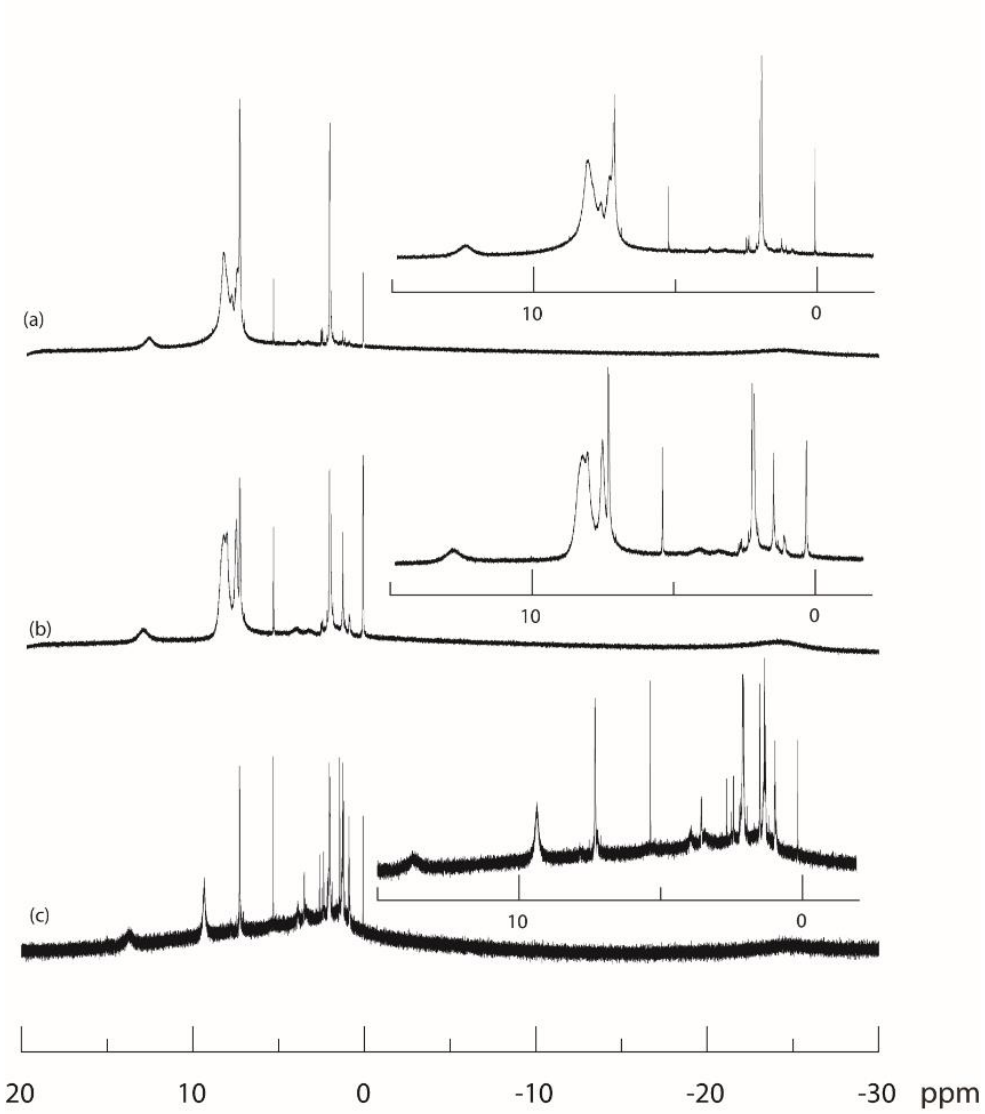

Figure II-6. ^{1}H NMR spectra of (a) II-13a, (b) II-13b, and (c) II-13c measured at 500 MHz in $CDCl_3$ at 23 °C with each inset magnified on the diamagnetic region.

Table II-1. Molar absorptivity (ε) ratios of the q-bands of II-13a, II-13d, II-13e, and II-12.[17] Band numbering is in accordance with Boucher's labeling (indicated on the plot below).[208, 209]

Entry	ε_{III} ($M^{-1}cm^{-1}$)	ε_{IV} ($M^{-1}cm^{-1}$)	$\varepsilon_{III}/\varepsilon_{IV}$
II-13a	4.6×10^3	4.1×10^3	0.89
II-13d	4.7×10^3	4.8×10^3	1.02
II-13e	7.8×10^3	8.2×10^3	1.05
II-12	4.1×10^3	4.1×10^3	1.00

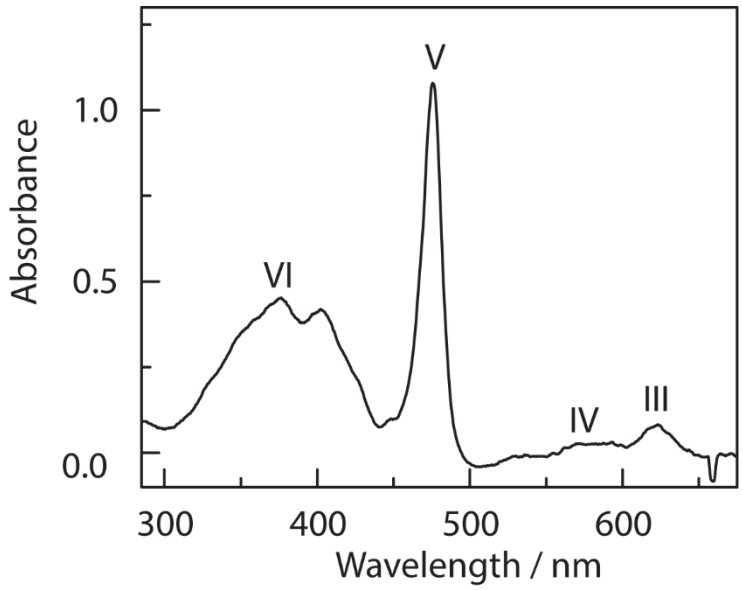

Figure II-7. A UV-vis spectrum of II-13e with the absorbance bands labeled with Boucher's numbering system.

Consistent with the S = 2 ground state typical of Mn(III) porphyrin complexes, compound **13e** displays a magnetic moment of 4.9 (Evans method, 23 °C) and does not display X-band EPR features at 4 K (2-Me-THF glass).[208, 211, 212] Due to the lack of X-band EPR features for S = 2 compounds, we pursued high-frequency and -field EPR (HFEPR) spectroscopic characterization of this suite of complexes (for spectra and resonance field versus microwave frequency plots of **II-13a**, **II-13d**, and **II-13e** see Figures II-8-II-15). The spectra consist of very broad signals apparently due to the presence of slightly different Mn moieties (two in **II-13a**, **II-13d**, and **II-13e**). Representative HFEPR spectra recorded at 319 GHz of the MnNXTs(tpp) X = Cl, Br, I series are illustrated in Figure II-8 and the derived spin Hamiltonian parameters (zero field splitting (ZFS): axial (D), rhombic (E) values, and g values) are collected in Table II-2.[213] The present study is the first, to our knowledge, to provide the ZFS parameters of a Mn(III) tetrapyrrole with a nitrogen-donor axial ligand. The D values of the compounds measured here are similar to each other and to other Mn(III) tetrapyrroles (*i.e.*, $D = -2.5 \pm 0.5$ cm^{-1}) bearing *O*- or *N*-bound axial ligands.[211, 212, 214, 215] Substitution of the amido halogen substituent has minimal impact on the D value, with D becoming slightly less negative from **II-13a** to **II-13d** to **II-13e**. This trend is significantly more dramatic in the corresponding MnX(tpp) series in which the halogen is bound directly to the Mn center.[216] This observation is a consequence of the extensive spin-orbit coupling of heavier donors.[217] The rhombicity does show a more significant dependence on the halogen identity, where **II-13a** is the least rhombic and **II-13e** is the most. We hypothesize that the high rhombicity value of MnNXTs(tpp) is due to the Ts–N–X apical unit breaking the

four-fold symmetry observed in manganese tetrapyrroles, which generally feature rhombicity values close to zero, even in the case of corroles/corrolazines, which lack the true four-fold symmetry of the porphyrin macrocycle.[99, 211, 212, 214-216, 218] Qualitatively, Mn–N □-bonding from N p_x (filled N lone pair) to Mn d_{xz} (half-filled), but not correspondingly from N p_y to Mn d_{yz} would distinguish the in-plane *x* and y directions (the principal ZFS direction is along *z*, normal to the porphyrin plane).[211]

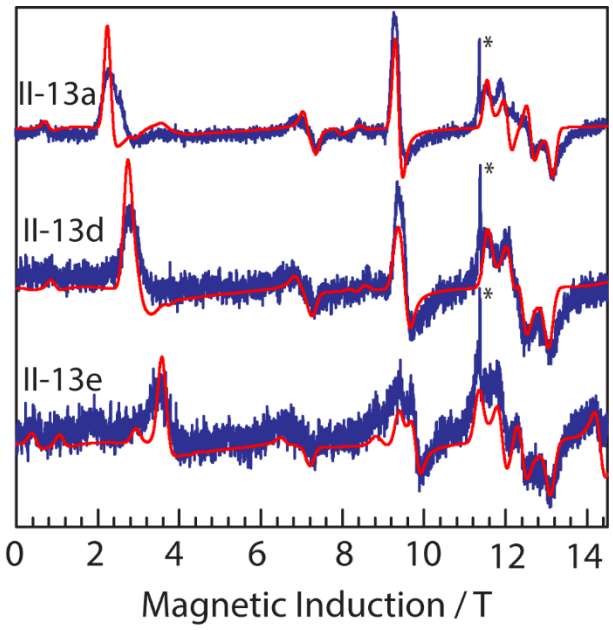

Figure II-8. HFEPR spectra of II-13a, II-13d, and II-13e collected at 319 GHz and 10 K. Blue: experimental; red: simulated with parameters given in Table II-2. The asterisk indicates an impurity signal at g = 2.003.

Table II-2. Comparison of HFEPR data for compounds II-13a, II-13d, and II-13e with other axially coordinated Mn(III) tetrapyrrole analogues. E is given in the same sign as D (TPFC = 5,10,15-tris(pentafluorophenyl)corrole trianion; TBP_8Cz = 2,3,7,8,12,13,17,18-octa(4-tert-butylphenyl)corrolazine).

	D / cm^{-1}	E / cm^{-1}	$\lvert E/D \rvert$	g_x, g_y, g_z
II-13a	–2.881	–0.095	0.033	1.994, 1.984, 1.979
II-13d	–2.707	–0.134	0.050	1.990, 1.995, 1.990
II-13e	–2.460	–0.243	0.099	2.004, 1.990, 1.991
Mn(tpp)Cl[211, 214]	–2.290	~0	0	1.98, 1.98, 2.00
Mn(tpp)Br·$CDCl_3$[216]	–1.091	–0.087	0.080	1.996, 1.985, 1.994
Mn(tpp)I·$CDCl_3$[216]	1.30	0.010	0.008	1,965, 1.971, 1.930
Mn(tpfc)($OPPh_3$)[218]	–2.69	–0.030	0.011	1.994, 1.994, 1.980
Mn(tbp_8cz)(HOMe)[99]	–2.60	–0.015	0.006	2.00 (isotropic)

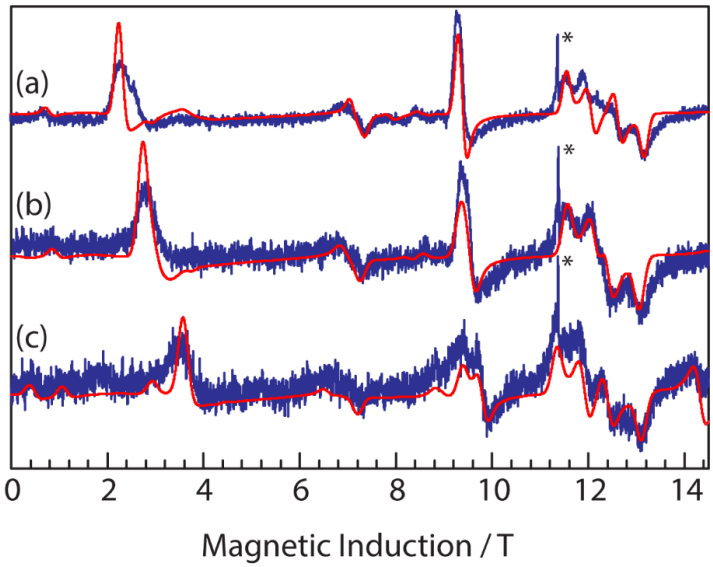

Figure II-9. HFEPR spectra of (a) II-13a, (b) II-13d, and (c) II-13e collected at 10 K and 319 GHz. Experimental data in blue and simulation in red. The * indicates a small Mn(II) impurity at g = 2.00, 11.4 T.

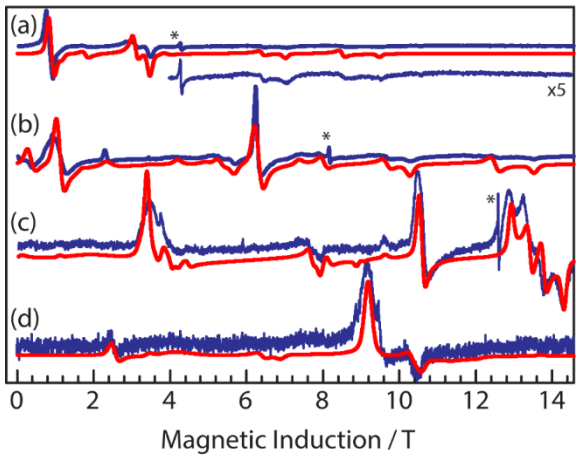

Figure II-10. HFEPR spectra of II-13a at (a) 120 GHz, (b) 229 GHz, (c) 353 GHz, and (d) 513 GHz collected at 10 K. Experimental data in blue and simulation in red. * indicates residual O_2 in the sample.

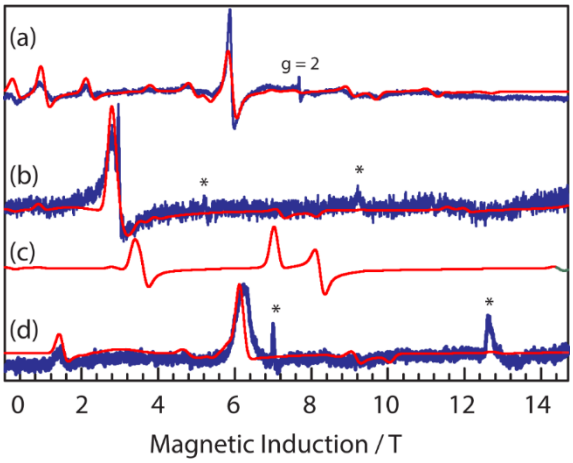

Figure II-11. HFEPR spectra of II-13d at (a) 216 GHz collected at 10 K, (b) 319 GHz collected at 3 K, (c) simulation of (b) where the D, E > 0 and (d) 413 GHz collected at 5 K. Experimental data in blue and simulation in red. * indicates residual O_2 in the sample.

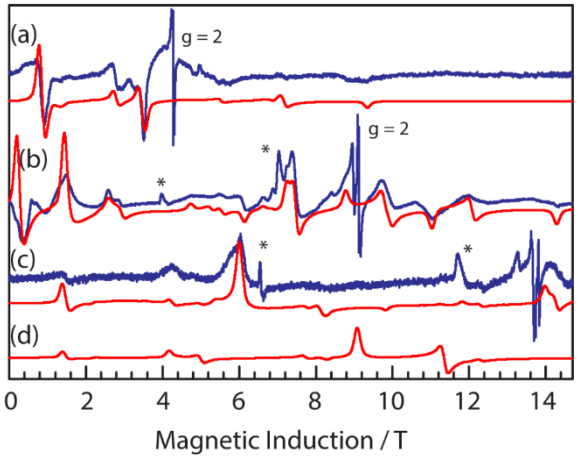

Figure II-12. HFEPR spectra of II-13e at (a) 120 GHz collected at 5 K, (b) 256 GHz collected at 10 K, (c) 387 GHz collected at 5 K, and (d) simulation of (c) where the D, E > 0. Experimental data in blue and simulation in red. * indicates residual O_2 in the sample.

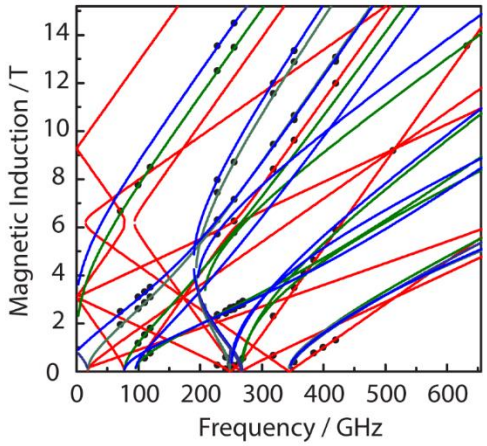

Figure II-13. Plot of resonance field versus microwave frequency for complex II-13a where the dots represent experimental points and the (–), (–), and (–) are the resonance positions calculated with parameters in Table II-2 at the molecular orientations X, Y and Z, respectively.

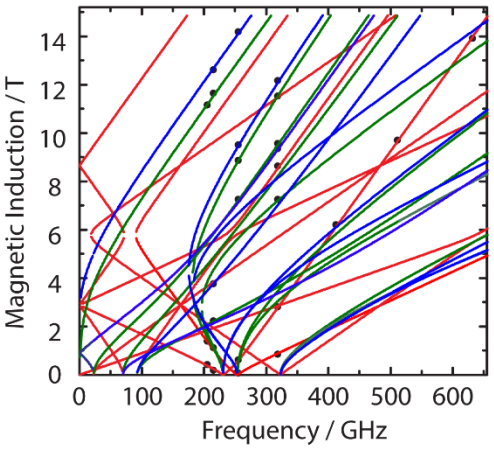

Figure II-14. Plot of resonance field versus microwave frequency for complex II-13d where the dots represent experimental points and the (–), (–), and (–) are the resonance positions calculated with parameters in Table II-2 at the molecular orientations X, Y and Z, respectively.

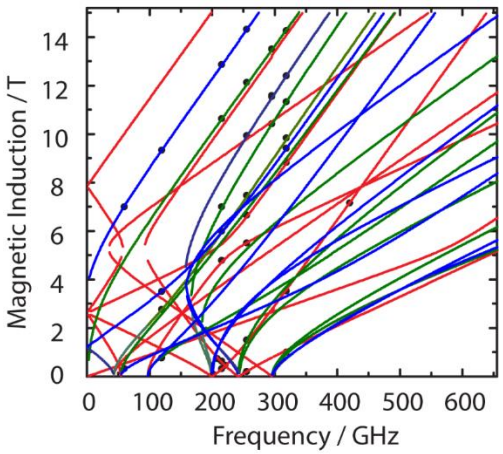

Figure II-15. Plot of resonance field versus microwave frequency for complex II-13e where the dots represent experimental points and the (–), (–), and (–) are the resonance positions calculated with parameters in Table II-2 at the molecular orientations X, Y and Z, respectively.

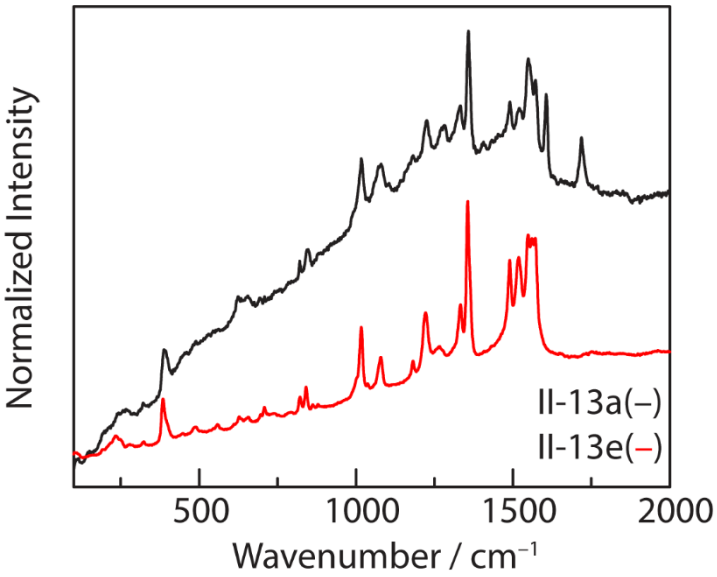

Figure II-16. Raman spectra of both II-13a (—) and II-13e (—).

X-ray quality crystals of each of the Mn(III) haloamide complexes were obtained by cooling concentrated acetonitrile solutions to –35 °C; solid-state structures of **II-13** are collected in Figure II-4. The Mn(III) center in **II-13e** is five-coordinate. The Mn ion lies 0.271 Å above the N_4 plane, and the *N*-iodoamide ligand occupies one of the axial coordination sites. The haloamide nitrogen is approximately trigonal planar, with Mn–N–I = 119.1(3)°, Mn–N–S = 128.8(4)°, and S–N–I = 112.1(4)°. The bond metrics of **II-13a-d** are consistent with those described for **II-13e** with two exceptions: 1) the N–X bond length varies predictably as a function of halogen identity (i.e., the N–Cl distance in **II-13a** is 1.745(3) Å, the N–Br distance in **II-13d** is 1.884(6) Å, and the N–I distance in **II-13e** is 2.056(7) Å) and 2) the Mn center in **II-13b** is six-coordinate with an MeCN ligand in the final coordination site, which results in elongation of Mn–N(1) in **II-13b** (2.252(4) Å) as compared to **II-13a** (2.070(3) Å) or **II-13c** (2.1112(7) Å). Of note, complexes **II-13d** and **II-13e** are the first crystallographically characterized *N*-bromoamide and *N*-iodoamide complexes of a transition metal, respectively. For comparison of the metrical parameters of **II-13** with known chloroamides, see Table II-3.

Table II-3. Relevant X-ray metrical parameters of II-13a, II-13b, II-13c, II-13d, II-13e, $Rh_2(espn)_2(MeCN)_2$ $[Rh_2(espn)_2(NClTs)_2]$,[203] $Na[Rh_2(espn)_2(NClTs)_2]$,[203] and $SnMe_3(NClTs)$.[204]

Entry	M–N / Å	X–N / Å	X–N–S / °
II-13a	2.133(3)	1.745(3)	111.6(2)
II-13b	2.252(4)	1.748(4)	109.5(2)
II-13c	2.1112 (7)	1.73667(7)	111.80(4)
II-13d	2.132(7)	1.884(6)	111.6(4)
II-13e	2.149(7)	2.056(7)	112.1(4)
$Na[Rh_2(espn)_2NClTs_2]$	2.253(4)	1.760(4)	108.91(2)
$Rh_2(espn)_2(MeCN)_2$ $[Rh_2(espn)_2NClTs_2]$	2.281(2)	1.745(3)	110.30(2)
$SnMe_3NClTs$	2.195(7)	1.734(7)	111.2(4)

II.2.2 Photolysis of Mn(III) Haloamides

Photolysis ($\lambda > 335$ nm) of an optically dilute solution of **II-13e** (4:1 MeCN:THF solution) affords Mn(II) complex **II-15**. UV-vis spectra collected periodically during the photolysis of a dilute solution of **II-13e** are characterized by well-anchored isosbestic points at 295, 408, 460, 514, 584, and 589 nm, which indicates the lack of steady state intermediates (Figure II-17). The final spectrum overlays with that of Mn(II)tpp (**II-15**), which was independently prepared by treatment of **II-12** with $NaBH_4$ (Figure II-18). ESI-MS analysis of the photolysis reaction mixture indicates the presence of sulfonamide **II-14**, the product of formal nitrene transfer to the α-C–H bond of THF. Preparative scale photolysis resulted in the isolation of sulfonamide **II-14** in 44% yield. The mass balance of the haloamide ligand is $TsNH_2$ (56% yield). Preparative scale photolyses of **II-13** result in isolation of Mn(tpp)X, which we hypothesize results from HX equivalents generated during photolysis via H-atom abstraction from solvent.

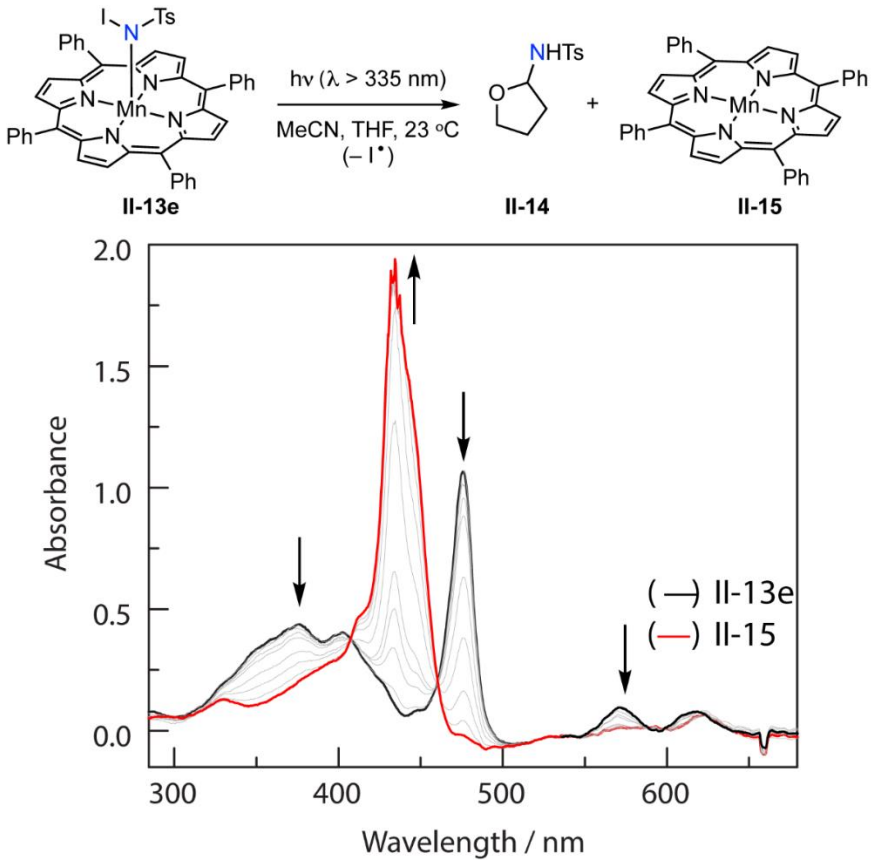

Figure II-17. Photolysis (λ > 335 nm) of II-13e affords sulfonamide II-14 and Mn(II) complex II-15. UV-vis spectra obtained periodically during the photolysis of II-13e display well-anchored isosbestic points at 295, 408, 460, 514, 584, and 589 nm, which indicate the lack of steady state intermediates during the conversion of II-13e to II-15.

The wavelength dependence of the observed photochemistry of **II-13e** was evaluated using 335, 400, and 495 nm long-pass filters. Only the 335 nm filter resulted in the spectral evolution illustrated in Figure II-17; no photoconversion was observed with a 400 or 495 nm long pass filter during the time scale of the experiment. However, prolonged photolysis (5 days) of **II-13e** with a 400 nm long pass filter yielded aminated THF (**II-14**) (40%, Table II-4). These data are consistent with photochemistry arising from excitation of the LMCT band at 386 nm. Similar observations were reported by Suslick,

that excitation of the analogous LMCT in Mn nitrate complexes was critical to accessing the corresponding Mn oxo complexes.[125]

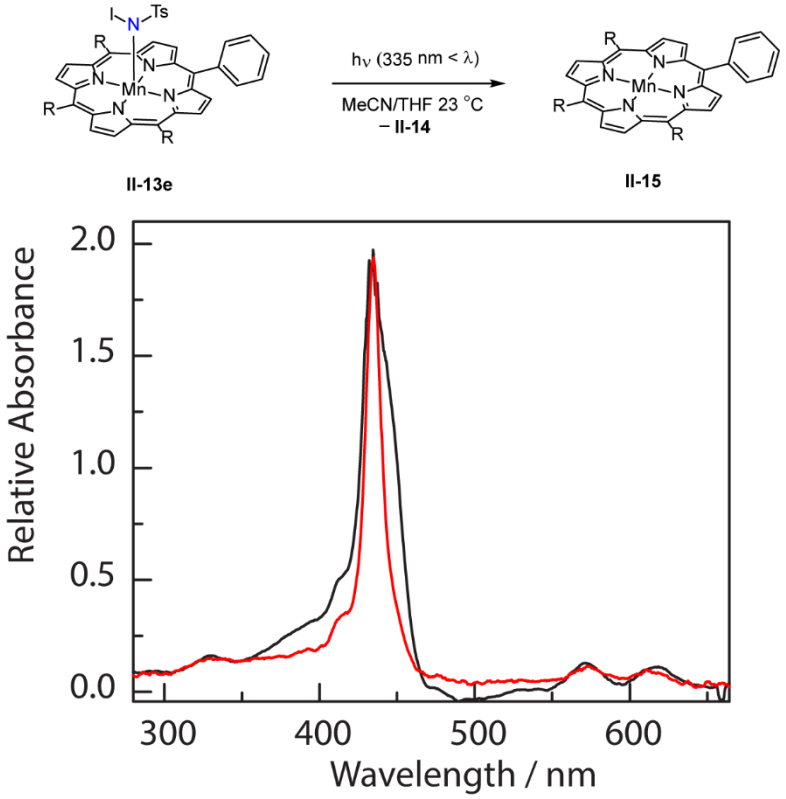

Figure II-18. Dilute photolysis of II-13e in a mixture of 4:1 MeCN:THF results in compound II-15 (–). This overlays well with the UV-vis spectrum of a sample of compound II-15 prepared by treatment of II-12 with $NaBH_4$ (–).

Table II-4. Tabulated yields of II-14, generated via photolysis of 13 in 4:1 MeCN:THF

Entry	λ > 335 nm	λ > 400 nm
II-13a	50%	27%
II-13b	55%	53%
II-13c	70%	54%
II-13d	63%	53%
II-13e	44%	40%

Complex **II-13e** participates in nitrene transfer photochemistry with a variety of substrates that are commonly encountered in Mn-catalyzed nitrene transfer chemistry (Figure II-19). Photolysis of **II-13e** (λ > 335 nm) in a 4:1 MeCN:2-Me-THF solution results in sulfonamide **II-16** (19% yield), the product of formal nitrene insertion into the less hindered α-C–H bond. To probe the C–H bond strength requirement for amination, we examined the photochemical amination of toluene (C–H bond dissociation energy (BDE) = 89.7 kcal/mol[1]) and cyclohexane (C–H BDE = 99.5 kcal/mol[219]): Toluene underwent benzylic amination to afford compound **II-17** in 40% yield; cyclohexane did not participate in detectable amination chemistry. Photolysis of **II-13e** in the presence of styrene results in aziridine **II-18** in 30% yield. In all cases, the mass balance is accounted for by $TsNH_2$ and transfer of the NTs fragment requires photochemical activation: Thermolysis of **II-13e** in the presence of these substrates results in **II-15** and $TsNH_2$.

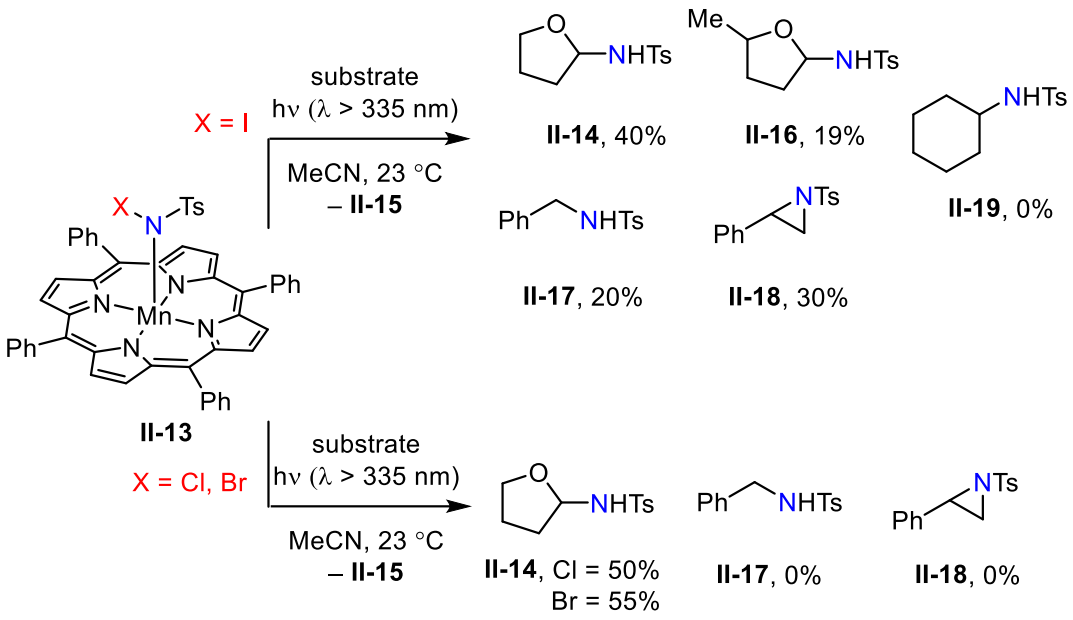

Figure II-19. Nitrene transfer photochemistry of N-iodoamide complex II-13e with various C–H bonds and olefinic substrates. All yields are determined via ^{1}H NMR with an internal standard of mesitylene. The formation of $TsNH_2$ accounts for the mass balance of nitrogen in these reactions.

Haloamide complexes **II-13a-d** also participate in photochemical amination of THF. Photolysis (λ > 335 nm) of a 4:1 MeCN:THF solution of **II-13a** afforded sulfonamide **II-14** in a 50% yield. Similar reactivity was observed for **II-13b**, **II-13c**, and **II-13d** (55, 70, and 63% yield of **II-14**, respectively). In contrast to iodoamide **II-13e**, photolysis of **II-13a-d** in the presence of either toluene or styrene does not result in the products of nitrene transfer.

II.2.3 Determination of Kinetic Isotope Effects

To gain insight into the mechanism of C–H amination, we measured the deuterium kinetic isotope effect (k_H/k_D) for THF amination. Experimentally, solutions of photoprecursors **II-13** were photolyzed in a 1:1 solution of THF:THF-d_8 and the k_H/k_D was

determined by integration of the ESI-MS signals for **II-14** and **II-14**-d_7. Photolysis of a solution of **II-13e** at 23 °C afforded a k_H/k_D = 18(3). For comparison, photolysis of **II-13a** in a 1:1 THF:THF-d_8 solution afforded a k_H/k_D = 6(1) (Table II-5).

Table II-5. Tabulated k_H/k_D values for THF amination via via II-13.

Entry	Steady-state k_H/k_D	Cryogenic k_H/k_D
II-13a	6(1)	4
II-13d	10(2)	8.2
II-13e	18(3)	18

II.2.4 Low Temperature Photolysis of N-*Chloramide* ***II-13a***

To evaluate the primary photoproducts obtained from the described *N*-haloamides, we pursued low-temperature photolyses of these compounds in frozen solvent matrices. Photolysis of a 2-Me-THF glass of **II-13a** at 77 K resulted in the evolution of two new peaks in the UV-vis spectrum at 427 and 439 nm (Figure II-20a). These peaks are well matched to spectral features of Mn(II) complex **II-15**, which could be generated by photoreduction of **II-13a** via Mn–N homolysis (for comparison of the UV vis spectrum following photolysis at 77 K with the spectrum of independently synthesized compound **II-15,** see Figure II-21). To further confirm that the photolysis of **II-13a** generates Mn(II)(tpp), we measured the X-band EPR at 4 K and 9.35 GHz following irradiation of a 2-Me-THF glass of **II-13a** at 77K (Figure II-20b). Mn(III) complex **II-13a** does not display an X-band EPR spectrum. Following photolysis, the measured spectrum exhibits features at $g_\perp$ = 6 and $g_\parallel$ = 2, which are consistent with those of independently prepared

Mn(II) complex **II-15** and are as expected for an axial S =5/2 system with D >> hv.[121, 156] The differences in peak shape shown in Figure II-20b are due to differential axial ligation. Compound **II-15** is formed via photocleavage of the Mn–N bond and thus has no axial ligand, whereas independently synthesized **II-15** has an axial THF ligand.[156] The observed EPR features were insensitive to the photolysis matrix: Photolysis of a solvent-free thin film of **II-13a** resulted in the evolution of an EPR spectrum of **II-15** (Figure II-22).

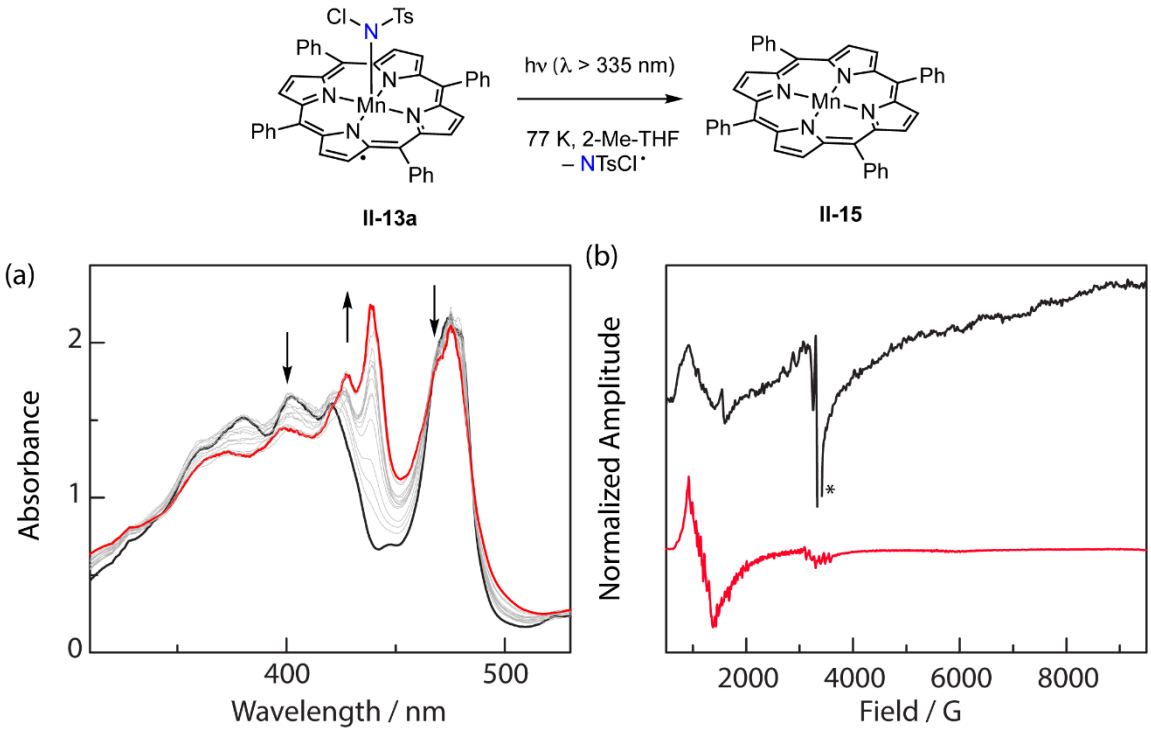

Figure II-20. Low-temperature (77K) photolysis of Mn(tpp)(NClTs) (II-13a) results in photoreduction to generate Mn(II) complex II-15. (a) UV-vis spectra obtained periodically during the photolysis of II-13a at 77K display well-anchored isosbestic points at 295, 408, 460, 514, 584, and 589 nm. The peaks that grow in at 427 and 439 nm are attributed to Mn(II) complex II-15 (a concentrated sample was utilized in this photolysis experiment, which resulted in detector saturation at 474 nm). (b) X-band EPR spectra following photolysis of II-13a (–) and of Mn(II)(tpp) (II-15) (–). *The peak at g = 2.0 has been truncated for clarity.

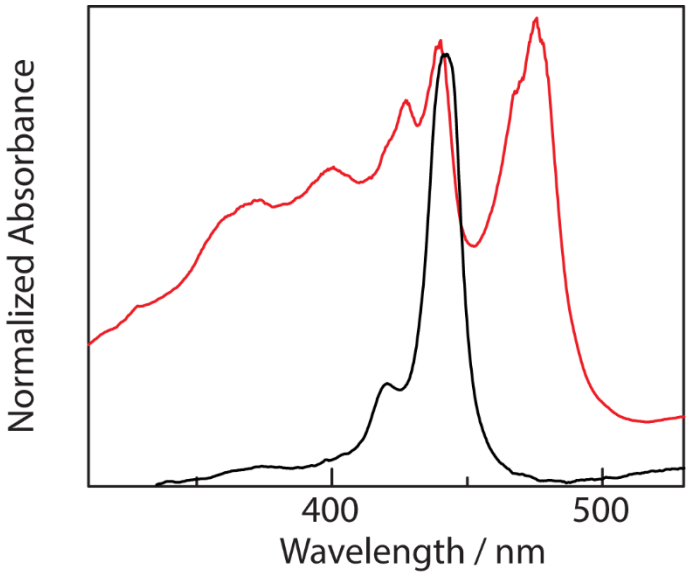

Figure II-21. Comparison of cryogenic UV-vis spectra of II-15 generated via photolysis of II-13a (—) and II-15 prepared by treatment of II-12 with $NaBH_4$ (—). Photogenerated II-15 has a peak at 427 and 440 nm, where the peaks at 396 and 475 nm are attributed leftover starting material II-13a. Externally synthesized II-15 has a peak at 419 and 442 nm.

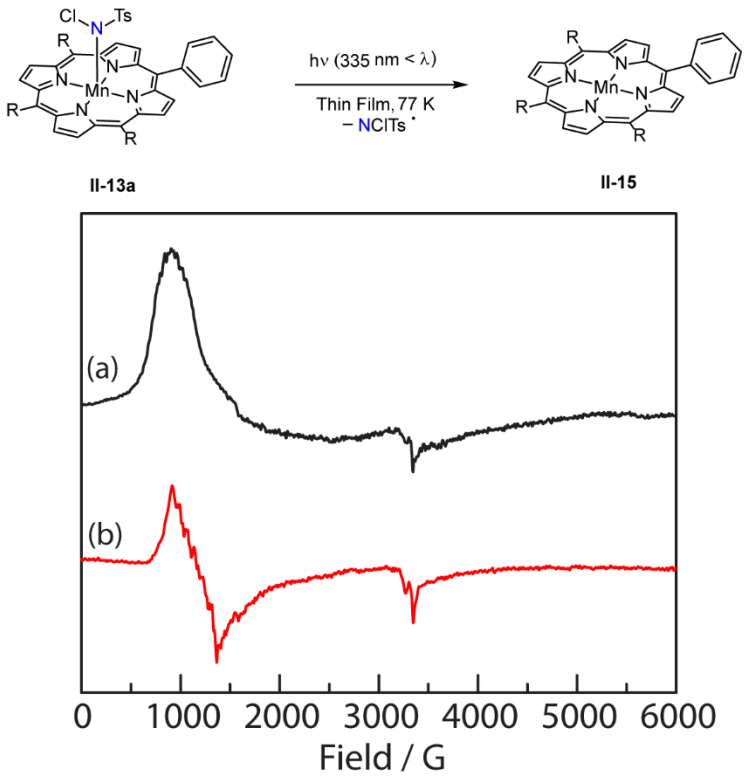

Figure II-22. Photolysis (λ > 335 nm) of a thin film of II-13a at 77 K results in formation of II-15. (a) EPR spectrum at 4 K of II-15; (b) EPR spectrum of a thin film of independently synthesized II-15 measured at 4 K. Differences in peak shape are due to differential axial ligation: Compound II-15 formed via photoreduction has no axial ligand due to Mn–N cleavage, whereas synthesized II-15 has a THF axial ligand.[156]

II.2.5 Low Temperature Photolysis of N-*Iodoamide* ***II-13e***

Photolysis of a 2-Me-THF glass of **II-13e** at 77K results in the evolution of a new peak in the UV-vis spectrum at 441 nm, which is distinct from the spectrum observed from photolysis of **II-13a** (Figure II-23a). The X-band EPR spectrum of this sample measured at 4K and 9.35 GHz (Figure II-23b) is significantly richer than that from the photolysis of **II-13a** (Figure II-21b). Features across the entire field range are observed, corresponding to g = 0.8, 1.2, 1.5, 2.0, 3.5, and 5.0. Such an EPR spectrum is inconsistent with either *S* = 3/2 or 5/2 with |D| >> hν. Rather, the EPR spectrum of **II-20** can be simulated as an *S* =

5/2 complex with relatively small zfs (|D| = 0.18 cm-1 (5.4 GHz) and |E| = 0.0037 cm-1; |E/D| = 0.020). The observed features are approximately consistent with the simulation provided with these parameters. A number of simulations with other parameters provide similar agreement with the experimental data and additional investigation, such as a HFEPR study, is needed to unambiguously resolve the problem. The spectral features of Mn(II) complex **II-15** are not observed in the spectrum obtained following photolysis of **II-13e**, nor are features expected of a potential Mn(IV) complex with simple X-type axial ligands or of free triplet tosyl nitrene.[220-222] Additionally, photolysis of a thin film of **II-13e** at 77 K also generates the same spectrum shown in Figure II-23b, thus the generated spectrum of **II-20** is independent of matrix used (Figure II-23).

Analysis of the temperature dependence of the EPR spectrum of **II-20** supports a high-spin configuration (*i.e.*, $S = 5/2$). Warming the sample from 4 K to 77 K results in the disappearance of the rich spectral features; only a signal at g = 2.0 which we hypothesize is from an organic radical generated in the photolysis. Subsequent re-cooling of the sample to 4 K results in the reappearance of the spectral features illustrated in Figure II-23b (Figure II-25). These observations confirm that the loss of spectral features upon warming to 77 K is due to spin-spin relaxation and not sample degradation.

Warming a sample of **II-20** generated in a 1 : 1 THF : THF-d_8 mixture at 77 K to 23 °C affords amination product **II-14** with $k_H/k_D = 18$, which indicates that low-temperature and room-temperature photolyses generate the same reactive intermediate (Table II-5).

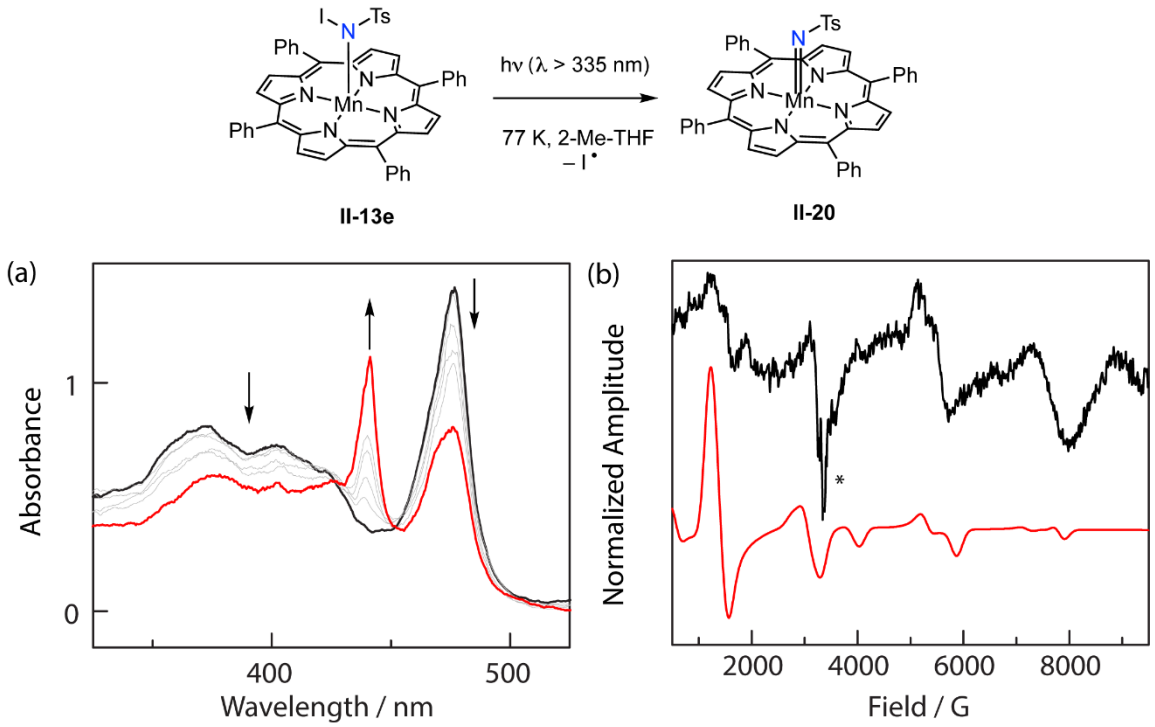

Figure II-23. Low-temperature (77 K) photolysis of Mn(tpp)(NITs) (II-13e) results in N–I cleavage to generate Mn(IV) nitrenoid complex II-20. (a) UV-vis spectra obtained periodically during the photolysis of II-13e at 77 K display well-anchored isosbestic points at 429, 449, 511 nm. (b) X-band EPR spectra following photolysis of a 2-Me-THF glass of II-13e at 77 K (–). This spectrum was simulated with parameters D = 0.18 cm^{-1} and E = 0.0037 cm^{-1} (–). *The peak at g = 2.0 has been truncated for clarity.

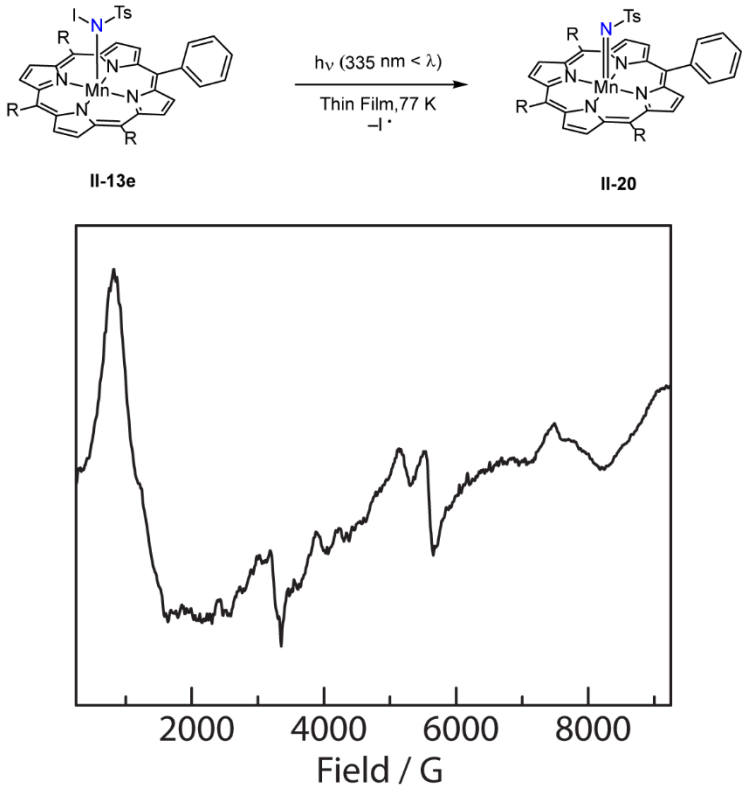

Figure II-24. EPR spectrum (measured at 4 K) following photolysis (λ > 335 nm) of a thin film of II-13e at 77 K.

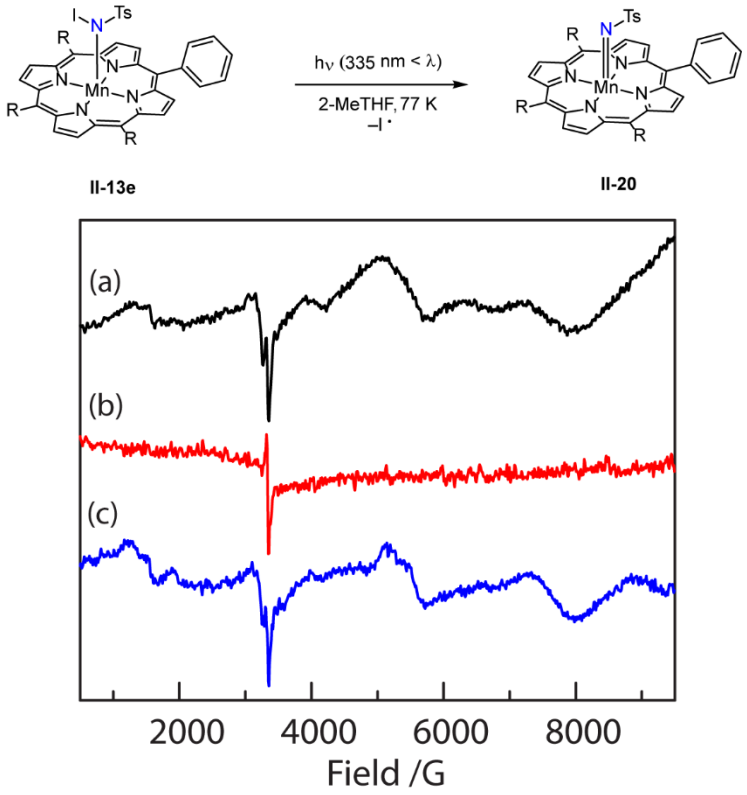

Figure II-25. Photolysis (λ > 335 nm) of II-13e in 2-Me-THF at 77 K results in formation of II-20. (a) EPR spectrum at 4 K of II-20; (b) EPR spectrum collected by warming the sample from (a) to 77 K; (c) EPR spectrum collected after cooling the sample from (b) back to 4 K.

II.2.6 Computational Analysis

Density functional theory (DFT) optimization of the geometry of compounds **II-13a**, **II-13d**, and **II-13e** have been pursued as singlet, triplet, and quintet electronic configurations. The singlet and triplet are higher in energy than the quintet by 35 kcal/mol and 17 kcal/mol, respectively (Table II-9). For comparison of optimized structures with crystallographically determined structures, see Tables II-6-II-8. Optimization of **II-20** indicates that doublet, quartet, sextet, and octet state are similar in energy, with the quartet being the lowest energy and the sextet and doublet states 2.6 kcal/mol and 3.9 kcal/mol

higher, respectively (Table II-10). The similarity of the various spin states of **II-20** suggests that accurate description of this species requires a multireference ground state.

Ground state reaction thermodynamics were calculated for Mn–N and N–X cleavage from compounds **II-13a**, **II-13d**, and **II-13e** (Table II-11). For **II-13a**, Mn–N cleavage is preferred to N–Cl cleavage while for **II-13e** these pathways are approximately isoenergetic. These results are consistent with the expectation that N–X bond strength decreases for the heavier halogens,[223] computationally determined N–X BDEs for complexes **II-13** (Table II-13), and the experimental observation of Mn–N cleavage for **II-13a** and N–I cleavage for **II-13e**.

Table II-6. Table comparing computed structure of II-13a at B3LYP level of theory against crystallographic data of II-13a.

	B3LYP	Experiment
Mn–N1 (Å)	2.168	2.133(3)
N1–Cl (Å)	1.864	1.745(3)
N1–S (Å)	1.660	1.610(3)
Cl–N1–S (°)	110.12	111.03(3)

Table II-7. Table comparing computed structure of II-13d at B3LYP level of theory against crystallographic data of II-13d.

	B3LYP	Experiment
Mn–N1 (Å)	2.165	2.132(7)
N1–Br (Å)	1.983	1.884(6)
N1–S (Å)	1.655	1.594(7)
Br–N1–S (°)	111.7	111.6(4)

Table II-8. Table comparing computed structure of II-13e at B3LYP level of theory against crystallographic data of II-13e.

	B3LYP	Experiment
Mn–N1 (Å)	2.166	2.149(7)
N1–I (Å)	2.118	2.056(7)
N1–S (Å)	1.649	1.593(7)
I–N1–S (°)	113.4	112.1(4)

Table II-9. Analysis of the ground state energies of II-13a, II-13d, and II-13e as different spin states.

Multiplicity	II-13a kcal/mol	II-13d kcal/mol	II-13e kcal/mol
Singlet	33.72	34.22	35.10
Triplet	17.19	17.40	17.64
Quintet	0	0	0

Table II-10. Analysis of the ground state energies of II-20 as different spin states.

Multiplicity	Energy / kcal/mol
Doublet	3.89
Quartet	0
Sextet	2.57
Octet	21.8

Table II-11. Thermodynamic electronic energies comparison of photoreduction vs N–X cleavage for II-13a, II-13d, and II-13e.

Cleavage	II-13a kcal/mol	II-13d kcal/mol	II-13e kcal/mol
Mn–N	41.84	39.28	37.20
N–X	47.07	41.40	37.72

Table II-12. Thermodynamic free energies comparison of photoreduction vs N–X cleavage for II-13a, II-13d, and II-13e.

Cleavage	II-13a kcal/mol	II-13d kcal/mol	II-13e kcal/mol
Mn–N	25.66	22.72	20.39
N–X	36.21	29.99	26.33

Table II-13. Calculated bond disassociation energies of the N–X bond in II-13a, II-13d, and II-13e.

Haloamide	BDE/ kcal/mol
II-13a	46.17
II-13d	40.62
II-13e	37.01

II.3. Discussion

Development of photochemical strategies to generate metal nitrenoid species promises to provide opportunities to study reactive intermediates that display fleeting lifetimes. Organic azide ligands have been recognized as potential photoprecursors to metal nitrenes, but few kinetically stable transition metal adducts of these ligands have been characterized.[35, 68, 200-202] We have been attracted to photoactivation of N–X bonds within haloamide ligands as a potentially generalizable strategy to photochemically generate nitrene fragments within the primary coordination sphere of transition metal ions. This strategy is motivated by the ubiquity of N–X photoactivation in the organic chemistry of haloamines[3, 205-207] and by analogy to the oxo photochemistry of metal oxyanion complexes.[97, 124-126, 193-195] Unlike the organic chemistry of *N*-haloamines, however, the synthetic chemistry and photoactivity of *N*-haloamide complexes is almost completely undeveloped.

Application of *N*-haloamide ligands in nitrene photochemistry requires predictable and selective N–X activation chemistry. In the context of Mn(III) haloamide photochemistry, homolytic N–X bond cleavage would afford a Mn(IV) nitrenoid while heterolytic N–X bond activation would result in Mn(V) nitrenoids (Figure II-26). In addition to these potential N–X activation modes, activation of the Mn–N bonds could

give rise to Mn(II) and amidyl radicals.[126, 224, 225] Analogous O–X homolysis and heterolysis as well as M–O homolysis pathways have been documented in the oxo photochemistry of metal oxyanion complexes.[97, 124-126, 193-195]

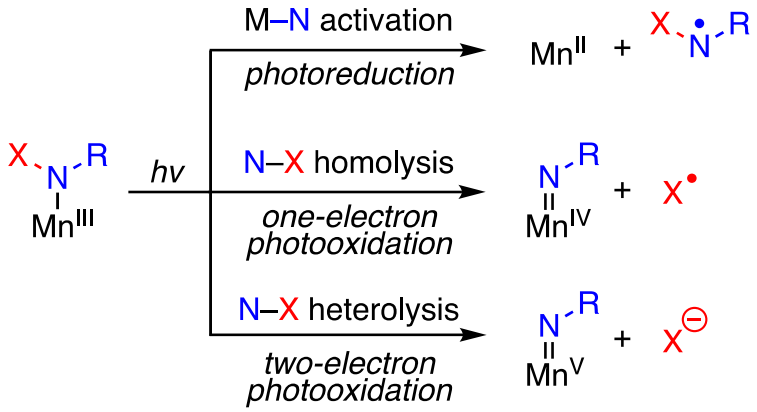

Figure II-26. Summary of potential photoactivation pathways for Mn(III) *N*-haloamide complexes.

The Mn nitrenoid fragment in **II-20** is potentially redox non-innocent; thus the formal oxidation states of the Mn nitrenoids in the forgoing discussion are based on counting the nitrenoid fragment as a 2– ligand (*i.e.*, imido nomenclature). In the context of a formally Mn(IV) imido complex, *N*-centered non-innocence could result in a species more appropriately described as either a Mn(III) adduct of an iminyl radical anion ($RN^{\bullet -}$, $S = 1/2$) or as a Mn(II) adduct of a singlet nitrene ligand ($S = 0$).[226] Applying the Enemark-Feltham nomenclature,[227] the Mn(IV) imide would be described as $[MnNR]^7$.

We have prepared a family of Mn(III) *N*-haloamides, Mn(tpp)(NXTs), as potential photoprecursors to reactive high-valent Mn nitrenoids relevant in Mn tetrapyrrole-catalyzed nitrene transfer (Figure II-2). Solution-phase and solid-state characterization indicate the family of prepared complexes are $S = 2$ Mn(III) species. UV-vis spectroscopic

measurements indicate that the donor strength of the *N*-haloamides is similar to that of chloride and is not meaningfully impacted by the identity of the *N*-halogen atom. HFEPR indicates that the haloamide complexes are representative of Mn tetrapyrroles with light-atom axial donors, with enhanced rhombicity that may be due to anisotropic Mn–N π-bonding.

Photolysis of each of the prepared *N*-haloamide complexes in the presence of weak C–H bond donors, such as THF, results in formal nitrene transfer chemistry. Given previous demonstrations of C–H amination via amidyl radical intermediates,[228-230] the observation of amination products is insufficient to differentiate between the potential photogeneration of a high-valent nitrenoid or *N*-centered radical intermediates. Halogen-dependent photochemistry is observed with other substrates that are commonly encountered in nitrene transfer chemistry. Whereas *N*-chloroamide **II-13a** does not participate in photochemical aziridination of styrenes, *N*-iodoamide **II-13e** does undergo photochemical aziridination. These observations suggest that reactive nitrogen fragments generated from **II-13a** and **II-13e** differ; if both haloamides underwent similar photoactivation, one would expect that the resultant reactive species would display homologous substrate functionalization activity.

Analysis of the kinetic isotope effects for C–H functionalization demonstrates the decisive role of the halogen substituent on the resultant photochemistry and provides a direct reporter on the nature of the C–H cleavage event. Amination of THF by photolysis of *N*-chloroamide **II-13a** proceeds with k_H/k_D = 6(1), which is consistent with values for H-atom abstraction reactions at *N*-centered radicals.[231] In contrast, amination of THF by

photolysis of *N*-iodoamide **II-13e** proceeds with k_H/k_D = 18(3). This large k_H/k_D value exceeds the classical limit for H-atom transfer reactions between light atoms and is consistent with the large KIEs that are often encountered for amination via metal nitrenoids.[232-239]

Cryogenic photolysis provides both the opportunity to directly evaluate the course of the described photoreactions and evidence for the decisive impact of halogen identity on the resultant reactive nitrogen species. Both UV-vis and EPR spectroscopies indicate that the primary photoproduct obtained from chloroamide **II-13a** is Mn(II) complex **II-15**. The M–N homolysis that would generate complex **II-13** would also afford an amidyl radical intermediate, which would give rise to the observed amination products. In contrast, photolysis of iodoamide **II-13e** affords Mn(IV) nitrenoid **II-20**, the product expected of homolytic activation of the N–I bond of **II-13e**. Experimental data is consistent with the formation of an S = 5/2 species (*i.e.* an Mn(III) iminyl radical complex). The Soret band of **II-20** (441 nm) is distinct from reported porphyrin-supported Mn(IV) oxo compounds (420 nm), which are all S = 3/2 (Table II-14).[193, 240-242] Additionally, the similarity of the UV-vis spectra of **II-15** and **II-20** suggests that **II-20** is a S = 5/2 system (Figure II-27). DFT analysis of the potential spin states of **II-20** suggests multireference contributions to the electronic ground state. The observed preference for Mn–N activation in **II-13a** and for N–I activation in **II-13e** is consistent with the relative N–Cl and N–I bond strengths and with computed ground state thermodynamics for Mn–N and N–X cleavage reactions. These results highlight the ability to control the course of the photoreaction by careful design of the photocleavable ligands.

Table II-14. Comparison of Mn(IV) and Mn (V) Soret bands in MnO(por) complexes.

Porphyrin	Mn(IV) Soret / nm	Mn(V) Soret / nm
Mn(tpp)	425[193]	435[193]
Mn(tpfpp)	422[193]	432[194]
Mn(tpymp)	438[193]	450[193]
Mn(tmp)	425[240]	
Mn_2(dtmp)	415[242]	423[242]
$Mn_2X_2(tpp)_2$	417[241]	

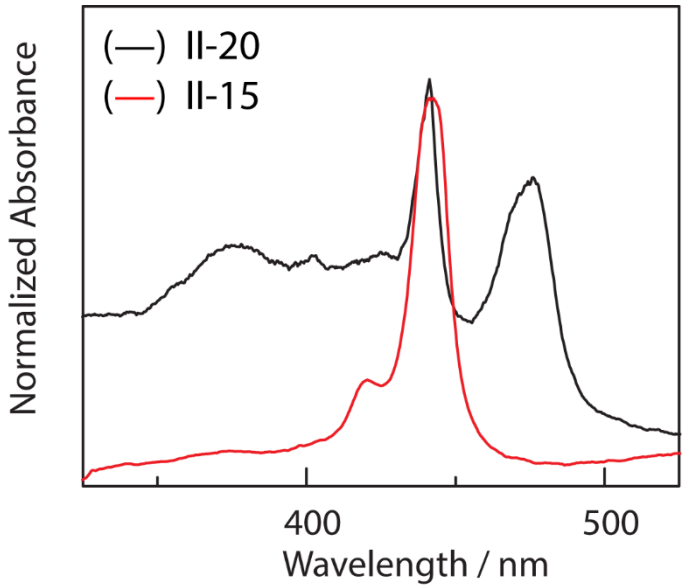

Figure II-27. Comparison of cryogenic UV-vis spectra of II-20 (—) and II-15 (—). Compound II-20 has a peak at 441 nm, where the peaks at 375 and 475 nm are attributed leftover starting material II-13e. Compound II-15, prepared by treatment of II-12 with $NaBH_4$, has a peak at 442 nm.

II.4. Conclusions

Synthesis and characterization of reactive intermediates capable of C–H functionalization reactions is central to the rational development of new selective and

efficient catalysts. Synthetic photochemistry provides a platform to generate reactive intermediates under conditions in which they can be kinetically trapped, for example by providing a synthetic strategy to generate these species under cryogenic conditions. Application of synthetic photochemistry requires the availability of appropriate photoprecursor molecules and specifically access to photolabile ligands that exhibit predictable photoactivation modes. Here we have advanced *N*-haloamide ligands as a photolabile ligand in the synthesis of Mn nitrenoids. Isolation of homologous Mn(III) complexes featuring *N*-chloro-, *N*-bromo-, and *N*-iodoamide ligands provided the opportunity to observe the decisive impact of the halogen substituent on the observed photochemistry. Whereas the Mn(III) chloroamide complex undergoes photoreduction via direct homolytic Mn–N activation, the corresponding Mn(III) iodoamide undergoes N–I activation to unveil a reactive Mn nitrenoid that participates in both C–H amination and olefin aziridination chemistry. A combination of low-temperature spectroscopy and analysis of C–H functionalization kinetic isotope effects indicates the critical photochemical difference between *N*-chloro- and *N*-iodoamide ligands. These observations mirror the competition between ligand-centered photoactivation chemistry and photoreduction reactions that are often encountered in the corresponding metal nitride and metal oxo photochemistries. The findings described here begin to delineate the design parameters needed to elicit ligand-centred bond activation to generate metal nitrenoids. We anticipate the development of general strategies in the synthetic photochemistry of metal nitrenoids will expand access to reactive nitrenoids relevant to catalysis, and we are actively working to expand the generality of the haloamide strategies described here.

II.5. Experimental Details

II.5.1 General Considerations

Materials All reactions were carried out in an N_2-filled glovebox, unless otherwise stated. Solvents were obtained as ACS reagent grade. Unless otherwise noted, all chemicals and solvents were used as received. 2,6-Dichlorobenzaledhyde, acetic acid (AcOH), chloramine-T trihydrate, manganese(II) chloride tetrahydrate ($MnCl_2 \cdot 4H_2O$), chloroform, and anhydrous 2-methyltetrahydrofuran (2-Me-THF) were obtained from Sigma Aldrich. Silica gel (0.06–0.20 mm, 60 Å for column chromatography) and $BF_3 \cdot OEt_2$ were obtained from Acros Organics. Benzaldehyde, styrene, and propionic acid were obtained from Bean Town Chemical. Nitrobenzene was obtained from Alfa Aesar and pyrrole was obtained from TCI America. Pentafluorobenzaldehyde was obtained from Matrix Scientific and acetonitrile was obtained from Fischer Scientific. 2,3-Dichloro-5,6-dicyano-p-benzoquinone (DDQ) was obtained from Chem Impex International and dimethyl formamide (DMF) was obtained from VWR. Ethanol (200 proof) was obtained from Koptec and silver tetrafluoroborate ($AgBF_4$) was obtained from Strem Chemicals. NMR solvents were purchased from Cambridge Isotope Laboratories and were degassed via three freeze-pump-thaw cycles. CD_3CN was stored over 3 Å molecular sieves, and all other NMR solvents were stored over 4 Å molecular sieves. Anhydrous acetonitrile, THF, and toluene were obtained from a drying column and stored over activated molecular sieves. All reactions were carried out at 23 °C unless otherwise noted. H_2tpp,[243] H_2tdclpp,[244] H_2tpfpp,[245] MnCl(tpp) (**II-12**),[246] MnCl(tdclpp) (**II-21**),[157] and MnCl(tpfpp) (**II-22**)[247] were prepared according to literature methods.

Characterization Details NMR spectra were recorded on Bruker Avance NEO 400 NMR operating at 400.09 MHz for ^{1}H acquisitions and were referenced against solvent signals: $CDCl_3$ (7.26 ppm, ^{1}H), $(CD_3)_2SO$ (2.50 ppm, ^{1}H), and CD_3CN (1.94 ppm, ^{1}H).[248] ^{1}H NMR data are reported as follows: chemical shift (δ, ppm), multiplicity (s (singlet), d (doublet), t (triplet), m (multiplet), br (broad), integration. UV-vis spectra were recorded at 293 K in quartz cuvettes on an Ocean Optics Flame-S miniature spectrometer with DH-mini UV-vis NIR light source (200–900 nm) and were blanked against the appropriate solvent. Solution magnetic moments were determined using the Evans method: the analyte was dissolved in a stock solution of $CDCl_3$ and trifluorotoluene at 23 °C; a capillary of trifluorotoluene in $CDCl_3$ was added to the sample tube and the ^{19}F NMR spectrum was recorded. Diamagnetic corrections were estimated from Pascal constants.[249] MALDI data was obtained using a Bruker Microflex LRF MALDI-TOF using reflection-TOF mode. The fluence of the ablation laser was controlled using Bruker Daltonics flexControl software that was pre-installed with the instrument. X-band EPR spectra were recorded on a Bruker ELEXSYS Spectrometer with a cryogen-free in-cavity temperature control system. X-band EPR spectra of photogenerated reactive intermediates were collected by irradiation (100 W Hg lamp) of samples in an N_2-cooled (77 K) quartz finger dewar (Wilmad Glass, WG819-B-Q) and subsequent transfer of the cold samples into a pre-cooled EPR cavity.

HFEPR Details HFEPR spectra were collected with finely ground crystalline samples of **II-13a**, **II-13d**, and **II-13e** at 5–20 K at the Electron Magnetic Resonance (EMR) Facility of the National High Magnetic Field Laboratory (NHMFL, Tallahassee, FL, USA) using

a transmission spectrometer described elsewhere,[250] which was modified by the use of phase-locked Virginia Diodes Inc. (VDI, Charlottesville, VA, USA) sources, generating sub-THz wave radiation in a 50–640 GHz frequency range. The spectrometer is associated with a 15/17-T warm-bore superconducting magnet.

X-Ray Diffraction Details X-ray crystal structures of **II-13a-c** were collected using synchrotron radiation (0.33062 Å or 0.41328 Å as specified in the respective cif) at ChemMatCARS located at the Advanced Photon Source (APS) housed at Argonne National Laboratory (ANL). Crystals suitable for X-ray diffraction were mounted on a glass fiber and data was collected at 100 K (Cryojet N_2 cold stream) using a vertically mounted Bruker D8 three-circle platform goniometer equipped with a PILATUS3 X CdTe 1M detector. Data were collected as a series of φ and/or ω scans. Data were integrated using SAINT and scaled with a multi-scan absorption correction using SADABS. Structures were solved by intrinsic phasing using SHELXT (Apex2 program suite v2014.1) and refined against F^2 on all data by full matrix least squares with SHELXL97.[251, 252] All non-hydrogen atoms were refined anisotropically. H atoms were placed at idealized positions and refined using a riding model. Refinement details are described in the relevant cif.

A Bruker APEX 2 Duo X-ray (three-circle) diffractometer was used for crystal screening, unit cell determination, and data collection for all other X-ray crystal structures. Crystal suitable for X-ray diffraction were mounted on a MiTeGen dual-thickness micro-mount and placed under a cold N_2 stream (Oxford). The X-ray radiation employed was generated from a Mo sealed X-ray tube (Kα = 0.70173 Å with a potential of 40 kV and a current of

40 mA). Bruker AXS APEX II software was used for data collection and reduction. Absorption corrections were applied using the program SADABS. A solution was obtained using XT/XS in APEX2 and refined in Olex2.[251-253] Hydrogen atoms were placed in idealized positions and were set riding on the respective parent atoms. All non-hydrogen atoms were refined with anisotropic thermal parameters. The structure was refined (weighted least squares refinement on F2) to convergence.[252]

Computational Details Calculations were performed using the Gaussian 16, Revision C.01 suite of software.[254] Geometry optimizations were carried out with the B3LYP functional[255-258] the LANL2DZ basis set[259] and corresponding ECP for Mn, Cl, Br, and I and the 6-311+G* basis set for other atoms; the coordinates for optimized geometries are tabulated in Tables II-25–II-29. Frequency calculations at this level of theory confirmed that optimized geometries represent ground state structures. Tables II-6-II-8 summarizes important bond distances obtained from B3LYP and compared to experimental structures.

II.5.2 Synthesis and Characterization

Synthesis of [Mn(tpp)]BF_4 (II-23)

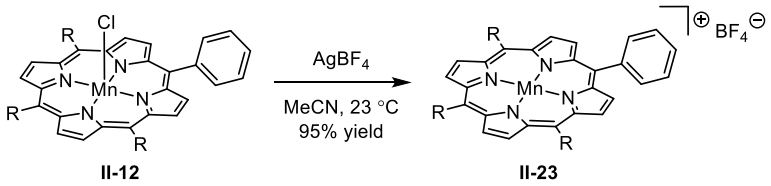

A 20-mL scintillation vial was charged with Mn(tpp)Cl (**II-12**, 51 mg, 0.070 mmol, 1.0 equiv) and MeCN (3.0 mL). Separately, a 20-mL scintillation vial (wrapped in electrical tape to exclude ambient light) was charged with $AgBF_4$ (15 mg, 0.080 mol, 1.1 equiv) and MeCN (2.0 mL). The two solutions were combined and the resulting reaction mixture was

stirred at 23 °C for 24 h. Solvent was removed *in vacuo.* The residue was taken up in CH_2Cl_2 (4.0 mL) and filtered through a Celite plug. Solvent was removed *in vacuo* to obtain the title compound as a dark red powder (50 mg, 95% yield). Single-crystals suitable for X-ray diffraction were obtained via a layering a concentrated CH_2Cl_2 solution with pentane at 23 °C; single-crystal X-ray diffraction data is collected in Figure II-28 and Table II-22. ^{1}H NMR (δ, 23 °C, CDCl3): 7.8 (br d, 20H), –36 (br s 8H). UV-vis (MeCN), λ_{max} (nm (ε ($M^{-1}cm^{-1}$))): 388 (3.6×10^4), 478 (3.2×10), 574 (6.3×10^3), 610 (5.3×10^3).

Synthesis of [Mn(tdclpp)]BF_4 (II-24)

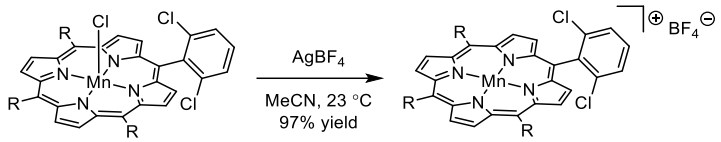

II-21 **II-24**

A 20-mL scintillation vial was charged with Mn(tdclpp)Cl (**II-21**, 70 mg, 0.070 mmol, 1.0 equiv) and MeCN (3.0 mL). Separately, a 20-mL scintillation vial (wrapped in electrical tape to exclude ambient light) was charged with $AgBF_4$ (15 mg, 0.080 mol, 1.1 equiv) and MeCN (2.0 mL). The two solutions were combined and the resulting reaction mixture was stirred at 23 °C for 24 h. Solvent was removed *in vacuo.* The residue was taken up in CH_2Cl_2 (4.0 mL) and filtered through a Celite plug. Solvent was removed from the filtrate *in vacuo* to obtain the title compound as a dark red powder (70 mg, 97% yield). ^{1}H NMR (δ, 23 °C, CDCl3): 7.6 (br s, 8H), 6.3 (br s, 4H), –37 (br s, 8H). UV-vis (MeCN), λ_{max} (nm (ε ($M^{-1}cm^{-1}$))): 385 (2.7×10^4), 477 (2.9×10^4), 569 (6.7×10^3).

Synthesis of [Mn(tpfpp)]BF_4 (II-25)

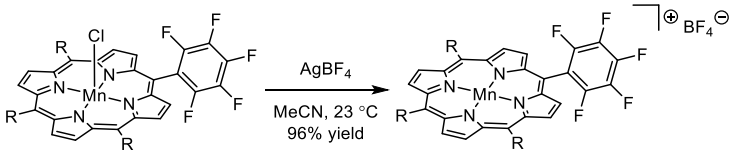

II-22 **II-25**

A 20-mL scintillation vial was charged with Mn(tpfpp)Cl (**II-22**, 75 mg, 0.070 mmol, 1.0 equiv) and MeCN (3.0 mL). Separately, a 20-mL scintillation vial (wrapped in electrical tape to exclude ambient light) was charged with $AgBF_4$ (15 mg, 0.080 mol, 1.1 equiv) and MeCN (2.0 mL). The two solutions were combined and the resulting reaction mixture was stirred at 23 °C for 24 h. Solvent was removed *in vacuo.* The residue was taken up in CH_2Cl_2 (4.0 mL) and filtered through a Celite plug. Solvent was removed from the filtrate *in vacuo* to obtain the title compound as a dark red powder (75 mg, 96% yield). ^{1}H NMR (δ, 23 °C, CD_3CN): –35 (br s 8H). ^{19}F (δ, 23 °C, CD_3CN): –124 (br s 1F), –149 (br s, 1F) –157 (br s, 3F) UV-vis (MeCN), λ_{max} (nm (ε ($M^{-1}cm^{-1}$))): 372 (3.8×10^4), 463 (4.5×10^4), 558 (7.3×10^3).

Synthesis of Mn(tpp)(NClTs) (II-13a)

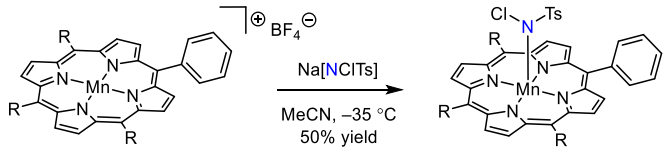

II-23 **II-13a**

A 20-mL scintillation vial was charged with **II-23** (50 mg, 0.070 mmol, 1.0 equiv) and MeCN (4 mL). A separate 20-mL scintillation vial was charged with NaNClTs trihydrate (20 mg, 0.080 mmol, 1.1 equiv) and MeCN (2 mL). Both solutions were cooled to –35 °C before being combined. The resulting reaction solution was allowed to stand at –35 °C for

24 h at which time a dark-green crystalline solid was obtained. The crystals were washed with minimal cold CH_3CN and dried at 23 °C to afford 30 mg of the title complex (50% yield). Single-crystals suitable for X-ray diffraction were obtained via a concentrated MeCN solution at –35 °C for 48 h; single-crystal X-ray diffraction data is collected in Figure II-4 and Table II-17. ^{1}H NMR (δ, 23 °C, $CDCl_3$): 12.6 (br s, 3H), 7.7 (br m, 24 H), –24 (br s, 8H). UV-vis (MeCN), λ_{max} (nm (ε ($M^{-1}cm^{-1}$))): 386 (2.2×10^4), 476 (3.0×10^4), 580 (4.6×10^3), 618 (4.1×10^3). Magnetic moment: 4.89 μ_B.

Synthesis of Mn(tdclpp)(NClTs) (II-13b)

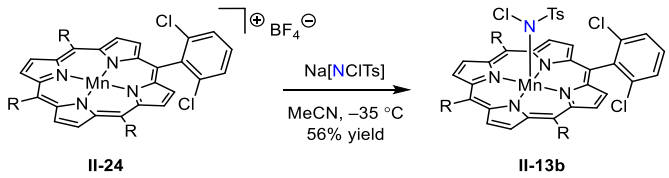

A 20-mL scintillation vial was charged with **II-24** (70 mg, 0.070 mmol, 1.0 equiv) and MeCN (4 mL). A separate 20-mL scintillation vial was charged with NaNClTs trihydrate (20 mg, 0.080 mmol, 1.1 equiv) and MeCN (2 mL). Both solutions were cooled to –35 °C before being combined. The resulting reaction solution was allowed to stand at –35 °C for 24 h at which time a dark-red crystalline solid was obtained. The crystals were washed with minimal amounts of cold MeCN and dried at 23 °C to afford 45 mg of the title complex (56% yield). Single-crystals suitable for X-ray diffraction were obtained via a concentrated MeCN solution at –35 °C for 48 h; single-crystal X-ray diffraction data is collected in Figure II-4 and Table II-18. ^{1}H NMR (δ, 23 °C, $CDCl_3$): 12.9 (br s, 3H), 8.1 (br s, 15H), 7.5 (br s, 4H), –25 (br s, 8H). UV-vis (MeCN), λ_{max} (nm (ε ($M^{-1}cm^{-1}$))): 383 (1.4×10^4), 478 (2.0×10^4), 568 (3.6×10^3). Magnetic moment: 4.90 μ_B.

Synthesis of Mn(tpfpp)(NClTs) (II-13c)

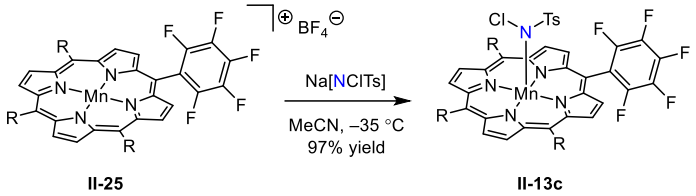

A 20-mL scintillation vial was charged with **II-25** (78 mg, 0.070 mmol, 1.0 equiv) and MeCN (4 mL). A separate 20-mL scintillation vial was charged with NaNClTs trihydrate (20 mg, 0.080 mmol, 1.1 equiv) and MeCN (2 mL). Both solutions were cooled to –35 °C before being combined. The resulting reaction solution was allowed to stand at –35 °C for 24 h. Solvent was removed *in vacuo* at 23 °C. The residue was dissolved in CH_2Cl_2 (5 mL) at 23 °C and filtered through a Celite plug. Solvent was removed *in vacuo* at 23 °C to afford 84 mg of the title complex as a red solid (97% yield). Single-crystals suitable for X-ray diffraction were obtained via a concentrated MeCN solution at –35 °C for 48 h; single-crystal X-ray diffraction data is collected in Figure II-4 and Table II-19. ^{1}H NMR (δ, 23 °C, $CDCl_3$): 13.8 (br s, 3H), 9.4 (br s, 4H), –24 (br s, 8H). ^{19}F (δ, 23 °C, CD_3CN): –124 (br s 1F), –149 (br s, 1F) –157 (br s, 3F). UV-vis (MeCN), λ_{max} (nm (ε ($M^{-1}cm^{-1}$))): 360 (3.5×10^4), 469 (4.3×10^4), 570 (7.5×10^3). Magnetic moment: 4.90 μ_B.

Synthesis of Mn(tpp)(NBrTs) (II-13d)

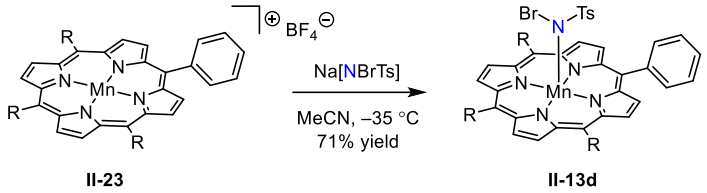

A 20-mL scintillation vial was charged with **II-23** (59 mg, 0.078 mmol, 1.0 equiv) and MeCN (4 mL). A separate 20-mL scintillation vial was charged with NaNBrTs (22 mg, 0.081 mmol, 1.1 equiv) and MeCN (2 mL). Both solutions were cooled to –35 °C before being combined. The resulting reaction solution was allowed to stand at –35 °C for 24 h at which time a dark-green crystalline solid was obtained. The crystals were washed with minimal cold MeCN and dried at 23 °C to afford 51 mg of the title complex (71% yield). Single-crystals suitable for X-ray diffraction were obtained via a concentrated MeCN solution at –35 °C for 48 h; single-crystal X-ray diffraction data is collected in Figure II-4 and Table II-20. ^{1}H NMR (δ, 23 °C, $CDCl_3$): 12.8 (br s, 3H), 8.3 (br m, 24 H), –24 (br s, 8H). UV-vis (MeCN), λ_{max} (nm (ε ($M^{-1}cm^{-1}$))): 385 (2.9×10^4), 478 (4.2×10^4), 578 (4.7×10^3), 618 (4.8×10^3). Magnetic moment: 4.89 μ_B.

Synthesis of Mn(tpp)(NITs) (II-13e)

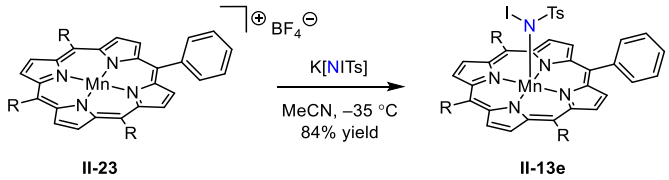

A 20-mL scintillation vial was charged with **II-23** (40 mg, 0.053 mmol, 1.0 equiv) and MeCN (4 mL). A separate 20-mL scintillation vial was charged with KNITs (23 mg, 0.067 mmol, 1.2 equiv) and MeCN (2 mL). Both solutions were cooled to –35 °C before being

combined. The resulting reaction solution was allowed to stand at –35 °C for 24 h at which time a dark-green crystalline solid was obtained. The crystals were washed with minimal cold MeCN and dried at 23 °C to afford 43 mg of the title complex (84% yield). Single-crystals suitable for X-ray diffraction were obtained via a concentrated MeCN solution at –35 °C for 48 h; single-crystal X-ray diffraction data is collected in Figure II-4 and Table II-21. ^{1}H NMR (δ, 23 °C, $CDCl_3$): 13.0 (br s, 3H), 8.3 (br m, 24 H), –22 (br s, 8H). UV-vis (MeCN), λ_{max} (nm (ε ($M^{-1}cm^{-1}$))): 383 (3.5×10^4), 479 (5.2×10^4), 585 (7.8×10^3), 620 (8.2×10^3). Magnetic moment: 4.89 μ_B.

Synthesis of Na[NBrTs] (II-26)

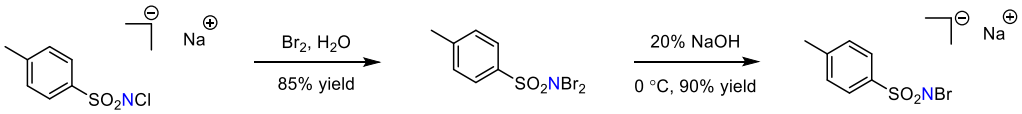

Compound **II-26** was prepared according to the following modification of literature methods.[260, 261] A 20-mL scintillation vial was charged with NaNClTs trihydrate (0.741 g, 2.63 mmol, 1.00 equiv) and H_2O (15 mL). Br_2 (0.200 mL, 3.90 mmol, 1.50 equiv) was added dropwise while stirring, upon which a yellow solid was obtained. The solid was isolated via filtration, washed with H_2O (20 mL) and dried *in vaccuo* to afford 0.738 g of dibromamine-T (85% yield). ^{1}H NMR (δ, 23 °C, ($CDCl_3$): 8.00 (d, 2H), 7.43 (d, 2 H), 2.52 (s, 3H).

A 20-mL scintillation vial was charged with dibromamine-T (0.738 g, 2.24 mmol, 1 equiv) and 3 mL of 20% NaOH solution. The resulting solution was allowed to stand at 0 °C for 5 minutes at which time a yellow solid was obtained. The solid was isolated via filtration

and dried *in vaccuo* to afford 0.706 g of the title complex (90% yield). ^{1}H NMR (δ, 23 °C, (CD_3CN): 7.64 (d, 2H), 7.21 (d, 2 H), 2.36 (s, 3H).

Synthesis of K[NITs] (II-27)

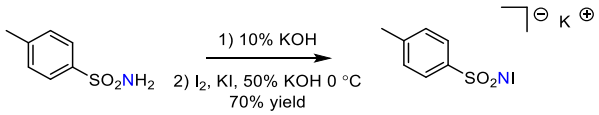

Compound **II-27** was prepared according to the following modification of literature methods.[262] A 20-mL scintillation vial was charged with p-toluenesulfonamide (1.00 g, 5.84 mmol, 1.00 equiv) and 10% KOH solution (2.5 mL). A separate 20-mL scintillation vial was charged with I_2 (1.97 g, 7.76 mmol, 1.33 equiv), KI (3.95 g, 23.8 mmol, 4.07 equiv), and H_2O (4.5 mL). Both solutions were combined and 50% KOH solution (1.5 mL) was added. The resulting solution was allowed to stand at 0 °C for 5 minutes at which time a yellow solid was obtained. The solid was isolated via filtration and washed with diethyl ether (20 mL) and dried *in vaccuo* to afford to afford 1.37 g of the title complex (70% yield). ^{1}H NMR (δ, 23 °C, $(CD_3)_2SO$): 7.47 (d, 2H), 7.14 (d, 2 H), 2.31 (s, 3H).

II.5.3 Photochemical Reaction Details

General Procedure for Photochemical Amination of THF with Compound II-13

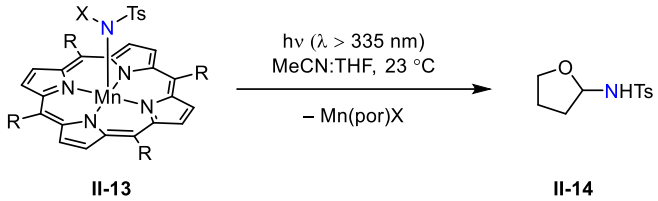

II-13 **II-14**

A 20-mL scintillation vial was charged with **II-13** (50 mg, 0.060 mmol, 1.0 equiv), MeCN (4 mL), and THF (1 mL). The reaction mixture was photolyzed for 24 h while stirring at 23 °C using a 100 W Hg lamp with a 335 nm long-pass filter. The reaction mixture was concentrated *in vacuo*, resulting in a dark green solid. Identical photolyses of **II-13** were carried out with a 400 nm long-pass filter. Wavelength dependent yields are tabulated in Table II-15.

Table II-15. Tabulated yields of II-14, generated via photolysis of II-13 in 4:1 MeCN:THF.

Entry	λ > 335 nm	λ > 400 nm
II-13a	50%	27%
II-13b	55%	53%
II-13c	70%	54%
II-13d	63%	53%
II-13e	44%	40%

General Procedure for Photochemical Amination of Other Substrates with Compound II-13e

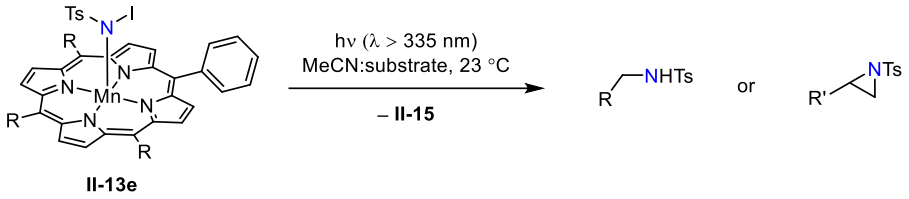

A 20-mL scintillation vial was charged with **II-13e** (25 mg, 0.026 mmol, 1.0 equiv), substrate (1 mL),* and MeCN (4 mL). The reaction mixture was photolyzed for 24 h while stirring at 23 °C using a 100 W Hg lamp with a 335 nm long-pass filter. The reaction mixture was concentrated *in vacuo*, resulting in a dark green solid. Based on the ^{1}H NMR (against mesitylene added as a standard) the yields of **II-16-II-19** were determined and tabulated in Table II-16.

Table II-16. Tabulated yields of substrates II-16-II-19, generated via photolysis of II-13e.

Substrate	Yield
2-Me-THF	19%
Toluene	20%
Styrene	30%
Cyclohexane	0%

* In the case of styrene, 40 μL were used.

Determination of Kinetic Isotope Effects (KIEs) for Photochemical Amination

*Steady-state KIE for amination of THF by photolysis of **II-13**.* A 20-mL vial was charged with **II-13** (30 mg, 1.0 equiv) and dissolved in 8:1:1 MeCN/THF/d_8-THF (5.0 mL). The reaction mixture was photolyzed for 24 h while stirring at 23 °C using a 100 W Hg lamp using a 335 nm longpass filter. Solvent was removed *in vacuo*. KIEs (k_H/k_D) were determined by integrating the $[M–H]^+$, $[M–Na]^+$, and $[M–NH_4]^+$ peaks for **II-**H_8**-14** versus **II-**d_8**-14** using HR-ESI-MS. The reaction was performed in triplicate. Steady-state k_H/k_D values are tabulated in Table II-5.

*KIE for amination of THF by cryogenic photolysis of and dark thermolysis of **II-13**.* A 4 mm quartz EPR tube was charged with **II-13** (1 mg, 1 equiv) and dissolved in 8:1:1 MeCN/THF/d_8-THF (5.0 mL). The reaction mixture was photolyzed for 12 h while frozen at 77 K in a quartz finger dewar using a 100 W Hg lamp using a 335 nm longpass filter. The sample was warmed to 23 °C in the dark and solvent was removed *in vacuo*. KIEs (k_H/k_D) were determined by integrating the $[M–H]^+$, $[M–Na]^+$, and $[M–NH_4]^+$ peaks for **II-**H_8**-14** versus **II-**d_8**-14** using HR-ESI-MS. Cryogenic photolysis and dark thermolysis k_H/k_D values are tabulated in Table II-5.

II.5.4 Crystallographic Data

Table II-17. X-ray experimental details of Mn(tpp)(NClTs) (II-13a) (CCDC 2070487).

Crystal data	
Chemical formula	$C_{51}H_{35}ClMnN_5O_2S{\cdot}2.5(C_2H_3N)$
M_r	974.92
Crystal system, space group	Monoclinic, $P2_1/c$
Temperature (K)	100
a, b, c (Å)	18.0762(2), 13.9592(1), 38.474(3)
β (°)	98.977(1)
V (Å^3)	9589.3(1)
Z	8
Radiation type	Synchrotron, λ = 0.41328 Å
μ (mm^{-1})	0.11
Crystal size (mm)	0.5 × 0.5 × 0.25
Data collection	
Diffractometer	Bruker *APEX*-II CCD
Absorption correction	Multi-scan *SADABS2016*/2 (Bruker, 2016/2) was used for absorption correction. wR2(int) was 0.0956 before and 0.0820 after correction. The ratio of minimum to maximum transmission is 0.9556. The λ/2 correction factor is not present.
T_{min}, T_{max}	0.661, 0.692
No. of measured, independent and observed [I > 2s(I)] reflections	217315, 18396, 12644
R_{int}	0.152
(sin θ/λ)$_{max}$ (Å^{-1})	0.613
Refinement	
R[F^2 > 2s(F^2)], wR(F^2), S	0.053, 0.151, 1.01
No. of reflections	18396
No. of parameters	1241
H-atom treatment	H-atom parameters constrained
Γ$_{max}$, Γ$_{min}$ (e Å^{-3})	1.21, –0.45

Table II-18. X-ray experimental details of Mn(tdclpp)(NClTs) (II-13b) (CCDC 2070488).

Crystal data	
Chemical formula	$C_{53}H_{30}Cl_9MnN_6O_2S{\cdot}3(CH_3CN)$
M_r	1312.04
Crystal system, space group	Monoclinic, $P2_1$
Temperature (K)	100
a, b, c (Å)	12.6099(1), 18.6746(2), 12.6985(1)
β (°)	106.916(1)
V (Å^3)	2860.9(4)
Z	2
Radiation type	Synchrotron, λ = 0.33062 Å
μ (mm^{-1})	0.10
Crystal size (mm)	0.25 × 0.25 × 0.1
Data collection	
Diffractometer	Synchrotron
Absorption correction	Multi-scan *SADABS2016*/2 (Bruker, 2016/2) was used for absorption correction. wR2(int) was 0.1743 before and 0.0647 after correction. The ratio of minimum to maximum transmission is 0.8948. The λ/2 correction factor is not present.
T_{min}, T_{max}	0.665, 0.744
No. of measured, independent and observed [I > 2s(I)] reflections	85061, 12746, 10757
R_{int}	0.102
$(\sin \theta/\lambda)_{max}$ (Å^{-1})	0.648
Refinement	
$R[F^2 > 2s(F^2)]$, $wR(F^2)$, S	0.039, 0.089, 1.04
No. of reflections	12746
No. of parameters	759
H-atom treatment	H-atom parameters constrained
Γ_{max}, Γ_{min} (e Å^{-3})	0.45, –0.37

Table II-19. X-ray experimental details of Mn(tpfpp)(NClTs) (II-13c) (CCDC 2070489).

Crystal data	
Chemical formula	$C_{51}H_{15}ClF_{20}MnN_5O_2S{\cdot}4(C_2H_3N)$
M_r	1396.34
Crystal system, space group	Monoclinic, $P2_1/c$
Temperature (K)	100
a, b, c (Å)	14.3644(7), 16.0198(7), 26.2583(1)
β (°)	104.289(1)
V (Å^3)	5855.5(5)
Z	2
Radiation type	Synchrotron, λ = 0.33062 Å
μ (mm^{-1})	0.07
Crystal size (mm)	0.5 × 0.25 × 0.25
Data collection	
Diffractometer	Synchrotron
Absorption correction	Multi-scan *SADABS2016*/2 (Bruker, 2016/2) was used for absorption correction. wR2(int) was 0.2056 before and 0.0572 after correction. The ratio of minimum to maximum transmission is 0.9514. The λ/2 correction factor is not present.
T_{min}, T_{max}	0.708, 0.744
No. of measured, independent and observed [I > 2s(I)] reflections	392909, 36782, 27121
R_{int}	0.075
$(\sin\theta/\lambda)_{max}$ (Å^{-1})	0.909
Refinement	
$R[F^2 > 2s(F^2)]$, $wR(F^2)$, S	0.038, 0.110, 1.04
No. of reflections	36782
No. of parameters	843
H-atom treatment	H-atom parameters constrained
Γ_{max}, Γ_{min} (e Å^{-3})	0.64, –0.59

Table II-20. X-ray experimental details of Mn(tpp)(NBrTs) (II-13d) (CCDC 2070490).

Crystal data	
Chemical formula	$C_{51}H_{35}BrMnN_5O_2S{\cdot}2.5(C_2H_3N)$
M_r	1019.38
Crystal system, space group	Monoclinic, $P2_1/c$
Temperature (K)	110
a, b, c (Å)	18.024(2), 13.929(1), 38.486(4)
β (°)	99.016(3)
V (Å^3)	9542.8(2)
Z	8
Radiation type	Mo $K\alpha$
μ (mm^{-1})	1.21
Crystal size (mm)	0.15 × 0.15 × 0.07
Data collection	
Diffractometer	Bruker *APEX*-II CCD
Absorption correction	Multi-scan *SADABS2016*/2 (Bruker, 2016/2) was used for absorption correction. wR2(int) was 0.1034 before and 0.0709 after correction. The ratio of minimum to maximum transmission is 0.8070. The λ/2 correction factor is not present.
T_{min}, T_{max}	0.345, 0.427
No. of measured, independent and observed [I > 2s(I)] reflections	138181, 14331, 11963
R_{int}	0.096
$(\sin\theta/\lambda)_{max}$ (Å^{-1})	0.566
Refinement	
$R[F^2 > 2s(F^2)]$, $wR(F^2)$, S	0.078, 0.196, 1.08
No. of reflections	14331
No. of parameters	1242
H-atom treatment	H-atom parameters constrained
Γ_{max}, Γ_{min} (e Å^{-3})	0.75, −0.87

Table II-21. X-ray experimental details of Mn(tpp)(NITs) (II-13e) (CCDC 2070491).

Crystal data	
Chemical formula	$C_{51}H_{35}IMnN_5O_2S{\cdot}1.5(C_2H_3N)$
M_r	1025.32
Crystal system, space group	Monoclinic, $P2_1/c$
Temperature (K)	110
a, b, c (Å)	17.0047(2), 13.8153(1), 40.796(4)
β (°)	97.134(3)
V (Å^3)	9509.7(2)
Z	8
Radiation type	Mo $K\alpha$
μ (mm^{-1})	1.02
Crystal size (mm)	0.03 × 0.02 × 0.01
Data collection	
Diffractometer	Bruker QUEST PHOTON-III
Absorption correction	Multi-scan *SADABS2016*/2 (Bruker, 2016/2) was used for absorption correction. wR2(int) was 0.1588 before and 0.0821 after correction. The Ratio of minimum to maximum transmission is 0.7344. The λ/2 correction factor is not present.
T_{min}, T_{max}	0.547, 0.745
No. of measured, independent and observed [$I > 2s(I)$] reflections	87832, 10008, 7629
R_{int}	0.124
$(\sin\theta/\lambda)_{max}$ (Å^{-1})	0.502
Refinement	
$R[F^2 > 2s(F^2)]$, $wR(F^2)$, S	0.057, 0.134, 1.04
No. of reflections	10008
No. of parameters	1185
H-atom treatment	H-atom parameters constrained
Γ_{max}, Γ_{min} (e Å^{-3})	0.78, −0.97

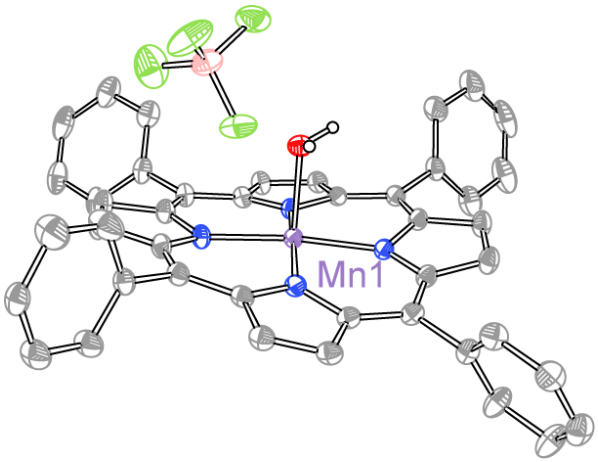

Figure II-28. Thermal ellipsoid plot of [Mn(tpp)]BF_4·H_2O (II-23·H_2O) plotted at 50% probability. H-atoms and solvents are removed for clarity. The crystalline sample used in this diffraction experiment was obtained from a concentrated CH_2Cl_2 solution layered with hexanes at 23 °C.

Table II-22. X-ray experimental details of [Mn(tpp)]BF_4·H_2O (II-23·H_2O) (CCDC 2070486).

Crystal data	
Chemical formula	$C_{44}H_{30}MnN_4O·BF_4·CH_2Cl_2$
M_r	857.39
Crystal system, space group	Triclinic, $P\bar{1}$
Temperature (K)	110
a, *b*, *c* (Å)	12.399(4), 13.0012(5), 14.5382(5)
α, β, γ (°)	107.748(1), 103.710(1), 109.368(1)
V (Å^3)	1951.10(1)
Z	2
Radiation type	Mo *K*α
μ (mm^{-1})	0.54
Crystal size (mm)	0.1 × 0.05 × 0.03
Data collection	
Diffractometer	Bruker QUEST PHOTON-III
Absorption correction	Multi-scan *SADABS2016*/2 (Bruker, 2016/2) was used for absorption correction. wR2(int) was 0.1314 before and 0.0530 after correction. The ratio of minimum to maximum transmission is 0.9088. The λ/2 correction factor is not present.
T_{min}, T_{max}	0.303, 0.333
No. of measured, independent and observed [$I > 2s(I)$] reflections	79506, 8926, 7956
R_{int}	0.039
$(\sin \theta/\lambda)_{max}$ (Å^{-1})	0.650
Refinement	
$R[F^2 > 2s(F^2)]$, $wR(F^2)$, *S*	0.046, 0.123, 1.04
No. of reflections	8926
No. of parameters	540
H-atom treatment	H-atom parameters constrained
Γ_{max}, Γ_{min} (e Å^{-3})	2.60, −0.71

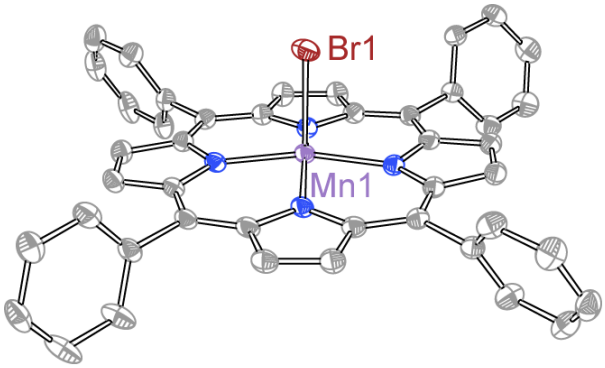

Figure II-29. Thermal ellipsoid plot of Mn(tpp)Br (II-28) plotted at 50% probability. H-atoms and solvents are removed for clarity. The crystalline sample used in this diffraction experiment was obtained from a concentrated benzene solution layered with pentane at 23 °C.

Table II-23. X-ray experimental details of Mn(tpp)Br (II-28) (CCDC 2070493).

Crystal data	
Chemical formula	$C_{44}H_{28}BrMnN_4 \cdot C_6H_6$
M_r	825.66
Crystal system, space group	Triclinic, $P\bar{1}$
Temperature (K)	110
a, b, c (Å)	13.333(2), 14.968(2), 20.893(3)
α, β, γ (°)	71.938(5), 84.655(5), 74.661(5)
V (Å^3)	3822.4(8)
Z	4
Radiation type	Mo $K\alpha$
μ (mm^{-1})	1.43
Crystal size (mm)	0.04 × 0.04 × 0.01
Data collection	
Diffractometer	Bruker PHOTON-III
Absorption correction	Multi-scan *SADABS2016*/2 (Bruker, 2016/2) was used for absorption correction. wR2(int) was 0.1249 before and 0.0637 after correction. The ratio of minimum to maximum transmission is 0.8623. The λ/2 correction factor is not present.
T_{min}, T_{max}	0.371, 0.431
No. of measured, independent and observed [$I > 2s(I)$] reflections	233021, 17546, 14273
R_{int}	0.64
$(\sin \theta/\lambda)_{max}$ (Å^{-1})	0.650
Refinement	
$R[F^2 > 2s(F^2)]$, $wR(F^2)$, S	0.041, 0.114, 1.06
No. of reflections	17546
No. of parameters	1071
H-atom treatment	H-atom parameters constrained
Γ_{max}, Γ_{min} (e Å^{-3})	0.57, −1.13

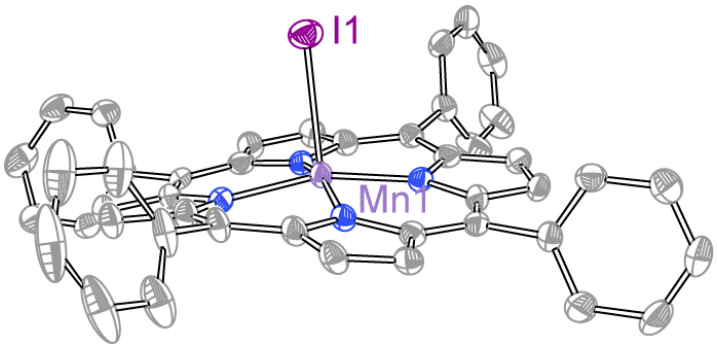

Figure II-30. Thermal ellipsoid plot of Mn(tpp)I (II-29) plotted at 50% probability. H-atoms and solvents are removed for clarity. The crystalline sample used in this diffraction experiment was obtained from a concentrated benzene solution layered with pentane at 23 °C.

Table II-24. X-ray experimental details of Mn(tpp)I (II-29) (CCDC 2070492).

Crystal data	
Chemical formula	$C_{44}H_{28}IMnN_4 \cdot 0.5(C_6H_6)$
M_r	833.60
Crystal system, space group	Triclinic, $P\bar{1}$
Temperature (K)	110
a, b, c (Å)	11.908(1), 13.128(1), 26.250(2)
α, β, γ (°)	86.419(3), 84.326(4), 64.069(3)
V (Å^3)	3671.1(5)
Z	4
Radiation type	Mo $K\alpha$
μ (mm^{-1})	1.24
Crystal size (mm)	0.05 × 0.04 × 0.01
Data collection	
Diffractometer	Bruker QUEST PHOTON-III
Absorption correction	Multi-scan *SADABS2016*/2 (Bruker, 2016/2) was used for absorption correction. wR2(int) was 0.0823 before and 0.0704 after correction. The ratio of minimum to maximum transmission is 0.9374. The λ/2 correction factor is not present.
T_{min}, T_{max}	0.506, 0.540
No. of measured, independent and observed [$I > 2s(I)$] reflections	71505, 7713, 6255
R_{int}	0.085
$(\sin \theta/\lambda)_{max}$ (Å^{-1})	0.0.501
Refinement	
$R[F^2 > 2s(F^2)]$, $wR(F^2)$, S	0.034, 0.084, 1.02
No. of reflections	7713
No. of parameters	955
H-atom treatment	H-atom parameters constrained
Γ_{max}, Γ_{min} (e Å^{-3})	0.49, −0.67

II.5.5 Computational Coordinates

Table II-25. X,Y,Z coordinates for the optimized geometry of II-13a computed as a quintet at the B3LYP level of theory with LANL2DZ (Mn, Cl) and 6-31G(d,p) (light atoms) basis sets.

Atom	X	Y	Z
Mn	0.29918	0.04057	-0.81134
Cl	1.22360	0.93537	2.24173
S	-0.67898	-1.21425	2.17706
O	-1.74905	-1.72120	1.26904
O	0.34458	-2.16098	2.70802
N	-1.62339	0.22611	-1.46990
N	2.33790	-0.12822	-0.76998
N	0.51894	2.06228	-1.02767
N	0.19160	-1.95780	-1.15684
N	-0.02923	0.07868	1.29148
C	3.26576	0.90373	-0.71839
C	-0.51566	2.98301	-1.12666
C	1.70020	2.79192	-1.09650
C	3.02007	-1.28287	-0.39833
C	-2.50604	-0.80659	-1.75711
C	4.16108	3.21858	-0.96008
C	3.00111	2.27025	-0.94385
C	1.39605	4.19261	-1.28352
H	2.13740	4.97989	-1.41114
C	5.13126	3.14298	-1.98540
C	4.39317	-0.96119	-0.08574
H	5.13762	-1.67727	0.25869
C	-0.89386	-2.68576	-1.62656
C	-2.17214	-2.16704	-1.90696
C	-3.79070	1.05038	-1.53939
H	-4.61338	1.76050	-1.47162
C	-2.39500	1.37823	-1.35330
C	-3.66255	4.17412	-2.23033
C	-1.89415	2.68435	-1.17946
C	4.55292	0.38389	-0.31313
H	5.45204	0.98429	-0.18270
C	-2.85746	3.83033	-1.12035
C	0.02734	4.31392	-1.27515
H	-0.56748	5.21749	-1.40073
C	-3.85581	-0.29382	-1.81491
H	-4.74097	-0.89783	-2.00849
C	-2.96290	4.60227	0.05955
C	-3.85694	5.68362	0.12989
C	-4.55232	5.25923	-2.16073
C	-1.48378	-0.46358	3.61666
C	4.31507	4.19665	0.04905
C	1.18738	-2.88087	-0.87219
C	2.48691	-2.58602	-0.41168
C	3.33668	-3.72970	0.05039
C	0.72825	-4.21157	-1.19735
H	1.32419	-5.11651	-1.08822
C	-0.54685	-4.08742	-1.69276
H	-1.20217	-4.87387	-2.06381
C	-2.70850	0.20462	3.44065
H	-3.16118	0.25597	2.44598
C	-4.65451	6.01544	-0.97956
C	6.22276	4.02735	-2.00584
C	5.24007	-5.24127	-0.22006
C	6.36565	4.99670	-0.99739
C	-0.88485	-0.55565	4.88078
H	0.06375	-1.08898	4.98997
C	-3.26110	-3.12148	-2.29319

C	-1.52796	0.03034	5.98470
H	-1.06489	-0.04114	6.97592
C	5.40990	5.07681	0.03103
C	3.76713	-5.47916	1.70150
C	4.46867	-4.15913	-0.67732
C	-2.75778	0.70466	5.84169
C	-3.33673	0.77931	4.55315
H	-4.29676	1.29313	4.42195
C	4.89212	-5.90254	0.97135
C	2.98922	-4.40209	1.24476
C	-3.75654	-4.05593	-1.35537
C	-3.81921	-3.09318	-3.59066
C	-5.33028	-4.91349	-3.00812
C	-4.78549	-4.94360	-1.71178
C	-4.84449	-3.98600	-3.94668
C	-3.45239	1.33041	7.03346
H	-2.87181	1.18822	7.95958
H	-4.45335	0.88924	7.19061
H	-3.59729	2.41631	6.88836
H	-6.13089	-5.60786	-3.28494
H	-5.26209	-3.95743	-4.95904
H	-3.43680	-2.37319	-4.32268
H	-3.34003	-4.06389	-0.34252
H	-5.16497	-5.65727	-0.97244
H	4.73188	-3.65125	-1.61188
H	6.11081	-5.57003	-0.79791
H	5.49506	-6.74455	1.32825
H	2.11927	-4.05650	1.81448
H	-5.16274	5.51681	-3.03310
H	-3.57362	3.59499	-3.15590
H	-5.34959	6.86012	-0.92529
H	-3.93083	6.26642	1.05444
H	-2.34497	4.33973	0.92502
H	5.01694	2.39152	-2.77434
H	6.96099	3.95941	-2.81227
H	7.21788	5.68448	-1.01172
H	5.51837	5.82324	0.82537
H	3.57798	4.25017	0.85742
H	3.49295	-5.98661	2.63274

Table II-26. X,Y,Z coordinates for the optimized geometry of II-13d computed as a quintet at the B3LYP level of theory with LANL2DZ (Mn, Br) and 6-31G(d,p) (light atoms) basis sets.

Atom	X	Y	Z
Mn	-0.22024	0.07078	-0.91570
S	0.91399	1.03468	2.12396
O	2.08847	1.34012	1.25336
O	0.09394	2.16026	2.66008
N	1.63976	-0.48968	-1.53641
N	-2.18274	0.64981	-0.91809
N	-0.83888	-1.85903	-1.17969
N	0.29846	2.01058	-1.20925
N	0.04787	-0.07642	1.19066
C	-3.30174	-0.17240	-0.91520
C	-0.00928	-2.96898	-1.26517
C	-2.14077	-2.33287	-1.29384
C	-2.62502	1.90934	-0.52467
C	2.71900	0.34742	-1.78674
C	-4.64004	-2.25147	-1.23391
C	-3.31289	-1.55991	-1.16641
C	-2.12043	-3.76361	-1.49798
H	-3.00122	-4.38260	-1.66162
C	-5.54663	-1.95653	-2.27764
C	-4.04266	1.86727	-0.25145
H	-4.63462	2.71114	0.09942
C	1.51893	2.51223	-1.64227
C	2.67056	1.74967	-1.91443
C	3.59772	-1.73284	-1.57017
H	4.25893	-2.59472	-1.49515
C	2.16048	-1.77485	-1.41983
C	2.86702	-4.76385	-2.29367
C	1.40213	-2.95448	-1.27662
C	-4.46668	0.58943	-0.52313
H	-5.47214	0.18209	-0.42849
C	2.11153	-4.27192	-1.20482
C	-0.80554	-4.16031	-1.45193
H	-0.40240	-5.16431	-1.57624
C	3.93863	-0.42660	-1.82460
H	4.93175	-0.01169	-1.98999
C	2.01889	-5.05758	-0.03284
C	2.67217	-6.29845	0.05027
C	3.51582	-6.00733	-2.21120
C	1.52112	0.10988	3.55994
C	-5.01752	-3.19896	-0.25487
C	-0.49427	3.11036	-0.91498
C	-1.83698	3.07540	-0.48638
C	-2.44520	4.35513	-0.00057
C	0.23338	4.32641	-1.19526
H	-0.16753	5.33108	-1.06915
C	1.46597	3.95635	-1.67575
H	2.27511	4.60116	-2.01501
C	2.56442	-0.81568	3.38180
H	2.99235	-0.96733	2.38639
C	3.42272	-6.77720	-1.03812
C	-6.79450	-2.59836	-2.34582
C	-3.98418	6.23837	-0.25422
C	-7.15903	-3.54011	-1.36744
C	0.96071	0.33340	4.82522
H	0.15535	1.06507	4.93588
C	3.93800	2.46924	-2.26340
C	1.45872	-0.38179	5.92797
H	1.02510	-0.20903	6.92005
C	-6.26770	-3.83630	-0.32085
C	-2.55167	6.09931	1.70733

C	-3.44110	5.03497	-0.73611
C	2.50566	-1.31475	5.78264
C	3.05071	-1.51661	4.49304
H	3.87080	-2.23256	4.35974
C	-3.54187	6.77228	0.96934
C	-2.00147	4.89925	1.22675
C	4.59656	3.26513	-1.29855
C	4.50157	2.35192	-3.55347
C	6.34134	3.81395	-2.91053
C	5.79115	3.93035	-1.62136
C	5.69339	3.02321	-3.87591
C	3.04611	-2.07886	6.97362
H	2.51191	-1.81253	7.90028
H	4.11982	-1.86917	7.13008
H	2.94809	-3.16996	6.82827
H	7.27153	4.33527	-3.16099
H	6.11431	2.92896	-4.88289
H	3.99349	1.73898	-4.30623
H	4.17237	3.33938	-0.29159
H	6.29498	4.53750	-0.86146
H	-3.77644	4.62444	-1.69511
H	-4.75018	6.76070	-0.83783
H	-3.96695	7.70929	1.34517
H	-1.23945	4.36051	1.80128
H	4.09024	-6.37715	-3.06751
H	2.92793	-4.17232	-3.21366
H	3.92985	-7.74582	-0.97389
H	2.59524	-6.89087	0.96845
H	1.43799	-4.68129	0.81614
H	-5.26039	-1.22706	-3.04322
H	-7.48141	-2.36314	-3.16604
H	-8.13280	-4.03875	-1.41903
H	-6.54745	-4.56191	0.45061
H	-4.32893	-3.41964	0.56771
H	-2.20576	6.50706	2.66334
Br	-1.49433	-0.75945	2.16910

Table II-27. X,Y,Z coordinates for the optimized geometry of II-13e computed as a quintet at the B3LYP level of theory with LANL2DZ (Mn, I) and 6-31G(d,p) (light atoms) basis sets.

Atom	X	Y	Z
I	1.43415	-0.79964	2.35476
Mn	0.24804	0.12885	-0.97219
S	-1.12810	1.00973	1.97204
O	-2.18197	1.33818	0.99371
O	-0.43621	2.12488	2.64162
N	-0.12762	-0.01688	1.15678
N	2.16047	0.78592	-0.90510
N	0.95492	-1.74893	-1.24123
N	-1.54046	-0.50460	-1.65613
N	-0.32470	2.02737	-1.30403
C	2.53272	2.05180	-0.49833
C	3.94827	2.08135	-0.26026
H	4.49898	2.94066	0.08890
C	4.43454	0.85114	-0.57701
H	5.45772	0.51253	-0.52730
C	3.31449	0.03271	-0.95224
C	3.39531	-1.33638	-1.21855
C	4.75369	-1.95793	-1.31315
C	5.56239	-1.72093	-2.43147
H	5.19102	-1.08996	-3.23258
C	6.83066	-2.29163	-2.52597
H	7.44204	-2.10231	-3.40257
C	7.31117	-3.10368	-1.49994
H	8.29945	-3.54632	-1.57181
C	6.51603	-3.34226	-0.37979
H	6.88528	-3.96757	0.42687
C	5.24617	-2.77514	-0.28792
H	4.63262	-2.95668	0.58836
C	2.27088	-2.15743	-1.33212
C	2.31583	-3.58484	-1.48653
H	3.21609	-4.16581	-1.61175
C	1.03368	-4.03736	-1.43767
H	0.68850	-5.05591	-1.52414
C	0.18210	-2.88859	-1.30665
C	-1.21452	-2.93745	-1.36834
C	-1.87280	-4.27910	-1.29894
C	-2.45109	-4.86790	-2.43066
H	-2.42067	-4.34219	-3.37955
C	-3.04987	-6.12395	-2.35082
H	-3.48745	-6.56883	-3.23895
C	-3.08189	-6.80904	-1.13690
H	-3.54926	-7.78651	-1.07463
C	-2.50789	-6.23282	-0.00481
H	-2.52912	-6.75859	0.94448
C	-1.90497	-4.97866	-0.08584
H	-1.45932	-4.53190	0.79695
C	-2.00341	-1.80229	-1.56914
C	-3.41713	-1.82228	-1.82847
H	-4.03928	-2.70326	-1.80758
C	-3.79102	-0.54703	-2.11749
H	-4.77698	-0.18754	-2.36760
C	-2.62346	0.27987	-1.98972
C	-2.63213	1.67031	-2.11035
C	-3.91236	2.33735	-2.50693
C	-4.31937	2.37390	-3.84493
H	-3.69334	1.91960	-4.60650
C	-5.51583	2.99376	-4.20447
H	-5.81696	3.02004	-5.24700
C	-6.32073	3.57896	-3.22844
H	-7.25282	4.06003	-3.50744

C	-5.92399	3.54228	-1.89184
H	-6.54831	3.99185	-1.12619
C	-4.72651	2.92670	-1.53160
H	-4.41692	2.88925	-0.49229
C	-1.54448	2.47204	-1.76572
C	-1.57614	3.90816	-1.72163
H	-2.40032	4.51875	-2.05551
C	-0.40689	4.31951	-1.16360
H	-0.08712	5.32966	-0.96024
C	0.37968	3.14380	-0.91345
C	1.69187	3.16463	-0.43443
C	2.21082	4.44548	0.13663
C	1.77473	4.84156	1.40826
H	1.08082	4.20795	1.95235
C	2.23880	6.03073	1.96831
H	1.89916	6.32496	2.95626
C	3.13409	6.83756	1.26687
H	3.49173	7.76417	1.70469
C	3.56713	6.45076	-0.00073
H	4.25876	7.07717	-0.55539
C	3.10901	5.25971	-0.56247
H	3.44119	4.96433	-1.55288
C	-1.91014	0.04203	3.28356
C	-2.78144	-0.99149	2.94106
H	-2.97129	-1.21751	1.89798
C	-3.40754	-1.71619	3.94806
H	-4.09213	-2.51648	3.68019
C	-3.17801	-1.42736	5.30094
C	-2.30460	-0.38311	5.61554
H	-2.11739	-0.13565	6.65659
C	-1.66863	0.35303	4.61629
H	-0.99715	1.16708	4.86039
C	-3.84699	-2.23794	6.38342
H	-3.34774	-3.20387	6.51897
H	-4.89228	-2.44815	6.14089
H	-3.82334	-1.72151	7.34559

Table II-28. X,Y,Z coordinates for the optimized geometry of II-15 computed as a sextet at the B3LYP level of theory with LANL2DZ (Mn) and 6-31G(d,p) (light atoms) basis sets.

Atom	X	Y	Z
Mn	0.00036	0.00015	-0.00358
N	0.80052	-1.94121	0.05776
N	-0.80072	1.94112	0.05779
N	1.94141	0.80031	-0.05727
N	-1.94123	-0.80026	-0.05825
C	-0.07781	3.11975	-0.03207
C	3.12013	0.07767	0.03312
C	2.26785	2.14393	0.03069
C	-2.14420	2.26789	-0.02987
C	0.07779	-3.11988	-0.03260
C	1.34300	3.22798	-0.00140
C	3.70621	2.27331	0.19192
H	4.24693	3.21060	0.31884
C	-2.27335	3.70634	-0.19073
H	-3.21054	4.24728	-0.31740
C	-2.26770	-2.14383	0.02979
C	-1.34302	-3.22803	-0.00226
C	2.27339	-3.70618	-0.19112
H	3.21066	-4.24700	-0.31784
C	2.14412	-2.26779	-0.02976
C	3.22834	-1.34312	0.00267
C	-1.00027	4.23116	-0.19230
H	-0.71709	5.27542	-0.32035
C	4.23129	1.00032	0.19365
H	5.27554	0.71731	0.32219
C	1.00036	-4.23113	-0.19315
H	0.71730	-5.27535	-0.32178
C	-3.11993	-0.07766	0.03233
C	-3.22834	1.34314	0.00208
C	-4.23113	-1.00027	0.19303
H	-5.27536	-0.71722	0.32167
C	-3.70608	-2.27323	0.19125
H	-4.24677	-3.21052	0.31830
C	1.91924	4.61291	-0.00235
C	1.66690	5.50229	1.06794
C	2.72787	5.05985	-1.07319
C	2.20861	6.79851	1.06870
C	3.26531	6.35786	-1.07521
C	3.00863	7.23147	-0.00361
C	-4.61327	1.91925	0.00322
C	-5.50294	1.66627	-1.06671
C	-5.06008	2.72827	1.07381
C	-6.79923	2.20779	-1.06738
C	-6.35817	3.26553	1.07593
C	-7.23202	3.00826	0.00468
C	-1.91938	-4.61288	-0.00355
C	-1.66694	-5.50260	1.06645
C	-2.72827	-5.05948	-1.07434
C	-2.20874	-6.79879	1.06695
C	-3.26579	-6.35745	-1.07664
C	-3.00898	-7.23139	-0.00534
C	4.61324	-1.91937	0.00393
C	5.50291	-1.66669	-1.06606
C	5.05999	-2.72816	1.07471
C	6.79918	-2.20829	-1.06662
C	6.35805	-3.26550	1.07695
C	7.23191	-3.00853	0.00563
H	-2.92145	-4.38327	-1.91423
H	-3.88338	-6.68722	-1.91924
H	-3.42977	-8.24262	-0.00605

H	-2.00801	-7.47021	1.90899
H	-1.05176	-5.16407	1.90725
H	-4.38397	2.92178	1.91369
H	-6.68807	3.88326	1.91837
H	-8.24334	3.42881	0.00525
H	-7.47063	2.00667	-1.90935
H	-5.16426	1.05090	-1.90731
H	1.05185	5.16346	1.90871
H	2.00798	7.46971	1.91095
H	3.42934	8.24273	-0.00410
H	3.88273	6.68792	-1.91782
H	2.92097	4.38387	-1.91328
H	5.16427	-1.05148	-1.90679
H	7.47058	-2.00742	-1.90865
H	8.24320	-3.42916	0.00629
H	6.68794	-3.88305	1.91953
H	4.38385	-2.92144	1.91463

Table II-29. X,Y,Z coordinates for the optimized geometry of II-20 computed as a sextet at the B3LYP level of theory with LANL2DZ (Mn) and 6-31G(d,p) (light atoms) basis sets.

c	X	Y	Z
Mn	-0.14630	0.00027	-0.84286
S	1.26767	0.00864	2.19021
O	2.03441	-1.27223	1.99906
O	2.00701	1.30639	2.00369
N	-0.15058	-2.02421	-1.09042
N	-0.17960	2.02498	-1.08692
N	-2.19900	-0.01422	-1.01427
N	1.85897	0.01511	-1.24737
N	-0.06299	-0.00234	1.27995
C	-1.29277	2.85123	-0.94939
C	-3.02239	-1.13039	-1.07779
C	-3.03838	1.08998	-1.07760
C	0.93056	2.86476	-1.05249
C	0.97157	-2.84802	-1.05900
C	-2.63998	2.43903	-0.98577
C	-4.40913	0.65642	-1.23512
H	-5.26367	1.32183	-1.34804
C	0.50585	4.22992	-0.85801
H	1.17744	5.08255	-0.77072
C	2.69205	-1.08822	-1.36815
C	2.30719	-2.43403	-1.21998
C	-0.80603	-4.23151	-0.80176
H	-1.46235	-5.08743	-0.65254
C	-1.25158	-2.86653	-0.95245
C	-2.60460	-2.47362	-0.98696
C	-0.86705	4.22225	-0.79607
H	-1.53583	5.06846	-0.64669
C	-4.39925	-0.71661	-1.23510
H	-5.24410	-1.39428	-1.34801
C	0.56675	-4.21943	-0.86609
H	1.25060	-5.06249	-0.78123
C	0.71441	-0.00050	3.91863
C	2.67625	1.13056	-1.36446
C	2.27212	2.47031	-1.21272
C	4.03639	0.71758	-1.62809
H	4.87091	1.39750	-1.79240
C	4.04613	-0.65500	-1.63056
H	4.89025	-1.32236	-1.79732
C	0.50237	-1.22448	4.57417
H	0.71742	-2.16150	4.05175
C	0.45648	1.21619	4.57203
H	0.63619	2.15975	4.04801
C	-0.01346	1.19972	5.89415
H	-0.21081	2.14959	6.40582
C	-0.23411	-0.01578	6.57844
C	0.03199	-1.22312	5.89661
H	-0.12955	-2.17868	6.41016
C	-3.70835	3.48852	-0.92420
C	-3.87076	4.42115	-1.97397
C	-4.57641	3.56189	0.18921
C	-4.87686	5.39998	-1.91305
C	-5.57797	4.54504	0.25233
C	-5.73229	5.46603	-0.79898
C	3.33626	3.52533	-1.17980
C	4.21246	3.59702	-0.07284
C	3.48105	4.45603	-2.23229
C	5.21201	4.58309	-0.02335
C	4.48640	5.43700	-2.18265
C	5.35347	5.50340	-1.07755
C	3.38621	-3.47393	-1.19151

C	3.54166	-4.40031	-2.24631
C	4.26594	-3.53567	-0.08675
C	4.56080	-5.36716	-2.20110
C	5.27938	-4.50768	-0.04168
C	5.43130	-5.42370	-1.09815
C	-3.65778	-3.53835	-0.92514
C	-4.52324	-3.62517	0.18932
C	-3.80827	-4.47212	-1.97566
C	-5.51060	-4.62255	0.25274

CHAPTER III

OXYGEN-ATOM TRANSFER PHOTOCHEMISTRY OF A MOLECULAR COPPER BROMATE COMPLEX

III.1. Introduction

Reactive ligand-supported metal-oxygen (M–O) complexes are at the heart of C–H hydroxylation catalysis in synthesis and biology. In addition, the bonding of M–O species has been central to the development of modern bonding theories. As a result, the development of synthetic methods that provide access to M–O species relevant to catalytic bond activations or that push the boundaries of established bonding theories has garnered significant interest.

Synthetic photochemistry can provide the opportunity to generate reactive species under cryogenic conditions and thus can enable observation and characterization of species that are short-lived under ambient conditions. Application of synthetic photochemistry requires the availability of appropriate photoprecursors and a well-defined photoactivation method to generate specific targets of interest. In the context of M–O complexes supported by porphyrins, such as Fe oxo complexes that mimic Compound 1 from cytochrome P450, photolysis of metal oxyanion precursors highlights the opportunities and challenges with synthetic photochemistry. Zhang and co-workers reported that steady-state photolysis of porphyrin-supported Fe(III) bromate complexes resulted in the products of heterolytic O–BrO_2 cleavage (*i.e.*, β-cleavage), namely an Fe(V) oxo (Figure III-1). Suslick demonstrated that photolysis of Mn oxyanion porphyrin

complexes in benzene ultimately affords Mn(IV) oxo complexes. [125, 126, 143] In contrast, photolysis in a frozen matrix at 10 K results in Mn–O bond cleavage affording Mn(II) porphyrin and the corresponding oxyradical. Thus, the Fe(V) oxo Zhang reported may be a formed via initial Fe–O homolysis followed by OAT from the generated $BrO_3^{\bullet}$. Similarly, Vincent and coworkers demonstrated that photolysis of a Cu(II) carboxylate complex results in cleavage of the apical Cu–O bond to afford Cu(I) and carboxy radical, which subsequently decomposes to CO_2 and $R^{\bullet}$.[263, 264] Together, these studies demonstrate that while metal oxo species are available from synthetic photochemistry, these complexes likely arise by initial M–L homolysis, and subsequent oxygen atom transfer (OAT) proceeds from the photoextruded radicals to generate the metal oxo intermediate of interest (Figure III-1).

Reactive copper–oxygen (Cu–O) species have gained significant attention from synthetic inorganic chemists by virtue of the importance of these species in biological OAT catalysis. For example, Cu–O fragments are encountered as critical intermediates in methane hydroxylation in the active site of particulate methane monooxygenase,[265-269] and significant synthetic effort has been directed towards the preparation of structural and functional mimics of these important co-factors in an effort both the harness these intermediates in potential catalytic reactions as well as to investigate the nuclearity of the reactive species responsible for biotic methane oxygenation.[270-276] Tolman *et al.* showed that a Cu(I)-α-ketocarboxylate complex can react with dioxygen to afford intramolecular hydroxylation of a pendant arene.[277] Computational analysis indicates the formation of a [Cu-O] intermediate. Similar intramolecular reactivity was also observed by Karlin and

coworkers.[278] When a Cu(II)(tren) peroxo complex was exposed to various H-atom donors such as 2,6-di^{t}Bu phenol or TEMP–OH, the O–O bond was cleaved generating H_2O and a putative Cu–O fragment, which inserted into the pendant methyl ligand. In both cases, the putative terminal Cu–O moiety was not characterized, highlighting the reactivity of these species. However, several bis-μ-oxo copper species have been spectroscopically and structurally characterized.[279] Roithová *et al.* reported the observation of Cu(tpa)O during collision-induced dissociation mass spectrometry (CID-MS) analysis of $[Cu(tpa)OClO_2]^+$. This is the first direct observation of a terminal Cu–O species reported, however spectroscopic or structural characterization were not been reported.[273]

Here we describe the synthesis, characterization, and photochemical oxygen-atom transfer activity of a new copper bromate complex. $[Cu(tpa)O–BrO_2]ClO_4$ (**III-2**) was identified as an attractive precursor to a reactive Cu–O species due to the potential to effect photopromoted BrO_2 extrusion. Steady-state photolysis of **III-2** results in OAT to olefinic, benzylic, and aliphatic substrates. A combination of mass spectrometry, *in situ* spectroscopy, and *in crystallo* photochemical experiments are consistent with initial α-cleavage of the Cu–O bond to generate $[Cu(tpa)]^+$ and $BrO_3^{\bullet}$. Subsequent OAT to the copper center from the extruded $BrO_3^{\bullet}$ would generate a transient Cu–O fragment that is responsible for substrate functionalization as well as BrO_2. These results provide new entry into reactive Cu–O species and highlight the power of *in crystallo* photochemistry to probe the mechanisms of synthetic inorganic photochemical processes.

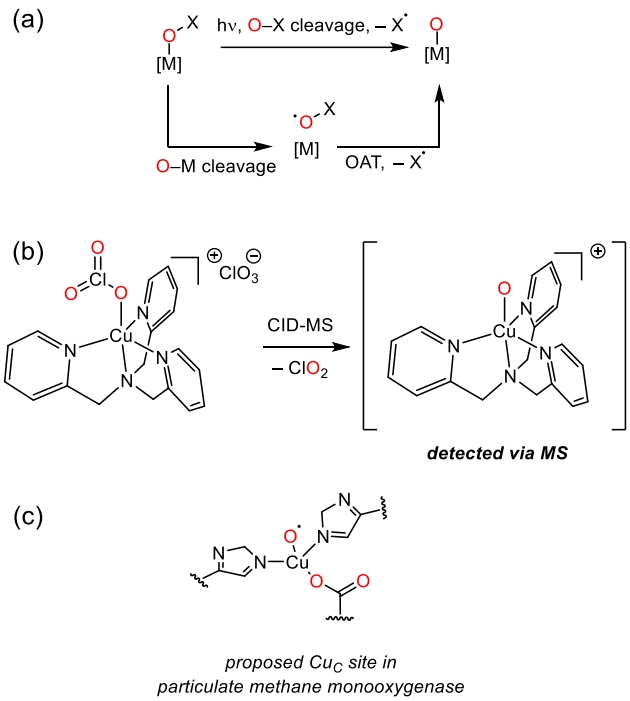

Figure III-1. Proposed pathways to access biologically relevant CuO fragments. (a) Photochemical excitation of metal oxo photoprecursors can undergo either photooxidation or photoreduction to afford M–O fragments. Photochemistry that results in cleavage of the O–X bond and affords a M–O fragment is photooxidation, where photoreduction involves photocleavage of the M–O bond, generating OX• and a reduced metal center. OAT from the extruded OX• radical to the reduced metal center affords the M–O fragment. (b) Collision-induced disassociation mass spectrometry (CID-MS) of Cu(II)($OClO_2$)(tpa) results in loss of ClO_2 affording a [CuO] fragment which was observed in the mass spectrum. (c) Particulate methane monooxygenase (PMMO) both feature Cu(II) centers at the active sites of the enzymes and are implicated in oxygenase chemistry.

III.2. Results and Discussion

Treatment of [Cu(tpa)Br]ClO_4 (**III-1**) with $AgBrO_3$ affords [Cu(tpa)$OBrO_2$]ClO_4 (**III-2**) in 65% yield (Figure III-2a). The ^{1}H NMR spectrum of **III-2** features two broad paramagnetically shifted peaks at 10 and 29 ppm, which based on relative integration we assign to the benzylic and aromatic hydrogens in **III-2**, respectively (Figure III-3). The UV-vis spectrum of **III-2** in acetone displays a weak absorbance centered at 426 (ε = 2.3

× 10 $M^{-1}cm^{-1}$) and stronger absorbances at 710 (ε = 3.0 × 10^2 $M^{-1}cm^{-1}$), and 920 nm (ε = 5.4 × 10^2 $M^{-1}cm^{-1}$) (Figure 2, black trace). The IR spectrum of **III-2** displays spectral features at 831, 842, and 852 cm^{-1}, which are attributed to stretching modes of the bromate ligand (Figure III-4).[280] Electrospray ionization mass spectrometry (ESI-MS) analysis of **III-2** displays a signal at *m/z* = 479.98 with the isotope distribution expected for **III-2**$^+$ (i.e., Cu(tpa)$OBrO_2^+$). Consistent with the *S* = 1/2 ground state typical of Cu(II) complexes in a trigonal bipyramidal geometry, the X-band EPR spectrum of **III-2** measured at 4 K features an isotropic signal at *g* = 2.147.

X-ray quality crystals of **III-2** were obtained by slow diffusion of diethyl ether into an acetone solution of **III-2**; the solid-state structure is illustrated in Figure III-2a (see Table III-1 for refinement details). The Cu(II) ion in **III-2** is five-coordinate and exhibits a distorted trigonal bipyramidal geometry (t_5 = 0.77),[281] with the three pyridine donors from the tpa ligand occupying the equatorial plane. The apical sites are coordinated by the tertiary amine donor of the tpa ligand and an *O*-bound bromate ligand (Figure III-2). The equatorial Cu–$N_{pyridine}$ bond distance is 2.072(4) Å and the apical Cu–N_{amine} bond distance is 2.023(3) Å, which are similar to other crystallographically characterized Cu(II)(tpa) structures (Table III-3). The apical Cu–O bond distance is 1.951(3) Å, which is well-matched to crystallographically characterized Cu(II)(tpa) complexes bearing apical oxyanions (Table III-3).

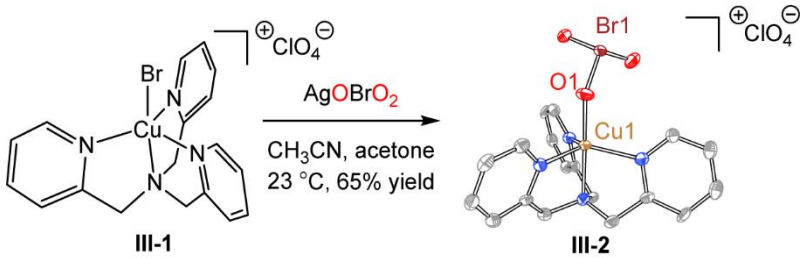

Figure III-2. Synthesis and solid-state characterization of Cu(II) complex III-2. Treatment of III-1 to $AgBrO_3$ affords Cu bromate III-2. Displacement ellipsoid plots of Cu bromate complex III-2. H-atoms and counter anions have been omitted for clarity. Ellipsoids drawn at 50% probability. Selected bond lengths (Å): Cu–O = 1.951(3), Cu–$N_{pyridine}$ = 2.072(4), and Cu–N_{amine} = 2.023(3).

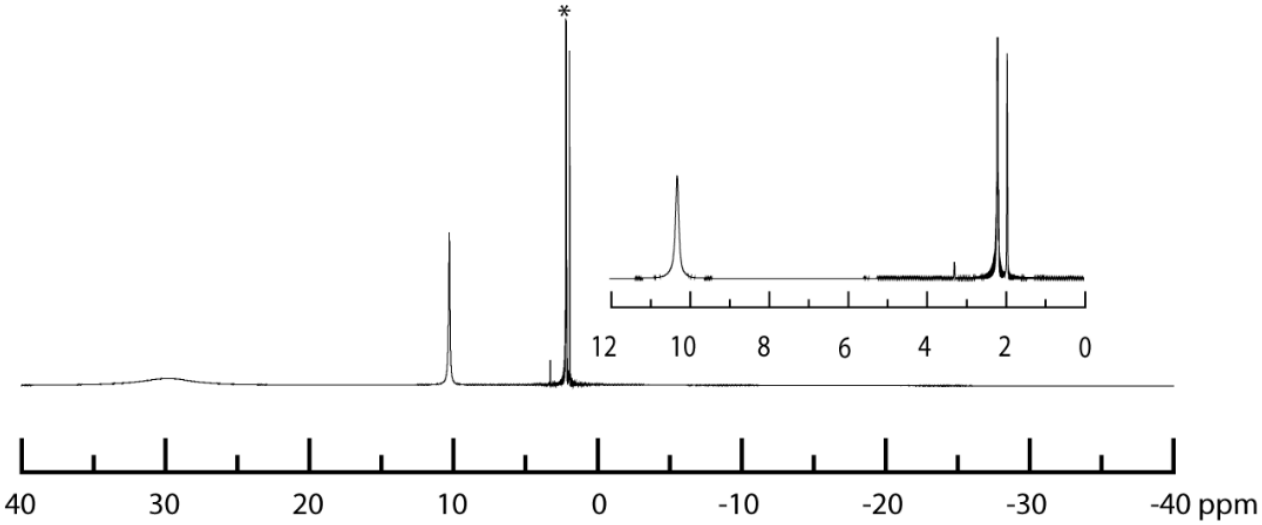

Figure III-3. ^{1}H NMR spectrum of III-2 measured in CD_3CN at 23 °C. The indicated peak [*] corresponds to residual water. Inset: expansion of the 0–12 ppm spectral range.

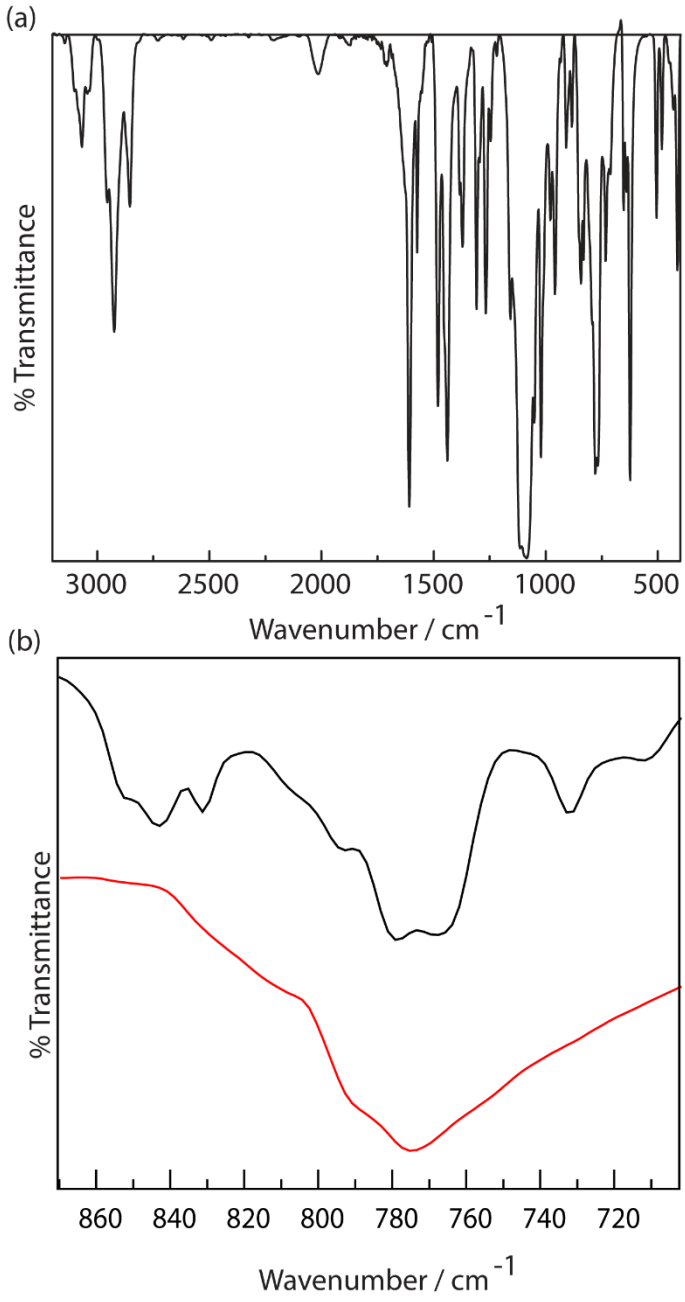

Figure III-4. (a) IR spectrum of III-2 recorded in a KBr pellet at 23 °C. (b) Expansion of spectral window depicting the bromate region. The spectrum of compound III-2 features peaks at 767 and 778 cm^{-1} (–), which are attributed to stretching modes characteristic of the bromate ligand. These features are distinct from those of $KBrO_3$, which are observed at 774 and 790 cm^{-1} (–).[282]

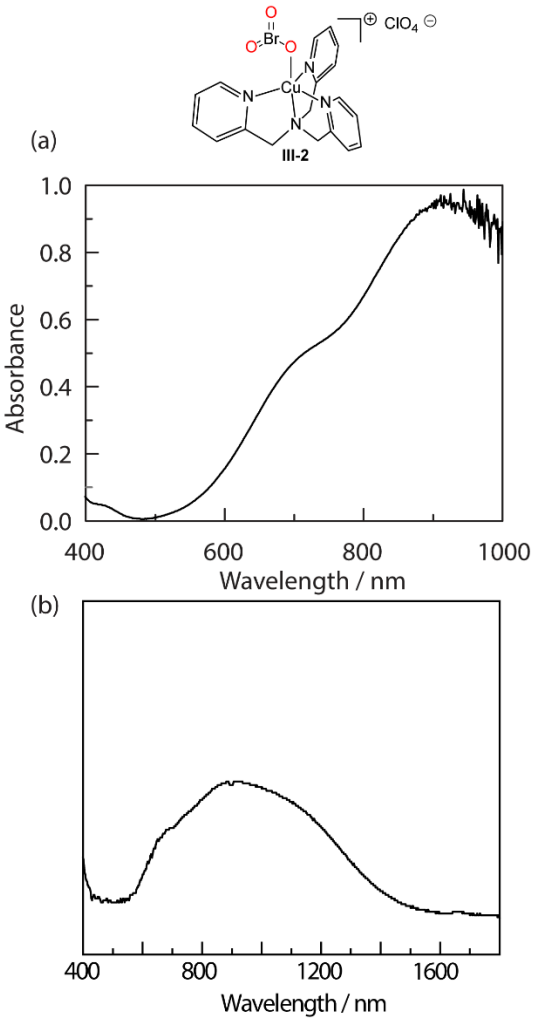

Figure III-5. UV-vis spectra of III-2. (a) UV-vis spectrum of III-2 measured in acetone at 23 °C. Absorptions are observed at 426 (ε = 2.3 × 10), 710 (ε = 3.0 × 10^2), and 920 nm (ε = 5.4 × 10^2). (b) Diffuse reflectance spectrum of III-2 measured in the solid-state at 23 °C. Absorptions are observed at 695 nm and 922 nm.

Copper(II) bromate **III-2** participates in photochemically promoted oxygen-atom transfer (OAT) and hydrogen-atom abstraction (HAA) reactions, which are characteristic of the reactivity patterns of reactive M–O species (Figure III-6). Photolysis (λ > 335 nm) of a CO-saturated CH_3CN solution of complex **III-2** afforded CO_2 (detected by GC analysis of the reaction headspace), which is the product of OAT to CO_2. Similar OAT to

olefinic substrates was observed: Photolysis of **III-2** in the presence of styrene or 1-octene afforded epoxides **III-4** and **III-5** in 91% and 36% yields, respectively. Photolysis in the presence of 1,4-cyclohexadiene (bond dissociation energy (BDE) = 76.0 kcal mol^{-1})[283] yielded benzene (84% yield). Photolysis of **III-2** in toluene (BDE = 89.7 kcal mol^{-1})[1] afforded benzyl alcohol in 76% yield. The KIE (k_H/k_D) for toluene C–H hydroxylation was measured to be 3.4(2) by integration of the ESI-MS signals for benzyl alcohol and d_7-benzyl alcohol following photolysis of a CH_3CN solution of **III-2** in the presence of 1:1 H_8-toluene/ D_8-toluene. Photolysis of **III-2** in the presence of cyclohexane (BDE = 99.5 kcal mol^{-1})[283] afforded a mixture of cyclohexanone (23% yield), cyclohexanol (17% yield), and bromocyclohexane (18% yield). Photolysis of **III-2** with pentane (BDE = 97.5)[284] or benzene (BDE = 112.9)[1] resulted in no observed substrate oxidation. For each of the reactions depicted in Figure III-6, no substrate activation products were observed without photolysis (*i.e.*, there are no thermal background reactions with the described substrates).

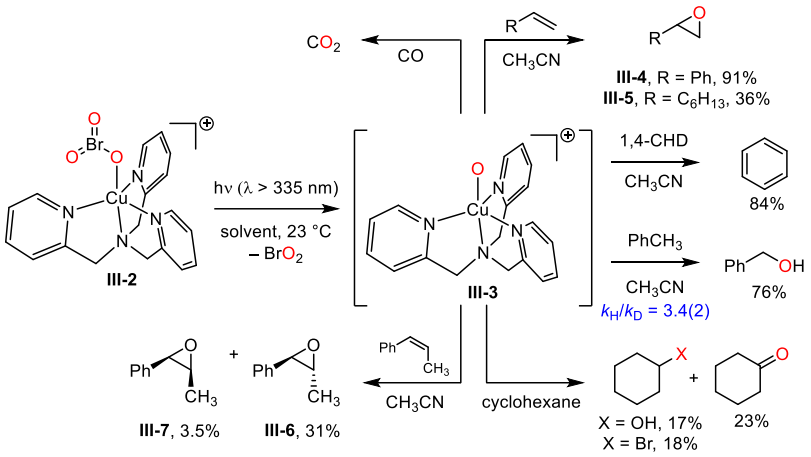

Figure III-6. Summary of photochemically promoted substrate functionalization chemistry. Both oxygen-atom transfer (OAT) and hydrogen-atom abstraction reactivity have been observed and can be envisioned as arising from a transiently generated reactive ligand-supported CuO fragment *(i.e.*, [(TPA)CuO] (III-3)).

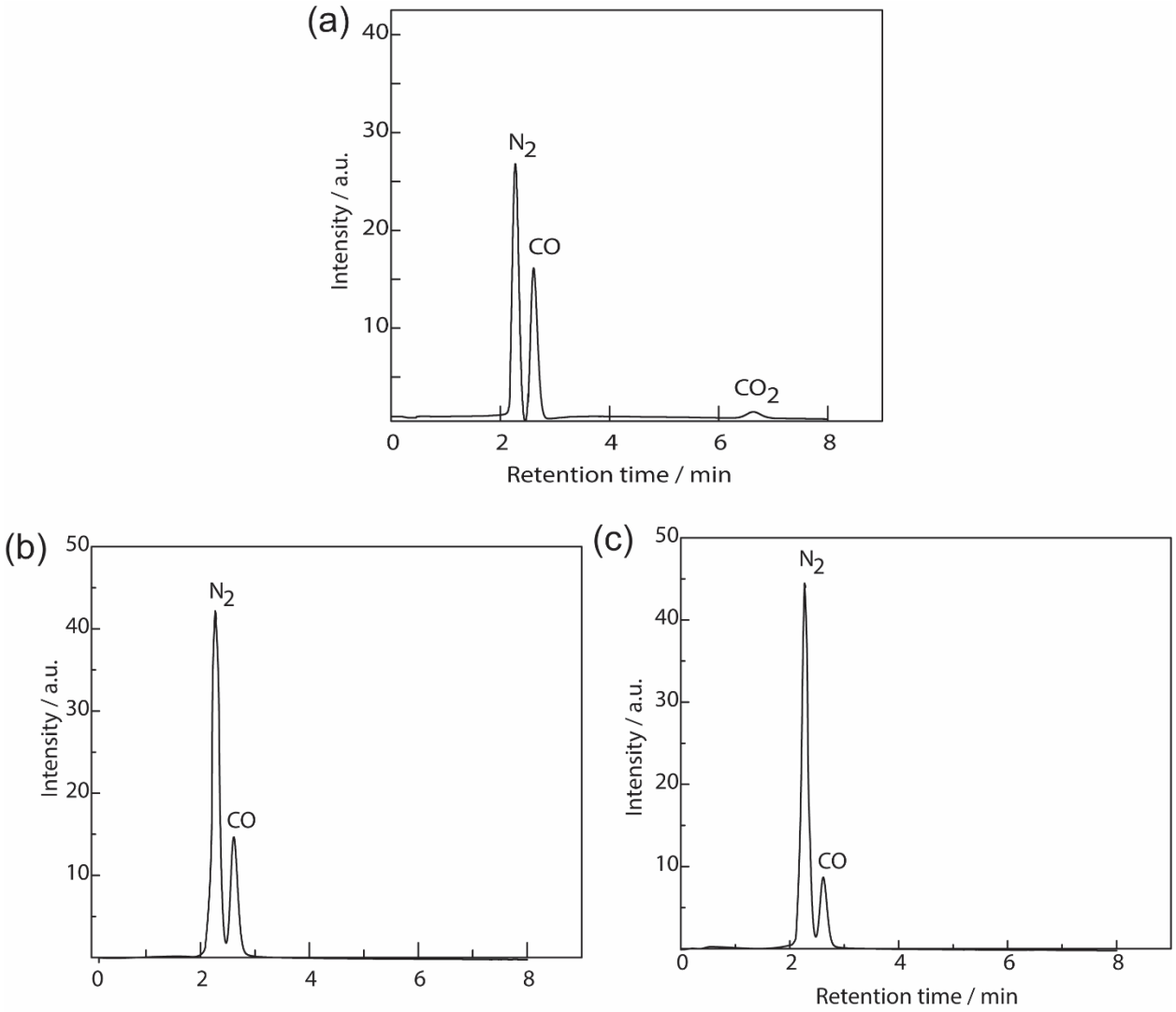

Figure III-7. Gas chromatograms (GC) of the headspace of reactions after 4 d photolysis ($335 < \lambda < 610$ nm). (a) Photolysis of III-2 dissolved in CH_3CN in the presence of CO results in the formation of CO_2. GC analysis of the headspace of the reaction shows N_2, CO, and CO_2. (b) Photolysis of a CH_3CN solution in the presence of CO. GC analysis of the headspace of the reaction shows only N_2 and CO. (c) Photolysis of $KBrO_3$ dissolved in CH_3CN in the presence of CO. GC analysis of the headspace of the reaction shows only N_2 and CO.

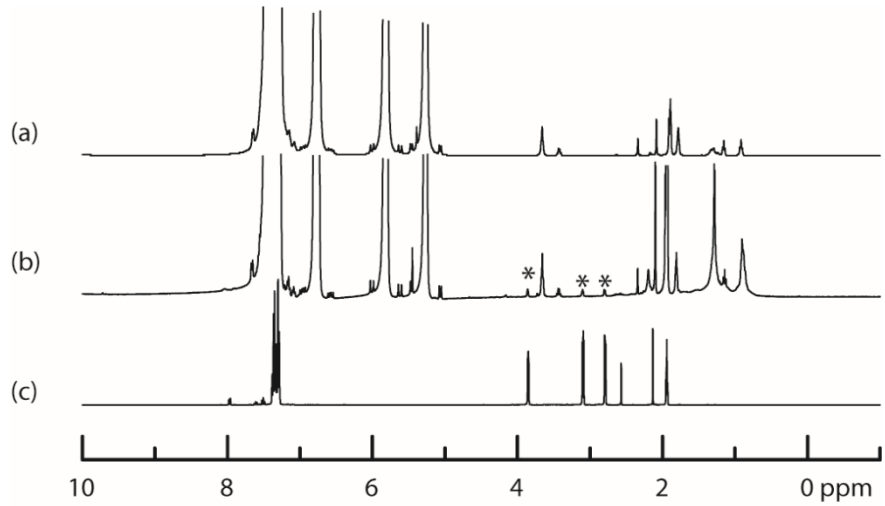

Figure III-8. Photolysis (335 < λ < 610 nm) of III-2 in CD_3CN and styrene results in the formation of styrene oxide (III-4). (a) ^1H NMR spectrum of the reactant mixture of III-2 and styrene; (b) ^1H NMR spectrum of the product mixture following photolysis of III-2; (c) ^1H NMR spectrum of isolated III-4 (spectral features attributed to styrene oxide (III-4) marked with *).

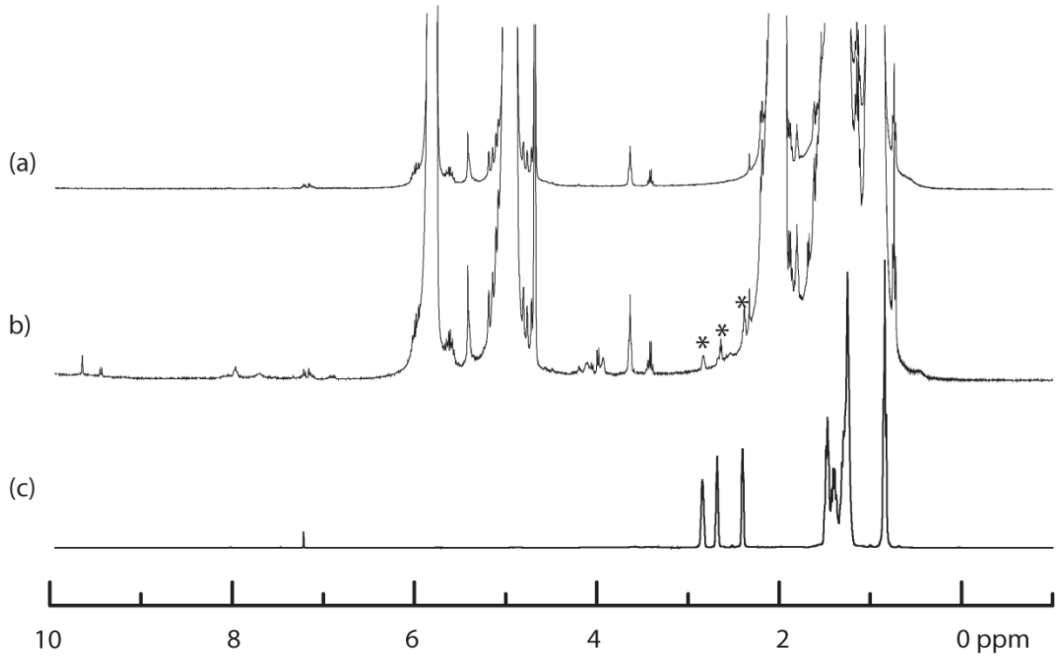

Figure III-9. Photolysis (335 < λ < 610 nm) of III-2 in CD_3CN and 1-octene results in the formation of epoxide III-5. (a) ^1H NMR spectrum of the reactant mixture of III-2 and 1-octene; (b) ^1H NMR spectrum of the product mixture following photolysis of III-2; (c) ^1H NMR spectrum of isolated III-5 (spectral features attributed to styrene oxide (III-5) marked with *).

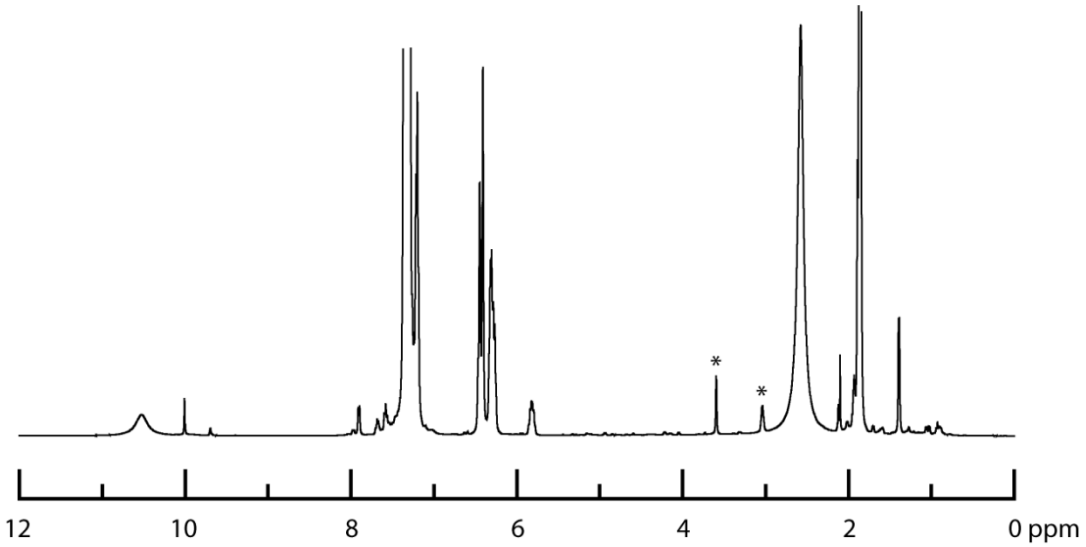

Figure III-10. Photolysis (335 < λ < 610 nm) of in III-2 CD_3CN and *cis*-β-methylstyrene results in the formation of *cis*-epoxide III-7 and *trans*-epoxide III-6. ^1H NMR spectrum of the product mixture following photolysis of III-7 (spectral features attributed to *cis*-epoxide (III-7) marked with *).

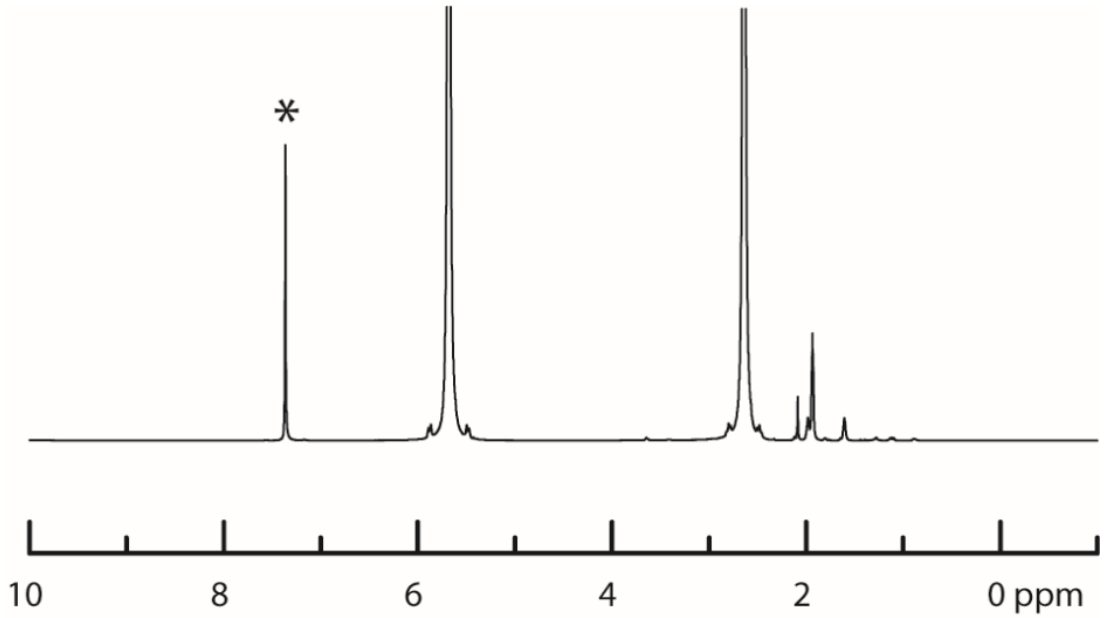

Figure III-11. Photolysis (335 < λ < 610 nm) of III-2 in CD_3CN and 1,4-cyclohexadiene results in the formation of benzene. ^1H NMR spectrum of the product mixture following photolysis of benzene (spectral features attributed to benzene marked with *).

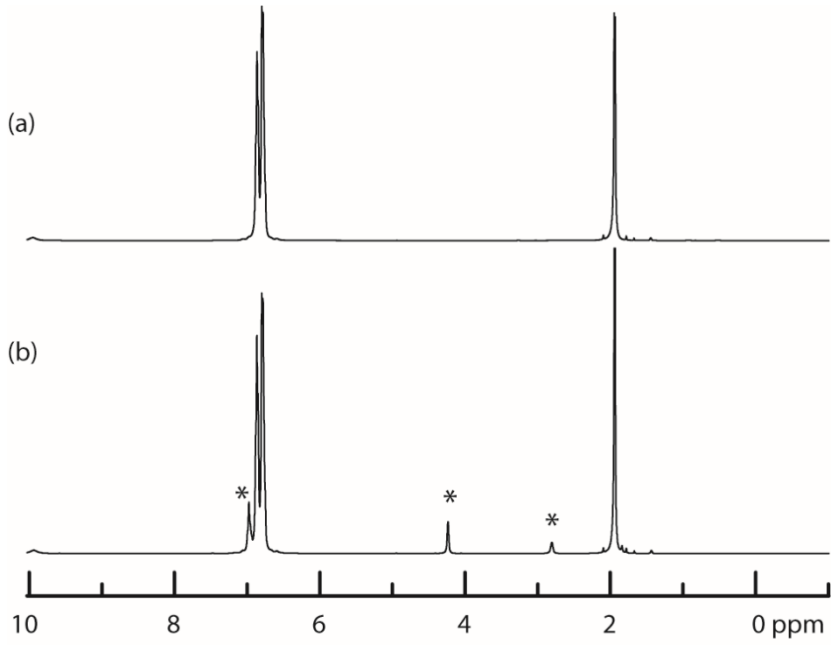

Figure III-12. Photolysis ($335 < \lambda < 610$ nm) of III-2 in CD_3CN and toluene results in the formation of benzyl alcohol. (a) ^1H NMR spectrum of the reactant mixture of III-2 and toluene; (b) ^1H NMR spectrum of the product mixture following photolysis of III-2 (spectral features attributed to benzyl alcohol marked with *).

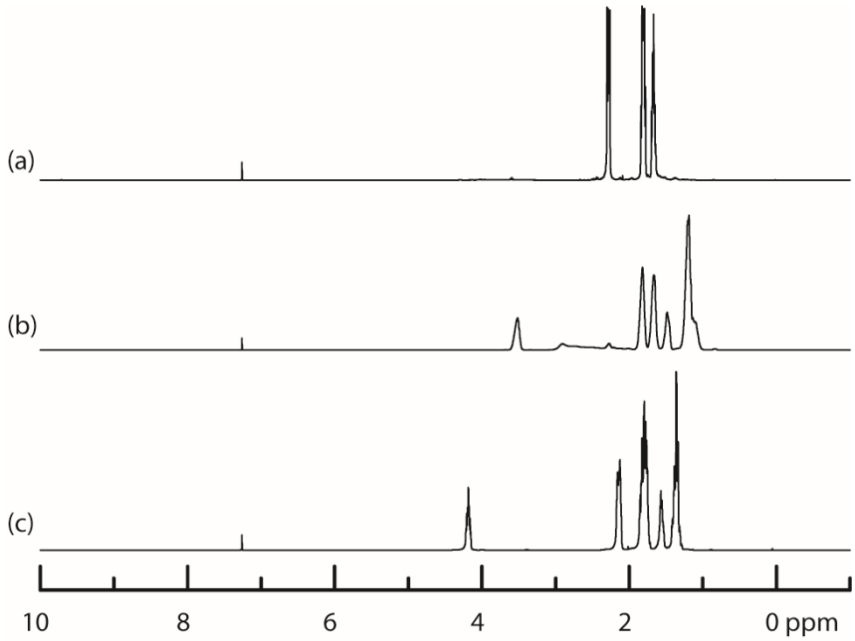

Figure III-13. Photolysis (335 < λ < 610 nm) of III-2 in cyclohexane results in the formation of cyclohexanone, cyclohexanol, and bromocyclohexane. (a) ^{1}H NMR spectrum of isolated cyclohexaone; (b) ^{1}H NMR spectrum of isolated cyclohexanol; (c) ^{1}H NMR spectrum of isolated bromocyclohexane.

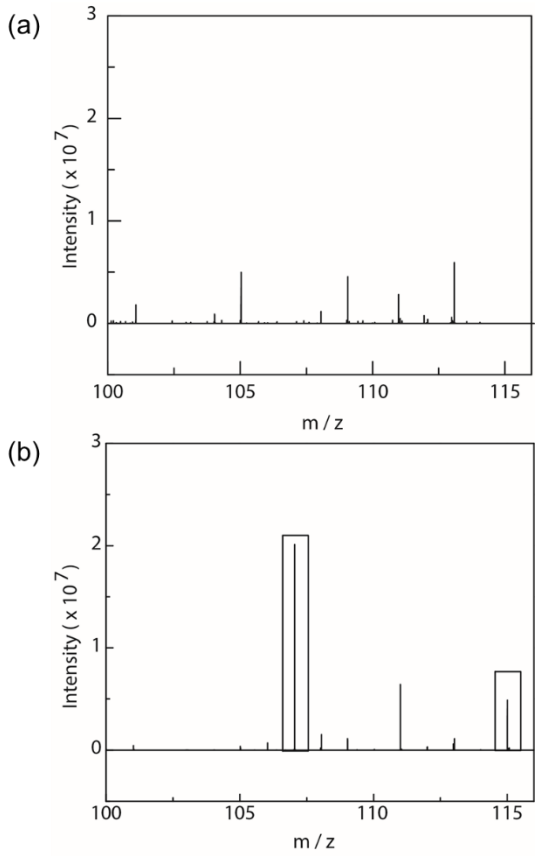

Figure III-14. APCI-MS trace for the intermolecular KIE determination. The m/z of benzyl alcohol ($C_7H_7O^-$, APCI negative) is 107.0489; the m/z of deuterated benzyl alcohol ($C_7D_7O^-$, APCI negative) is 115.0024. (a) The m/z spectrum of the reaction mixture without photolysis which indicates no traces of benzyl alcohols ($C_7H_7O^-$ or $C_7D_7O^-$). (b) The m/z spectrum of the reaction mixture after photolysis ($335 < \lambda < 610$ nm) which indicates the characteristic peaks of both benzyl alcohols which was used to calculate the k_H/k_D using the following equation:

$$Intermolecular\ KIE = \frac{Area\ of\ benzyl\ alcohol\ (107.0489)}{Area\ of\ deuterated\ benzyl\ alcohol\ (115.0024)}\ X\ \frac{D8-toluene}{H8-toluene}$$

Sample	Substrate	Average KIE*
III-2	H8-toluene/D8-toluene	3.4 ± 0.2

* The reaction was performed in triplicate.

A number of independent lines of evidence – both from observations of reactivity as well as spectroscopic and crystallographic data – are consistent with the intermediacy of transient [CuO] species in the photochemistry of **III-2**. Photochemically promoted epoxidation of stereochemically defined 1,2-disubstituted olefins is not stereospecific: Photolysis of **III-2** in the presence of *cis*-β-methylstyrene afforded a 10:1 mixture of **III-6/III-7** in 35% yield. To probe if a [CuO] fragment is involved in the epoxidation of *cis*-β-methylstyrene upon photolysis of **III-2**, Cu(I) TPA (**III-8**) was dissolved in a MeCN solution with PhIO and *cis*-β-methylstyrene. Oxidation of *cis*-β-methylstyrene using **III-8** afforded *trans*-epoxide **III-6** in 7% yield and *cis*-expoxide in 0.8% yield (Figure III-15). This features the same *trans:cis* epoxide ratio as photolysis of **III-2**, indicating that both processes pass through a similar intermediate, *e.g.* a CuO fragment. The lack of epoxidation stereospecificity and the primary KIE determined for the hydroxylation of toluene are consistent with stepwise substrate activation via carbon-centered radicals (*i.e.*, alkyl radicals generated by either radical addition to olefins or via H-atom abstraction (HAA) from alkanes).

The potential role of photogenerated $BrO_3^{\bullet}$, produced via photocleavage of the Cu–O bond, in OAT, was evaluated by photolysis of a mixture of $KBrO_3$ and $(NH_4)_2S_2O_8$ in the a toluene/MeCN mixture, which has been shown to photochemically produce $BrO_3^{\bullet}$.[285] Photogeneration of $BrO_3^{\bullet}$ affords benzyl alcohol, benzaldehyde, benzoate (Figure III-16). In contrast, photolysis of a $(NH_4)_2S_2O$ solution in toluene results in no C–H oxidation products. Additionally, we measured a k_H/k_D of 1.0 for the $BrO_3^{\bullet}$ oxidation toluene to benzyl alcohol, which does not match the 3.4(2) value measured for **III-2**. Comparison of

the resultant $BrO_3^{\bullet}$ chemistry to the photolysis of Cu bromate **III-2** highlights the selectivity of the latter; we conclude that $BrO_3^{\bullet}$ is not the active OAT agent upon photolysis of **III-2** due to the mismatch in k_H/k_D and selective nature of the Cu bromate oxidations.

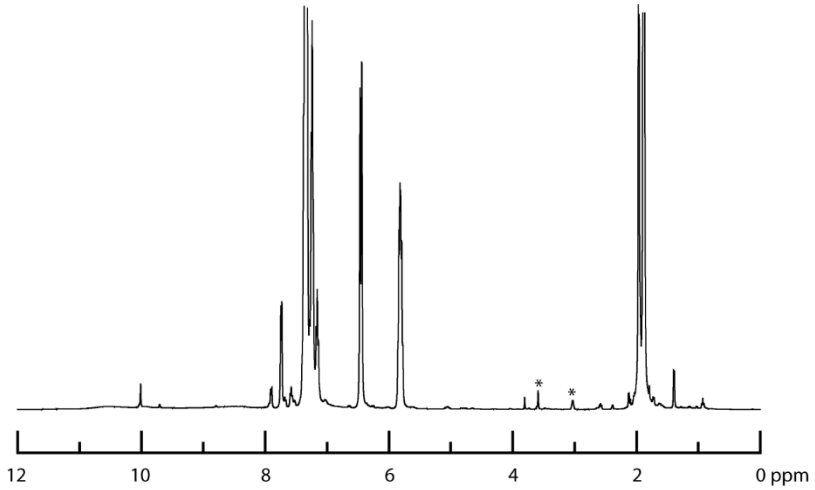

Figure III-15. Combination of [Cu(TPA)]BF_4 , PhIO, and *cis*-β-methylstyrene in CD_3CN results in epoxidation. ^{1}H NMR spectrum of the crude product mixture (spectral features attributed to *trans*-epoxide III-6 are marked with *).

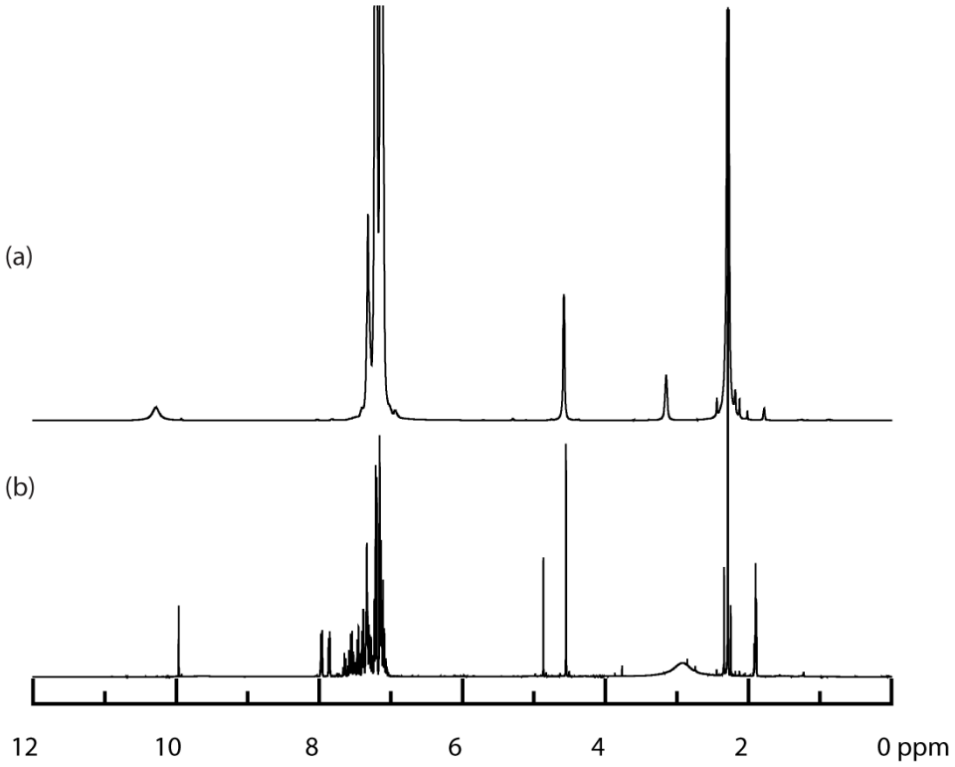

Figure III-16. Photolysis (white light) of $KBrO_3$ and $(NH_4)_2S_2O_8$ in CD_3CN and toluene results in formation of benzyl alcohol, benzaldehyde, and benzoate. (a) ^1H NMR spectrum of the product mixture following photolysis of III-2; (b) ^1H NMR spectrum of the crude product mixture following photolysis of $KBrO_3$ and $(NH_4)_2S_2O_8$ in CD_3CN and toluene.

We envisioned that the formation of a [CuO] intermediate could occur via direct photooxidation, *i.e.*, cleavage of the O–Br bond to generate $[Cu(tpa)O]^+$ (**III-3**) and BrO_2, or via a photoreduction / OAT sequence, *i.e.*, initial cleavage of the Cu–O bond to generate a $[Cu(tpa)]^+$ fragment and $BrO_3^\bullet$ following by OAT from $BrO_3^\bullet$ to $[Cu(tpa)]^+$. Several lines of evidence suggest the evolution of $BrO_3^\bullet$, and subsequent OAT to generate BrO_2 under steady-state photolysis of **III-2**. First, the major Cu-containing fragment during our MALDI-mass spectrometric experiments is Cu(I)tpa, which is indicated by the set of peaks at 353.0 and 355.0 *m/z* that display the expected isotopic distribution (Figure III-

17a). Furthermore, the photoextruded $BrO_3^{\bullet}$ fragment is detected via MALDI at 126.9 and 128.9 *m/z*, which are well matched to the simulated $BrO_3^{\bullet}$ mass spectrum (Figure III-17b). The formation of a [CuO] intermediate via OAT from the $BrO_3^{\bullet}$ fragment would be accompanied by the evolution of BrO_2. MALDI-MS analysis of **III-2** also shows peaks at 110.9 and 112.9 *m/z* which corresponds to the extruded BrO_2 fragment and is well-matched to the simulated BrO_2 mass spectrum (Figure III-17c). Finally, photogenerated BrO_2 has been observed by IR spectroscopy: The IR spectrum of Cu bromate **III-2** in a KBr pellet displays characteristic bromate stretches at 831, 842, and 852 cm^{-1}. Photolysis of this KBr pellet results in the consumption of these spectral features and the evolution of a new peak at 795 cm^{-1}, which is well-matched to a reported stretch for BrO_2 (Figure III-17d).[286] The other stretching mode expected BrO_2 (*i.e.*, 845 cm^{-1}) overlaps with a stretching mode of the Cu(tpa) fragment.

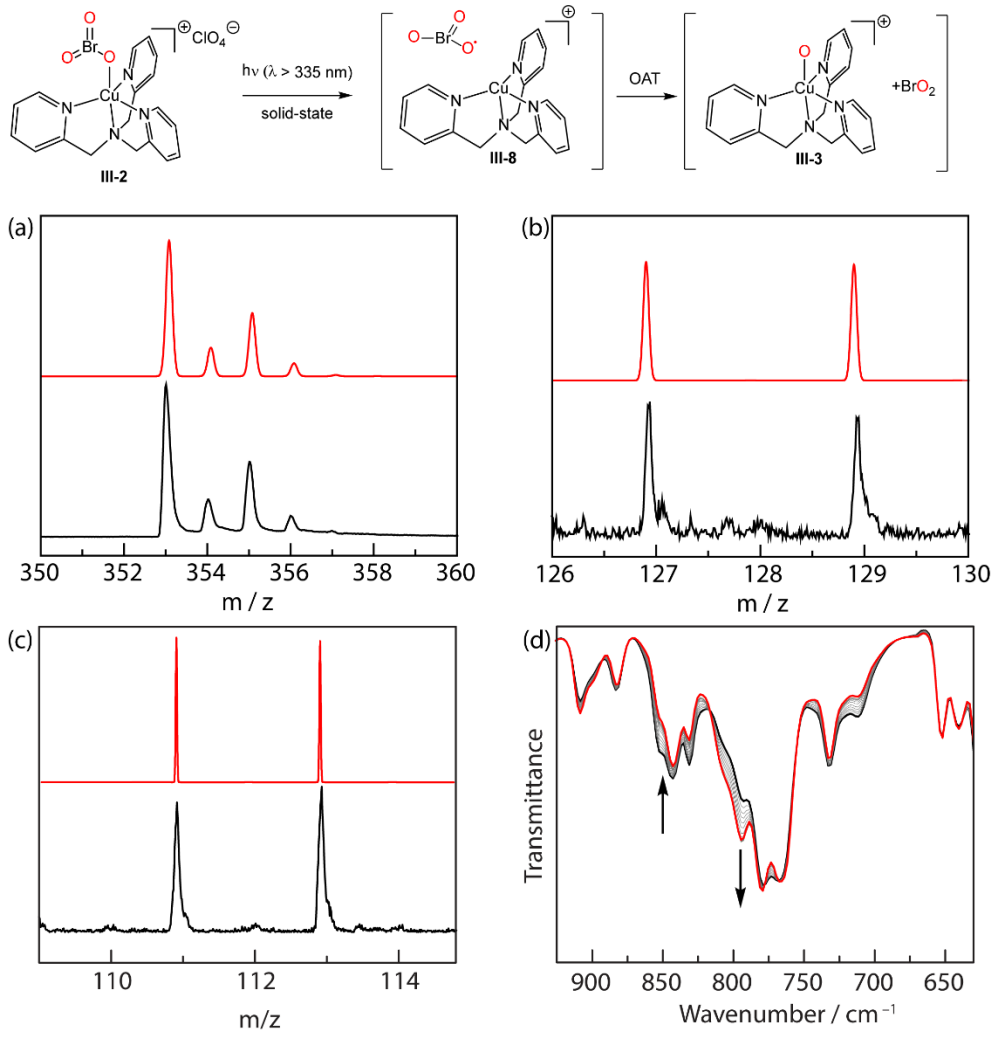

Figure III-17. Photoreduction of III-2 by Cu–OBrO$_2$ homolysis followed by OAT from BrO$_3$$^{\bullet}$ to the Cu(I) complex [Cu(tpa)]$^+$ would generate a Cu oxyl intermediate. Consistent with initial photoreduction. (a) MALDI-MS analysis shows peaks at 350.0 and 355.0 *m/z* which correspond to [Cu(tpa)]$^+$ (—), simulation (—); (b) MALDI-MS analysis shows peaks at 126.9 and 128.9 *m/z* which correspond to photoextruded BrO$_3$ (– –), simulation (—); (c) MALDI-MS analysis shows peaks at 110.9 and 112.9 *m/z* which correspond to BrO$_2$ (—), simulation (—); (d) IR spectra collected during the photolysis of a KBr pellet of III-2 shows a new peak at 795 cm^{-1}, which is attributed to BrO$_2$.

Attempts to characterize the primary photochemical processes available to $[Cu(tpa)O–BrO_2]^+$ by low-temperature spectroscopy have been stymied by a combination of insolubility in, or reaction with, common glassy solvents. To avoid these challenges and to build on emerging *in crystallo* photochemical strategies to characterize reactive species relevant to C–H functionalization, we were attracted to the potential to apply *in crystallo* photochemistry to directly visualize the primary photochemical events relevant to the OAT chemistry described above. We reasoned that photooxidation via BrO_2 loss would be differentiable from initial photoreduction via $BrO_3^{\bullet}$ elimination. To these ends, X-ray diffraction data was collected during 365 nm irradiation of a single crystal of **III-2** at 100 K using 30 keV synchrotron radiation. Solid-state reaction progress was monitored by free refinement of the Cu–$OBrO_2$ fragment.

The *in crystallo* structural data are consistent with photoreduction of [Cu(tpa)O–BrO_2]ClO_4 (**III-2**) to afford Cu(I) and $BrO_3^{\bullet}$. Following photolysis, the Cu–O distance elongates from 1.951(3) to 2.242(1) Å (Cu(1)–O(1)). The Br–O bonds shorten from an average of 1.655(3) to 1.53(3) Å, with the most drastic contraction occurring at the O(1)–Br(1) bond from 1.698(3) to 1.407(2) Å. Moreover, as the Cu–O bond elongates the Cu–O–Br bond angle changes from 124.28(2)° to 118.6(5)° (Cu(1)–O(1)–Br(1)).

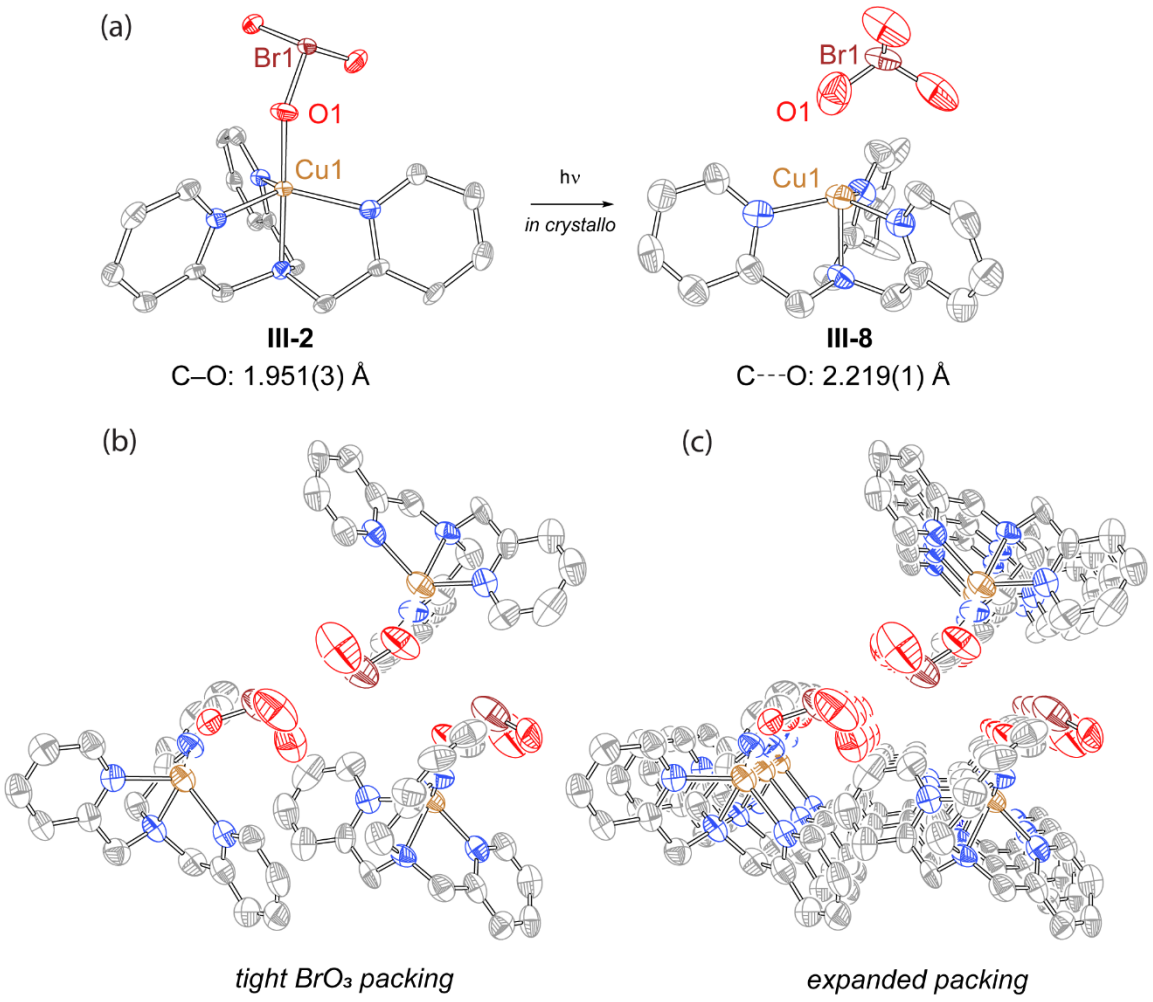

Figure III-18. Photocrystallography of III-2. (a) Solid-state structure of III-2 and III-8, generated by solid-state photolysis with 365 nm laser. Ellipsoids of III-2 are drawn at 50% and ellipsoids of III-8 are drawn at 30%. H-atoms and counter anions are removed for clarity. (b) Expansion of the crystalline lattice shows the tight packing of the photoextruded BrO3•. (c) Further expansion of the crystalline lattice shows the lack of room for the BrO• to diffuse to in all directions.

The collected data are consistent with initial Cu–OBrO$_2$ bond activation in the solid-state photolysis of [Cu(tpa)O–BrO$_2$]$^+$ to generate [Cu(tpa)]$^+$ and BrO$_3$•. These crystallographic data are supported by products observed in the MALDI-MS data presented here and other examples of photoreduction in the literature.[263, 264] The

refinement of free $BrO_3^{\bullet}$ and Cu(I)(tpa) is stymied by the small cavity size in between the two Cu moieties in the asymmetric unit; the $BrO_3^{\bullet}$ fragment is unable to move away from the residual Cu–$OBrO_2$ complicating the refinement of the generated Cu(I) fragment (Figure III-18b, computational details can be found in Table III-4). These challenges highlight the limitations of photocrystallography, where previous experiments involving a gaseous leaving group, such as N_2, facilitated refinement of both photoinduced structure and unreacted starting material. [200, 201, 287-290] In this case a solid-state leaving group such as $BrO_3^{\bullet}$ hinders the refinement.

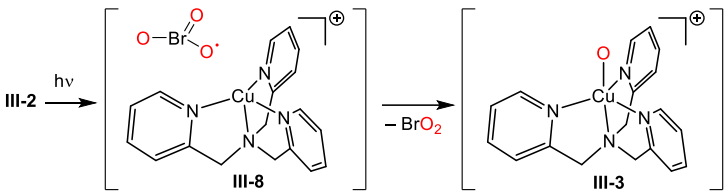

Figure III-19. Hypothesized reaction pathway to access Cu oxo III-3. Upon photolysis the Cu–O bond is cleaved, generating Cu(I) tpa III-8 and $BrO_3^{\bullet}$. These species undergo OAT from the extruded $BrO_3^{\bullet}$ yielding Cu oxo species III-8 and BrO_2.

III.3. Conclusion

In conclusion, we have described access to a copper oxo intermediate that is competent in C–H and C=C oxidation. Based on the observed oxidation products, KIE, and detection of BrO_2 via MALDI-MS and IR spectroscopy, we determine that the OAT agent is copper oxo **III-3**. However, the photolysis does not cleave the O–Br bond to yield **III-8**. Photolysis of a single-crystal of **III-2** at 100 K shows Cu–O cleavage, generating $BrO_3^{\bullet}$. We hypothesize that subsequent thermal recombination of **III-8** and $BrO_3^{\bullet}$ in

solution generates the Cu oxo species of interest as depicted in Figure III-19. We anticipate that closer inspection of most metal-oxyanion photolyses will yield similar results.

III.4. Experimental Details

III.4.1 General Considerations

Materials and Methods. Unless otherwise noted, all the chemicals and solvents (ACS reagent grade) were used as received. Potassium bromate, sodium iodide, benzyl alcohol, copper(II) bromide, and sodium perchlorate were purchased from Alfa Aesar. Ammonium persulfate, 2-picolyl amine, cesium carbonate, carbon monoxide, tetrakis(acetonitrile)copper(I) tetrafluoroborate, benzene, and molecular sieves (4 Å, MS) were purchased from Sigma Aldrich. Sodium tetrafluoroborate was purchased from AK Scientific. 2-(Chloromethyl)pyridine hydrochloride was purchased for Matrix Scientific. Cyclohexane, 1,4-cyclohexadiene, iodobenzene diacetate, and styrene were purchased from Acros Organics. 1-Octene was purchased from Oakwood chemical. Cyclohexane, cyclohexadiene, styrene, and 1-octene were dried according to literature methods[291] and subsequently degassed by three free-pump-thaw cycles. N_2, CO, and CO_2 were purchased from Airgas. NMR solvents were obtained from Cambridge Isotope Laboratories were degassed by three free-pump-thaw cycles and were stored over molecular sieve (3 Å) for 24 h prior to use. All reactions were carried out under an ambient atmosphere unless otherwise noted. Anhydrous acetonitrile and toluene were obtained from a drying column and stored over activated molecular sieves.[292] Anhydrous acetonitrile was stored over 3 Å molecular sieves, and all other solvents were stored over 4 Å molecular sieves. Tris(2-

pyridylmethyl)amine (TPA),[293] silver bromate,[294] and iodosyl benzene (PhIO),[295] were prepared according to literature methods.

Characterization Details. NMR spectra were recorded on Bruker Avance NEO 400 NMR operating at 400.09 MHZ for ^{1}H. The NMR spectra were referenced against residual proteo solvent signal: CD_3CN (1.94 ppm, ^{1}H) and $CDCl_3$ (7.26 ppm, ^{1}H).[248] ^{1}H NMR data are reported as follows: chemical shift (δ, ppm), multiplicity (s (singlet), d (doublet), t (triplet), m (multiplet), br (broad), integration. Solution-phase UV-vis spectra were recorded on an Ocean Optics Flame-S miniature spectrometer with DH-mini UV-Vis-NIR light source (200-900 nm). Solution-phase spectra were blanked against the appropriate solvent. IR spectra were recorded on a Shimadzu FTIR/IRAffinity-1 Spectrometer, were blanked against air, and were determined as the average of 64 scans. *In situ* IR spectra were measured in a KBr pellet with a Bruker VERTEX 70, were blanked against air, and were determined as the average of 64 scans. IR data are reported as follows: wavenumber (cm^{-1}), peak intensity (s, strong; m, medium; w, weak). MALDI data was obtained using a Bruker Microflex LRF MALDI-TOF in reflectron mode. No added matrix was used in the reported MALDI experiments. Mass spectrometry data was recorded on either Orbitrap Fusion™ Tribrid™ Mass Spectrometer or Q Exactive™ Focus Hybrid Quadrupole - Orbitrap™ Mass Spectrometer from Thermo Fisher Scientific. Kinetic isotope effects (k_H/k_D) were determined by integration of appropriate peaks in the mass spectrum. Atmospheric pressure chemical ionization mass spectrometry (APCI-MS) experiment was performed using a Thermo Scientific Q Exactive Focus. Sample was injected into a 10 µL loop and methanol was used as a mobile phase at a flow rate of 500

μL/min. The Q Exactive Focus APCI source was operated in full MS in positive mode. The mass resolution was tuned to 70000 FWHM at m/z = 200. The discharge current was set at 5 μA, the sheath gas and auxiliary gas flow rates were set to 25 and 5 arbitrary units, respectively, and the auxiliary gas temperature was set to 300 °C. The transfer capillary temperature was held at 250 °C and the S-Lens RF level was set at 50 V. Exactive Series 2.11/Xcalibur 4.02.47 software was used for data acquisition and processing. Elemental analyses were performed in Atlantic Microlab, Inc., Norcross, GA.

Photochemistry Details. *Steady-State Photolysis.* For a standard photochemical reaction, a J-young/Schlenk tube was charged with compound **III-2** (1 equiv.), the appropriate substrate (10 equiv.), and CD_3CN. The solution was photolyzed by a Nikon for Hg 100W lamp equipped with a glass filter ($335 < \lambda < 610$ nm) for 4-6 d at 23 °C, depending on the substrate. The reaction mixture was subsequently filtered through Celite and the products were characterized by GC/GCMS and ^1H NMR spectroscopy. GC retention times were established by comparison with authentic samples of the relevant products.

Analysis of Head-Space Gases. An Agilent Trace 1300GC with attached thermal conductivity detector and a custom-made 120 cm stainless steel column packed with Carbosieve-II was used for analysis of headspace gases. The column was kept at 200 °C and Ar was used as carrier gas. The detector was set to a temperature of 250 °C. Headspace gas (~300 μL) was transferred to the GC with a 0.50 mL Valco Precision Sampling Syringe (Series A-2) equipped with a Valco Precision sampling needle with a 5-point side port.

X-Ray Diffraction Details. X-ray crystal structures of **III-2** and **III-8** were collected using synchrotron radiation (0.41328 Å) at ChemMatCARS located at the Advanced Photon Source (APS) housed at Argonne National Laboratory (ANL). Crystals suitable for X-ray diffraction were mounted on a glass fiber and data was collected at 100 K (Cryojet N_2 cold stream) using a vertically mounted Bruker D8 three-circle platform goniometer equipped with a PILATUS3 X CdTe 1M detector. Data were collected as a series of φ and/or ω scans. Data were integrated using SAINT and scaled with a multi-scan absorption correction using SADABS. Structures were solved by intrinsic phasing using SHELXT (Apex2 program suite v2014.1) and refined against F^2 on all data by full matrix least squares with SHELXL97.[251, 252] All non-hydrogen atoms were refined anisotropically. H atoms were placed at idealized positions and refined using a riding model. Refinement details are described in the relevant cif.

Computational Details. Calculations were performed using the Gaussian 16, Revision C.01 suite of software.[254] Geometry optimizations were carried out with the PBE0 functional[296] in conjunction with Grimme's D3 empirical dispersion[297] and Becke-Johnson damping [EMP=GD3BJ],[298] the mod-LANL2DZ basis set[299] and corresponding ECP for Cu,[300] and the 6-311+G* basis set for other atoms;[301] the coordinates for optimized geometries are tabulated in Table III-4. Frequency calculations at this level of theory confirmed that optimized geometries represent ground state structures.

III.4.2 Synthesis and Characterization

Synthesis of [(TPA)CuBr]ClO$_4$ (III-1)

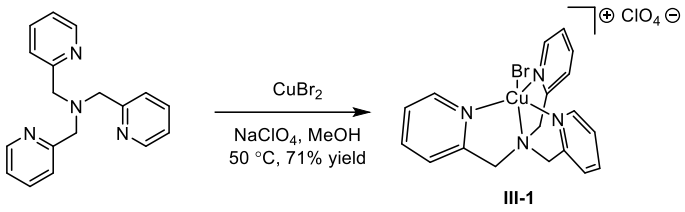

III-1

[(TPA)CuBr]ClO$_4$ (**III-1**) was prepared according to the following modification of literature methods.[302] A 100-mL round-bottom flask was charged with TPA (2.92 g, 10.1 mmol, 1.00 equiv.) and methanol (25 mL). The reaction solution was heated to 50 °C. $CuBr_2$ (2.25 g, 10.2 mmol, 1.01 equiv.) was slowly added to the reaction solution and the solution was stirred for 1 h. During this time, the color of the solution became dark green. $NaClO_4$ (1.52 g, 12.5 mmol, 1.24 equiv.) was added as a solid and the reaction mixture was stirred for 15 min. The resulting green precipitate was isolated by vacuum filtration. The precipitate was washed with diethyl ether to afford the title compound as a green powder (3.61 g, 71%). Crystals suitable for X-ray diffraction analysis were obtained by slow diffusion of diethyl ether into the acetonitrile solution of the compound. ^{1}H NMR (δ, 23 °C, CD_3CN): 29.8 (br s, 12H), 10.3 (br s, 6H). UV-Vis-NIR (solid) (nm): 258, 340, 988. UV-vis (acetonitrile), λ_{max} (nm, e ($M^{-1}cm^{-1}$)): 330 (18100), 995 (900). HRMS ESI-MS (acetonitrile): calculated for $[M]^+$ = 433.998, observed $[M]^+$ = 433.997. IR (KBr pellet, cm^{-1}): 3067 (m), 2959 (m), 2009 (w), 1607 (s), 1571 (m), 1478 (s), 1430 (s), 1364 (m), 1307 (s), 1260 (s), 1085 (s), 1023 (s), 951 (m), 899 (w), 832 (m), 755 (s), 719 (m), 620 (s), 512 (m), 476 (w), 408 (m). Spectral data are well-matched with those available in the literature.[302]

Synthesis of [(TPA)CuOBrO$_2$]ClO$_4$ (III-2)

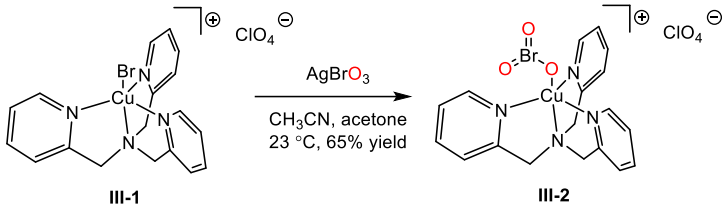

A 20-mL scintillation vial was charged with **III-1** (2.14 g, 4.04 mmol, 1.00 equiv.), acetone (8 mL), and acetonitrile (2 mL). To that solution, $AgBrO_3$ (2.88 g, 12.3 mmol, 3.07 equiv.) was added and the reaction mixture was stirred in the dark for 24 h at 23 °C. During this time, the color of the reaction mixture became dark blue. Solids were removed by filtration through Celite and the filtrate was concentrated *in vacuo*. The residue was washed with diethyl ether. The residue was taken up in acetone and slow diffusion of either diethyl ether or pentane into the acetone solution resulted in crystallization of the title compound (1.53 g, 65% yield following crystallization). ^{1}H NMR (δ, 23 °C, CD_3CN): 28.2 (br s, 12H), 10.7 (br s, 6H). IR (KBr pellet, cm^{-1}): 3067 (m), 2923 (s), 2849 (m), 2016 (w), 1606 (s), 1576 (m), 1481 (s), 1437 (s), 1367 (m), 1310 (s), 1266 (s), 1096 (s), 1020 (s), 957 (s), 900 (w), 881 (w), 844 (s), 744 (s), 730 (s), 649 (m), 623 (s), 496 (m), 484 (w), 433 (w). UV-Vis-NIR (solid) (nm): 267, 914. UV-vis (acetone), λ_{max} (nm, ε ($M^{-1}cm^{-1}$)): 426 (2.3×10^2), 710 (3.0×10^2), 920 nm (5.4×10^2). Anal. Calc. for $C_{18}H_{18}N_4O_7BrClCu$: C, 37.19; H, 3.12, N, 9.64. Found C, 37.22; H, 3.15, N, 9.59.

III.4.3 Photochemical Reaction Details

Oxygenation of Carbon Monoxide

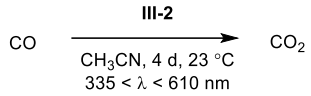

In an N_2-filled glovebox, a J-young tube was charged with **III-2** (0.040 g, 0.070 mmol) and dissolved in acetonitrile (0.75 mL). The reaction mixture was degassed by three freeze-pump-thaw cycles and the headspace was refilled with 1 atmosphere of carbon monoxide. The reaction mixture was photolyzed for 4 d at 23 °C using a 100 W Hg lamp with a 335-610 nm band-pass filter. The reaction headspace was analyzed by gas chromatography (Figure III-7), which indicated the formation of carbon dioxide.

Oxidation of 1,4-Cyclohexadiene

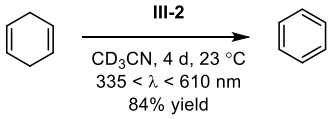

In an N_2-filled glovebox, a J-young tube was charged with **III-2** (0.040 g, 0.070 mmol, 1.0 equiv.), cyclohexadiene (0.70 mmol, 10 equiv), and CD_3CN (0.60 mL). The reaction mixture was photolyzed for 4 d at 23 °C using a 100 W Hg lamp with a 335-610 nm band-pass filter. The reaction mixture was filtered through Celite. The resulting solution was analyzed via ^1H NMR (ethylbenzene (10 μL) added as internal standard), which indicated formation of benzene (84%).

Epoxidation of α-Olefins

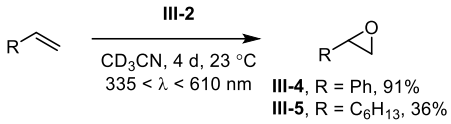

In an N_2-filled glovebox, a J-young tube was charged with **III-2** (0.100 g, 0.180 mmol, 1.00 equiv.), α-olefin (1.80 mmol, 10 equiv), and CD_3CN (2.40 mL). The reaction mixture was photolyzed for 4 d at 23 °C using a 100 W Hg lamp with a 335-610 nm band-pass filter. The product was analyzed via ^1H NMR (ethyl benzene (10 uL) added as an internal standard), which indicated the formation of epoxides **III-4** (0.0190 g, 91% yield) and **III-5** (0.0083 g, 36% yield), respectively. The resulting mixture was filtered through Celite and concentrated *in vacuo*. The residue was purified by column chromatography with EtOAc / hexanes system (v/v: 1:10) to afford products **III-4** (0.0190 g, 91% yield) and **III-5** (0.0083 g, 36% yield), respectively.

Epoxidation of *cis*-β-methylstyrene

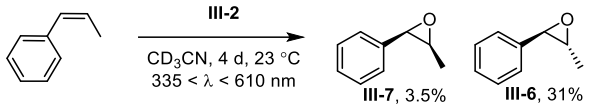

In an N_2-filled glovebox, a Schlenk tube was charged with **III-2** (0.040 g, 0.070 mmol, 1.00 equiv.), *cis*-β-methylstyrene (0.70 mmol, 10 equiv), and CD_3CN (0.60 mL). The reaction mixture was photolyzed for 4 d at 23 °C using a 100 W Hg lamp with a 335-610 nm band-pass filter. The resulting solution was analyzed via ^1H NMR (dichloromethane (10 μL) added as internal standard), which indicated formation of *cis*-epoxide (3.5%) and *trans*-epoxide (31%).

Hydroxylation of Toluene

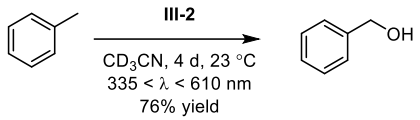

In an N_2-filled glovebox, a J-young tube was charged with **III-2** (0.040 g, 0.070 mmol, 1.0 equiv.), toluene (0.70 mmol, 10 equiv), and CD_3CN (0.60 mL). The reaction mixture was photolyzed for 4 d at 23 °C using a 100 W Hg lamp with a 335-610 nm band-pass filter. The reaction mixture was filtered through Celite. The resulting solution was analyzed via ^1H NMR (ethylbenzene (10 μL) added as internal standard), which indicated formation of benzyl alcohol (76%).

Determination of the kinetic isotope effect (KIE) of hydroxylation. In an N_2-filled glovebox, a J-young tube was charged with **III-2** (0.040 g, 0.070 mmol, 1.0 equiv.), toluene (0.70 mmol, 10 equiv), toluene-d_8 (0.70 mmol, 10 equiv.), and acetonitrile (0.40 mL). The reaction mixture was photolyzed for 4 d at 23 °C using a 100 W Hg lamp with

a 335-610 nm band-pass filter. The reaction mixture was filtered through Celite and the k_H/k_D was determined by integration of the APCI-MS data obtained from this solution (Figure III-14).

Oxidation of Cyclohexane

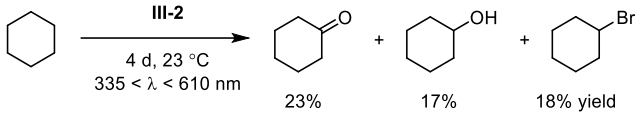

In an N_2-filled glovebox, a J-young tube was charged with **III-2** (0.100 g, 0.180 mmol, 1.00 equiv.) and cyclohexane (1.50 mL, 14.5 mmol, 80.5 equiv). The reaction mixture was photolyzed for 6 d at 23 °C using a 100 W Hg lamp with a 335-610 nm band-pass filter. The reaction mixture was filtered through Celite. The filtrate was purified by column chromatography with EtOAc / hexanes system (v/v: 3:7) to afford products cyclohexanone (0.0041 g, 23% yield), cyclohexanol (0.0031 g, 17% yield), and bromocyclohexane (0.0053 g, 18% yield) respectively.

Epoxidation of *cis*-β-methylstyrene with [Cu(tpa)]BF_4

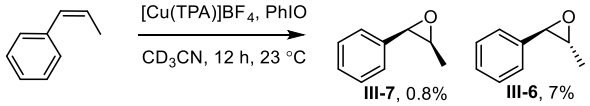

In an N_2-filled glovebox a Schlenk tube was charged with TPA (0.041 g, 0.14 mmol, 1.1 equiv.), $[Cu(MeCN)_4]BF_4$ (0.042 g, 0.13 mmol, 1.0 equiv.), and CD_3CN (0.60 mL). The reaction mixture was stirred for 30 m. PhIO (0.029 g, 0.13 mmol, 1.0 equiv), and cis-β-methylstyrene (0.42 mmol, 3 equiv) were added to the reaction mixture. The resulting reaction mixture was stirred overnight at 23 °C. The product was analyzed via ^1H NMR

(dichloromethane (10 μL) added as internal standard), which indicated formation of *cis*-epoxide (0.8%) and *trans*-epoxide (7%).

III.4.4 Crystallographic Data

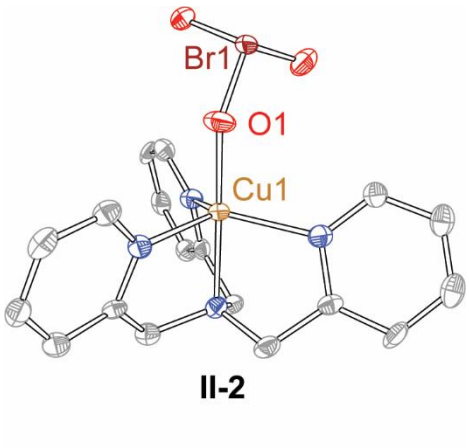

Figure III-20. Displacement ellipsoid plot of III-2 drawn at 50% probability. H-atoms and counter anion are removed for clarity. The crystalline sample used in this diffraction experiment was obtained by slow diffusion of diethyl ether into the acetone solution at 23 °C.

Table III-1. X-ray experimental details of III-2

Crystal data	
Chemical formula	$C_{18}H_{18}BrCuN_4O_3 \cdot ClO_4$
M_r	581.26
Crystal system, space group	Triclinic, $P\bar{1}$
Temperature (K)	100
a, b, c (Å)	9.4468(6), 14.4723(9), 15.792(1)
α, β, γ (°)	83.285(1), 80.507(1), 89.649(1)
V (Å^3)	2114.6(2)
Z	4
Radiation type	Synchrotron, λ = 0.41328 Å
μ (mm^{-1})	0.72
Crystal size (mm)	0.02 × 0.02 × 0.01
Data collection	
Diffractometer	Bruker
Absorption correction	Multi-scan SADABS2016/2 (Bruker,2016/2) was used for absorption correction. wR2(int) was 0.1097 before and 0.0813 after correction. The Ratio of minimum to maximum transmission is 0.8593. The λ/2 correction factor is Not present.
T_{min}, T_{max}	0.859, 1.000
No. of measured, independent and observed [I > 2s(I)] reflections	45899, 8155, 6474
R_{int}	0.066
(sin θ/λ)$_{max}$ (Å^{-1})	0.632
Refinement	
$R[F^2 > 2s(F^2)]$, $wR(F^2)$, S	0.047, 0.130, 1.06
No. of reflections	8155
No. of parameters	578
H-atom treatment	H-atom parameters constrained
Γ_{max}, Γ_{min} (e Å^{-3})	1.27, –1.38

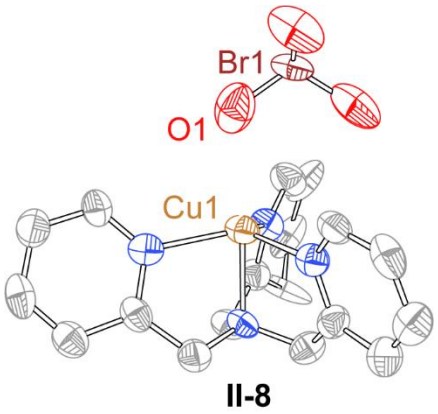

Figure III-21. Displacement ellipsoid plot of III-8 drawn at 50% probability. H-atoms and counter anion are removed for clarity. The crystalline sample used in this diffraction experiment was obtained by *in situ* photolysis of III-2 which resulted in the elongation of the Cu(1)–O(1) distance. Data was collected using synchrotron radiation (λ = 0.41328 Å) at 100 K. No restraints were used in the refinement.

Table III-2. X-ray experimental details of III-8

Crystal data	
Chemical formula	$C_{18}H_{18}BrCuN_4O_3 \cdot ClO_4$
M_r	581.26
Crystal system, space group	Triclinic, $P\bar{1}$
Temperature (K)	100
a, b, c (Å)	9.424(1), 14.590(2), 15.753(2)
α, β, γ (°)	84.606(2), 80.963(2), 89.819(2)
V (Å^3)	2129.5(4)
Z	4
Radiation type	Synchrotron, λ = 0.41328 Å
μ (mm^{-1})	0.72
Crystal size (mm)	0.02 × 0.02 × 0.01
Data collection	
Diffractometer	Bruker APEX-II CCD
Absorption correction	Multi-scan SADABS2016/2 (Bruker,2016/2) was used for absorption correction. wR2(int) was 0.0965 before and 0.0580 after correction. The Ratio of minimum to maximum transmission is 0.8552. The λ/2 correction factor is Not present.
T_{min}, T_{max}	0.636, 0.744
No. of measured, independent and observed [I > 2s(I)] reflections	13380, 4093, 3232
R_{int}	0.053
θ_{max} (°)	11.9
$(\sin \theta/\lambda)_{max}$ (Å^{-1})	0.499
Refinement	
$R[F^2 > 2s(F^2)]$, $wR(F^2)$, S	0.090, 0.276, 1.07
No. of reflections	4093
No. of parameters	577
H-atom treatment	H-atom parameters constrained $w = 1/[\sigma^2(F_o^2) + (0.1693P)^2 + 18.6438P]$ where $P = (F_o^2 + 2F_c^2)/3$
$\Delta\rho_{max}$, $\Delta_{\rho min}$ (e Å^{-3})	1.15, −1.38

Table III-3. Relevant X-ray metical parameters of III-2 and other Cu(II)(tpa) complexes that feature apical oxyanions.

Entry	$Cu–N_{pyridine}$ / Å	$Cu–N_{amine}$ / Å	Cu–O / Å	Ref.
III-2	2.072(4)	2.023(3)	1.951(3)	
$[Cu(tpa)NO_2]^+$	2.0741(3)	2.0399(2)	1.931(1)	303
$[(Cu(tpa))_2C_4O_4]^{2+}$	2.067(4)	2.005(4)	1.944(3)	304
$[(Cu(tpa))_2pyzdc]^{2+}$	2.0514(2)	2.0360(2)	1.9343(1)	305
$[(Cu(tpa))_2N_2O_2]^{2+}$	2.0678(2)	2.0572(2)	1.9114(1)	306
$[Cu(tpa)NO_2]^+$	2.076(6)	2.026(5)	1.935(6)	307
$[Cu(tpa)(BF)]^+$	2.071(2)	2.034(2)	1.932(2)	308

III.4.5 Computational Coordinates

Table III-4. X,Y,Z coordinates for the optimized geometry of III-8 computed as a singlet at the PBE0 level of theory with mod-LANL2DZ (Cu) and 6-31G(d,p) (light atoms) basis sets.

Atom	X	Y	Z
Cu	0.000284	0.000424	-0.89474
N	-1.6154	1.244599	-0.58532
N	1.88581	0.776376	-0.58521
N	-0.27055	-2.02092	-0.58525
N	-5.2E-05	0.000397	1.329712
C	-1.7631	1.605402	0.703055
C	-2.88123	2.30594	1.144384
H	-2.97298	2.56965	2.195162
C	-3.86718	2.66268	0.228629
H	-4.74768	3.211725	0.553126
C	-3.707	2.297796	-1.10392
H	-4.44904	2.549647	-1.85582
C	-2.56828	1.585744	-1.46105
H	-2.40613	1.270006	-2.48893
C	2.271832	0.724013	0.70325
C	3.437905	1.341464	1.14461
H	3.711924	1.289252	2.195459
C	4.24047	2.016074	0.228784
H	5.156477	2.50358	0.553289
C	3.844708	2.059585	-1.10387
H	4.434363	2.575598	-1.85583
C	2.658315	1.430191	-1.46103
H	2.303976	1.447577	-2.48896
C	-0.50893	-2.32899	0.703211
C	-0.55679	-3.64751	1.144751
H	-0.73908	-3.85863	2.195606
C	-0.37333	-4.67992	0.229076
H	-0.40877	-5.71693	0.553713
C	-0.13773	-4.359	-1.10358
H	0.014732	-5.12769	-1.85543
C	-0.09009	-3.01687	-1.4609
H	0.10213	-2.71875	-2.48886
C	-0.63118	1.26718	1.65341
H	0.135052	2.049213	1.552387
H	-0.99163	1.311382	2.695018
C	1.412489	-0.08658	1.653656
H	1.706389	-1.14127	1.552894
H	1.630944	0.203673	2.695218

CHAPTER IV

CHEMICAL NON-INNOCENCE OF PORPHYRIN FE NITRENES

IV.1. Introduction

The cytochrome P450 family of enzymes all feature a central heme unit that is responsible for catalyzing highly selective aerobic oxidation reactions under mild conditions to install C–O bonds in place of C–H bonds.[21, 309, 310] The identity of the reactive intermediate that installs these C–O bonds is a formally Fe(V) oxo complex (Compound I).[26, 309] Spectroscopic characterization of the critical reactive oxo indicate this species is best described as an Fe(IV) oxo complex supported by a singly oxidized porphyrin.[24] This formulation indicates *electronic* non-innocence of the supporting porphyrin ligand.

Cytochrome P450s are also competent catalysts for nitrene transfer chemistry and afford regio- and stereoselectivity unavailable to synthetic nitrene transfer catalysts. Dawson and Breslow first demonstrated that cytochrome P450 could be used to amidate C–H bonds, using iminoiodinanes as the nitrene precursor.[311] Furthering this chemistry, Fasan and Arnold independently demonstrated that engineered enzyme catalysts can efficiently mediate highly stereoselective intra- and intermolecular aminations of C–H and C=C bonds using cytochrome P450 and cytochrome P411, respectively.[312-315] In analogy to the metal oxo responsible for native hydroxylation activity (*i.e.* Compound I), cytochrome P450-catalysts nitrene transfer reactions have been hypothesized to proceed via the intermediacy of a Fe nitrenoid (Figure IV-1).[13, 316]

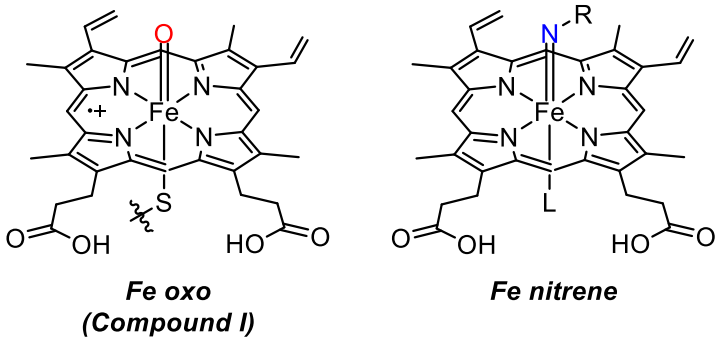

Figure IV-1. Comparison of both compound I and a Fe nitrene species generated in cytochrome P450.

Inspired by the activity of heme sites in P450s, metalloporphyrin complexes have been advanced as group-transfer catalysis in synthesis. Breslow and Groves demonstrated that this molecular complexes will catalyzed oxo and nitrene transfer to C–H bonds such as cyclohexane.[30, 61, 317] Similar to cytochrome P450, these transformations are hypothesized to occur from terminal metal oxos and metal nitrenes.[25, 34, 35, 62, 183, 318, 319]

While electronic (*i.e.*, redox) non-innocence has been widely studied and appreciated as operative in the reactive intermediates in these reactions, less appreciated is the potential for chemical non-innocence. Stoichiometric synthetic studies have shown that carbenes, nitrenes, and oxo ligands can insert into the M–L bond of the complexes to afford so-called tuck-in complexes (Figure IV-2).[320-339] While characterized, these species have not been investigated as potentially relevant to catalytic group transfer. Based on reports of redox-triggered reversible nitrene insertion into Fe-pyrrolide bonds and facile carbene insertion into Co porphyrin species (Figure IV-2),[340, 341] we have undertaken a study of the relevance of chemical non-innocence in nitrene transfer catalyzed by Fe porphyrin complexes.

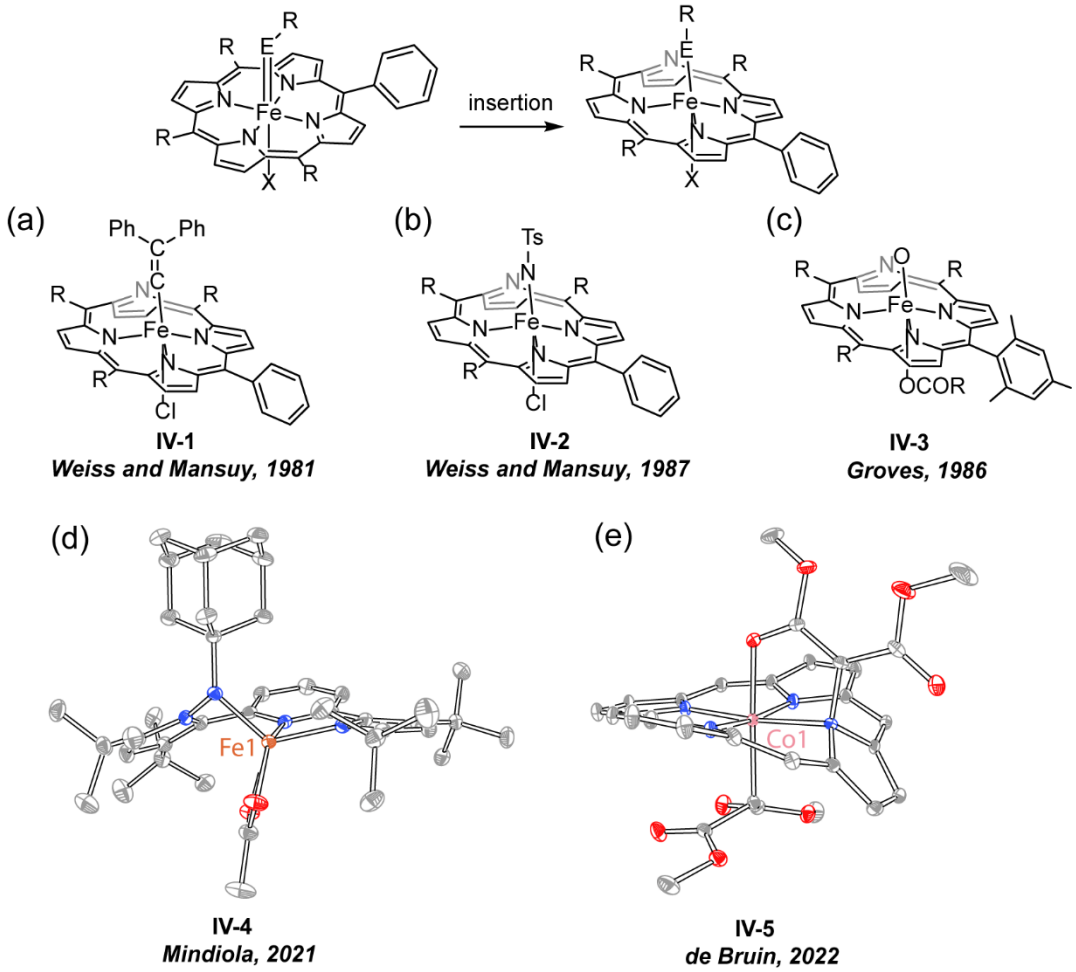

Figure IV-2. Transition metal complexes that feature chemically non-innocent supporting ligands. (a) Complex IV-1 arises from formal carbene insertion into an Fe–N bond in Fe(II)(tpp). Experimentally IV-1 was made by oxidizing Fe(II)tpp(C=CPh$_2$) by one electron. (b) Complex IV-2 arises from formal nitrene insertion into an Fe–N bond in Fe(tpp)Cl. Experimentally, IV-2 was made by adding Fe(tpp)Cl to a solution of PhINTs. (c) Complexs IV-3 arises from formal oxo insertion into an Fe–N bond in Fe(tmp)(MCPBA). Experimentally, IV-3 was made by thermolysis of Fe(III)(tmp)(MCPBA). (d) Fe(III) pyrrolide which features a N–Ad fragment inserted into an Fe–N bond. Disordered *t*-butyl and adamantyl groups removed for clarity. (e) Co(III) porphyrin carbene which features a carbene fragment bound to the pyrrole nitrogen. Phenyl and disordered enolate groups were removed for clarity.

Here we investigate the structure of Fe porphyrin catalysts during nitrene transfer catalysis. Specifically, we have focused attention of the potential that reversible nitrene

insertion into an N–N bond in **IV-6** is operative during catalysis in the presence of iminoiodinane nitrene transfer reagents. Stoichiometric studies show that complex **IV-7** will undergo N–N clevage to functionalize styrene under thermolytic conditions. Complex **IV-7** is also catalytically active, 5 mol% of **IV-7** in the presence of PhINTs will form aziridines from styrene, and sulfonamides from adamantane. Monitoring the Fe speciation during catalysis via EPR and ^{1}H NMR, we observe the resting state is **IV-7**. Isotopic labeling of tuck-in complex ^{14}N-**IV-7** and ^{15}N-PhINTs indicate that reversible nitrene extrusion of tuck in **IV-7** is not relevant to the catalytic aziridination of styrene. These results are consistent with amination from inserted a Fe(NTstpp)Cl nitrenoid (**IV-10**).

IV.2. Results

IV.2.1 Synthesis and Reactivity

Treatment of Fe(III)Cl(tpp) (**IV-6**) with excess PhINTs in CH_2Cl_2 affords FeCl(NTstpp) (**IV-7**).[320] Trituration of **IV-7** in MeOH provides analytically pure material in 53% yield. The ^{1}H NMR and UV-vis spectra of **IV-7** are in agreement with spectral data in the literature.[320]

Thermolysis of **IV-7** in the presence of excess styrene affords aziridine **IV-8**, where the mass balance of the NTs fragment is tosyl sulfonamide (23% yield, Figure IV-3a). The only Fe-containing product obtained from the thermolysis of **IV-7** is FeCl(tpp) (**IV-6**), which is observed in 100% yield. Importantly, no reaction was observed at room temperature. These observations are consistent with isomerization of FeCl(NTstpp) (**IV-7**) to Fe nitrenoid FeCl(tpp)(NTs) (**IV-10**) and group transfer from the transient nitrene.

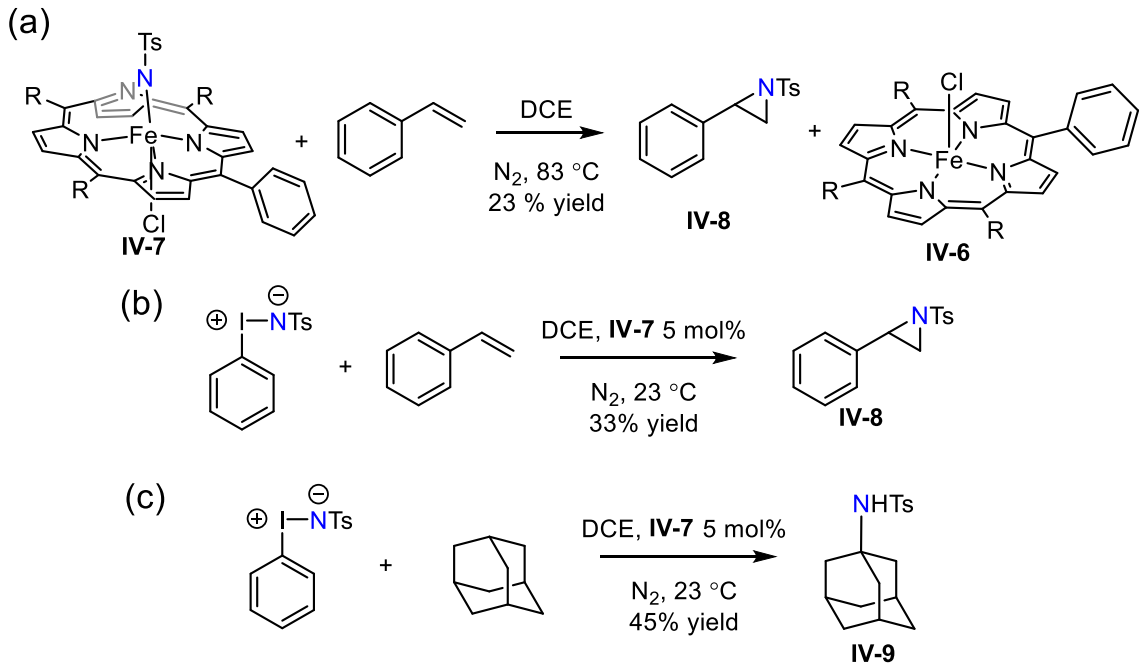

Figure IV-3. Reaction chemistry with IV-7. (a) Thermolysis of Fe(III) tuck-in complex IV-7 at 83 °C in DCE with excess styrene results in aziridine IV-8 in 23% yield. (b) Implementation of IV-7 as a catalyst (5 mol %) affords aziridine IV-8 in 33% yield. (c) Complex IV-7 serves as a C–H insertion catalyst (5 mol%) which affords sulfonamide IV-9 in 45% yield.

After demonstrating the N–N cleavage from complex **IV-7** results in the products of nitrene transfer, we sought to evaluate the potential for nitrene transfer catalysis by **IV-7**. Treatment of styrene with PhINTs in the presence of **IV-7** (5 mol%) afforded aziridine **IV-8** in 33% yield at 23 °C. Complex **IV-7** is also a competent catalyst for C–H amination: Treatment of adamantane with PhINTs in the presence of **IV-7** (5 mol%) affords sulfonamide **IV-9** in 45% yield. Of note, when FeCl(tpp) **IV-6** is used in place of **IV-7**, the same yields are observed for both aziridination and C–H amination, which indicates the chemical competence of **IV-6** as a catalyst for nitrene transfer.

IV.2. 2 Spectroscopic Characterization of the Fe Porphyrin.

With evidence for the chemical competence of nitrene de-insertion of **IV-7** to provide the products of nitrene transfer and the catalytic competence of **IV-6** in olefin aziridination and C–H amination, we sought to define the potential role of nitrene insertion/de-insertion chemistry on nitrene transfer catalysis. Fe complexes **IV-6** and **IV-7** are distinguishable by X-band EPR spectroscopy; whereas compound **IV-6** features a peak at 1180 G, compound **IV-7** features a peak at 1560 G as shown in Figure IV-4. Monitoring the aziridination of styrene with PhINTs in the presence of **IV-6** (5 mol%) indicates that while Fe(tpp)Cl is used as catalyst, at 1 h the only Fe-containing species detected is **IV-7**. Further monitoring of the reaction via EPR shows that nitrene de-insertion to regenerate Fe(tpp)Cl begins to be observed at 48 h and is complete by the 72 h time point. ^{1}H NMR of each timepoint shows that aziridine formation starts quickly and is complete by 12 h (Figures IV-5 and IV-6). Together, these data indicate that rapid conversion of Fe(tpp)Cl generates **IV-7**, which is the resting state of catalysis, and that nitrene de-insertion to regenerate **IV-6** is slow relative to catalyst turnover.

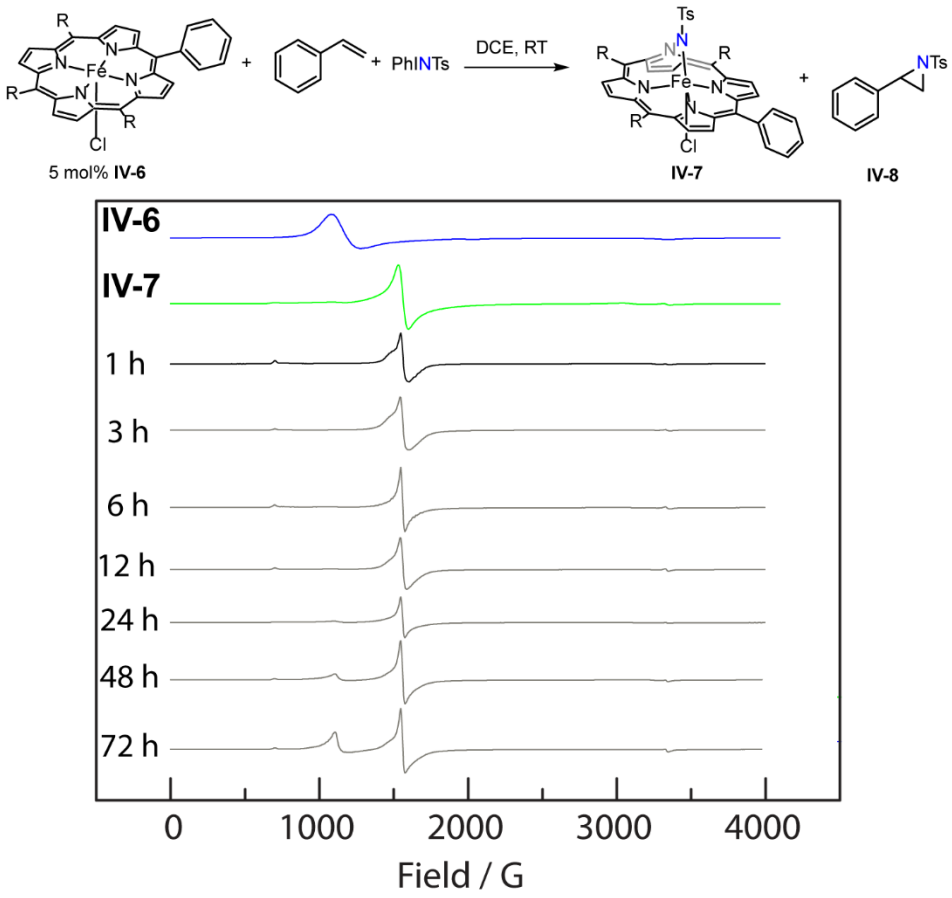

Figure IV-4. Monitoring the Fe speciation in the reaction between IV-6 and PhINTs in the presence of styrene via cryogenic X-band EPR. IV-6 (—) was used as 5 mol% catalyst with PhINTs in the presence of styrene. The reaction at 1 h (—) features a signal centered at 1600 G, which is well-matched to the EPR signal of IV-7 (—). Time-resolved EPR spectra show that the Fe speciation is comprised of solely IV-7 until 48 h, where a small peak at 1100 G starts to grow in, which is attributed to IV-6 (—). The peak at 1100 G continues to grow at the 72 h timepoint.

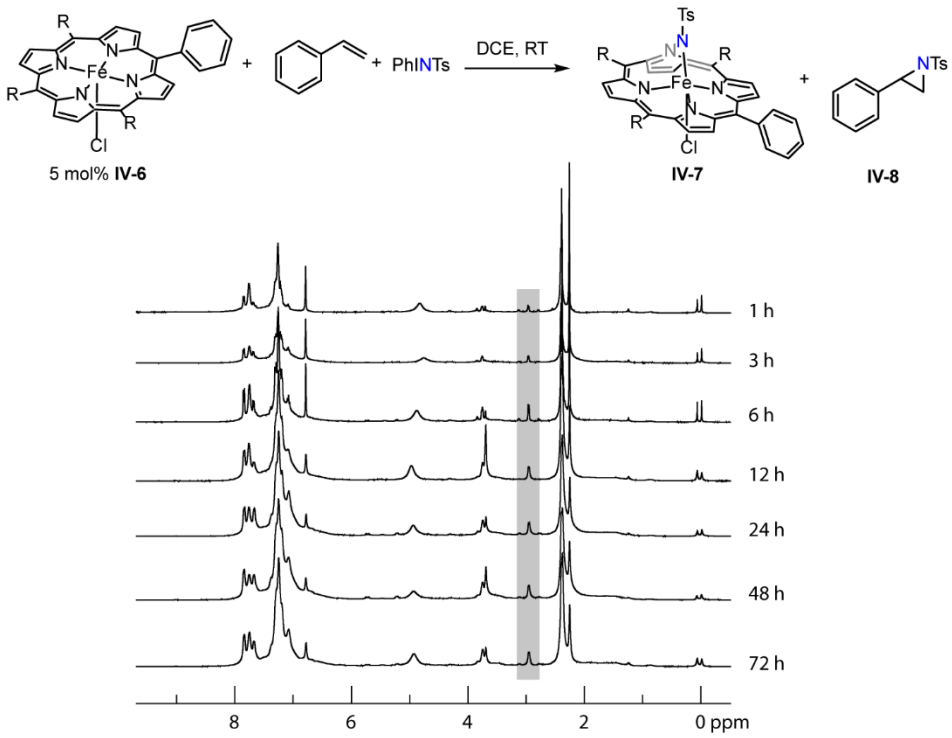

Figure IV-5. ^{1}H NMR spectra monitoring the yield of aziridine IV-8 over time. The peak highlighted at 2.95 ppm was used to track the yield of aziridine formation, measured against an internal standard of mesitylene (2 μL). Aziridine formation stopped after 12 h.

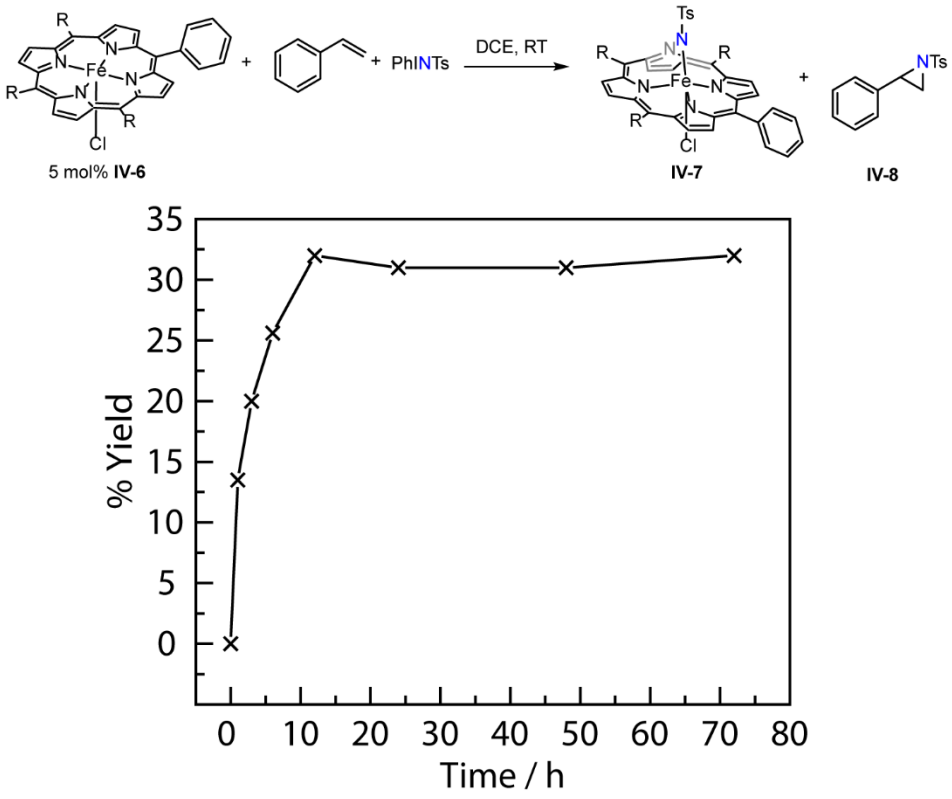

Figure IV-6. Plot of aziridine formation over time, determined by ^{1}H NMR spectroscopy.

To further evaluate the potential for reversible nitrene insertion/de-insertion under catalytic conditions we designed an isotope labeling experiment in which aziridination of styrene was carried out using ^{14}N-FeCl(NTs(tpp)) was used in conjunction with ^{15}N-PhINTs. The incorporation of ^{14}N versus ^{15}N was monitored via ESI-MS analysis of the resulting aziridine, which revealed 99.4% incorporation of ^{15}N into aziridine **IV-8** (Figure IV-7). Similar to aziridine **IV-8**, the C–H insertion of adamantane was also performed with ^{14}N-**IV-7** and ^{15}N-PhINTs, which also showed 99.6% ^{15}N-**IV-9** via ESI-MS (Figure IV-7). These data indicate that N–N cleavage is not kinetically competitive on the timescale of *N*-group transfer, and tuck-in porphyrin **IV-7** is the active catalyst, not **IV-6**.

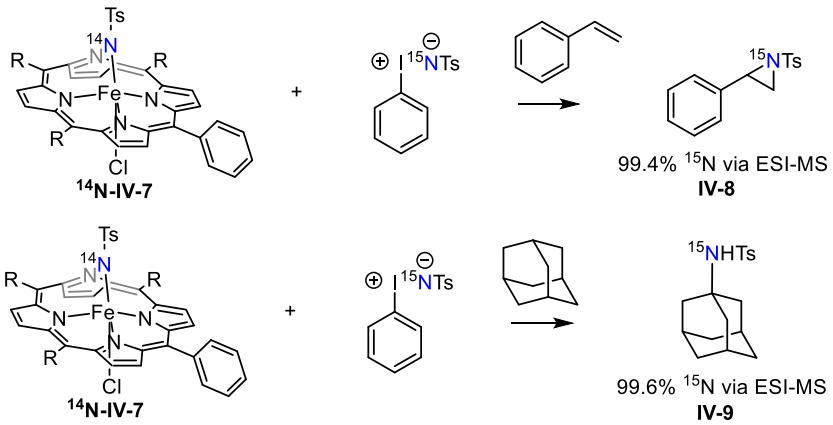

Figure IV-7. Utilization of ^{14}N-IV-7 in the presence of ^{15}N-PhINTs results in near complete incorporation of ^{15}N into the product. ^{14}N vs ^{15}N incorporation was monitored via ESI-MS.

IV.3. Discussion and Future Directions

Characterization of the active species involved in C–H catalysis is predicated on understanding the chemical identity of the catalyst. Previous work concerning Fe porphyrin catalyzed C–H and C=C insertion has not considered the chemical non-innocence of the porphyrin ring itself. We have shown via EPR and ^{1}H NMR spectroscopy that the resting state of the catalysis is **IV-7**, and that N–N cleavage is not operative on the timescale of nitrene transfer. Further, we have shown via isotope labeling that the *N*-tosyl of **IV-7** does not insert into substrate under catalytic conditions, and the *N*-tosyl fragment comes from the added PhINTs reagent. Thus, we conclude that N–N cleavage is not operative under catalytic conditions, and the active C–H insertion catalyst is a tucked-in Fe nitrene which is pictured in Figure IV-8.

Several porphyrin-supported *bis*-nitrenoid species or nitrenoid iminoiodinane adducts have been proposed to be the active oxidants in their respective C–H insertion

chemistry. Goldberg and coworkers have shown that a terminal Mn(V) corrolazine oxo will not insert into C–H bonds, and only when a Mn(V) oxo iodosylbenzene adduct forms, will OAT occur.[342] Abu-Omar and coworkers have also found a similar reaction, where an unreactive Mn(V) imido forms an adduct with a iminoiodinane, which then transfers the NR fragment which was bound to the iodine (Figure IV-8b).[104] Che has proposed similar structures regarding a perfluorinated porphyrin supported Fe nitrenoid, where they propose that the active NR transfer reagent is a Fe nitrenoid iminoiodinane adduct and is supported by ESI-MS and computational studies (Figure IV-8b).[343] However, the chemical non-innocence of the porphyrin ring was not considered in Che's study, where a tucked-in Fe iminoiodinane adduct would have the same ESI-MS signal as a Fe nitrenoid iminoiodinane adduct. Zhang and de Bruin have characterized a porphyrin supported Co(III) bis-nitrenoid via EPR, UV-vis, XAS, and ESI-MS, however the reactivity of this species has yet to be investigated (Figure IV-8b).[35]

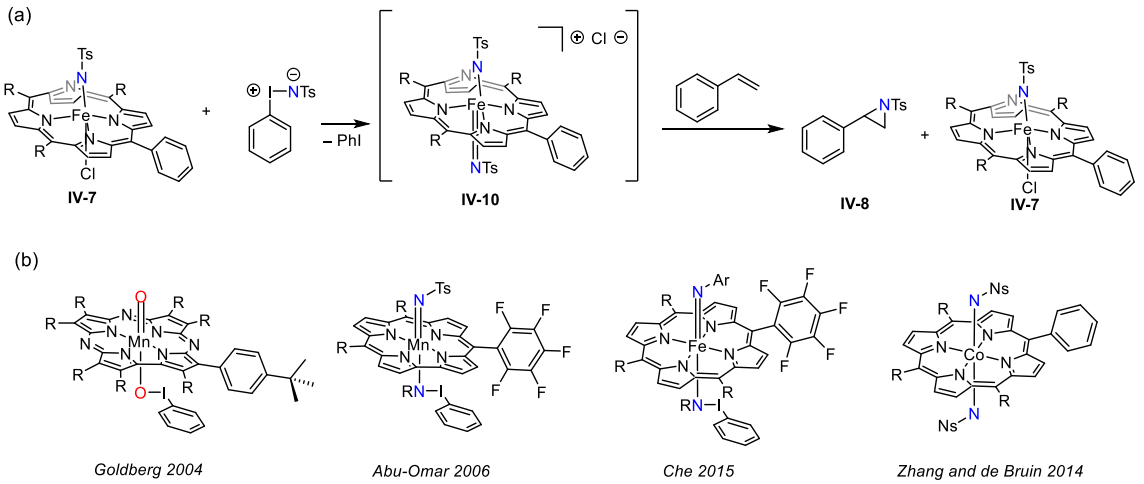

Figure IV-8. Proposed intermediates in C–H amination chemistry with IV-7 and the literature precedents. (a) Exposure of Fe tuck-in IV-7 to PhINTs makes putative Fe nitrenoid IV-10, which then transfers the *N*-tosyl fragment which was bound initially to PhINTs. (b) Proposed oxo and nitrenoid transfer reagents, which feature either a terminal nitrenoid hypervalent iodine adduct, or a bis-nitrenoid.

With the characterization data of complex **IV-7** in hand, and considering the precedent in the literature, we propose the catalytic cycle pictured in Figure IV-9. First, we propose that porphyrin **IV-6** and 2 equivalents of PhINTs forms Fe tuck-in iminoiodinane complex **IV-11**. Upon loss of iodobenzene and introduction of styrene, radical addition from the Fe nitrenoid to styrene forms intermediate **IV-12**. Subsequent radical cyclization generates the aziridine, which will then disassociate to afford complex **IV-13**. The cycle is completed once another molecule of PhINTs binds to **IV-7**, forming **IV-11**.

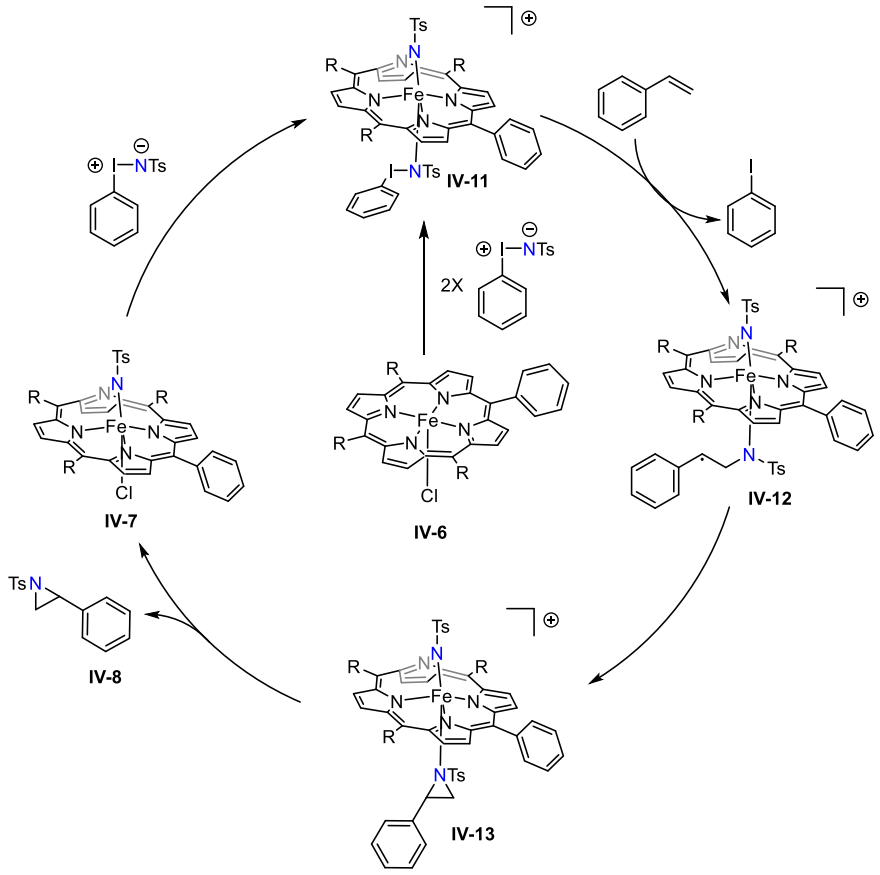

Figure IV-9. Proposed catalytic cycle of the aziridination of styrene via IV-7. Fe(tpp)Cl (IV-6) reacts with two equivalents of PhINTs to form tucked-in Fe iminoiodinane complex IV-11. Complex IV-11 reacts with one equivalent of styrene to form an aziridine and returns complex IV-7.

Future studies will be focused on elucidating the generality of porphyrin chemical non-innocence. We anticipate that use of both organic azides and hydroxyamines will also insert into the Fe–N bond, resulting in complexes similar to **IV-7**.[31, 67, 68] We will investigate if these tucked-in Fe porphyrin species participate in C–H insertion catalysis. The results of these molecular studies provide the spectroscopic markers needed to elucidate the structures of metal-binding sites in enzyme catalyzed processes. Based on

the successes herein, we envision that cryogenic EPR will be provide insight to differentiate the different Fe species *in situ*.

IV.4. Experimental Details

IV.4.1 General Considerations

Materials Solvents were obtained as ACS reagent grade. Unless otherwise noted, all chemicals and solvents were used as received. Benzaldehyde, styrene, and dichloroethane were obtained from Bean Town Chemical. Tosyl chloride was obtained from Alfa Aesar. Pyrrole was obtained from TCI America. Tosyl amine was obtained from Sigma Aldrich. Iodobenzene diacetate and adamantane were purchased from Acros. Potassium hydroxide and potassium bicarbonate were purchased from VWR Chemicals. Iron(II) chloride tetrahydrate was purchased from Fisher Scientific. ^{15}N-ammonium chloride was obtained from Cambridge Isotope Laboratories. NMR solvents were purchased from Cambridge Isotope Laboratories and were degassed via three freeze-pump-thaw cycles. All NMR solvents were stored over 4 Å molecular sieves. Anhydrous dichloromethane was obtained from a drying column and stored over activated molecular sieves. All reactions were carried out at 23 °C unless otherwise noted. H_2TPP[243] and PhINTs[344] were prepared according to literature methods.

Characterization Details NMR spectra were recorded on Bruker Avance NEO 400 NMR operating at 400.09 MHz for ^{1}H acquisitions and were referenced against solvent signals: $(CD_3)_2SO$ (2.50 ppm, ^{1}H) and $CDCl_3$ (7.26 ppm, ^{1}H).[248] ^{1}H NMR data are reported as follows: chemical shift (δ, ppm), multiplicity (s (singlet), d (doublet), t (triplet), m (multiplet), br (broad), integration. X-band EPR spectra were recorded on a Bruker

ELEXSYS Spectrometer with a cryogen-free in-cavity temperature control system. ESI-MS data was obtained using either Orbitrap Fusion™ Tribrid™ Mass Spectrometer or Q Exactive™ Focus Hybrid Quadrupole - Orbitrap™ Mass Spectrometer from Thermo Fisher Scientific.

IV.4.2 Synthesis and Characterization

Synthesis of FeCl(NTsTPP) IV-7

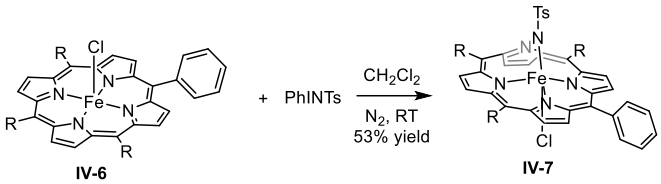

IV-7 was prepared according to the following modification of literature methods.[320] Under an N_2 atmosphere a 1-L round-bottom flask was charged with FeCl(tpp) (0.502 g, 0.713 mmol, 1.00 equiv), PhINTs (1.07 g, 2.77 mmol, 3.88 equiv), and CH_2Cl_2 (70 mL). The resulting reaction mixture was stirred at 23 °C for 25 min. Pentane (450 mL) was added slowly, resulting in a red precipitate. The obtained precipitate was isolated by vacuum filtration and washed with pentane. A 20-mL scintillation vial was charged with the resulting precipitate and MeOH (10 mL) and was allowed to stir vigorously for 10 min, resulting in a purple precipitate. The obtained precipitate was isolated by vacuum filtration and washed with cold MeOH and dried *in vacuo* to afford the title compound as a purple solid (0.330 g, 53% yield). ^{1}H NMR (δ, 23 °C, $CDCl_3$): 89.0 (br s, 2H), 84.1 (br s, 2H), 81.5 (br s, 2H) 14.4 (br s, 2H), 13.7 (br s, 2H), 12.7 (s, 2H), 11.3 (s, 2H), 10.9 (s, 2H), 10.4 (s, 2H), 6.9 (s, 2H), 6.1 (s, 4H), 4.0 (s, 4H), 2.5 (s, 3H), –28.4 (br s, 2H). Spectral data are well-matched to those reported in the literature.

Synthesis of ^{15}N-tosyl Amine

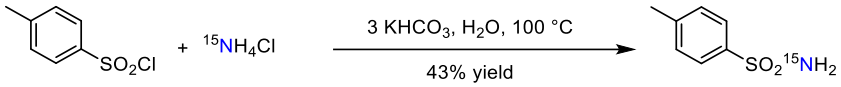

Na[^{15}NTsCl] was prepared according to the following three-step procedure, which is modified from literature methods.[345] A 25-mL round-bottom flask was charged with *p*-toluenesulfonyl chloride (0.729 g, 3.80 mmol, 1.82 equiv), $^{15}NH_4Cl$ (0.115 g, 2.10 mmol, 1.00 equiv), and distilled water (10 mL). The reaction mixture was heated at 50 °C and $KHCO_3$ (0.635 g, 6.40 mmol, 3.05 equiv) was added. The reaction mixture was then refluxed at 100 °C for 10 h. The reaction mixture was cooled to 0 °C for 2 h at which time a white precipitate was observed. The obtained precipitate was isolated by vacuum filtration, washed with cold water, and dried *in vacuo* to obtain ^{15}N-tosyl amine as white solid (0.155 g, 43% yield). ^{1}H NMR (δ, 23 °C, $CDCl_3$): 7.82 (d, J = 9 Hz, 2H), 7.33 (d, J = 6 Hz, 2H), 4.73 (d, J = 81 Hz, 2H), 2.44 (s, 3H). Spectral data are well-matched to those reported in the literature.

Synthesis of ^{15}N-PhINTs

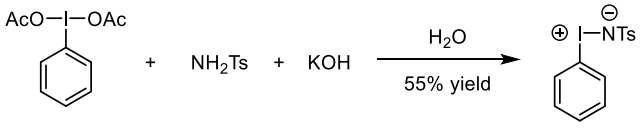

This compound was prepared according to the following modification of literature methods.[344] Under an N_2 atmosphere 100-mL Schlenk tube was charged with ^{15}N-tosyl amine (0.199 g, 0.00116 mmol, 1.00 equiv) potassium hydroxide (0.178 g, 0.00318 mmol, 2.74 equiv) and methanol (2 mL). Iodobenzene diacetate (0.412 g, 0.00128 mmol, 1.10 equiv) was added slowly at 0 °C and the reaction was let stir for 1 h at this temperature.

The resulting solution was let stir at 23 °C for 1 h. To this resulting solution ice water (15 mL) was added and the resulting solution was sonicated, upon which a white solid was obtained. The solid was isolated via filtration, washed with MeOH (5 mL), and dried *in vacuo* to afford 0.230 g of ^{15}N-PhINTs (53% yield). ^{1}H NMR (δ, 23 °C, $((CD_3)_2SO)$: 7.70 (d, 2H), 7.45 (d, 3H), 7.30 (t, 2H), 7.07 (d, 2H), 2.28 (s, 3H). Spectral data are well-matched to those reported in the literature.

IV.4.3 Reaction Details

Aziridination of Styrene

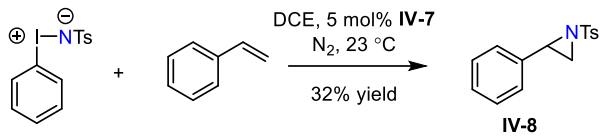

Under a N_2 atmosphere, a 25-mL Schlenk tube was charged with **IV-7** (0.0074 g, 0.0085 mmol, 1 equiv), styrene (0.063 g, 0.61 mmol, 72 equiv), PhINTs (0.077 g, 0.20 mmol, 24 equiv), and dichloroethane (2 mL). The reaction mixture was stirred at 23 °C overnight. The resulting reaction mixture was concentrated *in vacuo*, resulting in a dark red solid. The product was analyzed via ^{1}H NMR (mesitylene (2 μL) added as internal standard), which indicated formation of aziridine **IV-8** (32%).

Amination of Adamantane

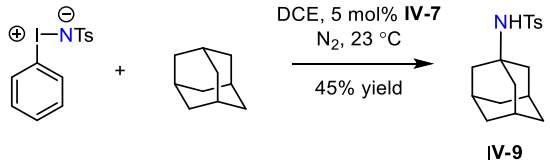

Under a N_2 atmosphere a 25-mL Schlenk tube was charged with **IV-7** (0.0090 g, 0.010 mmol, 1 equiv), adamantane (0.080 g, 0.58 mmol, 58 equiv), PhINTs (0.078 g, 0.21 mmol,

21 equiv), and dichloroethane (2 mL). The reaction mixture was stirred at 23 °C overnight. The resulting reaction mixture was concentrated *in vacuo*, resulting in a dark red solid. The product was analyzed via ^{1}H NMR (mesitylene (2 μL) added as internal standard), which indicated formation of sulfonamide **IV-9** (42%).

IV.4.4 In Situ ^{1}H NMR and EPR Details

General Procedure for Monitoring Fe Speciation During Catalysis

Under a N_2 atmosphere, a 25-mL Schlenk tube was charged with **IV-7** (0.0074 g, 0.0085 mmol, 1 equiv), styrene (0.063 g, 0.61 mmol, 72 equiv), PhINTs (0.077 g, 0.20 mmol, 24 equiv), and dichloroethane (2 mL). The reaction mixture was stirred at 23 °C for the appropriate time. An aliquot was removed from the reaction mixture and was analyzed via X-band EPR, which indicated the ratio of **IV-7** to **IV-6**. The remaining solution was concentrated *in vacuo*, resulting in a dark red solid. This product was analyzed via ^{1}H NMR (mesitylene (2 μL) added as internal standard), which indicated formation of sulfonamide **IV-9**.

CHAPTER V

STRUCTURAL CHARACTERIZATION OF A CU NITRENOID

V.1. Introduction

In a seminal study, Kwart and Khan demonstrated the utility of copper catalyzed C–H insertion of cyclohexane using sulfonyl azides as a nitrenoid source.[58, 59] Since then, copper catalyzed C–H and C=C transformations, which are hypothesized to proceed through a Cu nitrenoid intermediate, have become ubiquitous.[346-348] Despite the utility of Cu nitrenoids in synthesis, only a few systems have been either spectroscopically or structurally characterized.[349-351] Warren and coworkers have structurally characterized several Cu nitrenoid complexes (**V-1**, **V-2**, and **V-3**), which will disassociate in solution to form a terminal Cu nitrenoid and subsequently react with C–H bonds (Figure V-1).[237, 352-354] Lancaster and Betley structurally characterized the first monomeric terminal Cu nitrene (**V-4**). These structures feature a high degree of steric bulk about the Cu–N bond, which suppress bimolecular reaction chemistry, and the characterized structure is thus not reactive with C–H bonds or olefins (Figure V-1).[60] While these structures can provide new structural insights into copper nitrenes, they do not participate in the chemistry of interest and thus delineation of the structure-activity relationships that are critical to the rational design of new catalyst systems has not been possible.

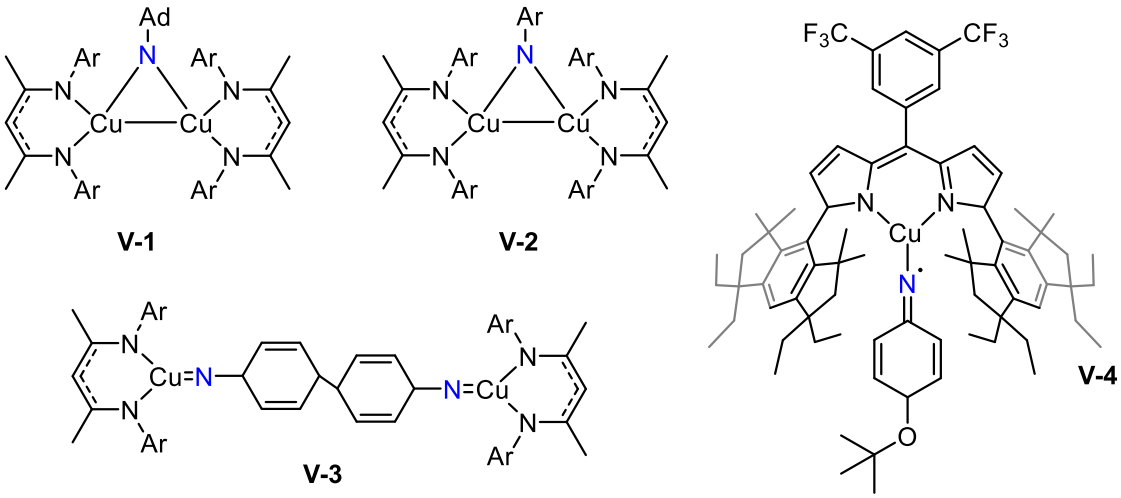

Figure V-1. Structurally characterized Cu nitrenoid complexes. Complexes V-1 and V-2 are dimeric bis-Cu nitrenoid complexes, which will disassociate in solution to afford reactive terminal Cu nitrenoid fragments. Similarly, V-3 is a dimeric terminal Cu nitrenoid, which will disassociate to form a reactive monomeric Cu nitrenoid. Terminal monomeric Cu nitrene V-4 features substantial steric bulk about the Cu–N bond, which precludes any C–H functionalization reactivity.

We have been interested in direct structural characterization of transient intermediates involved in C–H functionalization reactions via *in crystallo* photosynthesis.[287, 288] We have demonstrated that α-bound organic azide adducts of Rh centers serve as potent photoprecursors for Rh nitrenes, which has enabled the direct structural characterization of triplet nitrene Rh adducts.[200, 201] However, the poor Lewis basicity of organic azides makes them weakly coordinating ligands and thus easily displaced by coordinating solvent or substrates containing heteroatoms. In chapter II, we demonstrated that dissolution of *N*-haloamide Mn porphyrins in 2-Me-THF facilitated the characterization cryogenic UV-vis and EPR spectroscopies. This technique is unavailable in the Rh azide chemistry, due to 2-Me-THF displacement of the organic azide.

Here, we present a family of Cu(II) complexes featuring α-bound organic azide ligands in which a pyridine tether renders these complexes stable in coordinating solvents. This family of complexes is comprised of both mono- and bis-azide adducts with inner-sphere Cl and OTf ligands and are fully characterized in both solution phase and solid-state. These complexes are photoactive in the solution phase and solid-state, where prolonged photolysis ultimately yield Cu imine complexes via intramolecular HAT. Photolysis *in crystallo* at 100 K results in photopromoted extrusion of N_2 and furnishes both a formal Cu(III) iminyl radical and also a Cu(II) bis-imine, depending on the identity of inner sphere ligand used. These observations establish the utility of tethered organic azide complexes and their stability in coordinating solvents. Furthermore, these structures provide a complete snapshot of the N_2 loss and H-atom migration pathway that underpins the reaction chemistry of alkyl azides.

V.2. Results

V.2.1 Coordination Chemistry of Cu(II) with Pyridyl Azide Ligands

Complexes **V-6** and **V-7** were prepared according to the following modification of literature methods.[355] Titration of $CuCl_2$ with 2-(azidomethyl)pyridine (**V-5**) in MeOH resulted in sequential formation of two Cu azide adducts: ($CuCl_2$(2-(azidomethyl)pyridine))$_2$ (**V-6**) and $CuCl_2$(azidomethyl)pyridine)$_2$ (**V-7**) (Figure V-2 and V-3). Concentration-dependent UV-vis spectra display isosbestic points connecting $CuCl_2$ and **V-6** at 0-0.029 M [**IV-5**] and isosbestic points connecting **V-6** and **V-7** at 0.029-0.29 M [**V-5**] indicating the absence of steady-state intermediates in these reactions (Figures V-2 and V-3). The UV-vis spectrum of **V-6** displays an absorbance at 816 nm ($\varepsilon = 136$ M^{-}

$^{1}cm^{-1}$) and **V-7** displays an absorbance at 690 nm (ε = 144 $M^{-1}cm^{-1}$) (Figures V-2 and V-3). The infrared (IR) spectrum of **V-6** displays υ_{N3} at 2240 and 2167 cm^{-1} and **V-7** displays υ_{N3} at 2134 and 2101 cm^{-1}. Neither **V-6** or **V-7** display ^{1}H NMR features.

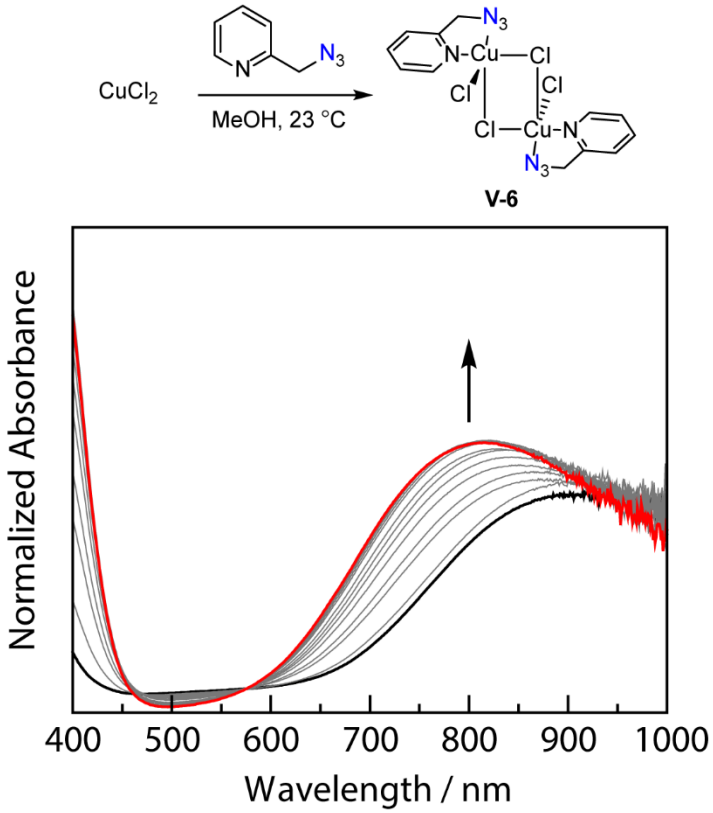

Figure V-2. UV-vis spectra obtained during titration of $CuCl_2$ with V-5. Treatment of $CuCl_2$ with **V-5**, results in formation of $CuCl_2$(2-(azidomethyl)pyridine) **V-6**. Spectra were collected in MeOH at 23 °C. The UV-vis spectra were collected at [**V-5**] of 0-0.029 M. The well-anchored isosbestic points at 466 nm and 574 nm indicate the absence of steady-state intermediates in the conversion of $CuCl_2$ (—) to **V-6** (—).

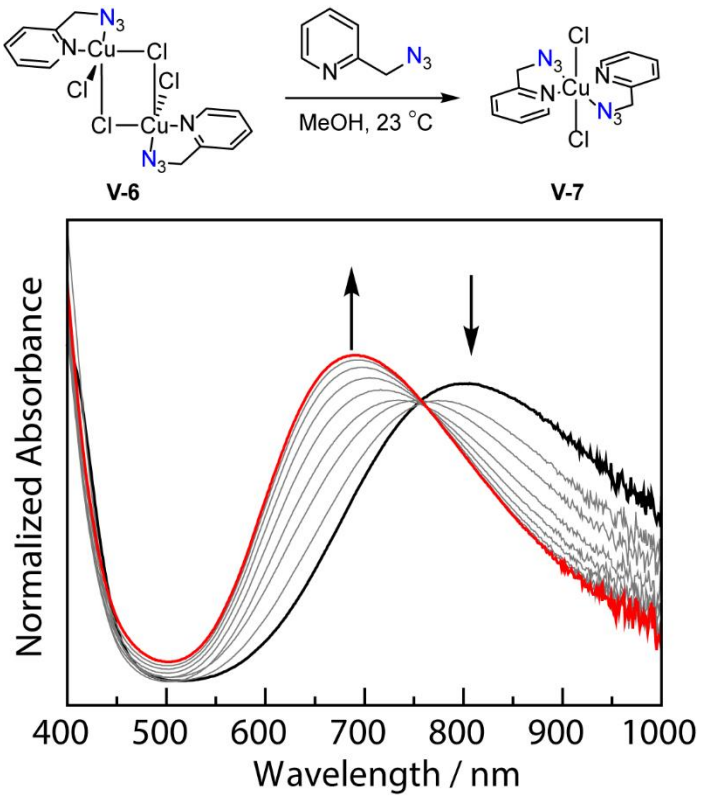

Figure V-3. UV-vis spectra obtained during titration of V-6 with V-5. Treatment of V-6 with V-5, results in formation of $CuCl_2$(2-(azidomethyl)pyridine)$_2$ **V-7**. Spectra were collected in MeOH at 23 °C. The UV-vis spectra were collected at [**V-7**] of 0.029-0.29 M. The well-anchored isosbestic point at 757 nm indicates the absence of steady-state intermediates in the conversion of **V-6** (—) to **V-7** (—).

Cu complexes **V-6** and **V-7** are only soluble in MeOH and cannot be redissolved once crystallized. Thus, we sought to use $Cu(OTf)_2$ as a more soluble Cu(II) source. Exposure of $Cu(OTf)_2$ to MeCN solutions of **V-6** resulted in formation of one Cu azide adduct: $Cu(OTf)_2(PyN_3)_2$ (**V-8**) (Figure V-4). The UV-vis spectrum of **V-8** displays an absorbance at 698 nm (ε = 61.6 $M^{-1}cm^{-1}$) The infrared (IR) spectrum of **V-8** displays υ_{N3} at 2161 and 2105 cm^{-1}. **V-8** is ^{1}H NMR silent.

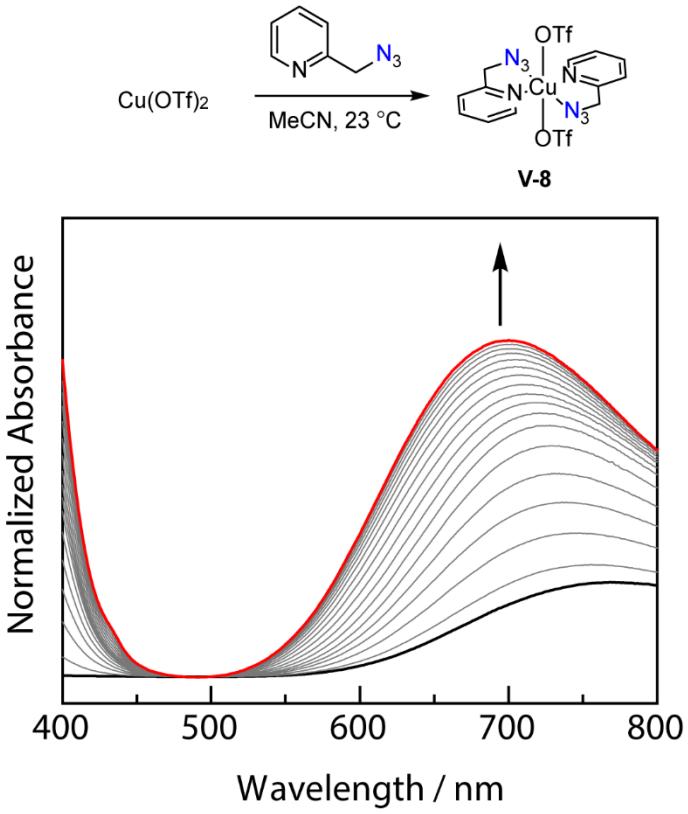

Figure V-4. UV-vis spectra obtained during titration of $Cu(OTf)_2$ with V-5. Treatment of $Cu(OTf)_2$ with 2-(azidomethyl)pyridine **V-5**, results in formation of $Cu(OTf)_2(PyN_3)_2$ **V-8**. Spectra were collected in MeCN at 23 °C. The UV-vis spectra were collected at [**V-5**] of 0-0.0634 M in the conversion of $Cu(OTf)_2$ (—) to **V-8** (—).

Single-crystals of **V-6** and **V-7** were obtained via ether vapor diffusion into a saturated MeOH solution of $CuCl_2$ and **V-5**, at the respective concentration. Solid-state structures of **V-6** and **V-7** are collected in Figure V-5 and the relevant refinement data are collected in Section V.5.3. All metrical parameters are well matched to the reported structure.[355]

Single crystals of **V-8** were obtained via vapor diffusion of Et_2O into a saturated MeCN solution of $Cu(OTf)_2$ and **V-5**. The solid-state structure of **V-8** is collected in Figure V-5 and the relevant refinement data are collected in Section V.5.3. The Cu(II)

center of **V-8** is 6-coordinate and is approximately octahedral. Two 2-(azidomethyl)pyridine ligands occupy the four equatorial sites with the azide moieties trans to each other, where Cu(1)–N(1) = 2.1034(2) Å and Cu(1)–N(2) = 1.9837(2) Å. The two apices are occupied by triflate groups where Cu(1)–O(1) = 2.3252(1) Å. Comparison of the Cu(1)–N(1) distance to other reported Cu(II)–N α-bound organic azide complexes in a pseudo-octahedral ligand field shows a relatively short Cu(1)–N(1) bond distance in **V-8** (Table V-1). For example, the Cu(1)–N(1) distance in $Cu(NO_3)_2$(**V-5**)$_2$ is 2.398(1) Å and changing the apical ligand to triflate in **V-8** results in a contraction of ~0.3 Å. We hypothesize that the Cu(1)–N(1) bond length is short in comparison of **V-7** due to the enhanced Lewis acidity from OTf being a weaker donor.

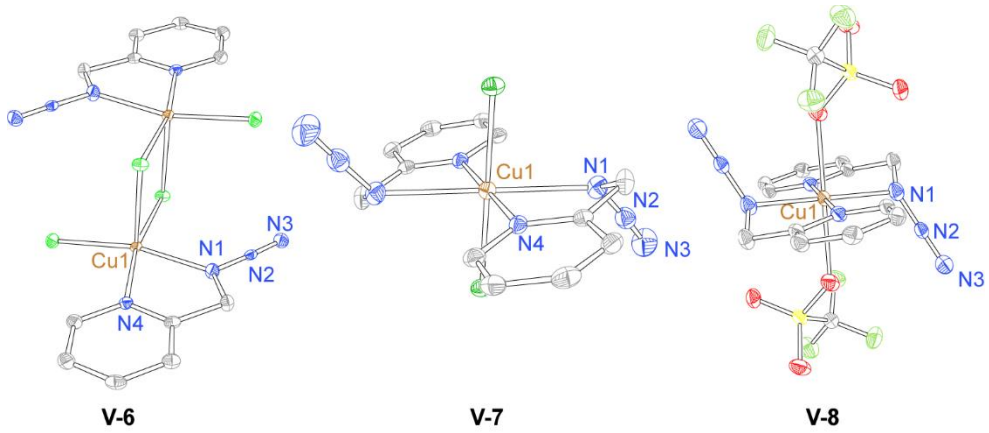

Figure V-5. Displacement ellipsoid plots of the Cu azide complexes. H-atoms have been omitted for clarity. Ellipsoids drawn at 50% probability. Selected bond lengths (Å): V-6, Cu1–N1 = 2.043(2); V-7, Cu1–N1 = 2.413(3); V-8, Cu1–N1 = 2.1034(2).

Table V-1. Comparison of Cu–N distances in crystallographically characterized Cu(II) α-bound organic azide complexes.

Complex	Cu–N / Å
V-6	2.043(2)
V-7	2.413(3)
V-8	2.1034(2)
$Cu(NO_3)_2$(**V-5**)$_2$	2.398(1)[355]
$CuCl_2(PyEtN_3)$	2.2008(2)[356]
$CuCl_2(Py(MeN_3)_2)$	2.0996(2)[355]
$Cu(NO_3)_2(Py(MeN_3)_2)$	2.0415(1)[355]
$Cu(hfac)_2(N_3TEMPO)$	2.5545(2)[357]
Cu(azidocyclohexylpyrazole)	2.079(2)[358]
$Cu_3Gd_2(hfac)_8(OH)_4(N_3TEMPO)$	2.656(6)[359]
$Cu_3Dy_2(hfac)_8(OH)_4(N_3TEMPO)$	2.663(6)[359]
$Cu_2(OAc)_4$(azidopropanoate)$_2$	2.2195(1)[360]

V.2.2 Photolysis of Cu Azide Complexes

To test the competency of Cu complexes **V-6**, **V-7**, and **V-8** as potential Cu nitrenoid precursors, steady state photolysis of optically dilute solutions of each of these complexes was performed. Here, only the photochemistry of complex **V-6** will be discussed, as the photochemistry is representative of all three complexes. Photolysis of dilute a MeOH solution of **V-6** (335 nm < hν) was monitored by UV-vis spectroscopy and resulted in new spectral features that are accessed via well-anchored isosbestic points at 457 and 764 nm (Figure V-6). *In situ* IR analysis of a photolyzed KBr pellet of **V-6**, indicates both facile loss of N_2, and formation of Cu imine **V-10** (Figure V-9). To verify the identity of the final product in the photolysis, single-crystals of **V-6** were photolyzed in a pentane suspension and subsequent dissolution and crystallization of the solid-state reaction mixture from MeOH afforded a single crystal of Cu amine **V-9** (Figure V-12).

Compound **V-9** can be envisioned as arising from N_2 loss to generate a nitrenoid (**V-15**), which then subsequently rearranges to an imine (**V-11**), which then undergoes nucleophilic addition from MeOH to afford Cu-bound hemiaminal ether **V-9** (Figure V-16). The observed structure is consistent with the known low-temperature rearrangement of alkyl nitrenes.[361] The data from the solution-phase and solid-state photolyses of **V-7** and **V-8** are collected in Figures V-7-V-11.

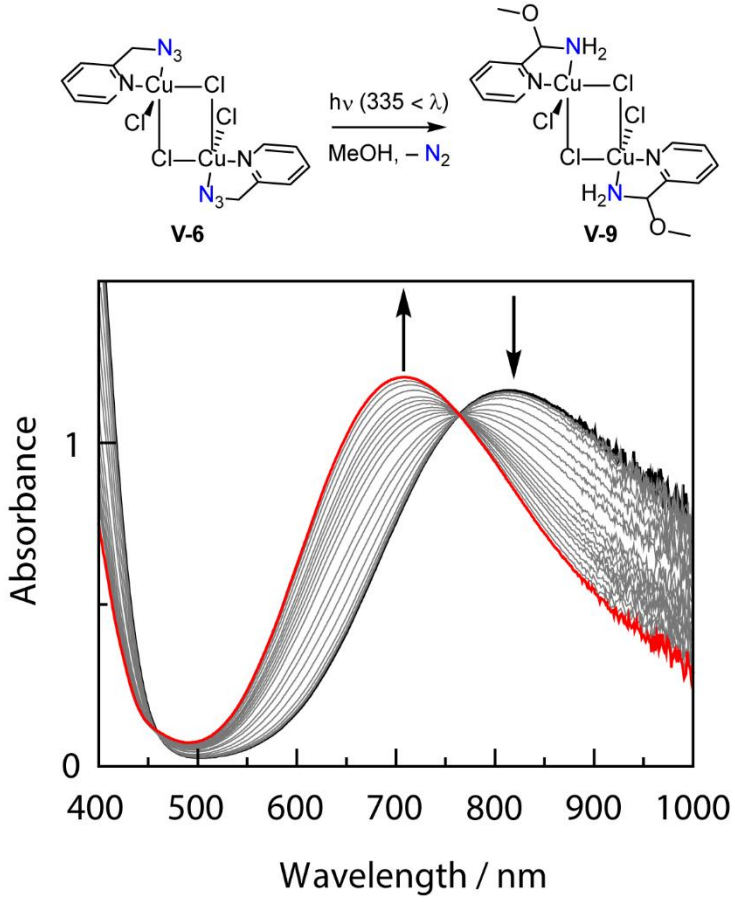

Figure V-6. UV−vis spectra collected during the photolysis of V-6 in MeOH (335 nm < λ). Isosbestic points are observed at 457 and 764 nm, which indicate the lack of a steady-state intermediates in the conversion of **V-6** (—) to **V-9** (—).

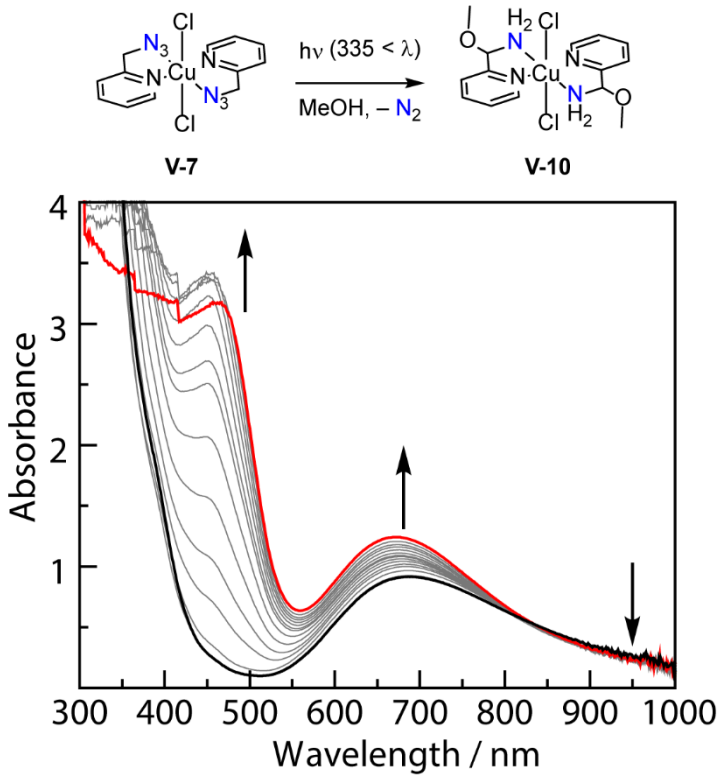

Figure V-7. UV−vis spectra collected during the photolysis of V-7 in MeOH (335 nm < λ). An isosbestic point is observed at 832 nm, which indicates the lack of a steady-state intermediates in the conversion of **V-7** (—) to **V-10** (—).

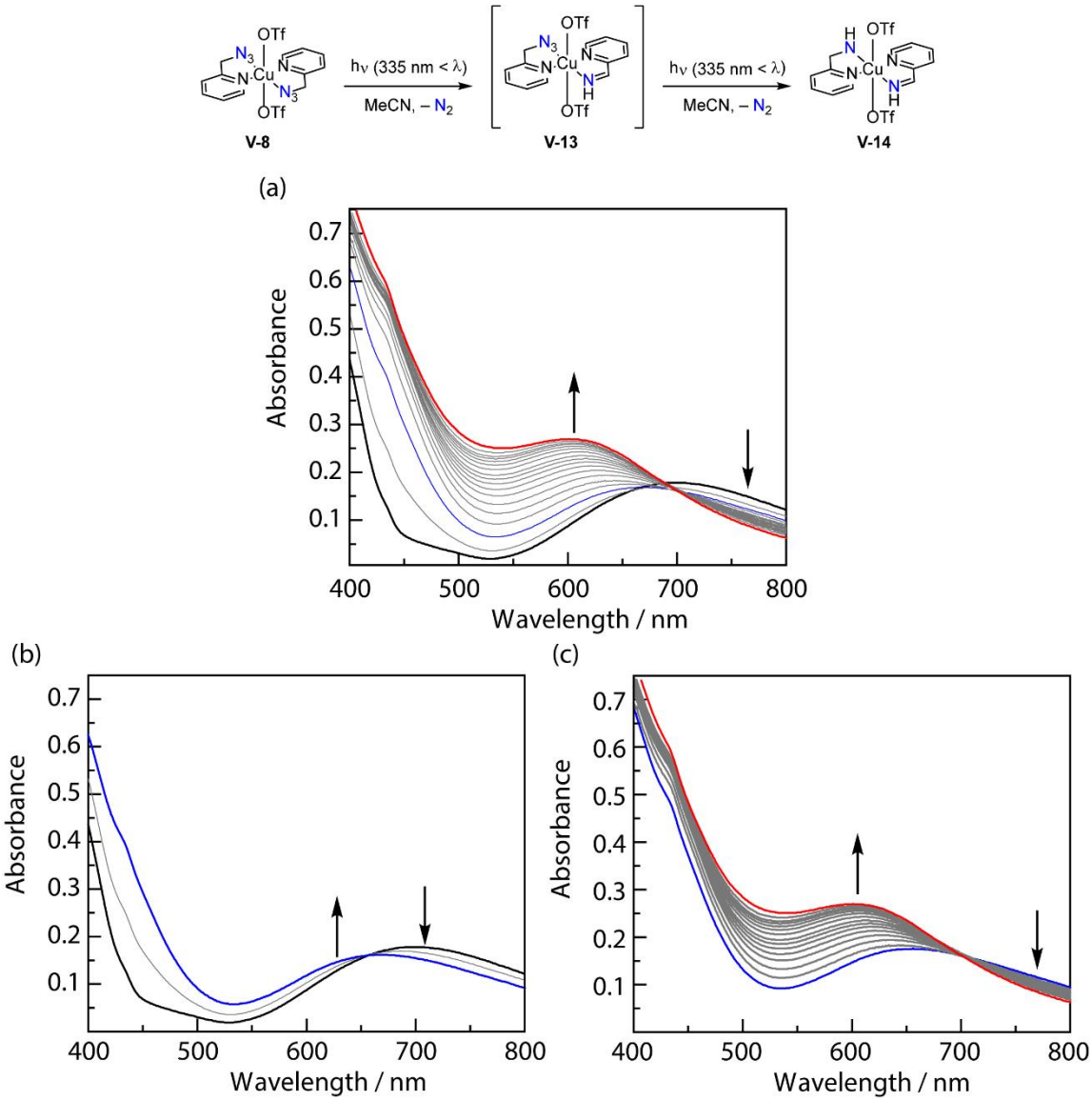

Figure V-8. UV−vis spectra collected during the photolysis of V-8 in MeCN (335 nm < λ). (a) UV-vis spectra obtained during the entire photolysis of **V-8** (—) to **V-14** (—), which feature two sets of isosbestic points. The two sets of isosbestic points suggest that each azide reacts sequentially, rather than both simultaneously, to form **V-14**. (b) UV-vis spectra that show the first isosbestic point at 658 nm upon the photolysis of **V-8**, forming mono-azide **V-13** (—). (c) UV-vis spectra that show the second isosbestic point at 703 nm, forming bis-imine complex **V-14** (—).

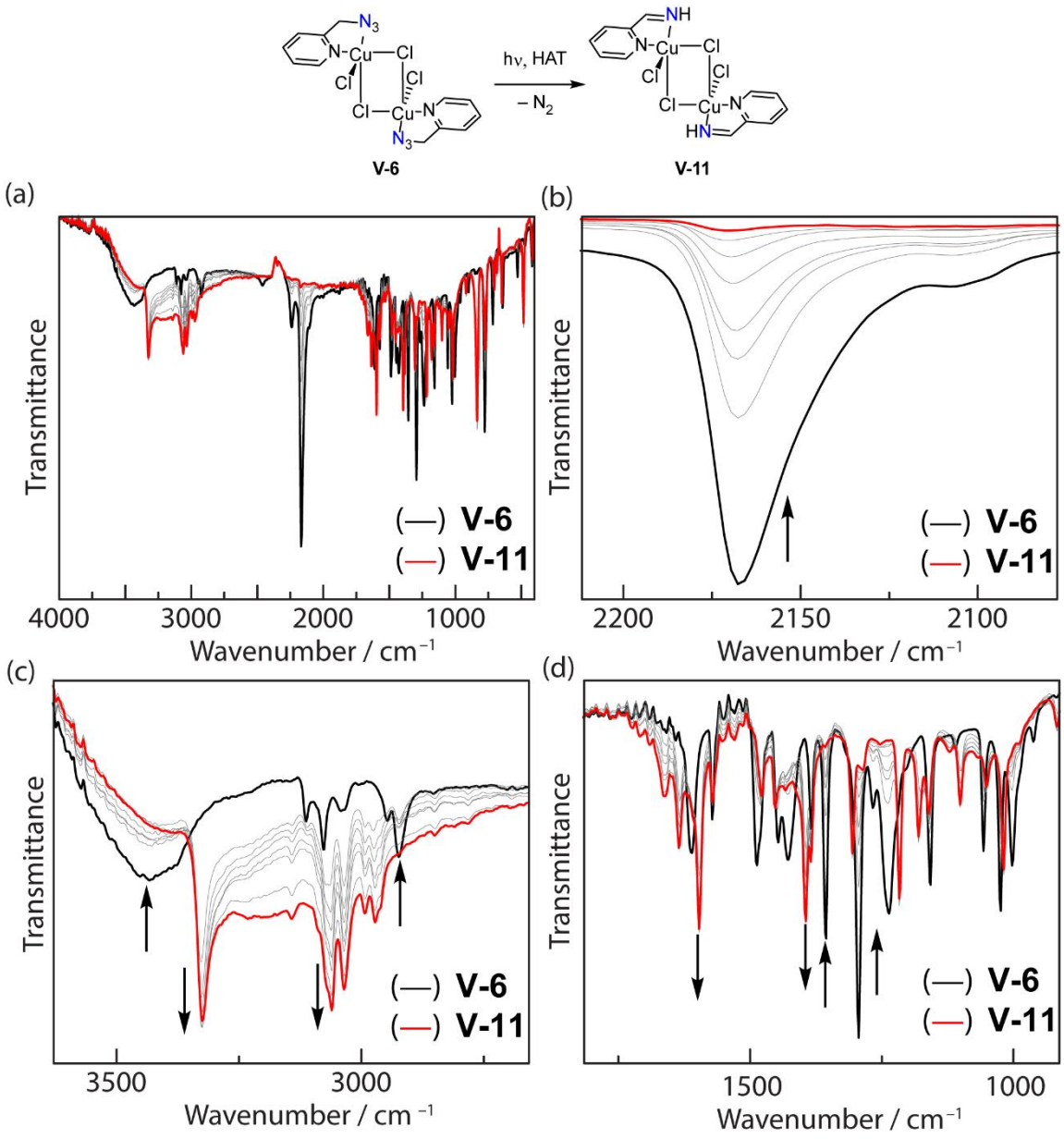

Figure V-9. IR spectra collected during the photolysis (335 nm < λ) of V-6 in a KBr pellet. (a) Full spectral range. (b) Expansion of the spectral window depicting the change in the azide stretching region, which features complete azide consumption to form **V-11**. (c) Expansion of the N–H and C–H strectching frequency region, which features a new peak at 3235 cm^{-1} which is attributed to the new N–H imine bond in **V-11**. (d) Expansion of the fingerprint region, which features a new peak at 1596 cm^{-1} which is attributed to the new C=N bond in **V-11**.

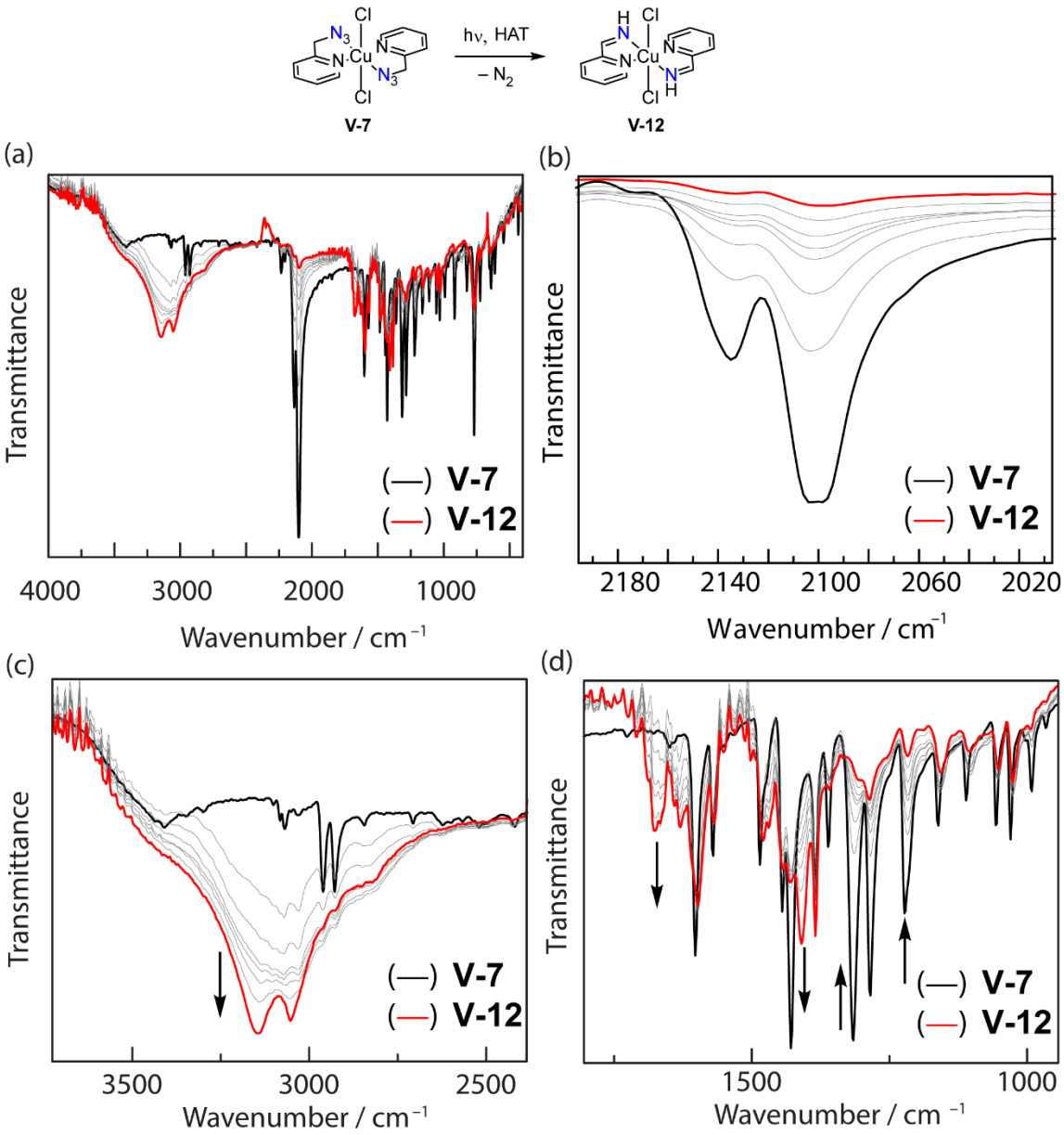

Figure V-10. IR spectra collected during the photolysis (335 nm < λ) of V-7 in a KBr pellet. (a) Full spectral range. (b) Expansion of the spectral window depicting the change in the azide stretching region, which features complete azide consumption to form **V-12**. (c) Expansion of the N–H and C–H strectching frequency region, which features a new peak at 3150 cm^{-1} which is attributed to the new N–H imine bond in **V-12**. (d) Expansion of the fingerprint region, which features a new peak at 1667 cm^{-1} which is attributed to the new C=N bond in **V-12**.

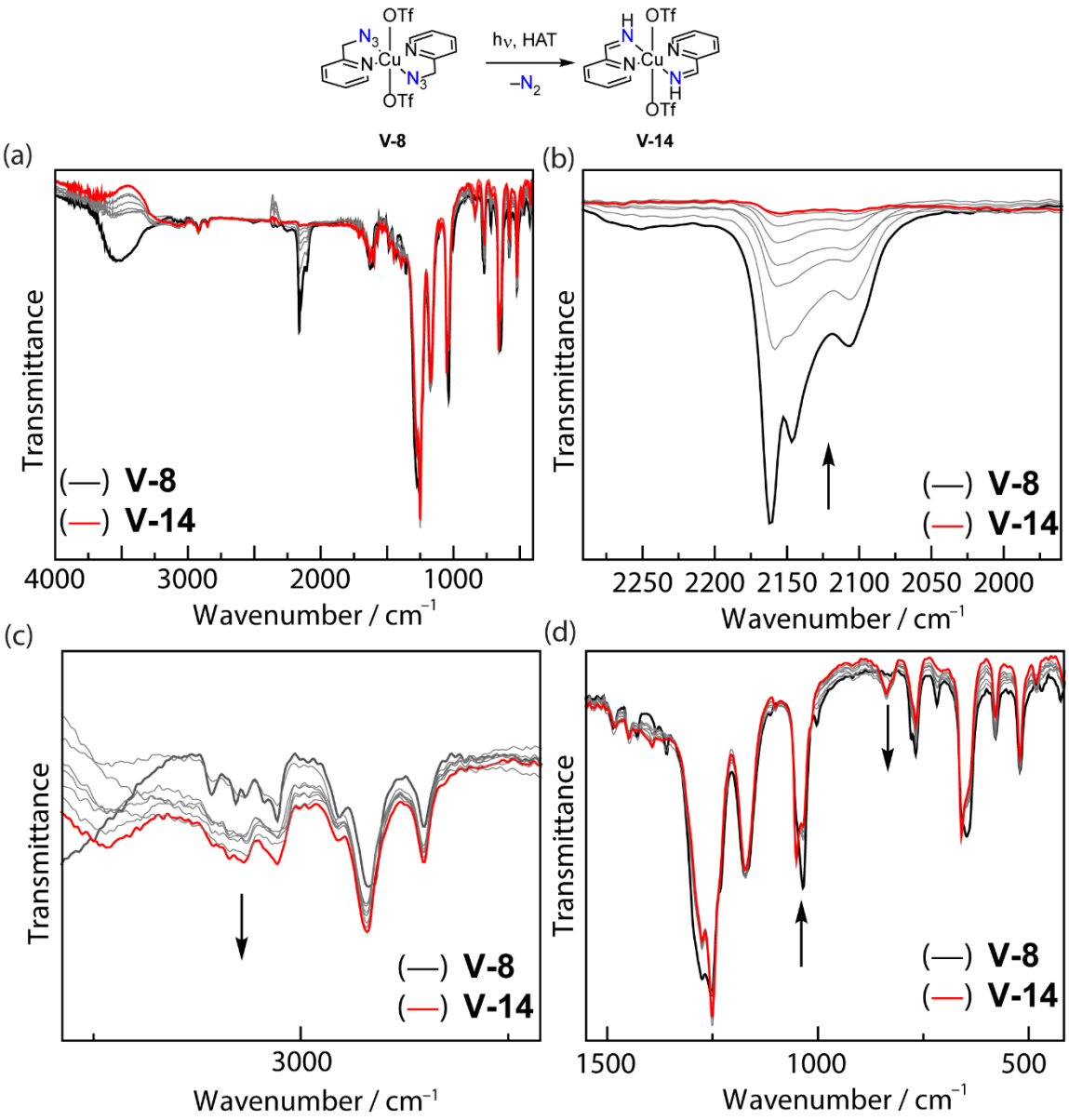

Figure V-11. IR spectra collected during the photolysis (335 nm < λ) of V-8 in a KBr pellet. (a) Full spectral range. (b) Expansion of the spectral window depicting the change in the azide stretching region, which features complete azide consumption to form **V-14**. (c) Expansion of the N–H and C–H strectching frequency region, which features a new peak at 3069 cm^{-1} which is attributed to the new N–H imine bond in **V-14**. (d) Expansion of the fingerprint region where the peak for the new C=N bond in **V-14** is obscured by the broad triflate peak at 1250 cm^{-1}.

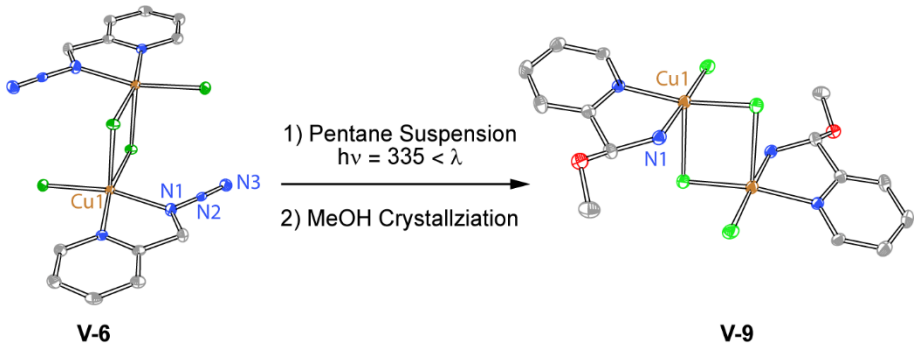

Figure V-12. Photolysis (335 < λ) of single-crystals of V-6 in a pentane suspension, and subseqent crystallization of the reaction product in MeOH, yields single crystals of V-9.

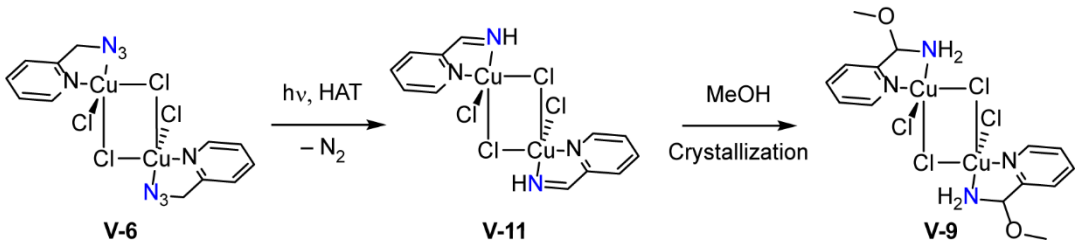

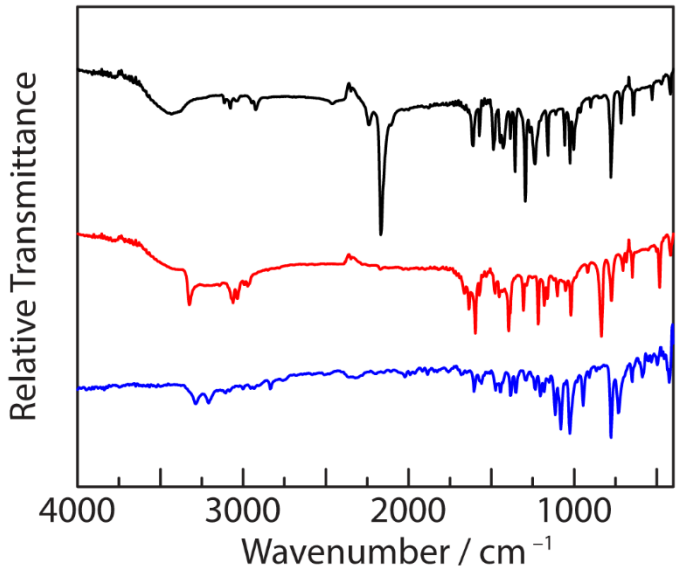

Figure V-13. Comparison of the IR spectra of Cu azide V-6 (—), Cu imine V-11 (—), and Cu hemiaminal ether V-9 (—).

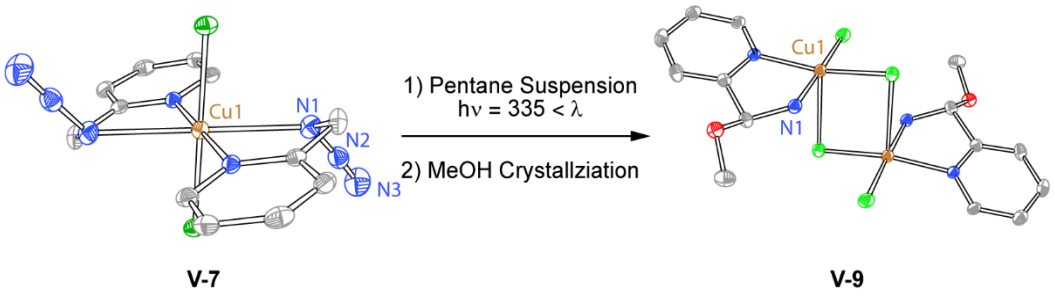

Figure V-14. Photolysis (335 < λ) of single-crystals of V-7 in a pentane suspension, and subseqent crystallization of the reaction product in MeOH, yields single crystals of V-9.

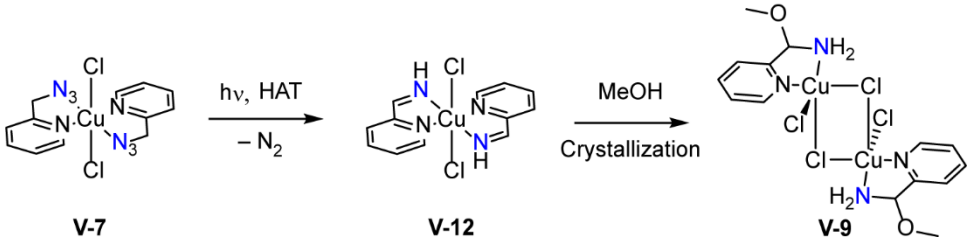

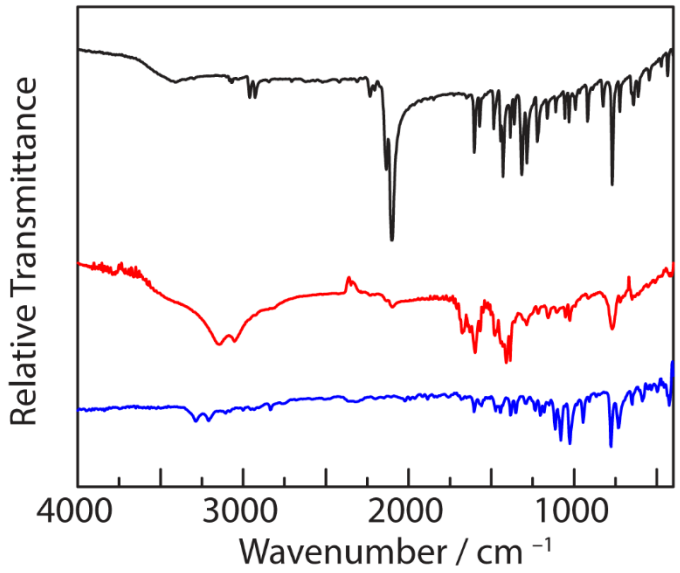

Figure V-15. Comparison of the IR spectra of Cu azide V-7 (—), Cu imine V-12 (—), and Cu hemiaminal ether V-9 (—).

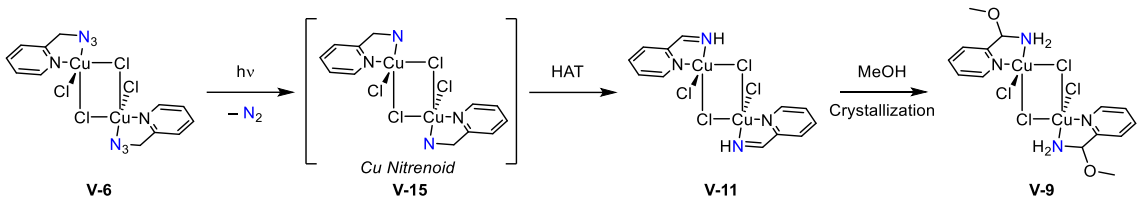

Figure V-16. Proposed reaction pathway. Photolysis of V-6 results in N_2 extrusion forming Cu nitrenoid V-15, which undergoes intramolecular HAT forming Cu imine V-11. Exposure of imine V-11 to MeOH furnishes hemiaminal ether V-9 upon crystallization.

V.2.3 Photocrystallography

Photolysis (λ = 365 nm) of a single-crystal of **V-6** at 100 K promoted *in crystallo* synthesis of Cu nitrenoid **V-15** (Figure V-17). Reaction progress was monitored by periodic collection of X-ray crystal structures (synchrotron radiation, λ = 0.41328 Å). Refinement of the resulting data indicated that the extrusion of N_2 generates Cu nitrenoid **V-15** with 30% chemical conversion (Figure V-17). Elimination of N_2 from **V-6** is accompanied by the elongation of Cu(1)–N(1) from 2.043(2) Å (**V-6**) to 2.13(4) Å (**V-15**). Concurrent with N_2 extrusion and Cu(1)–N(1) elongation, significant contraction of the C(1)–N(1) bond is also observed from 1.476(3) Å to 1.38(3) Å. The conversion of **V-6** to **V-15** is also accompanied by a contraction of the Cu(1)–N(1)–C(1) angle from 117.9(2)° to 114(2)°. Attempts to reach higher conversions via prolonged irradiation were unsuccessful due to loss of crystallinity.

DFT geometry optimization of **V-15** has been pursued as a triplet (*i.e.*, iminyl radical dimer) and a septet (*i.e.*, triplet nitrene dimer) electronic configuration (PBE0 functional, mod-LANL2DZ basis set for Cu, LANL2DZ(d,p) basis set for Cl, 6-31G(d') basis set for light atoms) and optimization of **V-11** has been pursued as a triplet (*i.e.* imine

dimer) electronic configuration (PBE0 functional, mod-LANL2DZ basis set for Cu, LANL2DZ(d,p) basis set for Cl, 6-31G(d') basis set for light atoms). The calculated Cu(1)–N(1), C(1)–N(1) distances and Cu(1)–N(1)–C(1) angle for ^{3}[**V-15**] are in excellent agreement with the experimentally defined parameters (Table V-2). In contrast, the optimized structures of ^{7}[**V-15**] and ^{3}[**V-11**] are not well matched to the experimental data. The optimized structure of ^{7}[**V-15**] overestimates the Cu(1)–N(1) bond length and underestimates the Cu(1)–N(1)–C(1) angle. The optimized structure of ^{3}[**V-11**] underestimates both the Cu(1)–N(1) and C(1)–N(1) bond lengths and overestimates the Cu(1)–N(1)–C(1) angle.

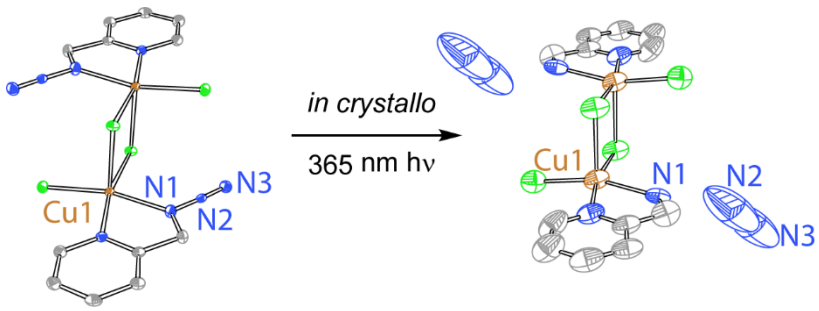

Figure V-17. Solid state structure of V-6 and V-15. Thermal ellipsoids are drawn at 50% probability. H atoms removed for clarity. The structure shown here results from refinement of a data set collected at 30% conversion. Comparison of the bond metrics derived from the X-ray structure with those computed for ^{3}[**V-15**], ^{7}[**V-15**], ^{3}[**V-11**] indicate excellent agreement with the triplet nitrenoid electronic configuration.

Table V-2. Comparison of computed and experimental bond lengths for V-15 (iminyl radical). Experimental distances are derived from the X-ray structure of compound **V-6**. Computed distances are derived from optimization of **V-15** as different spin states, and as the imine (**V-11**).

	V-6 (exp.)	**V-15** (exp.)	**^{3}[V-15]** (comp.)	**^{7}[V-15]** (comp.)	**^{3}[V-11]** (comp.)
Cu–N / Å	2.043(2)	2.13(4)	2.08	2.31	2.00
C–N / Å	1.476(3)	1.38(3)	1.40	1.41	1.27
Cu–N–C / °	117.9(2)	114(2)	114.5	110.	116.8
C–C–N–Cu / °	14.67	12.40	27.70	16.57	2.960

In contrast to the observed photoextrusion of N_2 *in crystallo* from **V-6**, which unveils a Cu iminyl radical, photopromoted (λ = 365 nm) N_2 extrusion from **V-8** *in crystallo* at 100 K affords Cu imine **V-14**. Reaction progress was monitored by periodic collection of X-ray crystal structures (synchrotron radiation, λ = 0.41328 Å). Refinement of the resulting data indicated that the extrusion of N_2 generates Cu imine **V-14** with 90% chemical conversion (Figure V-18). Elimination of N_2 from **V-8** is accompanied by the contraction of Cu(1)–N(1) from 2.103(2) Å (**V-8**) to 2.043(4) Å (**V-14**). Concurrent with N_2 extrusion and Cu(1)–N(1) elongation, significant contraction of the C(1)–N(1) bond is also observed from 1.478(2) Å to 1.323(6) Å. The conversion of **V-8** to **V-14** is also accompanied by expansion of the Cu(1)–N(1)–C(1) angle from 107.84(1)° to 112.8(3)°. Additionally, due to the high quality of data (synchrotron radiation), the position of H(2) was refined from the electron difference map, and not added using a riding model.

DFT geometry optimization of **V-14** has been pursued as a doublet (*i.e.* bis-imine) electronic configuration (PBE0 functional, mod-LANL2DZ basis set for Cu, 6-31G(d') basis set for light atoms) and optimization of **V-16** has also been pursued as a quartet (*i.e.* bis-iminyl radical) and sextet (*i.e.* bis-triplet nitrene) electronic configuration (PBE0

functional, mod-LANL2DZ basis set for Cu, 6-31G(d') basis set for light atoms). The calculated Cu(1)–N(1) and C(1)–N(1) distances for ^{2}[**V-14**] are in excellent agreement with the experimentally defined parameters (Table V-3). In contrast, the optimized structures of ^{4}[**V-16**] and ^{6}[**V-16**] are not well matched to the experimental data. The optimized structure of ^{4}[**V-16**] overestimates both the Cu(1)–N(1) and C(1)–N(1) bond length and underestimates the Cu(1)–N(1)–C(1) angle. The optimized structure of ^{6}[**V-16**] overestimates both the Cu(1)–N(1) and C(1)–N(1) bond lengths and underestimates the Cu(1)–N(1)–C(1) angle.

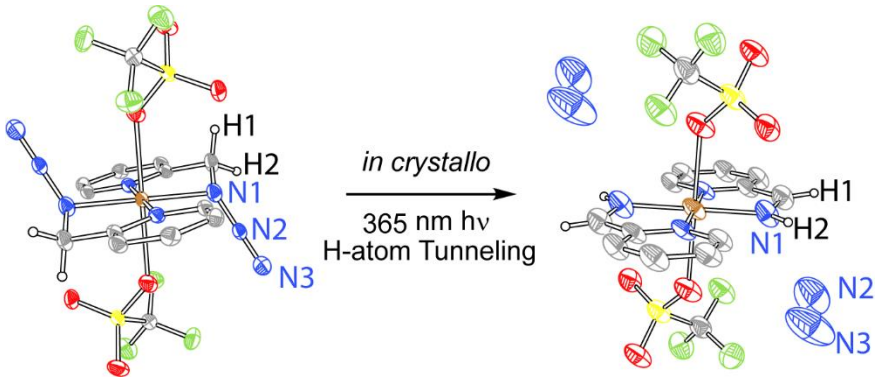

Figure V-18. Solid state structure of V-8 and V-14. Thermal ellipsoids are drawn at 50% probability. H atoms removed for clarity. The structure shown here results from refinement of a data set collected at 90% conversion. Comparison of the bond metrics derived from the X-ray structure with those computed for ^{2}[V-14], ^{4}[V-16], ^{6}[V-16] indicate excellent agreement with the doublet bis-imine electronic configuration.

Table V-3. Comparison of computed and experimental bond lengths for V-14. Experimental distances are derived from the X-ray structure of compound **V-8**. Computed distances are derived from optimization of V-14 and V-16.

	V-8 (exp.)	**V-14** (exp.)	**^{2}[V-14]** (comp.)	**^{4}[V-16]** (comp.)	**^{6}[V-16]** (comp.)
Cu–N / Å	2.103(2)	2.043(4)	2.003	2.373	2.356
C–N / Å	1.478(2)	1.323(6)	1.274	1.406	1.407
Cu–N–C / °	107.84(1)	112.8(3)	115.6	107.3	108.0

V.3. Discussion

In crystallo photochemistry provides a platform to investigate intermediates involved in reaction mechanisms. The photolysis of organic azides often result in rearrangements affording either imines via the Schmidt rearrangement or isocyanates via the Curtius rearrangement (Figure V-19).[50-52] When considering the mechanism of the Schmidt rearrangement, the imine could either occur from a singlet nitrene, which then undergoes intramolecular HAT. Alternatively, the imine could come from a concerted transition state, where the azide N_{α}–N_{β} bond is cleaved simultaneously as the vicinal C–H is transferred to the nitrogen, without ever passing through a nitrene (Figure V-19). The concerted pathway is understood to be the operative pathway in free alkyl azide molecules.[53-55, 361]

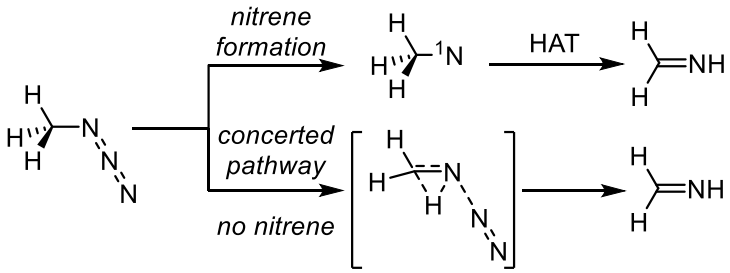

Figure V-19. The two possible pathways of imine formation via alkyl azide decomposition. The top pathway depicts a step-wise mechanism, where the N–N bond cleaves forming a singlet nitrene, which then undergoes HAT to form the imine. The bottom pathway shows a concerted pathway, where a nitrene is not involved in formation of the imine.

All of the prepared Cu azide complexes feature α-bound azide ligands, tethered to the Cu center via a pyridine directing group. Organic azide ligands are known as potential photoprecursors to metal nitrenes, but few kinetically stable adducts are known. Further, most known transition metal azide adducts are easily displaced by coordinating solvent, or other Lewis basic molecules. We have demonstrated that **V-6**, **V-7**, and **V-8** remain intact in coordinating solvents such as MeOH and MeCN due to the pyridine tether, thus we expect that use of chelating organic azides will be used to expand the synthetic utility of transition metal organic azide adducts.

We have demonstrated that each of the prepared Cu azide adducts are photoactive in the solution phase and solid-state, as indicated by the *in situ* UV-vis and IR experiments. Complexes **V-6** and **V-7** lose N_2 upon photolysis in MeOH to afford hemiaminal ether **V-9**. Solid-state photolysis of **V-6** and **V-7** shows that first photopromoted N_2 loss results in a Cu imine, which subsequently reacts with nucleophilic MeOH upon dissolution to form **V-9**. Similarly, solid-state photolysis of **V-8** results in a Cu imine complex. The

demonstrated proclivity of Cu alkyl azide adducts to undergo intramolecular HAT to afford Cu imines is well-matched to literature reports which find photolysis of alkyl azides leads to an alkyl imine via a concerted transition state (Figure V-19).

In crystallo photolyses of both **V-6** and **V-8** demonstrate that both Cu nitrenoid and Cu imine complexes can be directly accessed at 100 K. Photolysis of **V-6**, which features chloride ligands in the primary coordination sphere, in a single-crystal results in formation of iminyl radical **V-15** with no evidence of imine formation. In contrast, photolysis of **V-8**, which features OTf ligands, in a single-crystal affords imine **V-14** without passing through an observable Cu nitrenoid at 100 K.

We have shown that by changing the primary coordination sphere, either via geometry (*i.e.* octahedral vs trigonal bipyramidal) or ligand identity, affects the relative barrier height between concerted and stepwise reactivity. Importantly, this study demonstrates the possibility that an alkyl nitrene might be implicated in imine formation from alkyl azides. These results are consistent with a Co(III) iminyl radical complex we structurally characterized in collaboration with Betley and coworkers.[288] Co complex **V-18** features an alkyl iminyl radical, which will undergo intramolecular HAT to form imine **V-19** upon warming, similar to iminyl radical **V-15** (Figure V-20). We anticipate that *in crystallo* photolysis of functionalized alkyl azides with proximal methyl and phenyl groups will afford the same result, formation of an iminyl radical and then subsequent group transfer to form alkyl imines.

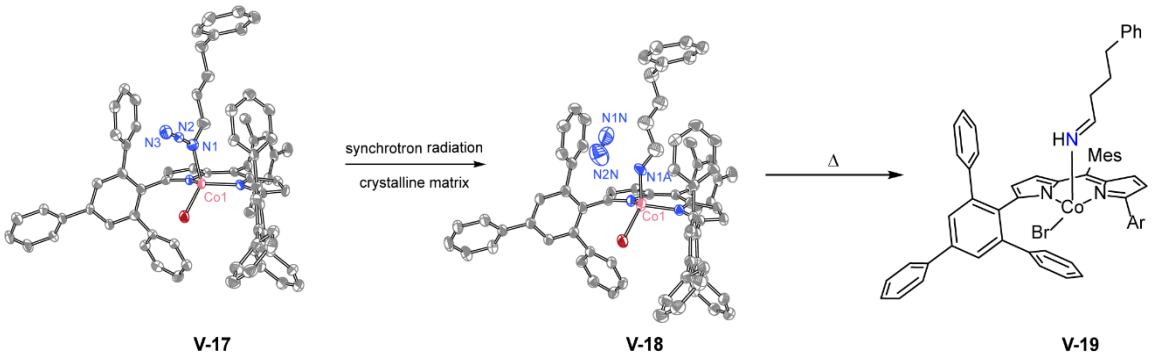

Figure V-20. *In crystallo* generation of iminyl radical V-18 proceeds from azide V-17 with no evidence of imine formation. Thermolysis of V-18 affords imine V-19.

V.4. Concluding Remarks

Here, we have shown the characterization of Cu bound alkyl nitrenoid intermediate **V-15**, which rapidly rearranges to the corresponding imine at room temperature, but can be observed *in crystallo* at 100 K. Furthermore, we have evidence which suggests that perturbation of the primary coordination sphere changes the relative barrier height to select for stepwise vs. concerted reaction pathways. *In crystallo* photolysis of **V-8**, which features two apical triflate anions and two azide ligands, at 100 K affords Cu imine **V-14** in high yield with no evidence of Cu nitrenoid formation. Further spectroscopic and structural investigations at 10 K will be undertaken to see if a Cu nitrenoid can be trapped upon the photolysis of **V-8**. Future experiments, such as the *in crystallo* photolysis of **V-7**, will be diagnostic in our understanding of the importance of the apical triflate ligand vs. two azide ligands bound in the equatorial plane for *in crystallo* formation of **V-16**.

V.5. Experimental Details

V.5.1 General Considerations

Materials

Unless otherwise noted, all the chemicals and solvents (ACS reagent grade) were used as received. 2-(Chloromethyl)pyridine hydrochloride was purchased from Matrix Scientific. Copper(II) trifluoromethanesulfonate ($Cu(OTf)_2$) was purchased from TCI America. Sodium azide was purchased from Bean Town Chemical. Copper(II) chloride dihydrate ($CuCl_2 \cdot 2H_2O$) was purchased from J.T. Baker. NMR solvents were purchased from Cambridge Isotope Laboratories. CD_3CN was stored over 3 Å molecular sieves and all other NMR solvents were stored over 4 Å molecular sieves. 2-(Azidomethyl)pyridine (**V-5**)[362] was prepared according to literature methods.

Characterization Details NMR spectra were recorded on Bruker Avance NEO 400 NMR operating at 400.09 MHz for ^1H acquisitions and were referenced against solvent signals: CD_3CN (1.94 ppm, ^1H) CD_3OD (3.31, ^1H).[248] ^1H NMR data are reported as follows: chemical shift (δ, ppm), multiplicity (s (singlet), d (doublet), t (triplet), m (multiplet), br (broad), integration. UV-vis spectra were recorded at 293 K in quartz cuvettes on a Shimadzu UV-2501PC UV-vis-NIR spectrophotometer (200–1000 nm) and were blanked against the appropriate solvent. IR spectra were recorded on a Shimadzu FTIR/IRAffinity-1 spectrometer. Spectra were blanked against air and were determined as the average of 64 scans. IR data are reported as follows: wavenumber (cm^{-1}), peak intensity (s, strong; m, medium; w, weak).

X-ray Diffraction Details X-ray crystal structures of **V-6**, **V-8**, **V-14**, and **V-15** were collected using synchrotron radiation (0.41328 Å) at ChemMatCARS located at the Advanced Photon Source (APS) housed at Argonne National Laboratory (ANL). Crystals suitable for X-ray diffraction were mounted on a glass fiber and data was collected at 100 K (Cryojet N_2 cold stream) using a vertically mounted Bruker D8 three-circle platform goniometer equipped with a PILATUS3 X CdTe 1M detector. Data were collected as a series of φ and/or ω scans. Data were integrated using SAINT and scaled with a multi-scan absorption correction using SADABS. Structures were solved by intrinsic phasing using SHELXT (Apex2 program suite v2014.1) and refined against F^2 on all data by full matrix least squares with SHELXL97.[251, 252] All non-hydrogen atoms were refined anisotropically. H atoms were placed at idealized positions and refined using a riding model. Refinement details are described in the relevant cif.

All other X-ray crystal structures were collected via a Bruker APEX 2 Duo X-ray (three-circle) diffractometer was used for crystal screening, unit cell determination, and data collection for all other X-ray crystal structures. Crystal suitable for X-ray diffraction were mounted on a MiTeGen dual-thickness micro-mount and placed under a cold N_2 stream (Oxford). The X-ray radiation employed was generated from a Mo sealed X-ray tube (Kα = 0.70173 Å with a potential of 40 kV and a current of 40 mA). Bruker AXS APEX II software was used for data collection and reduction. Absorption corrections were applied using the program SADABS. A solution was obtained using XT/XS in APEX2 and refined in Olex2.[251-253] Hydrogen atoms were placed in idealized positions and were set riding on the respective parent atoms. All non-hydrogen atoms were refined with anisotropic

thermal parameters. The structure was refined (weighted least squares refinement on F2) to convergence.[252]

Computational Details Calculations were performed using the Gaussian 16, Revision C.01 suite of software.[254] Geometry optimizations were carried out with the PBE0 functional[296] in conjunction with Grimme's D3 empirical dispersion[297] and Becke-Johnson damping [EMP=GD3BJ],[298] the mod-LANL2DZ basis set[299] and corresponding ECP for Cu,[300] the LANL2DZ(d,p) basis set[259, 363] and corresponding ECP for Cl,[364] and the 6-311+G* basis set for other atoms;[301] the coordinates for optimized geometries are tabulated in Tables V-11–V-17. Frequency calculations at this level of theory confirmed that optimized geometries represent ground state structures.

V.5.2 Synthesis and Characterization

Synthesis of 2-(azidomethyl)pyridine (V-5)

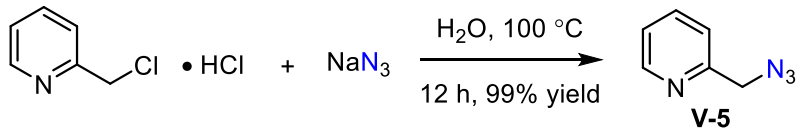

Compound **V-5** was prepared according to the following modification of literature methods.[362] A 50-mL round-bottom flask was charged with 2-(chloromethyl)pyridine hydrochloride (0.070 g, 0.43 mmol, 1.0 equiv.), NaN_3 (0.11 g, 1.7 mmol, 4.0 equiv.), and H_2O (10 mL). The reaction mixture heated to 100 °C and stirred for 12 h. The reaction mixture was then cooled to 23 °C and CH_2Cl_2 (20 mL) was added. The organic phase was separated and the aqueous phase was extracted with CH_2Cl_2. The combined organic layers were dried over Na_2SO_4. Solvent was removed *in vacuo* to afford the title compound as a pale-yellow oil (0.073 g, 99% yield). ^{1}H NMR (δ, 23 °C, CDCl3): 8.81 (d, 1H), 7.72 (td,

1H) 7.36 (d, 1H), 7.23 (d, 1H), 4.49 (s, 2H). IR (ATR, cm^{-1}): 2098 (s). Spectral data are well-matched to those reported in the literature.

Synthesis of $(CuCl_2(PyN_3))_2$ (V-6)

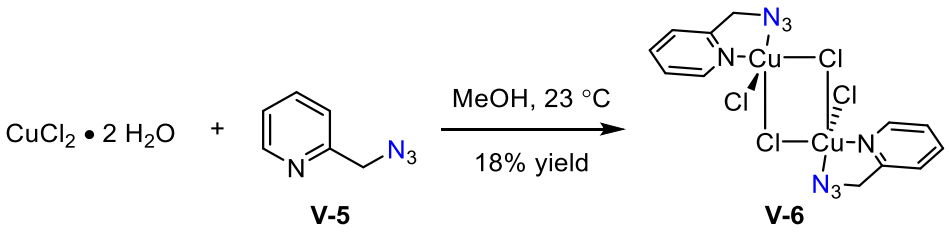

Compound **V-6** was prepared according to the following modification of literature methods.[355] A 20-mL scintillation vial was charged with $CuCl_2 \cdot 2H_2O$ (0.0056 g, 0.033 mmol, 1.0 equiv.) and MeOH (1.0 mL). Separately, a 20-mL scintillation vial was charged with 2-(azidomethyl)pyridine (0.0011 g, 0.085 mmol, 2.6 equiv.) and MeOH (1.8 mL). The two solutions were combined, and the resulting reaction mixture was stirred at 23 °C for 5 min. Slow diffusion of diethyl ether into the MeOH solution resulted in crystallization of the title compound (0.0025 g, 18% yield following crystallization); single-crystal X-ray diffraction data is collected in Figure V-21 and Table V-4. IR (KBr pellet, cm^{-1}): 3428 (m), 3112 (w), 3079 (w), 3041 (w), 2942 (w), 2923 (w), 2238 (m), 2167 (s), 1611 (w), 1570 (w), 1485 (w), 1447 (w), 1426 (w), 1383 (w), 1355 (w), 1293 (m), 1238 (w), 1157 (w), 1110 (w), 1057 (w), 1024 (w), 1001 (w), 960 (w), 898 (w), 777 (m), 714 (w), 640 (w), 529 (w), 472 (w), 417(w). UV-vis (MeOH), λ_{max} (nm, ε ($M^{-1}cm^{-1}$)): 816 (ε 1.3×10^2).

Synthesis of $CuCl_2(PyN_3)_2$ (V-7)

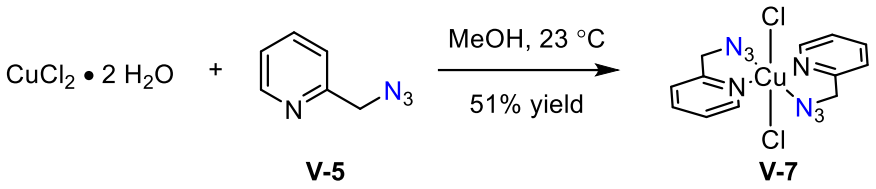

V-5 **V-7**

Compound **V-7** was prepared according to the following modification of literature methods.[355] A 20-mL scintillation vial was charged with $CuCl_2 \cdot 2H_2O$ (0.0041 g, 0.024 mmol, 1.0 equiv.) and MeOH (1.0 mL). Separately, a 20-mL scintillation vial was charged with 2-(azidomethyl)pyridine (0.096 g, 0.72 mmol, 30 equiv.) and MeOH (1.4 mL). The two solutions were combined, and the resulting reaction mixture was stirred at 23 °C for 5 min. Slow diffusion of diethyl ether into the MeOH solution resulted in crystallization of the title compound (0.0040 g, 51% yield following crystallization); single-crystal X-ray diffraction data is collected in Figure V-22 and Table V-5. IR (KBr pellet, cm^{-1}): 3074 (w), 2961 (w), 2293 (w), 2234 (w), 2205 (w), 2135 (s), 2101 (s), 1644 (w), 1602 (m), 1571 (m), 1483 (m), 1444 (m), 1428 (m), 1384 (m), 1363 (w), 1314 (m), 1284 (m), 1220 (m), 1160 (w), 1110 (w), 1055 (w), 1028 (w), 990 (w), 918 (m), 824 (m), 769 (s), 639 (m), 610 (w), 543 (w), 471 (w), 433 (m), 401 (w). UV-vis (MeOH), λ_{max} (nm, ε ($M^{-1}cm^{-1}$)): 690 (1.4×10^2).

Synthesis of $Cu(OTf)_2(PyN_3)_2$ (V-8)

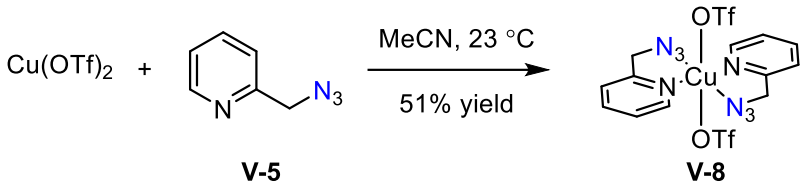

V-5 **V-8**

A 20-mL scintillation vial was charged with $Cu(OTf)_2$ (0.034 g, 0.094 mmol, 1.0 equiv.) and MeCN (1.0 mL). Separately, a 20-mL scintillation vial was charged with 2-(azidomethyl)pyridine (0.041 g, 0.31 mmol, 3.3 equiv.) and MeCN (3.8 mL). The two solutions were combined, and the resulting reaction mixture was stirred at 23 °C for 5 min. Slow diffusion of diethyl ether into the MeOH solution resulted in crystallization of the title compound (0.030 g, 51% yield following crystallization); single-crystal X-ray diffraction data is collected in Figure V-23 and Table V-6. IR (KBr pellet, cm^{-1}): 3107 (w), 3070 (w), 3033 (w), 2918 (w), 2852 (w), 2160 (s), 2147 (m), 2107 (m), 1629 (m), 1572 (w), 1487 (w), 1448 (w), 1429 (w), 1359 (w), 1274 (s), 1251 (s), 1172 (s), 1035 (s), 766 (m), 716 (w), 648 (s), 579 (w), 518 (m), 428 (w). UV-vis (MeOH), λ_{max} (nm, ε ($M^{-1}cm^{-1}$)): 698 (6.1×10^2).

General Procedure for Photochemistry in a Pentane Suspension with Cu Azide Complexes

A 20-mL Schlenk tube was charged with **V-6** (0.0100 g, 0.0186 mmol, 1 equiv), pentane (3 mL). The reaction mixture was photolyzed for 24 h while stirring at 23 °C using a 100 W Hg lamp with a 335 nm long-pass filter. The resulting suspension was filtered, and the recovered solids were dissolved in MeOH to afford a light blue solution. Single-crystals suitable for X-ray diffraction were obtained via slow diffusion of diethyl ether into the

MeOH solution for 1 d; single-crystal X-ray diffraction data is collected in Figure V-25 and Table V-8.

V.5.3 Crystallographic Data

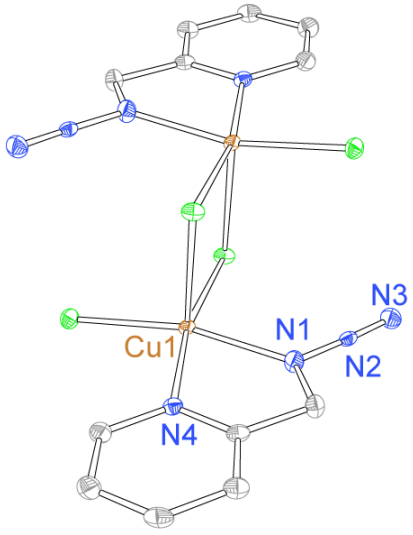

V-6

Figure V-21. Displacement ellipsoid plot of $(CuCl_2(C_6H_7N_4))_2$ (V-6) plotted at 50% probability. H-atoms are removed for clarity. The crystalline sample used in this diffraction experiment was obtained from vapor diffusion of diethyl ether into a saturated MeOH solution of **V-6** at 23 °C.

Table V-4. X-ray experimental details of $(CuCl_2(C_6H_7N_4))_2$ (V-6).

Crystal data	
Chemical formula	$C_6H_6Cl_2Cu_1N_4$
M_r	268.06
Crystal system, space group	Triclinic, *P*1
Temperature (K)	100
a, *b*, *c* (Å)	6.8198(5), 8.0550(6), 9.7707(8)
α, β, γ (°)	68.112(3), 71.544(5), 89.271(4)
V (Å^3)	469.04(6)
Z	2
Radiation type	Synchrotron, λ = 0.41328 Å
M (mm^{-1})	0.63
Crystal size (mm)	0.2 × 0.2 × 0.1
Data collection	
Diffractometer	Bruker *APEX*-II CCD
No. of measured, independent and observed [$I > 2s(I)$] reflections	5382, 1782, 1731
R_{int}	0.046
$(\sin \theta/\lambda)_{max}$ (Å^{-1})	0.625
Refinement	
$R[F^2 > 2s(F^2)]$, $wR(F^2)$, *S*	0.039, 0.107, 1.23
No. of reflections	1782
No. of parameters	129
H-atom treatment	H-atom parameters constrained
Γ_{max}, Γ_{min} (e Å^{-3})	0.61, −1.37

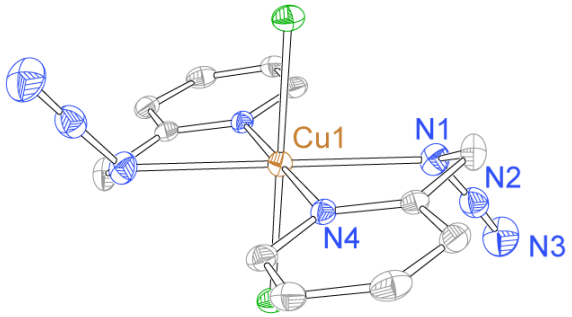

V-7

Figure V-22. Displacement ellipsoid plot of $CuCl_2(C_6H_7N_4)_2$ (V-7) plotted at 50% probability. H-atoms are removed for clarity. The crystalline sample used in this diffraction experiment was obtained from vapor diffusion of diethyl ether into a saturated MeOH solution of **V-7** at 23 °C.

Table V-5. X-ray experimental details of $CuCl_2(C_6H_7N_4)_2$ (V-7).

Crystal data	
Chemical formula	$C_{12}H_{12}Cl_2Cu_1N_8$
M_r	402.74
Crystal system, space group	Monoclinic, $P2_1/n$
Temperature (K)	100
a, b, c (Å)	8.3113(9), 9.382(1), 10.015(1)
β (°)	100.712(3)
V (Å^3)	767.4(2)
Z	4
Radiation type	Mo $K\alpha$
μ (mm^{-1})	1.78
Crystal size (mm)	0.2 × 0.2 × 0.1
Data collection	
Diffractometer	Bruker *APEX*-II CCD
No. of measured, independent and observed [$I > 2s(I)$] reflections	5779, 1574, 1186
R_{int}	0.059
$(\sin \theta/\lambda)_{max}$ (Å^{-1})	0.625
Refinement	
$R[F^2 > 2s(F^2)]$, $wR(F^2)$, S	0.037, 0.068, 1.02
No. of reflections	1574
No. of parameters	129
H-atom treatment	H-atom parameters constrained
Γ_{max}, Γ_{min} (e Å^{-3})	0.36, −0.42

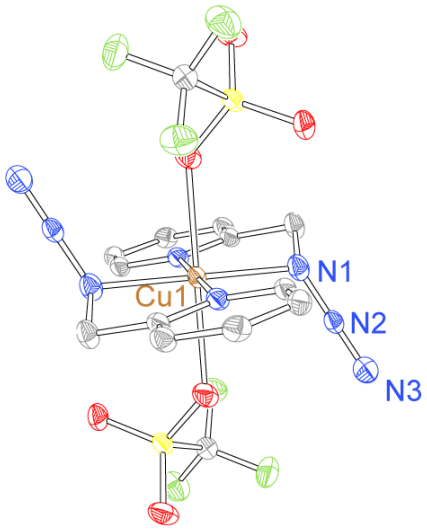

V-8

Figure V-23. Displacement ellipsoid plot of $Cu(CF_3SO_3)_2(C_6H_7N_4)_2$ (V-8) plotted at 50% probability. H-atoms are removed for clarity. The crystalline sample used in this diffraction experiment was obtained from vapor diffusion of diethyl ether into a saturated MeCN solution of **V-8** at 23 °C.

Table V-6. X-ray experimental details of $Cu(CF_3SO_3)_2(C_6H_7N_4)_2$ (V-8).

Crystal data	
Chemical formula	$C_7H_6Cu_{0.5}F_3N_2O_3S \cdot N_2$
M_r	314.99
Crystal system, space group	Monoclinic, $P2_1/n$
Temperature (K)	100
a, b, c (Å)	9.974(1), 8.3710(9), 14.231(2)
β (°)	100.603(2)
V (Å^3)	1167.9(2)
Z	4
Radiation type	Synchrotron, λ = 0.41328 Å
μ (mm^{-1})	0.28
Crystal size (mm)	0.2 × 0.2 × 0.1
Data collection	
Diffractometer	Bruker *APEX*-II CCD
No. of measured, independent and observed [$I > 2s(I)$] reflections	13339, 2356, 1910
R_{int}	0.044
(sin θ/λ$_{max}$ (Å^{-1})	0.627
Refinement	
$R[F^2 > 2s(F^2)]$, $wR(F^2)$, S	0.056, 0.162, 1.10
No. of reflections	2365
No. of parameters	173
H-atom treatment	H atoms treated by a mixture of independent and constrained refinement
Γ$_{max}$, Γ$_{min}$ (e Å^{-3})	1.77, −0.54

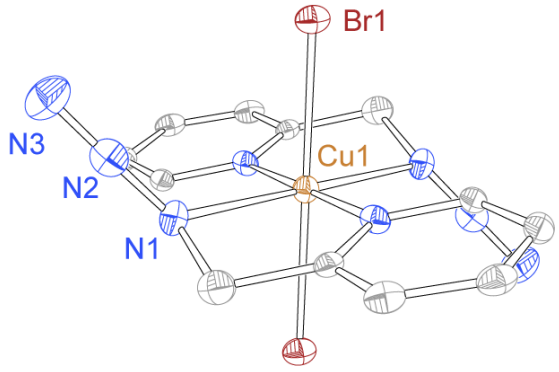

Figure V-24. Displacement ellipsoid plot of $CuBr_2(C_6H_7N_4)_2$ plotted at 50% probability. H-atoms are removed for clarity. The crystalline sample used in this diffraction experiment was obtained from vapor diffusion of diethyl ether into a saturated MeCN solution of Cu(**V-5**)$_2$Br$_2$ at 23 °C.

Table V-7. X-ray experimental details of $CuBr_2(C_6H_7N_4)_2$.

Crystal data	
Chemical formula	$C_{12}H_{12}Br_2CuN_8$
M_r	491.66
Crystal system, space group	Monoclinic, $P2_1/n$
Temperature (K)	110
a, b, c (Å)	8.4316(8), 9.317(1), 10.314(1)
β(°)	98.137 (3)
V (Å^3)	802.1(1)
Z	2
Radiation type	Mo $K\alpha$
μ (mm^{-1})	6.35
Crystal size (mm)	0.2 × 0.1 × 0.1
Data collection	
Diffractometer	Bruker *APEX*-II CCD
No. of measured, independent and observed [$I > 2s(I)$] reflections	7333, 1641, 1271
R_{int}	0.071
$(\sin \theta/\lambda)_{max}$ (Å^{-1})	0.625
Refinement	
$R[F^2 > 2s(F^2)]$, $wR(F^2)$, S	0.040, 0.068, 1.05
No. of reflections	1641
No. of parameters	106
H-atom treatment	H-atom parameters constrained
Γ_{max}, Γ_{min} (e Å^{-3})	0.59, −0.51

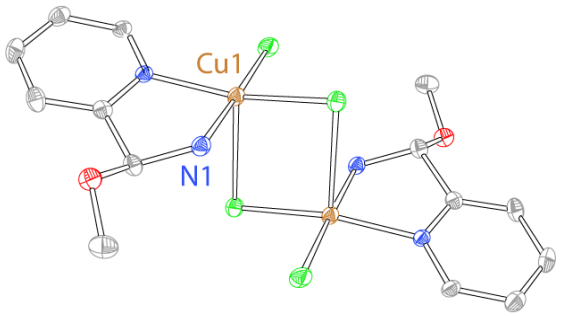

V-9

Figure V-25. Displacement ellipsoid plot of $(CuCl_2(C_7H_{10}ON_2))_2$ (V-9) plotted at 50% probability. H-atoms are removed for clarity. The crystalline sample used in this diffraction experiment was obtained from vapor diffusion of diethyl ether into a saturated MeOH solution of **V-9** at 23 °C.

Table V-8. X-ray experimental details of V-9.

Crystal data	
Chemical formula	$C_7H_{10}C_{l2}CuN_2O$
M_r	272.61
Crystal system, space group	Monoclinic, $P2_1/n$
Temperature (K)	110
a, b, c (Å)	8.9101(8), 12.880(1), 9.739(1)
β (°)	115.432(2)
V (Å^3)	1009.3(2)
Z	4
Radiation type	Mo $K\alpha$
μ (mm^{-1})	2.65
Crystal size (mm)	0.2 × 0.2 × 0.1
Data collection	
Diffractometer	Bruker *APEX*-II CCD
No. of measured, independent and observed [$I > 2s(I)$] reflections	18588, 2514, 1964
R_{int}	0.088
$(\sin \theta/\lambda)_{max}$ (Å^{-1})	0.668
Refinement	
$R[F^2 > 2s(F^2)]$, $wR(F^2)$, S	0.044, 0.084, 1.06
No. of reflections	2514
No. of parameters	119
H-atom treatment	H-atom parameters constrained
Γ_{max}, Γ_{min} (e Å^{-3})	0.90, −0.63

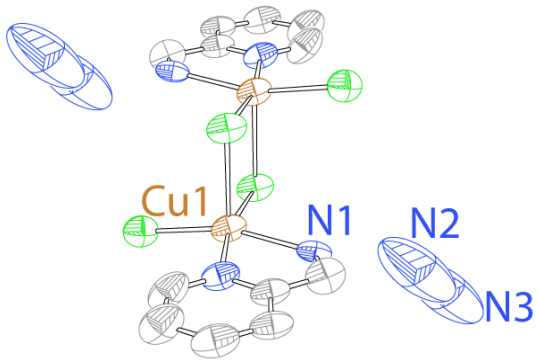

V-15

Figure V-26. Displacement ellipsoid plot of $(CuCl_2(C_6H_7N_4))_2$ (V-15) plotted at 50% probability. H-atoms are removed for clarity. The crystal used in this picture was obtained by *in situ* photolysis of **V-6** which resulted in the expulsion of N_2. Data was collected using synchrotron radiation ($\lambda = 4.1328$ Å) at 100 K. DFIX was used to refine the distance between N(2) and N(3) of the N_2 molecule. The restraint SIMU was also used on the disordered *N*-atoms of the N_2 molecule.

Table V-9. X-ray experimental details of $(CuCl_2(C_6H_7N_4))_2$ (V-15).

Crystal data	
Chemical formula	$C_6H_6Cl_2CuN_{3.319}\cdot 0.34(N_2)$
M_r	267.97
Crystal system, space group	Triclinic, *P*1
Temperature (K)	100
a, *b*, *c* (Å)	6.953(1), 8.163(1), 9.707(2)
α, β, γ (°)	67.984(4), 70.155(4), 88.946(4)
V (Å^3)	476.67(1)
Z	2
Radiation type	Synchrotron, λ = 0.41328 Å
μ (mm^{-1})	0.63
Crystal size (mm)	0.2 × 0.2 × 0.1
Data collection	
Diffractometer	Bruker *APEX*-II CCD
No. of measured, independent and observed [$I > 2s(I)$] reflections	6116, 1819, 1553
R_{int}	0.056
$(\sin\theta/\lambda)_{max}$ (Å^{-1})	0.621
Refinement	
$R[F^2 > 2s(F^2)]$, $wR(F^2)$, *S*	0.061, 0.177, 1.11
No. of reflections	1819
No. of parameters	146
No. of restraints	7
H-atom treatment	H-atom parameters constrained
Γ_{max}, Γ_{min} (e Å^{-3})	1.79, −0.41

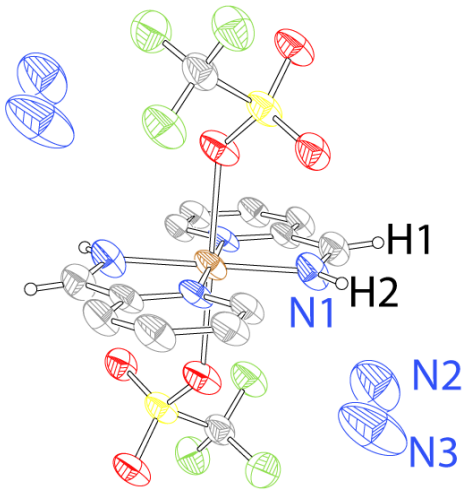

V-14

Figure V-27. Displacement ellipsoid plot of $(Cu(CF_3SO_3)_2(C_6H_7N_4))_2$ (V-14) plotted at 50% probability. H-atoms are removed for clarity. The crystal used in this picture was obtained by *in situ* photolysis of **V-8** which resulted in the expulsion of N_2. Data was collected using synchrotron radiation (λ = 4.1328 Å) at 100 K. H-atoms H(1) and H(2) were refined from the electron difference map. No restraints were used in the refinement.

Table V-10. X-ray experimental details of $(Cu(CF_3SO_3)_2(C_6H_7N_4))_2$ (V-14).

Crystal data	
Chemical formula	$C_7H_6Cu_{0.5}F_3N_2O_3S \cdot N_2$
M_r	314.99
Crystal system, space group	Monoclinic, $P2_1/c$
Temperature (K)	100
a, b, c (Å)	9.974(1), 8.3710(9), 14.231(2)
β (°)	100.603(2)
V (Å^3)	1167.9(2)
Z	4
Radiation type	Synchrotron, λ = 0.41328 Å
μ (mm^{-1})	0.28
Crystal size (mm)	0.2 × 0.2 × 0.1
Data collection	
Diffractometer	Bruker *APEX*-II CCD
No. of measured, independent and observed [$I > 2s(I)$] reflections	13339, 2356, 1910
R_{int}	0.044
$(\sin \theta/\lambda)_{max}$ (Å^{-1})	0.627
Refinement	
$R[F^2 > 2s(F^2)]$, $wR(F^2)$, S	0.056, 0.162, 1.10
No. of reflections	2356
No. of parameters	173
H-atom treatment	H-atoms treated by a mixture of independent and constrained refinement
Γ_{max}, Γ_{min} (e Å^{-3})	1.77, −0.54

V.5.4 Computational Coordinates

Table V-11. X,Y,Z coordinates for the optimized geometry of V-15 computed as a triplet at the PBE0 level of theory with mod-LANL2DZ (Cu), LANL2DZ(d,p) (Cl), and 6-31G(d,p) (light atoms) basis sets.

Atom	X	Y	Z
Cu	3.173	5.397	4.795
Cl	2.962	3.164	4.881
Cl	2.411	5.538	2.654
N	4.037	5.64	6.619
N	3.862	7.317	4.69
C	4.985	6.16	9.202
H	5.29	6.336	10.062
C	4.839	7.192	8.273
H	5.045	8.069	8.506
C	4.379	6.889	6.985
C	4.189	4.628	7.532
H	3.965	3.76	7.282
C	4.664	4.854	8.814
H	4.768	4.148	9.409
C	4.258	7.979	5.948
H	3.588	8.628	6.215
H	5.106	8.437	5.838
Cu	0.022	6.26	3.744
Cl	0.234	8.494	3.658
Cl	0.785	6.12	5.885
N	-0.841	6.018	1.92
N	-0.667	4.34	3.849
C	-1.79	5.498	-0.663
H	-2.095	5.321	-1.523
C	-1.644	4.466	0.266
H	-1.849	3.589	0.033
C	-1.183	4.768	1.554
C	-0.993	7.029	1.007
H	-0.769	7.897	1.257
C	-1.468	6.803	-0.275
H	-1.572	7.51	-0.87
C	-1.062	3.679	2.591
H	-0.392	3.03	2.324
H	-1.911	3.22	2.701

Table V-12. X,Y,Z coordinates for the optimized geometry of V-15 computed as a septet at the PBE0 level of theory with mod-LANL2DZ (Cu), LANL2DZ(d,p) (Cl), and 6-31G(d,p) (light atoms) basis sets.

Atom	X	Y	Z
Cu	3.173	5.397	4.795
Cl	2.962	3.164	4.881
Cl	2.411	5.538	2.654
N	4.037	5.64	6.619
N	3.862	7.317	4.69
C	4.985	6.16	9.202
H	5.29	6.336	10.062
C	4.839	7.192	8.273
H	5.045	8.069	8.506
C	4.379	6.889	6.985
C	4.189	4.628	7.532
H	3.965	3.76	7.282
C	4.664	4.854	8.814
H	4.768	4.148	9.409
C	4.258	7.979	5.948
H	3.588	8.628	6.215
H	5.106	8.437	5.838
Cu	0.022	6.26	3.744
Cl	0.234	8.494	3.658
Cl	0.785	6.12	5.885
N	-0.841	6.018	1.92
N	-0.667	4.34	3.849
C	-1.79	5.498	-0.663
H	-2.095	5.321	-1.523
C	-1.644	4.466	0.266
H	-1.849	3.589	0.033
C	-1.183	4.768	1.554
C	-0.993	7.029	1.007
H	-0.769	7.897	1.257
C	-1.468	6.803	-0.275
H	-1.572	7.51	-0.87
C	-1.062	3.679	2.591
H	-0.392	3.03	2.324
H	-1.911	3.22	2.701

Table V-13. X,Y,Z coordinates for the optimized geometry of V-11 computed as a triplet at the PBE0 level of theory with mod-LANL2DZ (Cu), LANL2DZ(d,p) (Cl), and 6-31G(d,p) (light atoms) basis sets.

Atom	X	Y	Z
Cu	1.40604	0.99748	0.79364
Cl	1.49053	3.027	-0.26964
Cl	-0.63772	1.27299	1.68017
N	3.20478	0.30763	0.1577
N	1.56593	-0.63478	1.99136
C	5.53287	-0.94992	-0.62254
H	6.45437	-1.43794	-0.9274
C	4.67409	-1.56645	0.29517
H	4.90007	-2.53737	0.72467
C	3.50418	-0.90179	0.6566
C	4.00577	0.89081	-0.72108
H	3.68054	1.86377	-1.08343
C	5.19075	0.29196	-1.14231
H	5.82349	0.80489	-1.86147
C	2.52255	-1.44166	1.61534
Cu	-1.38541	-0.93412	-0.79649
Cl	-1.35106	-2.93925	0.30885
Cl	0.72032	-1.22083	-1.64863
N	-3.21565	-0.32656	-0.15516
N	-1.72121	0.61484	-2.08939
C	-5.60617	0.80031	0.64108
H	-6.55105	1.23667	0.95265
C	-4.81693	1.43374	-0.32584
H	-5.12252	2.36565	-0.79101
C	-3.61461	0.83412	-0.69426
C	-3.9551	-0.92843	0.7645
H	-3.55459	-1.8615	1.15525
C	-5.16703	-0.39455	1.19647
H	-5.74444	-0.92024	1.95203
C	-2.7109	1.3822	-1.7171
H	-2.90783	2.36252	-2.1633
H	2.63596	-2.4564	2.01072
H	-1.50685	0.43244	-3.06568
H	1.32517	-0.49845	2.96912

Table V-14. X,Y,Z coordinates for the optimized geometry of V-14 computed as a triplet at the PBE0 level of theory with mod-LANL2DZ (Cu) and 6-31G(d,p) (light atoms) basis sets.

Atom	X	Y	Z
Cu	3.678	4.186	6.994
S	2.188	3.45	3.882
F	0.157	4.411	2.502
F	0.352	5.217	4.507
O	2.999	4.54	3.382
F	-0.422	3.218	4.208
O	2.17	2.248	3.059
O	2.32	3.193	5.31
N	4.357	2.36	7.461
N	5.277	4.127	5.72
C	5.427	1.959	6.73
C	3.892	1.539	8.422
H	3.154	1.803	8.924
C	5.583	-0.093	7.955
H	6.001	-0.905	8.13
C	4.488	0.303	8.689
H	4.146	-0.248	9.356
C	6.058	0.75	6.939
H	6.785	0.499	6.417
C	5.863	2.939	5.692
H	6.51	2.727	5.06
C	0.478	4.1	3.764
S	5.168	4.921	10.106
F	7.199	3.96	11.486
F	7.004	3.154	9.481
O	4.356	3.831	10.606
F	7.777	5.153	9.78
O	5.185	6.123	10.929
O	5.035	5.178	8.678
N	2.998	6.011	6.527
N	2.079	4.244	8.268
C	1.929	6.412	7.258
C	3.463	6.832	5.566
H	4.201	6.568	5.064
C	1.773	8.464	6.033
H	1.355	9.276	5.858
C	2.868	8.068	5.299
H	3.21	8.619	4.632
C	1.298	7.621	7.049
H	0.57	7.872	7.571
C	1.493	5.432	8.296
H	0.846	5.644	8.928
C	6.877	4.271	10.224
H	5.957	4.818	6.02
H	2.4	4.018	9.204

Table V-15. X,Y,Z coordinates for the optimized geometry of V-16 computed as a quartet at the PBE0 level of theory with mod-LANL2DZ (Cu) and 6-31G(d,p) (light atoms) basis sets.

Atom	X	Y	Z
Cu	0	0.00003	0.00002
S	2.79253	1.44428	-0.552
F	5.30419	0.92456	-0.04697
F	3.93064	-0.57588	0.67554
O	2.8282	0.6501	-1.77504
F	4.11134	1.30929	1.7125
O	3.10551	2.86383	-0.65126
O	1.57712	1.19239	0.30626
N	-1.24232	1.81159	0.33852
N	-0.38526	0.83083	-2.19753
C	-1.59806	2.55908	-0.72339
C	-1.59067	2.1987	1.56292
H	-1.27608	1.55475	2.3781
C	-2.70073	4.13675	0.69403
H	-3.27451	5.04953	0.83327
C	-2.32416	3.3632	1.78404
H	-2.58903	3.6439	2.79894
C	-2.33045	3.72958	-0.58751
H	-2.6005	4.30331	-1.46958
C	-1.17093	2.06439	-2.04937
H	-0.60267	2.84907	-2.50354
C	4.1167	0.73282	0.51665
S	-2.79252	-1.44431	0.55196
F	-5.30419	-0.9247	0.04688
F	-3.93068	0.57581	-0.67556
O	-2.82826	-0.65015	1.77501
F	-4.11128	-1.30935	-1.71257
O	-3.10543	-2.86388	0.6512
O	-1.57712	-1.19234	-0.30628
N	1.24232	-1.81154	-0.33847
N	0.38521	-0.83078	2.19756
C	1.59803	-2.55903	0.72344
C	1.5907	-2.19865	-1.56286
H	1.27612	-1.55469	-2.37805
C	2.70073	-4.1367	-0.69396
H	3.27451	-5.04948	-0.83318
C	2.32418	-3.36314	-1.78397
H	2.58908	-3.64384	-2.79887
C	2.33043	-3.72953	0.58758
H	2.60046	-4.30327	1.46965
C	1.17088	-2.06434	2.04942
H	0.6026	-2.84902	2.50356
C	-4.11669	-0.7329	-0.51671
H	-2.05905	1.93696	-2.63239
H	2.05898	-1.93692	2.63245

Table V-16. X,Y,Z coordinates for the optimized geometry of V-16 computed as a sextet at the PBE0 level of theory with mod-LANL2DZ (Cu) and 6-31G(d,p) (light atoms) basis sets.

Atom	X	Y	Z
Cu	0	0.00003	0.00002
S	2.79253	1.44428	-0.552
F	5.30419	0.92456	-0.04697
F	3.93064	-0.57588	0.67554
O	2.8282	0.6501	-1.77504
F	4.11134	1.30929	1.7125
O	3.10551	2.86383	-0.65126
O	1.57712	1.19239	0.30626
N	-1.24232	1.81159	0.33852
N	-0.38526	0.83083	-2.19753
C	-1.59806	2.55908	-0.72339
C	-1.59067	2.1987	1.56292
H	-1.27608	1.55475	2.3781
C	-2.70073	4.13675	0.69403
H	-3.27451	5.04953	0.83327
C	-2.32416	3.3632	1.78404
H	-2.58903	3.6439	2.79894
C	-2.33045	3.72958	-0.58751
H	-2.6005	4.30331	-1.46958
C	-1.17093	2.06439	-2.04937
H	-0.60267	2.84907	-2.50354
C	4.1167	0.73282	0.51665
S	-2.79252	-1.44431	0.55196
F	-5.30419	-0.9247	0.04688
F	-3.93068	0.57581	-0.67556
O	-2.82826	-0.65015	1.77501
F	-4.11128	-1.30935	-1.71257
O	-3.10543	-2.86388	0.6512
O	-1.57712	-1.19234	-0.30628
N	1.24232	-1.81154	-0.33847
N	0.38521	-0.83078	2.19756
C	1.59803	-2.55903	0.72344
C	1.5907	-2.19865	-1.56286
H	1.27612	-1.55469	-2.37805
C	2.70073	-4.1367	-0.69396
H	3.27451	-5.04948	-0.83318
C	2.32418	-3.36314	-1.78397
H	2.58908	-3.64384	-2.79887
C	2.33043	-3.72953	0.58758
H	2.60046	-4.30327	1.46965
C	1.17088	-2.06434	2.04942
H	0.6026	-2.84902	2.50356
C	-4.11669	-0.7329	-0.51671
H	-2.05905	1.93696	-2.63239
H	2.05898	-1.93692	2.63245

CHAPTER VI

CONCLUDING REMARKS AND FUTURE DIRECTIONS

In the preceding chapters, we have described strategies towards the spectroscopic and structural characterization of reactive M–L multiply bonded species. We have demonstrated that design of appropriate photoprecursors can engender N–X cleavage over M–N cleavage, which facilitates generation and spectroscopic characterization of reactive intermediates. Moreover, we have demonstrated the potential for photochemical synthesis of reactive M–O complexes via photolysis of metal oxyanion precursors. Challenges with translating solution-phase photoreactions to the solid state have thus far prevented structure characterization of either the photogenerated Mn nitrenoid or Cu oxo species. In contrast, we have demonstrated the utility of *in crystallo* photolysis to structurally characterize a Cu iminyl radical *en route* to a Cu imine complex. The combination of cryogenic spectroscopy and *in situ* structural characterization presents a unique opportunity to characterize reactive species without synthetic derivatization. Furthermore, application of these techniques to catalytically relevant species would resolve questions of chemical and electronic structure, facilitating informed design of next-generation catalysts. However, realizing this strategy requires the development of new classes of photoprecursors to that will allow the capture of both the structural and spectroscopic data.

VI.1. Development of Non-Standard Photoprecursors

Our group has structurally characterized several Rh_2 nitrenes via photocrystallography.[200, 201] These experiments are predicated on organic azide adducts of Rh_2 paddlewheels in which the azide binds through the α-nitrogen (Figure VI-1). Complex **VI-1** serves as a photoprecursor to access reactive a Rh nitrene in either solution or suspended in a KBr pellet as a solid, which results in carbazole formation via nitrene insertion into the *o*-C–H. Generation of nitrene **VI-2** *in crystallo* at 100 K results in a species that is stable under these conditions.

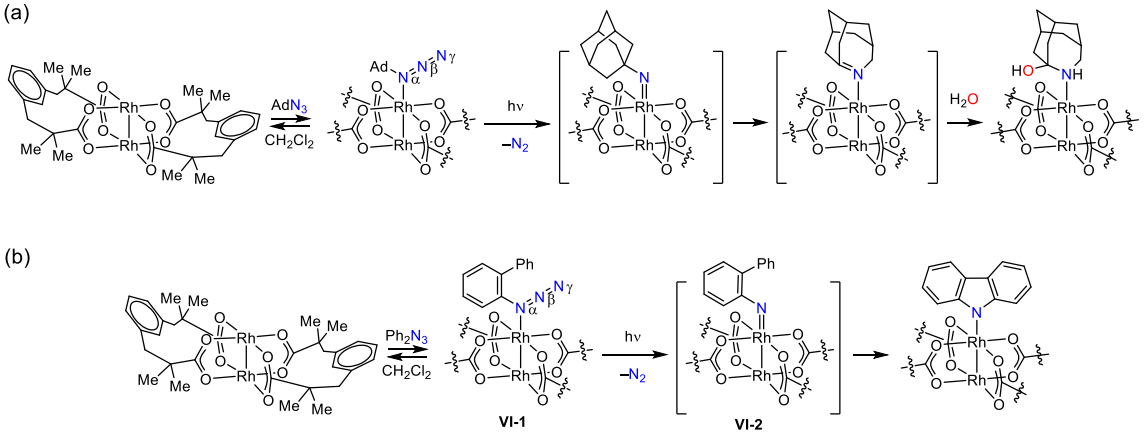

Figure VI-1. Rh_2 molecules with apical azide ligands, that serve as Rh nitrene photoprecursors. (a) $Rh_2(esp)_2(AdN_3)$ serves as a photoprecursor to form a Rh nitrene, which results in a hemiaminal complex. (b) Rh azide **VI**-1 extrudes N_2 upon photolysis affording Rh nitrene **VI-2**. Nitrene **VI-2** will insert into a C–H bond in an intramolecular fashion to afford the Rh carbazole adduct.

While we have had success in structurally characterizing metal nitrenoids *in crystallo* we have been unable to observe the subsequent C–H insertion within the crystalline environment. Room temperature thermolysis of photogenerated Rh nitrenes *in crystallo* results in complete destruction of the crystalline lattice, which we hypothesize is

driven by the expulsion of N_2 from the crystal lattice. Thus, motivated to observe a single-crystal to single-crystal intramolecular C–H insertion, we sought to design new solid-state photoprecursors which extrude non-gaseous leaving groups. Thermolysis of a single-crystal with extruded solids should not lead to crystal degradation, thus facilitating the observation of a *in crystallo* intramolecular C–H insertion.

We synthesized a family of Rh_2 complexes that each feature solid-state leaving groups at 100 K, to serve as prototypes which would lead to the eventual observation of intramolecular C–H chemistry (Figure VI-2). *N*-substituted sulfilimines have been shown to heterolytically cleave the N=S bond upon photolysis, affording a dibenzothiophene fragment and a free nitrene.[39, 365, 366] We hypothesized that a *N*-bound sulfilimine could photochemically generate a Rh nitrene via extrusion of dibenzothiophene, which is a solid under ambient conditions.[367] Despite the photoactivity of **VI-3** in the solution phase, **VI-3** is photochemically inert under *in crystallo* conditions.

Additionally, we hypothesized that *N*-bound aminopyridiniums could also serve as nitrene photoprecursors that feature a solid-state leaving group at 100 K.[368-372] Exposure of $Rh_2(esp)_2$ to either pyridinium tosylamide or pyridinium benzylamide afforded complexes **VI-4** and **VI-5**. Complex **VI-4** features an *O*-bound benzylamide, and complex **VI-5** features an *N*-bound tosylamide. Both complexes **VI-4** and **VI-5** are photochemically inert. Thus, all three Rh_2 complexes, **VI-3**, **VI-4**, and **VI-5** did not exhibit any photochemistry *in crystallo*.

Based on the difficulties photogenerating reactive intermediates using solid-state leaving groups *in crystallo*, we hypothesize that introducing porosity will engender both

gas escape from the crystalline lattice and observation of intramolecular C–H chemistry. Future work will focus on porous materials, such as metal-organic frameworks (MOFs),[373-377] and porous single-crystals,[378-381] to fully structurally characterize the C–H insertion chemistry of photogenerated metal nitrenoids.

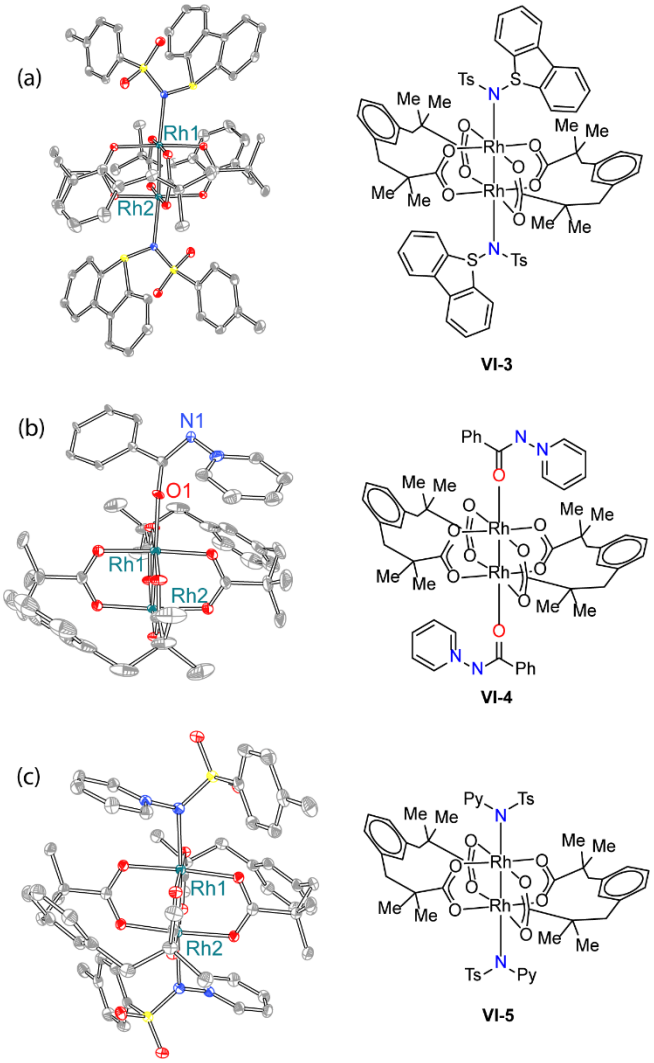

Figure VI-2. Solid-state structures of substituted $Rh_2(esp)_2$ species designed as photoprecursors. Ellipsoids drawn at 50%. H-atoms and solvent molecules are removed for clarity. (a) $Rh_2(esp)_2(sulf\text{-}NTs)_2$ species generated via exposure of $Rh_2(esp)_2$ to sulf-NTs. (b) $Rh_2(esp)_2(py\text{-}ONBz)_2$ species is generated by exposure of $Rh_2(esp)_2$ to py-ONBz. (c) $Rh_2(esp)_2(py\text{-}NTs)_2$ species generated via exposure of $Rh_2(esp)_2$ to py-NTs.

Our group has also been pursuing the development and subsequent characterization of reactive metal imidogen complexes. To this end, we have characterized a $Rh_2(esp)_2(HN_3)_2$ complex via NMR and IR spectroscopy, and single-crystal X-ray diffraction (Figure VI-3). Hydrazoic acid complex **VI-7** is generated via dissolving $Rh_2(esp)_2$ in DCM at –35 °C in the presence of **VI-6**. The IR spectrum of **VI-7** shows stretches at 2358 and 2142 cm^{-1}, which is similar to free hydrazoic acid.[382] Single-crystals of **VI-7** are afforded upon cooling a solution of **VI-7** in DCM at –35 °C. The single-crystal X-ray structure of **VI-7** features a Rh(1)–N(1) bond length of 2.354(4) Å, a N(1)–N(2) bond length of 1.241(4) Å, and a N(2)–N(3) bond length of 1.114(5) Å. Importantly, the H-atom (H(1)) on N(1) was refined from the electron difference map, not added via a riding model, which suggests that **VI-7** is an authentic Rh–N_3H adduct and is the first characterized hydrazoic acid adduct of a transition metal. Additionally, the N(1)–N(2) and N(2)–N(3) distances are well-matched to the only other structurally characterized HN_3 adduct, a $B(C_6F_5)_3$–N_3H complex.[383]. Future work will include investigating the potential reactivity of a putative Rh–NH nitrene via photolysis and thermolysis of **VI-7**, however preliminary photocrystallographic studies were not successful in generating a Rh nitrene.

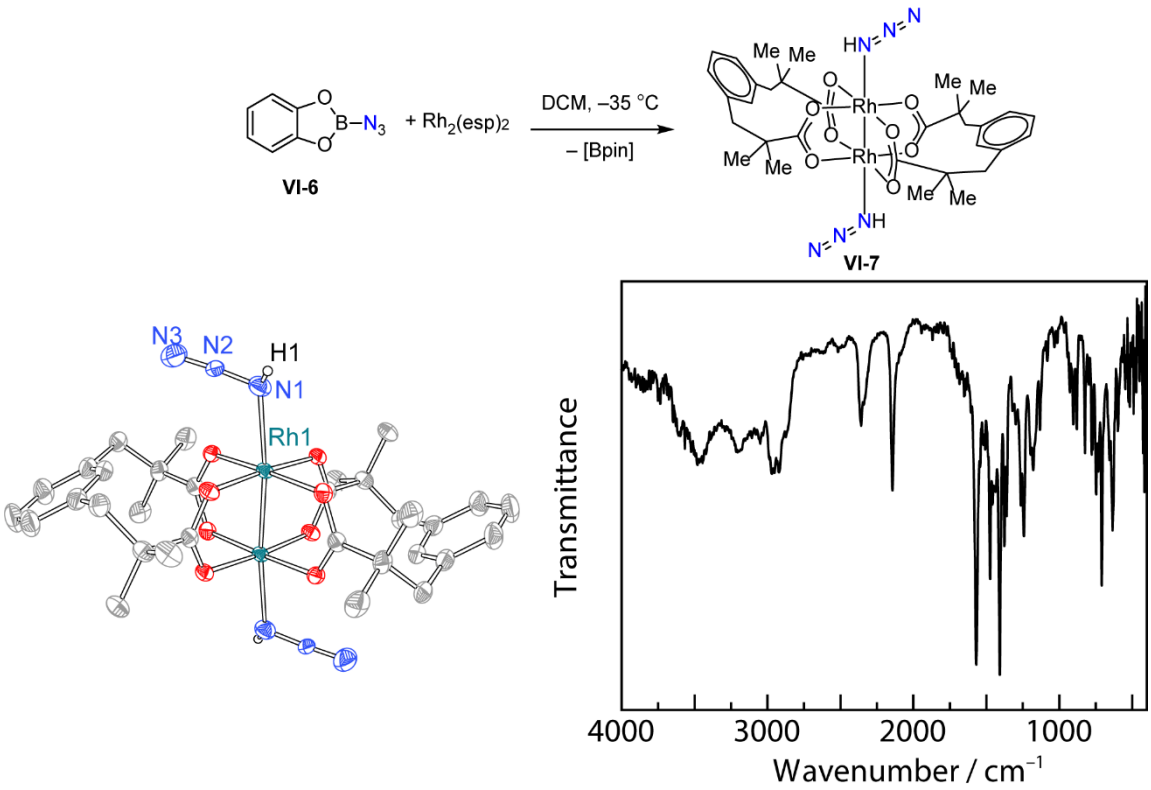

Figure VI-3. $Rh_2(esp)_2(HN_3)_2$ species generated by exposure of $Rh_2(esp)_2$ and pinacolboryl azide. Left: Thermal ellipsoid plot of **VI-7**. H-atoms and solvents are removed for clarity. H(1) was refined from the electron difference map and was not added via riding model. Right: IR spectrum of **VI-7**, which features stretches at 2358 and 2142 cm^{-1} and are well matched to free HN_3.

VI.2. Extension to Characterization of Other M–L Species

Extension of our preliminary experiments in reactive nitrenes to the characterization of other reactive transition metal fragments would demonstrate the generality of the developed photocrystallography experiments. In collaboration with Schneider, Holthausen, and co-workers, we have characterized a palladium metallonitrene via photocrystallography (Figure VI-4).[289] Photolysis (λ = 365 nm) of a single-crystal of **VI-8** under cryogenic conditions (100 K) promoted *in crystallo* synthesis of Pd nitrene

VI-9. Reaction progress was monitored by periodic collection of X-ray crystal structures (synchrotron radiation λ = 0.41328 Å). Refinement of the resulting data indicated that the extrusion of N_2 gas generates Pd nitrene with 40% conversion (Figure VI-4). Extrusion of N_2 from **VI-9** is accompanied by the contraction of Pd–N from 2.050(2) Å to 1.92(2) Å, which agrees with the computed distance of 1.891 Å. This observation is similar to *in crystallo* photopromoted N_2 extrusion in Pt azide complexes, which forms a Pt nitrene with a Pt–N bond of 1.87(1) Å.[384]

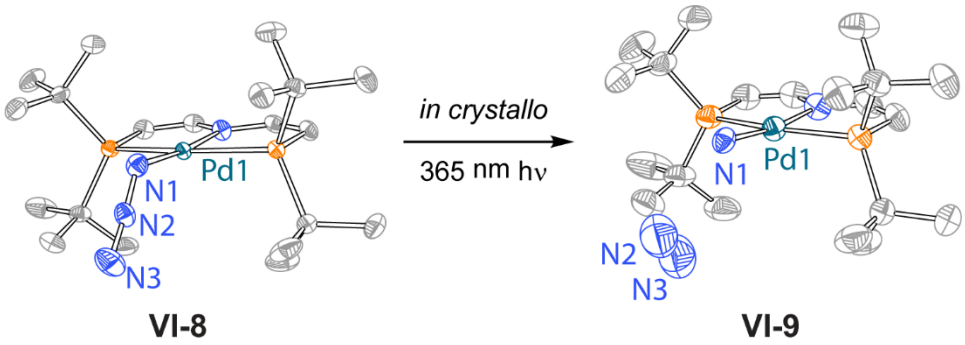

Figure VI-4. Solid state structures of Pd azide VI-8 and Pd nitrene VI-9. Thermal ellipsoid plot of **VI-9** generated by solid-state N_2 extrusion from **VI-8**. Ellipsoids are drawn at 50% probability. H-atoms are removed for clarity. The structure illustrated here comes from refinement of a data set collected at 40% conversion. Data was collected using synchrotron radiation (λ = 0.41328 Å). The restraint SIMU was used on the disordered *N*-atoms of the N_2 molecule. Comparison of the bond metrics derived from the X-ray structure with those computed for ^{3}[**VI-9**] are in excellent agreement.

Additionally, we have structurally characterized a terminal Pt phospide, which in solution will dimerize to form a P_2 molecule.[385] Photolysis (λ = 365 nm) of a single-crystal of **VI-10** under cryogenic conditions (100 K) promoted *in crystallo* synthesis of Pt phosphide **VI-11**. Reaction progress was monitored by periodic collection of X-ray crystal structures (synchrotron radiation λ = 0.41328 Å). Refinement of the resulting data

indicated that the extrusion of CO gas generates Pt phosphide with 42% conversion (Figure VI-5). Extrusion of CO from **VI-11** is accompanied by the contraction of Pt–P from 2.357(2) Å to 2.28(4) Å. Refinement of CO in the resulting structure was complicated due to the partial loss of the molecule from the crystalline lattice; CO occupancies were found to be 15%, whereas the Pt phosphide was 42%, thus the refinement of the CO was not pursued further. This is the first example of photopromoted *in crystallo* CO extrusion from a phosphaethynolate (PCO) to form a terminal metal phosphide. We hypothesize that photosynthesis of reactive intermediates *in crystallo* is facilitated by good leaving groups, such as gasses like N_2 and CO. We anticipate that other reactive metal phosphides can be structurally characterized *in crystallo* via extrusion of CO from metal phosphaethynolate photoprecursors.

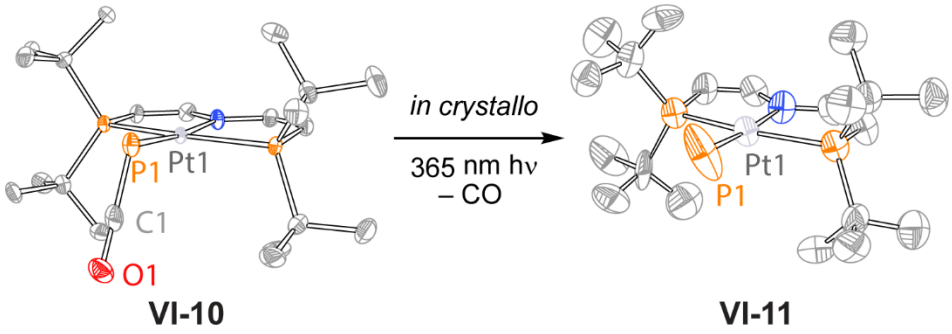

Figure VI-5. Solid state structures of Pt phosphaethynolate VI-10 and terminal Pt phosphide VI-11. Thermal ellipsoid plot of **VI-11** generated by solid-state CO extrusion from VI-10. Ellipsoids are drawn at 50% probability. H-atoms are removed for clarity. The structure illustrated here comes from refinement of a data set collected at 42% conversion. Data was collected using synchrotron radiation (λ = 0.41328 Å).

We have also structurally characterized a Cu carbene complex in collaboration with Severin and co-workers, which will dimerize in solution to form a C=C bonds.[386]

Photolysis (λ = 365 nm) of a single-crystal of **VI-12** under cryogenic conditions (100 K) promoted *in crystallo* synthesis of Cu carbene **VI-13**. Reaction progress was monitored by periodic collection of X-ray crystal structures (synchrotron radiation λ = 0.41328 Å). Refinement of the resulting data indicated that the extrusion of N_2 gas generates the Cu carbene with 62% conversion (Figure VI-6). Extrusion of N_2 from **VI-12** is accompanied by the contraction of C–C from 1.425(6) Å to 1.39(3) Å and contraction of the Cu–C bond from 1.900(4) Å to 1.88(2) Å. Preliminary DFT computational studies of ^{3}[**VI-13**] match well with experiment, which predicts a bent C(2)–C(1)–Cu(1) bond angle, whereas the computed structure of ^{1}[**VI-13**] predicts a linear C(2)–C(1)–Cu(1) bond angle. However, the difference in energy between ^{3}[**VI-13**] and ^{1}[**VI-13**] is 0.28 kcal/mol, thus multi-reference calculations are required to make an accurate comment on the electronic structure of **VI-13**. While the electronic structure of **VI-13** is currently being investigated, this preliminary study suggests potential covalency in the Cu(1)–C(1) bond. The C(2)–C(1)–Cu(1) bond angle increases upon conversion of **VI-12** to **VI-13**, from 129.5(3)° to 138.1(2)°, which suggests that a lone pair could reside on C(1). This bonding picture is reminiscent of free carbenes, which feature two R-groups (*e .g.* C(2) and Cu(1)) and a lone pair on the carbene carbon.[387, 388]

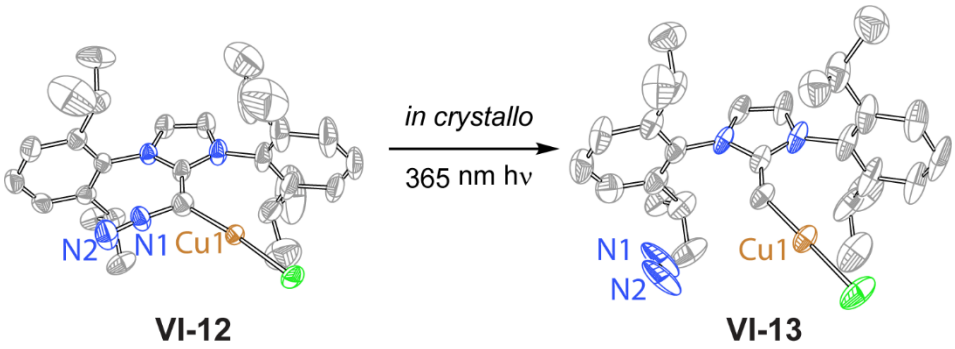

Figure VI-6. Solid state structures of Cu diazoolefin VI-12 and Cu carbene VI-13. Thermal ellipsoid plot of VI-13 generated by solid-state N_2 extrusion from **VI-12**. Ellipsoids are drawn at 50% probability. H-atoms are removed for clarity. The structure illustrated here comes from refinement of a data set collected at 62% conversion. Data was collected using synchrotron radiation ($\lambda = 0.41328$ Å). The restraints DFIX and EADP were used to refine the disordered *N*-atoms in the N_2 molecule. The restraints DFIX, EADP, SADI, and SAME_LIG were used to refine the disordered Cu carbene molecule.

The impact of photocrystallography towards studying reactive intermediates is limited by the availability of photoprecursors which are photoactive in the solid state. We have been successful in structurally characterizing a diverse set of M–L multiply bound reactive intermediates *in crystallo* via extrusion of gaseous species at 100 K. To continue to expand the library of reactive photoprecursors, which facilitate reactive intermediate structural characterization *in crystallo*, we propose two criteria that need to be met when designing solid-state photoprecursors: First, the molecule must exhibit photoactivity in the solid-state and second, the molecule should feature a leaving group that is a gas at 100 K to help drive the photochemistry in the solid-state.

Lewis base stabilized borylene complexes are similar to both carbene and nitrenes, where the boron atom features only six valence electrons, thus borylenes are exquisitely electrophilic and will insert into a variety of bonds, *e.g.* C–H bonds. Braunschweig *et al.*

reported an CAAC supported aryl boron complex **VI-14**, which meets both criteria listed above to be an excellent solid-state photoprecursor towards structurally characterizing a reactive borylene (Figure VI-7).[387, 389] Compound **VI-14** extrudes CO upon photolysis, affording putative borylene **VI-15,** which then undergoes intramolecular C–H insertion affording cyclized product **VI-16**. The *in crystallo* structural characterization of borylene **VI-15** should be an important addition to the small library of extant structurally characterized borylenes.[390, 391]

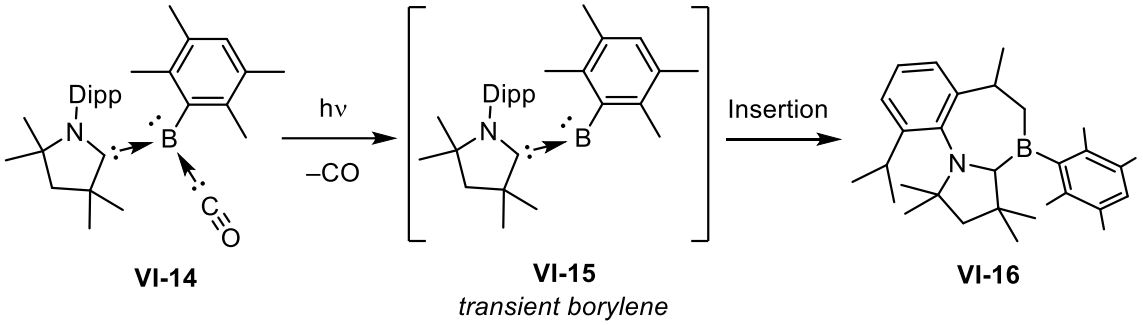

Figure VI-7. Trapped three-coordinate borylene VI-14 extrudes CO upon photolysis, to afford two-coordinate borylene VI-15. VI-15 can either be trapped via addition of Lewis bases, or in via intramolecular C–H insertion to afford VI-16.

Furthermore, we hypothesize that development of new metal phosphaethynolate complexes will provide a platform to synthesize novel metal phosphide compounds, examine their reactivity, and characterize both the chemical and electronic structure. Metal porphyrin complexes are an ideal scaffold to support a metal phosphide, as they support a myriad of structurally characterized metal oxos,[392-394] metal nitrides,[105, 395] metal imides,[202, 396-398] and metal carbene complexes.[325, 399-401] We hypothesize that utilization of early transition metals such as Ti, V, Cr, Zr, Nb, and Mo will form stable porphyrin supported terminal phosphides. Potential difficulties stem from the ambidentate character

of the PCO^- ion, which can bind either *P*- or *O*-bound.[402, 403] Additionally, Mindiola and coworkers have studied early transition metal complexes with PCO, and while stable metal PCO adducts are known,[404] they have found that the relative stability of metal PCO complexes can be low, and thus many dimerized and other phosphorus incorporated products were isolated.[405-408] Cryogenic synthesis and crystallization of metal phosphaethynolate complexes should be feasible, and subsequent photolysis *in crystallo* could circumvent most decomposition pathways.

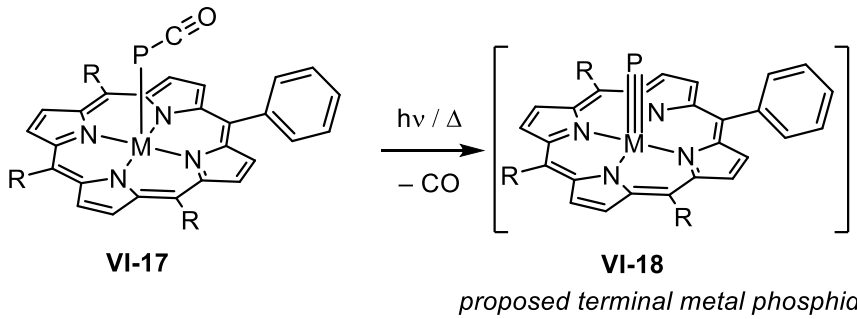

VI-17 **VI-18**

proposed terminal metal phosphide

Figure VI-8. Proposed M(tpp)P synthesis via photolysis or thermolysis of M(tpp)PCO, extruding CO and affording a terminal metal phosphide.

VI.3. Future Directions

We have demonstrated that photocrystallography is a unique tool which elucidates the chemical structure of M–L multiply bound reactive intermediates. Moving forward, we envision that the combination of photocrystallography with single-crystal spectroscopy preformed on the beamline such as UV-Vis, Raman, and XAS will facilitate the interrogation of the electronic structure of these reactive intermediates. Chapter II described efforts to spectroscopically characterize the photogenerated reactive Mn nitrenoids present in solution, which are responsible for inserting into C–H bonds. To fully

understand the active species in solution, we propose that once both the chemical and electronic structure of a reactive intermediate is understood, via the single-crystal experiments, comparison to the solution/frozen matrix spectroscopy will allow unambiguous determination of the reactive intermediate involved in the chemistry. We anticipate that the discoveries made via the combination of photocrystallography and spectroscopy will be used to leverage the design of more reactive and selective catalysts.

REFERENCES

1. Blanksby, S. J.; Ellison, G. B., Bond Dissociation Energies of Organic Molecules. *Acc. Chem. Res.* **2003,** *36*, 255–263.

2. Breslow, R.; Heyer, D., Catalytic multiple template-directed steroid chlorinations. *J. Am. Chem. Soc.* **1982,** *104*, 2045–2046.

3. Wolff, M. E., Cyclization of N-Halogenated Amines (The Hofmann-Löffler Reaction). *Chem. Rev.* **1963,** *63*, 55–64.

4. Davies, H. M. L. M., Daniel, Recent Advances in C–H Functionalization. *The Journal of Organic Chemistry* **2016,** *81*, 343–350.

5. Arndtsen, B. A.; Bergman, R. G.; Mobley, T. A.; Peterson, T. H., Selective Intermolecular Carbon-Hydrogen Bond Activation by Synthetic Metal Complexes in Homogeneous Solution. *Acc. Chem. Res.* **1995,** *28*, 154–162.

6. Cho, S. H.; Kim, J. Y.; Kwak, J.; Chang, S., Recent advances in the transition metal-catalyzed twofold oxidative C–H bond activation strategy for C–C and C–N bond formation. *Chem. Soc. Rev.* **2011,** *40*, 5068–5083.

7. Arockiam, P. B.; Bruneau, C.; Dixneuf, P. H., Ruthenium(II)-Catalyzed C–H Bond Activation and Functionalization. *Chem. Rev.* **2012,** *112*, 5879–5918.

8. Mkhalid, I. A. I.; Barnard, J. H.; Marder, T. B.; Murphy, J. M.; Hartwig, J. F., C−H Activation for the Construction of C−B Bonds. *Chem. Rev.* **2010,** *110*, 890–931.

9. Song, G.; Wang, F.; Li, X., C–C, C–O and C–N bond formation via rhodium(iii)-catalyzed oxidative C–H activation. *Chem. Soc. Rev.* **2012,** *41*, 3651–3678.

10. Wencel-Delord, J.; Dröge, T.; Liu, F.; Glorius, F., Towards mild metal-catalyzed C–H bond activation. *Chem. Soc. Rev.* **2011,** *40*, 4740–4761.

11. Guo, X.-X.; Gu, D.-W.; Wu, Z.; Zhang, W., Copper-Catalyzed C–H Functionalization Reactions: Efficient Synthesis of Heterocycles. *Chem. Rev.* **2015,** *115*, 1622–1651.

12. Lyons, T. W.; Sanford, M. S., Palladium-Catalyzed Ligand-Directed C−H Functionalization Reactions. *Chem. Rev.* **2010,** *110*, 1147–1169.

13. Yang, Y.; Arnold, F. H., Navigating the Unnatural Reaction Space: Directed Evolution of Heme Proteins for Selective Carbene and Nitrene Transfer. *Acc. Chem. Res.* **2021,** *54*, 1209–1225.

14. Lewis, J. C.; Coelho, P. S.; Arnold, F. H., Enzymatic functionalization of carbon–hydrogen bonds. *Chem. Soc. Rev.* **2011,** *40*, 2003–2021.

15. Ren, X.; Fasan, R., Engineered and artificial metalloenzymes for selective C–H functionalization. *Current Opinion in Green and Sustainable Chemistry* **2021,** *31*, 100494.

16. Ju, M.; Schomaker, J. M., Nitrene transfer catalysts for enantioselective C–N bond formation. *Nat. Rev. Chem.* **2021,** *5*, 580–594.

17. Davies, H. M. L.; Manning, J. R., Catalytic C–H functionalization by metal carbenoid and nitrenoid insertion. *Nature* **2008,** *451*, 417–424.

18. Davies, H. M. L.; Beckwith, R. E. J., Catalytic Enantioselective C−H Activation by Means of Metal−Carbenoid-Induced C−H Insertion. *Chem. Rev.* **2003,** *103*, 2861–2904.

19. Davies, H. M. L.; Morton, D., Guiding principles for site selective and stereoselective intermolecular C–H functionalization by donor/acceptor rhodium carbenes. *Chem. Soc. Rev.* **2011,** *40*, 1857–1869.

20. Shin, K.; Kim, H.; Chang, S., Transition-Metal-Catalyzed C–N Bond Forming Reactions Using Organic Azides as the Nitrogen Source: A Journey for the Mild and Versatile C–H Amination. *Acc. Chem. Res.* **2015,** *48*, 1040–1052.

21. Huang, X.; Groves, J. T., Oxygen Activation and Radical Transformations in Heme Proteins and Metalloporphyrins. *Chem. Rev.* **2018,** *118*, 2491–2553.

22. Stavropoulos, P., Metal-Catalyzed and Metal-Free Intermolecular Amination of Light Alkanes and Benzenes. *Comments Inorg. Chem.* **2017,** *37*, 1–57.

23. Berry, J. F., TERMINAL NITRIDO AND IMIDO COMPLEXES OF THE LATE TRANSITION METALS. *Comments Inorg. Chem.* **2009,** *30*, 28–66.

24. Rittle, J.; Green, M. T., Cytochrome P450 Compound I: Capture, Characterization, and C-H Bond Activation Kinetics. *Science* **2010,** *330*, 933–937.

25. Nam, W., High-Valent Iron(IV)–Oxo Complexes of Heme and Non-Heme Ligands in Oxygenation Reactions. *Acc. Chem. Res.* **2007,** *40*, 522–531.

26. Meunier, B.; de Visser, S. P.; Shaik, S., Mechanism of Oxidation Reactions Catalyzed by Cytochrome P450 Enzymes. *Chem. Rev.* **2004,** *104*, 3947–3980.

27. Meinhold, P.; Peters, M. W.; Chen, M. M. Y.; Takahashi, K.; Arnold, F. H., Direct Conversion of Ethane to Ethanol by Engineered Cytochrome P450 BM3. *Chem. Bio. Chem.* **2005,** *6*, 1765–1768.

28. Castillo, R. G.; Banerjee, R.; Allpress, C. J.; Rohde, G. T.; Bill, E.; Que, L.; Lipscomb, J. D.; DeBeer, S., High-Energy-Resolution Fluorescence-Detected X-ray Absorption of the Q Intermediate of Soluble Methane Monooxygenase. *J. Am. Chem. Soc.* **2017,** *139*, 18024–18033.

29. Che, C.-M.; Lo, V. K.-Y.; Zhou, C.-Y.; Huang, J.-S., Selective functionalisation of saturated C–H bonds with metalloporphyrin catalysts. *Chem. Soc. Rev.* **2011,** *40*, 1950–1975.

30. Breslow, R.; Gellman, S. H., Intramolecular nitrene carbon-hydrogen insertions mediated by transition-metal complexes as nitrogen analogs of cytochrome P-450 reactions. *J. Am. Chem. Soc.* **1983,** *105*, 6728–6729.

31. Singh, R.; Mukherjee, A., Metalloporphyrin Catalyzed C–H Amination. *ACS Catal.* **2019,** *9*, 3604–3617.

32. Groves, J. T.; Gross, Z.; Stern, M. K., Preparation and Reactivity of Oxoiron(IV) Porphyrins. *Inorg. Chem.* **1994,** *33*, 5065–5072.

33. Groves, J. T.; Haushalter, R. C.; Nakamura, M.; Nemo, T. E.; Evans, B. J., High-valent iron-porphyrin complexes related to peroxidase and cytochrome P-450. *J. Am. Chem. Soc.* **1981,** *103*, 2884–2886.

34. Song, W. J.; Seo, M. S.; DeBeer George, S.; Ohta, T.; Song, R.; Kang, M.-J.; Tosha, T.; Kitagawa, T.; Solomon, E. I.; Nam, W., Synthesis, Characterization, and Reactivities of Manganese(V)−Oxo Porphyrin Complexes. *J. Am. Chem. Soc.* **2007,** *129*, 1268–1277.

35. Goswami, M.; Lyaskovskyy, V.; Domingos, S. R.; Buma, W. J.; Woutersen, S.; Troeppner, O.; Ivanović-Burmazović, I.; Lu, H.; Cui, X.; Zhang, X. P.; Reijerse, E. J.; DeBeer, S.; van Schooneveld, M. M.; Pfaff, F. F.; Ray, K.; de Bruin, B., Characterization of Porphyrin-Co(III)-'Nitrene Radical' Species Relevant in Catalytic Nitrene Transfer Reactions. *J. Am. Chem. Soc.* **2015,** *137*, 5468–5479.

36. Fairchild, P. W.; Smith, G. P.; Crosley, D. R.; Jeffries, J. B., Lifetimes and transition probabilities for NH(A3Πi-X3Σ−). *Chem. Phys. Lett.* **1984,** *107*, 181–186.

37. Rauk, A.; Alewood, P. F., A theoretical study of the Curtius rearrangement. The electronic structures and interconversions of the CHNO species. *Can, J. Chem.* **1977,** *55*, 1498–1510.

38. L'Abbe, G., Decomposition and addition reactions of organic azides. *Chem. Rev.* **1969,** *69*, 345–363.

39. Desikan, V.; Liu, Y.; Toscano, J. P.; Jenks, W. S., Photochemistry of N-Acetyl-, N-Trifluoroacetyl-, N- Mesyl-, and N-Tosyldibenzothiophene Sulfilimines. *J. Org. Chem.* **2008,** *73*, 4398–4414.

40. Liu, J.; Mandel, S.; Hadad, C. M.; Platz, M. S., A Comparison of Acetyl- and Methoxycarbonylnitrenes by Computational Methods and a Laser Flash Photolysis Study of Benzoylnitrene. *J. Org. Chem.* **2004,** *69*, 8583–8593.

41. Pritchina, E. A.; Gritsan, N. P.; Bally, T., Ground state multiplicity of acylnitrenes: computational and experimental studies. *Russ. Chem. Bull.* **2005,** *54*, 525–532.

42. Faustov, V. I.; Baskir, E. G.; Biryukov, A. A., Thermal isomerization of acetylnitrene: a quantum-chemical study. *Russ. Chem. Bull.* **2003,** *52*, 2328–2333.

43. Sigman, M. E.; Autrey, T.; Schuster, G. B., Aroylnitrenes with singlet ground states: photochemistry of acetyl-substituted aroyl and aryloxycarbonyl azides. *J. Am. Chem. Soc.* **1988,** *110*, 4297–4305.

44. Pritchina, E. A.; Gritsan, N. P.; Maltsev, A.; Bally, T.; Autrey, T.; Liu, Y.; Wang, Y.; Toscano, J. P., Matrix isolation, time-resolved IR, and computational study of the photochemistry of benzoyl azide. *Phys. Chem. Chem. Phys.* **2003,** *5*, 1010–1018.

45. McConaghy, J. S.; Lwowski, W., Singlet and triplet nitrenes. I. Carbethoxynitrene generated by .alpha. elimination. *J. Am. Chem. Soc.* **1967,** *89*, 2357–2364.

46. Meth-Cohn, O., New synthetic applications of oxycarbonylnitrenes. *Acc. Chem. Res.* **1987,** *20*, 18–27.

47. Wasserman, E., Electron Spin Resonance of Nitrenes. In *Progress in Physical Organic Chemistry*, 1971; pp 319-336.

48. Hafner, K.; Kaiser, W.; Puttner, R., Zur stereoselektivität der addition der alkoxycarbonyl-nitrene an olefine. *Tetrahedron Lett.* **1964,** *5*, 3953–3956.

49. Buron, C.; Platz, M. S., Laser Flash Photolysis Study of Carboethoxynitrene. *Org. Lett.* **2003,** *5*, 3383–3385.

50. Moriarty, R. M.; Serridge, P., Thermal decomposition of geminal diazides. *J. Am. Chem. Soc.* **1971,** *93*, 1534–1535.

51. Pinto, R. M.; Guerra, M.; Copeland, G.; Olariu, R. I.; Rodrigues, P.; Barros, M. T.; Costa, M. L.; Dias, A. A., The Mechanism of Pyrolysis of Benzyl Azide: Spectroscopic Evidence for Benzenemethanimine Formation. *J. Phys. Chem. A* **2015,** *119*, 4118–4126.

52. Boyer, J. H.; Straw, D., Azidocarbonyl Compounds. II. The Pyrolysis of α-Azidocarbonyl Compounds1a. *J. Am. Chem. Soc.* **1953,** *75*, 1642–1644.

53. Bock, H.; Dammel, R., Gas-phase reactions. 66. Gas-phase pyrolyses of alkyl azides: experimental evidence for chemical activation. *J. Am. Chem. Soc.* **1988,** *110*, 5261–5269.

54. Abramovitch, R. A.; Kyba, E. P., Photodecomposition of alkyl azides. Absence of freedom of choice and nonnitrene mechanism. *J. Am. Chem. Soc.* **1971,** *93*, 1537–1538.

55. Morawietz, J.; Sander, W.; Traeubel, M., Intramolecular Hydrogen Transfer in (2-Aminophenyl)carbene and 2-Tolylnitrene. Matrix Isolation of 6-Methylene-2,4-cyclohexadien-1-imine. *J. Org. Chem.* **1995,** *60*, 6368–6378.

56. Mandel, S. M.; Krause Bauer, J. A.; Gudmundsdottir, A. D., Photolysis of α-Azidoacetophenones: Trapping of Triplet Alkyl Nitrenes in Solution. *Org. Lett.* **2001,** *3*, 523–526.

57. Klima, R. F.; Gudmundsdóttir, A. D., Intermolecular triplet-sensitized photolysis of alkyl azides: Trapping of triplet alkyl nitrenes. *J. Photochem. Photobiol., A* **2004,** *162*, 239–247.

58. Kwart, H.; Kahn, A. A., Copper-Catalyzed Decomposition of Benzenesulfonyl Azide in Hydroxylic Media. *J. Am. Chem. Soc.* **1967,** *89*, 1950–1951.

59. Kwart, H.; Khan, A. A., Copper-Catalyzed Decomposition of Benzenesulfonyl Azide in Cyclohexene Solution. *J. Am. Chem. Soc.* **1967,** *89*, 1951–1953.

60. Carsch, K. M.; DiMucci, I. M.; Iovan, D. A.; Li, A.; Zheng, S.-L.; Titus, C. J.; Lee, S. J.; Irwin, K. D.; Nordlund, D.; Lancaster, K. M.; Betley, T. A., Synthesis of a

copper-supported triplet nitrene complex pertinent to copper-catalyzed amination. *Science* **2019,** *365*, 1138–1143.

61. Breslow, R.; Gellman, S. H., Tosylamidation of cyclohexane by a cytochrome P-450 model. *J. Chem. Soc., Chem. Commun.* **1982**, 1400–1401.

62. Mahy, J. P.; Bedi, G.; Battioni, P.; Mansuy, D., Allylic amination of alkenes by tosyliminoiodobenzene: manganese porphyrins as suitable catalysts. *Tetrahedron Lett.* **1988,** (16), 1927–1930.

63. Yang, J.; Weinberg, R.; Breslow, R., The hydroxylation and amidation of equilenin acetate catalyzed by chloro[5,10,15,20-tetrakis(pentafluorophenyl)porphyrinato]manganese(). *Chem. Commun.* **2000**, 531–532.

64. Liang, J.-L.; Huang, J.-S.; Yu, X.-Q.; Zhu, N.; Che, C.-M., Metalloporphyrin-Mediated Asymmetric Nitrogen-Atom Transfer to Hydrocarbons: Aziridination of Alkenes and Amidation of Saturated C−H Bonds Catalyzed by Chiral Ruthenium and Manganese Porphyrins. *Chem. Eur. J.* **2002,** *8*, 1563–1572.

65. Clark, J. R.; Feng, K.; Sookezian, A.; White, M. C., Manganese-catalysed benzylic C(sp3)–H amination for late-stage functionalization. *Nat. Chem.* **2018,** *10*, 583–591.

66. Liu, Y.; You, T.; Wang, H.-X.; Tang, Z.; Zhou, C.-Y.; Che, C.-M., Iron- and cobalt-catalyzed C(sp3)–H bond functionalization reactions and their application in organic synthesis. *Chem. Soc. Rev.* **2020,** *49*, 5310–5358.

67. Liu, Y.; Che, C.-M., [FeIII(F20-tpp)Cl] Is an Effective Catalyst for Nitrene Transfer Reactions and Amination of Saturated Hydrocarbons with Sulfonyl and Aryl

Azides as Nitrogen Source under Thermal and Microwave-Assisted Conditions. *Chem. Eur. J.* **2010,** *16*, 10494–10501.

68. Liu, Y.; Wei, J.; Che, C.-M., [Fe(F20TPP)Cl] catalyzed intramolecular C–N bond formation for alkaloid synthesis using aryl azides as nitrogen source. *Chem. Commun.* **2010,** *46*, 6926–6928.

69. Shing, K.-P.; Liu, Y.; Cao, B.; Chang, X.-Y.; You, T.; Che, C.-M., N-Heterocyclic Carbene Iron(III) Porphyrin-Catalyzed Intramolecular C(sp3)–H Amination of Alkyl Azides. *Angew. Chem. Int. Ed.* **2018,** *57*, 11947–11951.

70. Lu, H.; Zhang, X. P., Catalytic C–H functionalization by metalloporphyrins: recent developments and future directions. *Chem. Soc. Rev.* **2011,** *40* (4), 1899–1909.

71. Cenini, S.; Tollari, S.; Penoni, A.; Cereda, C., Catalytic amination of unsaturated hydrocarbons: reactions of p-nitrophenylazide with alkenes catalysed by metallo-porphyrins. *J. Mol. Catal. A: Chem.* **1999,** *137*, 135–146.

72. Ragaini, F.; Penoni, A.; Gallo, E.; Tollari, S.; Li Gotti, C.; Lapadula, M.; Mangioni, E.; Cenini, S., Amination of Benzylic C□H Bonds by Arylazides Catalyzed by CoII–Porphyrin Complexes: A Synthetic and Mechanistic Study. *Chem. Eur. J.* **2003,** *9*, 249–259.

73. Vyas, R.; Gao, G.-Y.; Harden, J. D.; Zhang, X. P., Iron(III) Porphyrin Catalyzed Aziridination of Alkenes with Bromamine-T as Nitrene Source. *Org. Lett.* **2004,** (12), 1907–1910.

74. Gao, G.-Y.; Harden, J. D.; Zhang, X. P., Cobalt-Catalyzed Efficient Aziridination of Alkenes. *Org. Lett.* **2005,** *7*, 3191–3193.

75. Harden, J. D.; Ruppel, J. V.; Gao, G.-Y.; Zhang, X. P., Cobalt-catalyzed intermolecular C–H amination with bromamine-T as nitrene source. *Chem. Commun.* **2007**, 4644–4646.

76. Gao, G.-Y.; Jones, J. E.; Vyas, R.; Harden, J. D.; Zhang, X. P., Cobalt-Catalyzed Aziridination with Diphenylphosphoryl Azide (DPPA): Direct Synthesis of N-Phosphorus-Substituted Aziridines from Alkenes. *J. Org. Chem.* **2006,** *71*, 6655–6658.

77. Ruppel, J. V.; Kamble, R. M.; Zhang, X. P., Cobalt-Catalyzed Intramolecular C−H Amination with Arylsulfonyl Azides. *Org. Lett.* **2007,** *9*, 4889–4892.

78. Lu, H.; Subbarayan, V.; Tao, J.; Zhang, X. P., Cobalt(II)-Catalyzed Intermolecular Benzylic C−H Amination with 2,2,2-Trichloroethoxycarbonyl Azide (TrocN3). *Organometallics* **2010,** *29*, 389–393.

79. Ruppel, J. V.; Jones, J. E.; Huff, C. A.; Kamble, R. M.; Chen, Y.; Zhang, X. P., A Highly Effective Cobalt Catalyst for Olefin Aziridination with Azides: Hydrogen Bonding Guided Catalyst Design. *Org. Lett.* **2008,** *10*, 1995–1998.

80. Subbarayan, V.; Ruppel, J. V.; Zhu, S.; Perman, J. A.; Zhang, X. P., Highly asymmetric cobalt-catalyzed aziridination of alkenes with trichloroethoxysulfonyl azide (TcesN3). *Chem. Commun.* **2009**, 4266–4268.

81. Lu, H.; Jiang, H.; Wojtas, L.; Zhang, X. P., Selective Intramolecular C□H Amination through the Metalloradical Activation of Azides: Synthesis of 1,3-Diamines under Neutral and Nonoxidative Conditions. *Angew. Chem. Int. Ed.* **2010,** *49*, 10192–10196.

82. Lu, H.; Jiang, H.; Hu, Y.; Wojtas, L.; Zhang, X. P., Chemoselective intramolecular allylic C–H aminationversus C□C aziridination through Co(ii)-based metalloradical catalysis. *Chem. Sci.* **2011,** *2*, 2361–2366.

83. Lu, H.; Hu, Y.; Jiang, H.; Wojtas, L.; Zhang, X. P., Stereoselective Radical Amination of Electron-Deficient C(sp3)–H Bonds by Co(II)-Based Metalloradical Catalysis: Direct Synthesis of α-Amino Acid Derivatives via α-C–H Amination. *Org. Lett.* **2012,** *14*, 5158–5161.

84. Jin, L.-M.; Xu, X.; Lu, H.; Cui, X.; Wojtas, L.; Zhang, X. P., Effective Synthesis of Chiral N-Fluoroaryl Aziridines through Enantioselective Aziridination of Alkenes with Fluoroaryl Azides. *Angew. Chem. Int. Ed.* **2013,** *52*, 5309–5313.

85. Jin, L.-M.; Lu, H.; Cui, Y.; Lizardi, C. L.; Arzua, T. N.; Wojtas, L.; Cui, X.; Zhang, X. P., Selective radical amination of aldehydic C(sp2)–H bonds with fluoroaryl azides via Co(ii)-based metalloradical catalysis: synthesis of N-fluoroaryl amides from aldehydes under neutral and nonoxidative conditions. *Chem. Sci.* **2014,** *5*, 2422–2427.

86. Lu, H.; Li, C.; Jiang, H.; Lizardi, C. L.; Zhang, X. P., Chemoselective Amination of Propargylic C(sp3)□H Bonds by Cobalt(II)-Based Metalloradical Catalysis. *Angew. Chem. Int. Ed.* **2014,** *53*, 7028–7032.

87. Lu, H.; Lang, K.; Jiang, H.; Wojtas, L.; Zhang, X. P., Intramolecular 1,5-C(sp3)–H radical amination via Co(ii)-based metalloradical catalysis for five-membered cyclic sulfamides. *Chem. Sci.* **2016,** *7*, 6934–6939.

88. Jiang, H.; Lang, K.; Lu, H.; Wojtas, L.; Zhang, X. P., Intramolecular Radical Aziridination of Allylic Sulfamoyl Azides by Cobalt(II)-Based Metalloradical Catalysis:

Effective Construction of Strained Heterobicyclic Structures. *Angew. Chem. Int. Ed.* **2016,** *55*, 11604–11608.

89. Jiang, H.; Lang, K.; Lu, H.; Wojtas, L.; Zhang, X. P., Asymmetric Radical Bicyclization of Allyl Azidoformates via Cobalt(II)-Based Metalloradical Catalysis. *J. Am. Chem. Soc.* **2017,** *139*, 9164–9167.

90. Li, C.; Lang, K.; Lu, H.; Hu, Y.; Cui, X.; Wojtas, L.; Zhang, X. P., Catalytic Radical Process for Enantioselective Amination of C(sp3)−H Bonds. *Angew. Chem. Int. Ed.* **2018,** *57*, 16837–16841.

91. Hu, Y.; Lang, K.; Tao, J.; Marshall, M. K.; Cheng, Q.; Cui, X.; Wojtas, L.; Zhang, X. P., Next-Generation D2-Symmetric Chiral Porphyrins for Cobalt(II)-Based Metalloradical Catalysis: Catalyst Engineering by Distal Bridging. *Angew. Chem. Int. Ed.* **2019,** *58*, 2670–2674.

92. Lang, K.; Torker, S.; Wojtas, L.; Zhang, X. P., Asymmetric Induction and Enantiodivergence in Catalytic Radical C–H Amination via Enantiodifferentiative H-Atom Abstraction and Stereoretentive Radical Substitution. *J. Am. Chem. Soc.* **2019,** *141*, 12388–12396.

93. Hu, Y.; Lang, K.; Li, C.; Gill, J. B.; Kim, I.; Lu, H.; Fields, K. B.; Marshall, M.; Cheng, Q.; Cui, X.; Wojtas, L.; Zhang, X. P., Enantioselective Radical Construction of 5-Membered Cyclic Sulfonamides by Metalloradical C–H Amination. *J. Am. Chem. Soc.* **2019,** *141*, 18160–18169.

94. Jin, L.-M.; Xu, P.; Xie, J.; Zhang, X. P., Enantioselective Intermolecular Radical C–H Amination. *J. Am. Chem. Soc.* **2020,** *142*, 20828–20836.

95. Lang, K.; Li, C.; Kim, I.; Zhang, X. P., Enantioconvergent Amination of Racemic Tertiary C–H Bonds. *J. Am. Chem. Soc.* **2020,** *142*, 20902–20911.

96. Riart-Ferrer, X.; Sang, P.; Tao, J.; Xu, H.; Jin, L.-M.; Lu, H.; Cui, X.; Wojtas, L.; Zhang, X. P., Metalloradical activation of carbonyl azides for enantioselective radical aziridination. *Chem* **2021,** *7*, 1120–1134.

97. Newcomb, M.; Zhang, R.; Pan, Z.; Harischandra, D. N.; Chandrasena, R. E. P.; Horner, J. H.; Martinez, E., Laser flash photolysis production of metal-oxo derivatives and direct kinetic studies of their oxidation reactions. *Catalysis Today* **2006,** *117*, 98–104.

98. Zhang, R.; Harischandra, D. N.; Newcomb, M., Laser Flash Photolysis Generation and Kinetic Studies of Corrole–Manganese(v)-Oxo Intermediates. *Chem. Eur. J.* **2005,** *11*, 5713–5720.

99. Lansky, D. E.; Mandimutsira, B.; Ramdhanie, B.; Clausén, M.; Penner-Hahn, J.; Zvyagin, S. A.; Telser, J.; Krzystek, J.; Zhan, R.; Ou, Z.; Kadish, K. M.; Zakharov, L.; Rheingold, A. L.; Goldberg, D. P., Synthesis, Characterization, and Physicochemical Properties of Manganese(III) and Manganese(V)−Oxo Corrolazines. *Inorg. Chem.* **2005,** *44*, 4485–4498.

100. Harischandra, D. N.; Lowery, G.; Zhang, R.; Newcomb, M., Production of a Putative Iron(V)−Oxocorrole Species by Photo-Disproportionation of a Bis-Corrole−Diiron(IV)−μ-Oxo Dimer: Implication for a Green Oxidation Catalyst. *Org. Lett.* **2009,** *11*, 2089–2092.

101. Mahammed, A.; Gray, H. B.; Meier-Callahan, A. E.; Gross, Z., Aerobic Oxidations Catalyzed by Chromium Corroles. *J. Am. Chem. Soc.* **2003,** *125*, 1162–1163.

102. Eikey, R. A.; Khan, S. I.; Abu-Omar, M. M., The Elusive Terminal Imido of Manganese(V). *Angew. Chem. Int. Ed.* **2002,** *41*, 3591–3595.

103. Lansky, D. E.; Kosack, J. R.; Narducci Sarjeant, A. A.; Goldberg, D. P., An Isolable, Nonreducible High-Valent Manganese(V) Imido Corrolazine Complex. *Inorg. Chem.* **2006,** *45*, 8477–8479.

104. Zdilla, M. J.; Abu-Omar, M. M., Mechanism of Catalytic Aziridination with Manganese Corrole: The Often Postulated High-Valent Mn(V) Imido Is Not the Group Transfer Reagent. *J. Am. Chem. Soc.* **2006,** *128*, 16971–16979.

105. Groves, J. T.; Takahashi, T., Activation and transfer of nitrogen from a nitridomanganese(V) porphyrin complex. Aza analog of epoxidation. *J. Am. Chem. Soc.* **1983,** *105*, 2073–2074.

106. Bottomley, L. A.; Neely, F. L., Nitrogen atom activation: the influence of porphyrin ring structure on the kinetics of the reaction of trifluoroacetic anhydride with nitrido manganese(V) porphyrins. *J. Am. Chem. Soc.* **1988,** *110*, 6748–6752.

107. Chen, T.-H.; Asiri, N.; Kwong, K. W.; Malone, J.; Zhang, R., Ligand control in the photochemical generation of high-valent porphyrin-iron–oxo derivatives. *Chem. Commun.* **2015,** *51*, 9949–9952.

108. Nam, W.; Park, S.-E.; Lim, I. K.; Lim, M. H.; Hong, J.; Kim, J., First Direct Evidence for Stereospecific Olefin Epoxidation and Alkane Hydroxylation by an Oxoiron(IV) Porphyrin Complex. *J. Am. Chem. Soc.* **2003,** *125*, 14674–14675.

109. Yamaguchi, K.; Watanabe, Y.; Morishima, I., Preparation and characterization of an oxo–iron(V)–porphyrin complex. *J. Chem. Soc., Chem. Commun.* **1992**, 1721–1723.

110. Tatsuya, M.; Kazuya, Y.; Yoshihito, W.; Isao, M., A New Active Intermediate in Monooxygenations Catalyzed by Iron Porphyrin Complexes. *Bull. Chem. Soc. Jpn.* **1998,** *71*, 1343–1353.

111. Zhang, R.; Chandrasena, R. E. P.; Martinez, E.; Horner, J. H.; Newcomb, M., Formation of Compound I by Photo-Oxidation of Compound II. *Org. Lett.* **2005,** *7*, 1193–1195.

112. Pan, Z.; Wang, Q.; Sheng, X.; Horner, J. H.; Newcomb, M., Highly Reactive Porphyrin−Iron−Oxo Derivatives Produced by Photolyses of Metastable Porphyrin−Iron(IV) Diperchlorates. *J. Am. Chem. Soc.* **2009,** *131*, 2621–2628.

113. Pan, Z.; Zhang, R.; Fung, L. W. M.; Newcomb, M., Photochemical Production of a Highly Reactive Porphyrin−Iron−Oxo Species. *Inorg. Chem.* **2007,** *46*, 1517–1519.

114. Pan, Z.; Harischandra, D. N.; Newcomb, M., Formation of stable and metastable porphyrin- and corrole-iron(IV) complexes and isomerizations to iron(III) macrocycle radical cations. *J. Inorg. Biochem* **2009,** *103*, 174–181.

115. Phillippi, M. A.; Goff, H. M., Electrochemical synthesis and characterization of the single-electron oxidation products of ferric porphyrins. *J. Am. Chem. Soc.* **1982,** *104*, 6026–6034.

116. Groves, J. T.; Quinn, R.; McMurry, T. J.; Lang, G.; Boso, B., Iron(IV) porphyrins from iron(III) porphyrin cation radicals. *J. Chem. Soc,. Chem. Commun.* **1984**, 1455–1456.

117. Gans, P.; Buisson, G.; Duee, E.; Marchon, J. C.; Erler, B. S.; Scholz, W. F.; Reed, C. A., High-valent iron porphyrins: synthesis, x-ray structures, .pi.-cation radical formulation, and notable magnetic properties of chloro(meso-

tetraphenylporphinato)iron(III) hexachloroantimonate and bis(perchlorato)(meso-tetraphenylporphinato)iron(III). *J. Am. Chem. Soc.* **1986,** *108,* 1223–1234.

118. Pan, Z.; Newcomb, M., Kinetics and Mechanism of Oxidation Reactions of Porphyrin−Iron(IV)−Oxo Intermediates. *Inorg. Chem.* **2007,** *46,* 6767–6774.

119. Pan, Z.; Zhang, R.; Newcomb, M., Kinetic studies of reactions of iron(IV)-oxo porphyrin radical cations with organic reductants. *J. Inorg. Biochem* **2006,** *100,* 524–532.

120. Buchler, J. W.; Dreher, C., Metallkomplexe mit Tetrapyrrol-Liganden, XXXIII [1] Darstellung von Azidochrom(III)-, Azidomangan(III)- und Azidoeisen(III)-Porphyrinen und deren Photolyse zu terminalen oder verbrückten Nitridometallporphyrinen / Metal Complexes with Tetrapyrrole Ligands XXXIII [1] Preparation of Azidochromium(III)-, Azidomanganese(III)-, and Azidoiron(III) Porphyrins and their Photolysis to Terminal or Bridged Nitridometal Porphyrins. *Z. Naturforsch., B: Chem. Sci* **1984,** *39,* 222–230.

121. Jin, T.; Suzuki, T.; Imamura, T.; Fujimoto, M., Photoirradiated and .gamma.-ray-irradiated reactions of manganese(III, IV, V) tetraphenylporphyrins in 2-methyltetrahydrofuran. Reactions of azidomanganese(III) porphyrin. *Inorg. Chem.* **1987,** *26,* 1280–1285.

122. Taira, I.; Takashi, J.; Toru, S.; Masatoshi, F., PHOTOREDUCTION OF MANGANESE(III), IRON(III), COBALT(III), AND MOLYBDENUM(V) TETRAPHENYLPORPHYRINS IN 2-METHYLTETRAHYDROFURAN. *Chem. Lett.* **1985,** *14,* 847–850.

123. Taira, I.; Yuichi, Y.; Toru, S.; Masatoshi, F., Competitive Photochemical Reactions of Azidomanganese(III) Tetraphenylporphyrin in 2-Methyltetrahydrofuran. *Chem. Lett.* **1987,** *16*, 2185–2186.

124. Suslick, K. S.; Watson, P. A., The photochemistry of chromium, manganese, and iron porphyrin complexes. *New J. Chem* **1992,** *16*, 633–642.

125. Suslick, K. S.; Watson, R. A., Photochemical reduction of nitrate and nitrite by manganese and iron porphyrins. *Inorg. Chem.* **1991,** *30*, 912–919.

126. Suslick, K. S.; Bautista, J. F.; Watson, R. A., Metalloporphyrin photochemistry with matrix isolation. *J. Am. Chem. Soc.* **1991,** *113*, 6111–6114.

127. Kräutler, B., Photochemical reactions of vitamin B12 derivatives. *Coord. Chem. Rev* **1991,** *111*, 215–220.

128. Hanson, P.; R. Lindsay Smith, J.; A. Osborne, V., The mechanism of the photo-decarboxylation of alkyl- and arylmethyl-carboxylates using visible light and iron(III) tetra(2-N-methylpyridyl)porphyrin pentachloride in aqueous solution. *J. Chem. Soc., Perkin Trans. 2* **1998**, 2653–2658.

129. Tohara, A.; Sato, M., Photoreduction of Hydroxo(tetramesitylporphinato)iron(III) in Aromatic Hydrocarbons and the Concurrent Generation of Hydroxyl Radical. *Chem. Lett.* **1989,** *18*, 153–156.

130. Bartocci, C.; Maldotti, A.; Varani, G.; Carassiti, V.; Battioni, P.; Mansuy, D., Iron meso-tetra(2,6-dichlorophenyl)porphyrin as a very efficient catalyst for the photoreduction of carbon tetrachloride by alcohols. *J. Chem. Soc,. Chem. Commun.* **1989**, 964–965.

131. Maldotti, A.; Bartocci, C.; Amadelli, R.; Polo, E.; Battioni, P.; Mansuy, D., Oxidation of alkanes by dioxygen catalysed by photoactivated iron porphyrins. *J. Chem. Soc,. Chem. Commun.* **1991**, 1487–1489.

132. Bartocci, C.; Maldotti, A.; Varani, G.; Battioni, P.; Carassiti, V.; Mansuy, D., Photoredox and photocatalytic characteristics of various iron meso-tetraarylporphyrins. *Inorg. Chem.* **1991,** *30*, 1255–1259.

133. Ito, Y.; Kunimoto, K.; Miyachi, S.; Kako, T., Photocatalytic cleavage of 1,2-diols by a cofacially hindered water-soluble iron(III) porphyrin. *Tetrahedron Lett.* **1991,** *32*, 4007–4010.

134. Hoshino, M.; Ueda, K.; Takahashi, M.; Yamaji, M.; Hama, Y., Photoreduction of iron(III) tetraphenylporphyrin in ethanol studied by laser flash photolysis: effects of concentration on quantum yields. *J. Chem. Soc. Farady Trans* **1992,** *88*, 405–408.

135. Maldotti, A.; Amadelli, R.; Bartocci, C.; Carassiti, V.; Polo, E.; Varani, G., Photochemistry of Iron-porphyrin complexes. Biomimetics and catalysis. *Coord. Chem. Rev* **1993,** *125*, 143–154.

136. Maldotti, A.; Bartocci, C.; Varani, G.; Molinari, A.; Battioni, P.; Mansuy, D., Oxidation of Cyclohexane by Molecular Oxygen Photoassisted by meso-Tetraarylporphyrin Iron(III)−Hydroxo Complexes. *Inorg. Chem.* **1996,** *35*, 1126–1131.

137. Maldotti, A.; Molinari, A.; Andreotti, L.; Fogagnolo, M.; Amadelli, R., Novel reactivity of photoexcited iron porphyrins caged into a polyfluoro sulfonated membrane in catalytic hydrocarbon oxygenation. *Chem. Commun.* **1998**, 507–508.

138. Gilbert, B. C.; Smith, J. R. L.; MacFaul, P.; Taylor, P., Photolytic cleavage of the iron–carboxyalkyl ligand bond in some iron(III) tetra(N-methylpyridyl)porphyrins: evidence for reversible photodecomposition and fragmentation from EPR and UV spectroscopy. *J. Chem. Soc., Perkin Trans. 2* **1993**, 2033–2037.

139. Gilbert, B. C.; Smith, J. R. L.; MacFaul, P.; Taylor, P., Reactions of carboxyl radicals generated by the photocleavage of complexes of iron(III) tetra(2-N-methylpyridyl)porphyrin with unsaturated and aromatic carboxylic acids in aqueous solution. *J. Chem. Soc., Perkin Trans. 2* **1996**, 511–518.

140. Gilbert, B. C.; Hodges, G. R.; Smith, J. R. L.; MacFaul, P.; Taylor, P., Photo-decarboxylation of substituted alkylcarboxylic acids brought about by visible light and iron(III) tetra(2-N-methylpyridyl)porphyrin in aqueous solution. *J. Chem. Soc., Perkin Trans. 2* **1996**, 519–524.

141. Gilbert, B. C.; Hodges, G. R.; Smith, J. R. L.; MacFaul, P.; Taylor, P., The photoreactions of the carboxylate complexes of 5,10,15,20-tetra(2-N-methylpyridyl)porphyrin. *J. Mol. Catal. A: Chem.* **1997,** *117*, 249–257.

142. C. Gilbert, B.; R. Lindsay Smith, J.; F. Parsons, A.; K. Setchell, P., Photo-decarboxylation of iron(III) porphyrin–amino acid complexes in aqueous solution. *J. Chem. Soc., Perkin Trans. 2* **1997**, 1065–1074.

143. Hendrickson, D. N.; Kinnaird, M. G.; Suslick, K. S., Photochemistry of (5,10,15,20-tetraphenylporphyrinato)iron(III) halide complexes, Fe(TPP)(X). *J. Am. Chem. Soc.* **1987,** *109*, 1243–1244.

144. Bizet, C.; Morlière, P.; Brault, D.; Delgado, O.; Bazin, M.; Santus, R., PHOTOREDUCTION OF IRON(III)PORPHYRINS. *Photochem. Photobiol.* **1981,** *34*, 315–321.

145. Bartocci, C.; Scandola, F.; Ferri, A.; Carassiti, V., Photoreduction of hemin in alcohol-containing mixed solvents. *J. Am. Chem. Soc.* **1980,** *102*, 7067–7072.

146. Maldotti, A.; Bartocci, C.; Chiorboli, C.; Ferri, A.; Carassiti, V., The role of oxygen in the mechanism of the intramolecular photoredox reaction of Fe protoporphyrin IX in alkaline aqueous ethanol. *J. Chem. Soc,. Chem. Commun.* **1985**, 881–882.

147. Maldotti, A.; Bartocci, C.; Amadelli, R.; Carassiti, V., Photocatalytic reactions in the 2,3,7,8,12,13,17,18-octaethylporphyrinatoiron(III)–ethanol–carbon tetrachloride system. *J. Chem. Soc. Dalton Trans* **1989**, 1197–1201.

148. Maldotti, A.; Bartocci, C.; Locatelli, C.; Carassiti, V.; Ferri, A.; Bortolloti, F., Photoredox reactions in cytochrome c and cytochrome c551. *Inorg. Chim. Acta* **1986,** *125*, 129–133.

149. Bartocci, C.; Maldotti, A.; Carassiti, V.; Traverso, O.; Ferri, A., Intramolecular photoredox reactions in iron(III) cytochrome c and its azide derivative. *Inorg. Chim. Acta* **1985,** *107*, 5–12.

150. Bartocci, C.; Maldotti, A.; Traverso, O.; Bignozzi, C. A.; Carassiti, V., Photoreduction of chlorohemin in pure pyridine. *Polyhedron* **1983,** *2*, 97–102.

151. Richman, R. M.; Peterson, M. W., Photodisproportionation of .mu.-oxo-bis[(tetraphenylporphinato)iron(III)]. *J. Am. Chem. Soc.* **1982,** *104*, 5795–5796.

152. Peterson, M. W.; Rivers, D. S.; Richman, R. M., Mechanistic considerations in the photodisproportionation of .mu.-oxo-bis((tetraphenylporphinato)iron(III)). *J. Am. Chem. Soc.* **1985,** *107*, 2907–2915.

153. Guest, C. R.; Straub, K. D.; Hutchinson, J. A.; Rentzepis, P. M., Picosecond absorption studies on the excited state of (.mu.-oxo)-bis[(tetraphenylporphinato)iron(III)]. *J. Am. Chem. Soc.* **1988,** *110*, 5276–5280.

154. Rehorek, D.; Berthold, T.; Hennig, H.; Kemp, T. J., Nachweis von Azidylradikalen (*N3) bei der Photolyse von Azido(tetraphenylporphyrinato)eisen(III) und -oxomolybdän(V). *Z Chem* **1988,** *28*, 72–73.

155. Ozaki, Y.; Iriyama, K.; Ogoshi, H.; Kitagawa, T., Ligand-aided photoreduction of iron-porphyrin complexes probed by resonance Raman spectroscopy. *J. Am. Chem. Soc.* **1987,** *109*, 5583–5586.

156. Konishi, S.; Hoshino, M.; Imamura, M., Constrained complexes of manganese(II) tetraphenylporphyrin in rigid solution. *J. Phys. Chem.* **1982,** *86*, 1412–1414.

157. Farhadi, S.; Zabardasti, A.; Rahmati, M. H., Manganese(III) Porphyrin Covalently Bound to sol-gel Derived Silica (Mn(III) Porphyrinosilica): A Reusable and Green Heterogeneous Photocatalyst for Oxidative Decarboxylation of α-Arylacetic Acids with H2O2. *J. Chem. Res.* **2011,** *35*, 157–160.

158. Hoshino, M.; Iimura, Y.; Konishi, S., Photochemistry of molybdenum(V) tetraphenylporphyrin studied by laser flash photolysis: light-induced homolysis of the molybdenum-oxygen bond of oxoalkoxo- and oxo(nitrito)molybdenum(V) tetraphenylporphyrin. *J. Phys. Chem.* **1992,** *96*, 179–185.

159. Hoshino, M.; Yasufuku, K.; Seki, H.; Yamazaki, H., Wavelength-dependent photochemical reaction of methylrhodium(III) octaethylporphyrin. Studies on methyl-rhodium (CH3-Rh) bond cleavage. *J. Phys. Chem.* **1985,** *89*, 3080–3085.

160. Šima, J., Photochemistry of tetrapyrrole complexes. In *Metal Complexes with Tetrapyrrole Ligands III*, Springer Berlin Heidelberg: Berlin, Heidelberg, 1995; pp 135-193.

161. Treacy, S. M.; Rovis, T., Copper Catalyzed C(sp3)–H Bond Alkylation via Photoinduced Ligand-to-Metal Charge Transfer. *J. Am. Chem. Soc.* **2021,** *143*, 2729–2735.

162. Kang, Y. C.; Treacy, S. M.; Rovis, T., Iron-Catalyzed Photoinduced LMCT: A 1° C–H Abstraction Enables Skeletal Rearrangements and C(sp3)–H Alkylation. *ACS Catal.* **2021,** *11*, 7442–7449.

163. Rohe, S.; Morris, A. O.; McCallum, T.; Barriault, L., Hydrogen Atom Transfer Reactions via Photoredox Catalyzed Chlorine Atom Generation. *Angew. Chem. Int. Ed.* **2018,** *57*, 15664–15669.

164. Deng, H.-P.; Zhou, Q.; Wu, J., Microtubing-Reactor-Assisted Aliphatic C−H Functionalization with HCl as a Hydrogen-Atom-Transfer Catalyst Precursor in Conjunction with an Organic Photoredox Catalyst. *Angew. Chem. Int. Ed.* **2018,** *57*, 12661–12665.

165. Deng, H.-P.; Fan, X.-Z.; Chen, Z.-H.; Xu, Q.-H.; Wu, J., Photoinduced Nickel-Catalyzed Chemo- and Regioselective Hydroalkylation of Internal Alkynes with Ether and Amide α-Hetero C(sp3)–H Bonds. *J. Am. Chem. Soc.* **2017,** *139*, 13579–13584.

166. Shields, B. J.; Doyle, A. G., Direct C(sp3)–H Cross Coupling Enabled by Catalytic Generation of Chlorine Radicals. *J. Am. Chem. Soc.* **2016,** *138*, 12719–12722.

167. Zidan, M.; Morris, A. O.; McCallum, T.; Barriault, L., The Alkylation and Reduction of Heteroarenes with Alcohols Using Photoredox Catalyzed Hydrogen Atom Transfer via Chlorine Atom Generation. *Eur. J. Org. Chem.* **2020,** *2020*, 1453–1458.

168. Nielsen, M. K.; Shields, B. J.; Liu, J.; Williams, M. J.; Zacuto, M. J.; Doyle, A. G., Mild, Redox-Neutral Formylation of Aryl Chlorides through the Photocatalytic Generation of Chlorine Radicals. *Angew. Chem. Int. Ed.* **2017,** *56*, 7191–7194.

169. Kariofillis, S. K.; Doyle, A. G., Synthetic and Mechanistic Implications of Chlorine Photoelimination in Nickel/Photoredox C(sp3)–H Cross-Coupling. *Acc. Chem. Res.* **2021,** *54*, 988–1000.

170. Ackerman, L. K. G.; Martinez Alvarado, J. I.; Doyle, A. G., Direct C–C Bond Formation from Alkanes Using Ni-Photoredox Catalysis. *J. Am. Chem. Soc.* **2018,** *140*, 14059–14063.

171. Yang, Q.; Wang, Y.-H.; Qiao, Y.; Gau, M.; Carroll, P. J.; Walsh, P. J.; Schelter, E. J., Photocatalytic C–H activation and the subtle role of chlorine radical complexation in reactivity. *Science* **2021,** *372*, 847–852.

172. Hu, A.; Guo, J.-J.; Pan, H.; Zuo, Z., Selective functionalization of methane, ethane, and higher alkanes by cerium photocatalysis. *Science* **2018,** *361*, 668–672.

173. Abderrazak, Y.; Bhattacharyya, A.; Reiser, O., Visible-Light-Induced Homolysis of Earth-Abundant Metal-Substrate Complexes: A Complementary Activation Strategy in Photoredox Catalysis. *Angew. Chem. Int. Ed.* **2021,** *60*, 21100–21115.

174. Gygi, D.; Gonzalez, M. I.; Hwang, S. J.; Xia, K. T.; Qin, Y.; Johnson, E. J.; Gygi, F.; Chen, Y.-S.; Nocera, D. G., Capturing the Complete Reaction Profile of a C–H Bond Activation. *J. Am. Chem. Soc.* **2021,** *143*, 6060–6064.

175. Gonzalez, M. I.; Gygi, D.; Qin, Y.; Zhu, Q.; Johnson, E. J.; Chen, Y.-S.; Nocera, D. G., Taming the Chlorine Radical: Enforcing Steric Control over Chlorine-Radical-Mediated C–H Activation. *J. Am. Chem. Soc.* **2022,** *144*, 1464–1472.

176. Hwang, S. J.; Anderson, B. L.; Powers, D. C.; Maher, A. G.; Hadt, R. G.; Nocera, D. G., Halogen Photoelimination from Monomeric Nickel(III) Complexes Enabled by the Secondary Coordination Sphere. *Organometallics* **2015,** *34*, 4766–4774.

177. Hwang, S. J.; Powers, D. C.; Maher, A. G.; Anderson, B. L.; Hadt, R. G.; Zheng, S.-L.; Chen, Y.-S.; Nocera, D. G., Trap-Free Halogen Photoelimination from Mononuclear Ni(III) Complexes. *J. Am. Chem. Soc.* **2015,** *137*, 6472–6475.

178. Fantauzzi, S.; Caselli, A.; Gallo, E., Nitrene transfer reactions mediated by metallo-porphyrin complexes. *Dalton Trans.* **2009**, 5434–5443.

179. Park, Y.; Kim, Y.; Chang, S., Transition Metal-Catalyzed C–H Amination: Scope, Mechanism, and Applications. *Chem. Rev.* **2017,** *117*, 9247–9301.

180. Jeffrey, J. L.; Sarpong, R., Intramolecular C(sp3)–H amination. *Chem. Sci.* **2013,** *4*, 4092–4106.

181. Liu, W.; Ackermann, L., Manganese-Catalyzed C–H Activation. *ACS Catal.* **2016,** *6*, 3743–3752.

182. Yu, X.-Q.; Huang, J.-S.; Zhou, X.-G.; Che, C.-M., Amidation of Saturated C−H Bonds Catalyzed by Electron-Deficient Ruthenium and Manganese Porphyrins. A Highly Catalytic Nitrogen Atom Transfer Process. *Org. Lett.* **2000,** *2*, 2233–2236.

183. Mahy, J.-P.; Bedi, G.; Battioni, P.; Mansuy, D., Amination of Alkanes Catalyzed by Iron- and Manganese-Porphyrins: Particular Selectiveity for ω and ω-1 Oxidations of Linear Alkanes. *New. J. Chem.* **1989,** *3*, 651–657.

184. Mansuy, D.; Mahy, J.-P.; Dureault, A.; Bedi, G.; Battioni, P., Iron- and manganese-porphyrin catalysed aziridination of alkenes by tosyl- and acyl-iminoiodobenzene. *J. Chem. Soc., Chem. Commun.* **1984**, 1161–1163.

185. Cenini, S.; Penoni, A.; Tollari, S., Tetraalkylammonium N-chloro-p-toluenesulfonamide as aminating agent of olefins. *J. Mol. Catal. A: Chem.* **1997,** *124*, 109–113.

186. Simonato, J.-P.; Pécaut, J.; Marchon, J.-C.; Robert Scheidt, W., Antagonistic metal-directed inductions in catalytic asymmetric aziridination by manganese and iron tetramethylchiroporphyrins. *Chem. Commun.* **1999**, 989–990.

187. Paradine, S. M.; Griffin, J. R.; Zhao, J.; Petronico, A. L.; Miller, S. M.; Christina White, M., A manganese catalyst for highly reactive yet chemoselective intramolecular C(sp3)–H amination. *Nat. Chem.* **2015,** *7*, 987–994.

188. Wang, J.; Zheng, K.; Li, T.; Zhan, X., Mechanism and Chemoselectivity of Mn-Catalyzed Intramolecular Nitrene Transfer Reaction: C–H Amination vs. C=C Aziridination. *Catalysts* **2020,** *10* (3), 292.

189. Liu, Z.; Lu, Y.; Guo, J.; Hu, W.; Dang, Y.; Wang, Z.-X., DFT Mechanistic Account for the Site Selectivity of Electron-Rich C(sp3)–H Bond in the Manganese-Catalyzed Aminations. *Org. Lett.* **2020,** *22*, 453–457.

190. Li, P.; Cao, Z., Mechanism Insight into the Csp3–H Amination Catalyzed by the Metal Phthalocyanine. *Organometallics* **2019,** *38*, 343–350.

191. The term nitrenoid is used to describe a M–NR fragment where the electronic structure is still ambiguous

192. Shi, H.; Xie, J.; Lam, W. W. Y.; Man, W.-L.; Mak, C.-K.; Yiu, S.-M.; Lee, H. K.; Lau, T.-C., Generation and Reactivity of a One-Electron-Oxidized Manganese(V) Imido Complex with a Tetraamido Macrocyclic Ligand. *Chem. Eur. J.* **2019,** *25*, 12895–12899.

193. Zhang, R.; Horner, J. H.; Newcomb, M., Laser Flash Photolysis Generation and Kinetic Studies of Porphyrin−Manganese−Oxo Intermediates. Rate Constants for Oxidations Effected by Porphyrin−MnV−Oxo Species and Apparent Disproportionation Equilibrium Constants for Porphyrin−MnIV−Oxo Species. *J. Am. Chem. Soc.* **2005,** *127*, 6573–6582.

194. Zhang, R.; Newcomb, M., Laser Flash Photolysis Formation and Direct Kinetic Studies of Manganese(V)-Oxo Porphyrin Intermediates. *J. Am. Chem. Soc.* **2003,** *125*, 12418–12419.

195. Zhang, R.; Newcomb, M., Laser Flash Photolysis Generation of High-Valent Transition Metal−Oxo Species: Insights from Kinetic Studies in Real Time. *Acc. Chem. Res.* **2008,** *41*, 468–477.

196. Klaine, S.; Bratcher, F.; Winchester, C. M.; Zhang, R., Formation and kinetic studies of manganese(IV)-oxo porphyrins: Oxygen atom transfer mechanism of sulfide oxidations. *J. Inorg. Biochem* **2020,** *204*, 110986.

197. Lee, N. F.; Malone, J.; Jeddi, H.; Kwong, K. W.; Zhang, R., Visible-light photolysis of corrole-manganese(IV) nitrites to generate corrole-manganese(V)-oxo complexes. *Inorg. Chem. Commun.* **2017,** *82*, 27–30.

198. Ka, W. K.; Ngo, F. L.; Ranburger, D.; Malone, J.; Zhang, R., Visible light-induced formation of corrole-manganese(V)-oxo complexes: Observation of multiple oxidation pathways. *J. Inorg. Biochem.* **2016,** *163*, 39–44.

199. Kwong, K. W.; Winchester, C. M.; Zhang, R., Photochemical generation of manganese(IV)-oxo porphyrins by visible light photolysis of dimanganese(III) μ-oxo bis-porphyrins. *Inorg. Chim. Acta* **2016,** *451*, 202–206.

200. Das, A.; Chen, Y.-S.; Reibenspies, J. H.; Powers, D. C., Characterization of a Reactive Rh2 Nitrenoid by Crystalline Matrix Isolation. *J. Am. Chem. Soc.* **2019,** *141*, 16232–16236.

201. Das, A.; Wang, C.-H.; Van Trieste, G. P.; Sun, C.-J.; Chen, Y.-S.; Reibenspies, J. H.; Powers, D. C., In Crystallo Snapshots of Rh2-Catalyzed C–H Amination. *J. Am. Chem. Soc.* **2020,** *142*, 19862–19867.

202. Guo, Z.; Guan, X.; Huang, J.-S.; Tsui, W.-M.; Lin, Z.; Che, C.-M., Bis(sulfonylimide)ruthenium(VI) Porphyrins: X-ray Crystal Structure and Mechanism of C□H Bond Amination by Density Functional Theory Calculations. *Chem. Eur. J.* **2013,** *19*, 11320–11331.

203. Das, A.; Maher, A. G.; Telser, J.; Powers, D. C., Observation of a Photogenerated Rh2 Nitrenoid Intermediate in C–H Amination. *J. Am. Chem. Soc.* **2018,** *140*, 10412–10415.

204. Shcherbakov, V. I.; Kuznetsova, V. P.; Chuprunov, E. V.; Ovsetsina, T. I.; Stolyarova, N. E.; Zakharov, L. N.; Novgorod, N., Reactions of di- and trialkyltin chlorides with chloramine in aqueous media. The crystal structure of the N-chloro-N-(trimethylstannyl)amide of 4-chlorobenzene-sulphonic acid. *Organomet. Chem. (USSR)* **1991,** *4*, 1350–1354.

205. Neale, R. S., Nitrogen Radicals as Synthesis Intermediates. N-Halamide Rearrangements and Additions to Unsaturated Hydrocarbons. *Synthesis* **1971,** *1971*, 1–15.

206. Stateman, L. M.; Nakafuku, K. M.; Nagib, D. A., Remote C–H Functionalization via Selective Hydrogen Atom Transfer. *Synthesis* **2018,** *50*, 1569–1586.

207. Zard, S. Z., Recent progress in the generation and use of nitrogen-centred radicals. *Chem. Soc. Rev.* **2008,** *37*, 1603–1618.

208. Boucher, L. J., Manganese porphyrin complexes. *Coord. Chem. Rev* **1972,** *7*, 289–329.

209. Mu, L.; Huang, J.; Zhou, Y.; Shen, P., Synthesis and spectroscopic studies of manganese porphyrin-thiolate complexes. *Polyhedron* **1997,** *16*, 2885–2888.

210. Gozet, T.; Huynh, L.; Bohme, D. K., Generation and dissociation of oxygen- and chloride-bridged iron(III) and manganese(III) tetraphenylporphyrin dimer ions in the gas phase. *J. Mass. Spectrom.* **2010,** *45*, 35–42.

211. Krzystek, J.; Telser, J.; Pardi, L. A.; Goldberg, D. P.; Hoffman, B. M.; Brunel, L.-C., High-Frequency and -Field Electron Paramagnetic Resonance of High-Spin Manganese(III) in Porphyrinic Complexes. *Inorg. Chem.* **1999,** *38*, 6121–6129.

212. Krzystek, J.; Schnegg, A.; Aliabadi, A.; Holldack, K.; Stoian, S. A.; Ozarowski, A.; Hicks, S. D.; Abu-Omar, M. M.; Thomas, K. E.; Ghosh, A.; Caulfield, K. P.; Tonzetich, Z. J.; Telser, J., Advanced Paramagnetic Resonance Studies on Manganese and Iron Corroles with a Formal d4 Electron Count. *Inorg. Chem.* **2020,** *59*, 1075–1090.

213. Hˆ=μ_B B{g} Sˆ+D{Sˆ_z^2-1/3 S(S+1)}+E(Sˆ_x^2-Sˆ_y^2)

214. Krzystek, J.; Pardi, L. A.; Brunel, L.-C.; Goldberg, D. P.; Hoffman, B. M.; Licoccia, S.; Telser, J., High-frequency and -field electron paramagnetic resonance of high-spin manganese(III) in tetrapyrrole complexes. *Spectrochim. Acta, Part A* **2002,** *58*, 1113–1127.

215. Krzystek, J.; Telser, J.; Hoffman, B. M.; Brunel, L.-C.; Licoccia, S., High-Frequency and Field EPR Investigation of (8,12-Diethyl-2,3,7,13,17,18-hexamethylcorrolato)manganese(III). *J. Am. Chem. Soc.* **2001,** *123*, 7890–7897.

216. Bone, A. N.; Stavretis, S. E.; Krzystek, J.; Liu, Z.; Chen, Q.; Gai, Z.; Wang, X.; Steren, C. A.; Powers, X. B.; Podlesnyak, A. A.; Chen, X.-T.; Telser, J.; Zhou, H.; Xue, Z.-L., Manganese tetraphenylporphyrin bromide and iodide. Studies of structures and magnetic properties. *Polyhedron* **2020,** *184*, 114488.

217. Mossin, S.; Weihe, H.; Barra, A.-L., Is the Axial Zero-Field Splitting Parameter of Tetragonally Elongated High-Spin Manganese(III) Complexes Always Negative? *J. Am. Chem. Soc.* **2002,** *124*, 8764–8765.

218. Bendix, J.; Gray, H. B.; Golubkov, G.; Gross, Z., High-field (high-frequency) EPR spectroscopy and structural characterization of a novel manganese(III) corrole. *Chem. Commun.* **2000**, 1957–1958.

219. Luo, Y.-R., *Handbook of Bond Dissociation Energies in Organic Compounds*. CRC Press: Boca Raton, 2002; p 392.

220. Camenzind, M. J.; Hollander, F. J.; Hill, C. L., Synthesis, characterization, and ground electronic state of the unstable monomeric manganese(IV) porphyrin complexes diazido- and bis(isocyanato)(5,10,15,20-tetraphenylporphinato)manganese(IV). Crystal and molecular structure of the bis(isocyanato) complex. *Inorg. Chem.* **1983,** *22*, 3776–3784.

221. Smolinsky, G.; Wasserman, E.; Yager, W. A., The E.P.R. of Ground State Triplet Nitrenes. *J. Am. Chem. Soc.* **1962,** *84*, 3220–3221.

222. Garay, J.-C.; Maloney, V.; Marlow, M.; Small, P., Spectroscopy and Kinetics of Triplet 4-Methylbenzenesulfonylnitrene. *J. Phys. Chem.* **1996,** *100*, 5788–5793.

223. N–X BDE values (kcal/mol): N–Cl = 93.0, N–Br 66.0, and N–I 38.0. See, T. L. Cottrell, The Strengths of Chemical Bonds, 2nd ed., Butterworth, London, 1958.

224. Yamaji, M.; Hama, Y.; Miyazaki, Y.; Hoshino, M., Photochemical formation of oxochromium(IV) tetraphenylporphyrin from nitritochromium(III) tetraphenylporphyrin in benzene. *Inorg. Chem.* **1992,** *31*, 932–934.

225. Hoshino, M.; Nagashima, Y.; Seki, H.; De Leo, M.; Ford, P. C., Laser Flash Photolysis Studies of Nitritomanganese(III) Tetraphenylporphyrin. Reactions of O2, NO,

and Pyridine with Manganese(II) Tetraphenylporphyrin. *Inorg. Chem.* **1998,** *37*, 2464–2469.

226. Suarez, A. I. O.; Lyaskovskyy, V.; Reek, J. N. H.; van der Vlugt, J. I.; de Bruin, B., Complexes with Nitrogen-Centered Radical Ligands: Classification, Spectroscopic Features, Reactivity, and Catalytic Applications. *Angew. Chem. Int. Ed.* **2013,** *52*, 12510–12529.

227. Enemark, J. H.; Feltham, R. D., Principles of structure, bonding, and reactivity for metal nitrosyl complexes. *Coord. Chem. Rev* **1974,** *13*, 339–406.

228. Nazran, A. S.; Griller, D., Hydrogen abstraction from amines: formation of aminyl vs. .alpha.-aminoalkyl radicals. *J. Am. Chem. Soc.* **1983,** *105*, 1970–1971.

229. Davies, J.; Svejstrup, T. D.; Fernandez Reina, D.; Sheikh, N. S.; Leonori, D., Visible-Light-Mediated Synthesis of Amidyl Radicals: Transition-Metal-Free Hydroamination and N-Arylation Reactions. *J. Am. Chem. Soc.* **2016,** *138*, 8092–8095.

230. Kärkäs, M. D., Photochemical Generation of Nitrogen-Centered Amidyl, Hydrazonyl, and Imidyl Radicals: Methodology Developments and Catalytic Applications. *ACS Catal.* **2017,** *7*, 4999–5022.

231. Martínez, C.; Muñiz, K., An Iodine-Catalyzed Hofmann–Löffler Reaction. *Angew. Chem. Int. Ed.* **2015,** *54*, 8287–8291.

232. Dong, Y.; Clarke, R. M.; Porter, G. J.; Betley, T. A., Efficient C–H Amination Catalysis Using Nickel-Dipyrrin Complexes. *J. Am. Chem. Soc.* **2020,** *142*, 10996–11005.

233. Baek, Y.; Betley, T. A., Catalytic C–H Amination Mediated by Dipyrrin Cobalt Imidos. *J. Am. Chem. Soc.* **2019,** *141*, 7797–7806.

234. Wilding, M. J. T.; Iovan, D. A.; Betley, T. A., High-Spin Iron Imido Complexes Competent for C–H Bond Amination. *J. Am. Chem. Soc.* **2017,** *139*, 12043–12049.

235. King, E. R.; Hennessy, E. T.; Betley, T. A., Catalytic C−H Bond Amination from High-Spin Iron Imido Complexes. *J. Am. Chem. Soc.* **2011,** *133*, 4917–4923.

236. Au, S.-M.; Huang, J.-S.; Yu, W.-Y.; Fung, W.-H.; Che, C.-M., Aziridination of Alkenes and Amidation of Alkanes by Bis(tosylimido)ruthenium(VI) Porphyrins. A Mechanistic Study. *J. Am. Chem. Soc.* **1999,** *121*, 9120–9132.

237. Badiei, Y. M.; Dinescu, A.; Dai, X.; Palomino, R. M.; Heinemann, F. W.; Cundari, T. R.; Warren, T. H., Copper–Nitrene Complexes in Catalytic C□H Amination. *Angew. Chem. Int. Ed.* **2008,** *47*, 9961–9964.

238. Slaughter, L. M.; Wolczanski, P. T.; Klinckman, T. R.; Cundari, T. R., Inter- and Intramolecular Experimental and Calculated Equilibrium Isotope Effects for (silox)2(tBu3SiND)TiR + RH (silox = tBu3SiO): Inferred Kinetic Isotope Effects for RH/D Addition to Transient (silox)2TiNSitBu3. *J. Am. Chem. Soc.* **2000,** *122*, 7953–7975.

239. Truong, P. T.; Miller, S. G.; McLaughlin Sta. Maria, E. J.; Bowring, M. A., Large Isotope Effects in Organometallic Chemistry. *Chem. Eur. J.* **2021,** *n/a* (n/a).

240. Czernuszewicz, R. S.; Su, Y. O.; Stern, M. K.; Macor, K. A.; Kim, D.; Groves, J. T.; Spiro, T. G., Oxomanganese(IV) porphyrins identified by resonance Raman and infrared spectroscopy. Weak bonds and the stability of the half-filled t2g subshell. *J. Am. Chem. Soc.* **1988,** *110*, 4158–4165.

241. Hill, C. L.; Hollander, F. J., Structural characterization of a complex of Manganese(V) nitrido[tetrakis(p-methoxyphenyl)porphinato] manganese(V). *J. Am. Chem. Soc.* **1982,** *104*, 7318–7319.

242. Shimazaki, Y.; Nagano, T.; Takesue, H.; Ye, B.-H.; Tani, F.; Naruta, Y., Characterization of a Dinuclear MnV□O Complex and Its Efficient Evolution of O2 in the Presence of Water. *Angew. Chem. Int. Ed.* **2004,** *43*, 98–100.

243. Adler, A. D.; Longo, F. R.; Finarelli, J. D.; Goldmacher, J.; Assour, J.; Korsakoff, L., A simplified synthesis for meso-tetraphenylporphine. *J. Org. Chem.* **1967,** *32*, 476–476.

244. d'A Rocha Gonsalves, A. M.; Varejão, J. M. T. B.; Pereira, M. M., Some new aspects related to the synthesis of meso-substituted porphyrins. *J. Heterocycl. Chem.* **1991,** *28*, 635–640.

245. Lindsey, J. S.; Wagner, R. W., Investigation of the synthesis of ortho-substituted tetraphenylporphyrins. *J. Org. Chem.* **1989,** *54*, 828–836.

246. Zhang, F.; Xie, Y.; Liu, P.; Hao, F.; Yao, Z.; Luo, H. a., Cycloaddition Reaction of Propylene Oxide and Carbon Dioxide Over NaX Zeolite Supported Metalloporphyrin Catalysts. *Catal. Lett.* **2014,** *144*, 1894–1899.

247. Jannuzzi , S. A. V.; Arruda, E. G. R. d.; Lima, F. A.; Ribeiro, M. A.; Brinatti, C.; Formiga, A. L. B., Enzyme-Like Selectivity on Metalloporphyrin-Catalyzed Oxidation by a Linear Homopolymer. *ChemistrySelect* **2016,** *1*, 2235–2243.

248. Fulmer, G. R.; Miller, A. J. M.; Sherden, N. H.; Gottlieb, H. E.; Nudelman, A.; Stoltz, B. M.; Bercaw, J. E.; Goldberg, K. I., NMR Chemical Shifts of Trace Impurities:

Common Laboratory Solvents, Organics, and Gases in Deuterated Solvents Relevant to the Organometallic Chemist. *Organometallics* **2010,** *29* (9), 2176-2179.

249. Bain, G. A.; Berry, J. F., Diamagnetic Corrections and Pascal's Constants. *J. Chem. Ed.* **2008,** *85*, 532–536.

250. Hassan, A. K.; Pardi, L. A.; Krzystek, J.; Sienkiewicz, A.; Goy, P.; Rohrer, M.; Brunel, L. C., Ultrawide Band Multifrequency High-Field EMR Technique: A Methodology for Increasing Spectroscopic Information. *J. Mag. Reson.* **2000,** *142*, 300–312.

251. Sheldrick, G., A short history of SHELX. *Acta Crystallographica Section A* **2008,** *64* (1), 112-122.

252. Sheldrick, G., Crystal structure refinement with SHELXL. *Acta Crystallographica Section C* **2015,** *71* (1), 3-8.

253. Dolomanov, O. V.; Bourhis, L. J.; Gildea, R. J.; Howard, J. A. K.; Puschmann, H., OLEX2: a complete structure solution, refinement and analysis program. *Journal of Applied Crystallography* **2009,** *42* (2), 339-341.

254. Frisch, M. J.; Trucks, G. W.; Schlegel, H. B.; Scuseria, G. E.; Robb, M. A.; Cheeseman, J. R.; Scalmani, G.; Barone, V.; Petersson, G. A.; Nakatsuji, H.; Li, X.; Caricato, M.; Marenich, A. V.; Bloino, J.; Janesko, B. G.; Gomperts, R.; Mennucci, B.; Hratchian, H. P.; Ortiz, J. V.; Izmaylov, A. F.; Sonnenberg, J. L.; Williams; Ding, F.; Lipparini, F.; Egidi, F.; Goings, J.; Peng, B.; Petrone, A.; Henderson, T.; Ranasinghe, D.; Zakrzewski, V. G.; Gao, J.; Rega, N.; Zheng, G.; Liang, W.; Hada, M.; Ehara, M.; Toyota, K.; Fukuda, R.; Hasegawa, J.; Ishida, M.; Nakajima, T.; Honda, Y.; Kitao, O.;

Nakai, H.; Vreven, T.; Throssell, K.; Montgomery Jr., J. A.; Peralta, J. E.; Ogliaro, F.; Bearpark, M. J.; Heyd, J. J.; Brothers, E. N.; Kudin, K. N.; Staroverov, V. N.; Keith, T. A.; Kobayashi, R.; Normand, J.; Raghavachari, K.; Rendell, A. P.; Burant, J. C.; Iyengar, S. S.; Tomasi, J.; Cossi, M.; Millam, J. M.; Klene, M.; Adamo, C.; Cammi, R.; Ochterski, J. W.; Martin, R. L.; Morokuma, K.; Farkas, O.; Foresman, J. B.; Fox, D. J. *Gaussian 16 Rev. C.01*, Wallingford, CT, 2016.

255. Becke, A. D., Density-functional thermochemistry. III. The role of exact exchange. *J. Chem. Phys.* **1993,** *98*, 5648–5652.

256. Lee, C.; Yang, W.; Parr, R. G., Development of the Colle-Salvetti correlation-energy formula into a functional of the electron density. *Phys. Rev. B* **1988,** *37*, 785–789.

257. Stephens, P. J.; Devlin, F. J.; Chabalowski, C. F.; Frisch, M. J., Ab Initio Calculation of Vibrational Absorption and Circular Dichroism Spectra Using Density Functional Force Fields. *J. Phys. Chem.* **1994,** *98*, 11623–11627.

258. Vosko, S. H.; Wilk, L.; Nusair, M., Accurate spin-dependent electron liquid correlation energies for local spin density calculations: a critical analysis. *Can, J. Phys.* **1980,** *58*, 1200–1212.

259. Hay, P. J.; Wadt, W. R., Ab initio effective core potentials for molecular calculations. Potentials for K to Au including the outermost core orbitals. *J. Chem. Phys.* **1985,** *82*, 299–310.

260. Nair, C. G. R.; Indrasenan, P., New redox titrants in non-aqueous or partially aqueous media—VI11Part V: Talanta, 1975, 22, 57.: Potentiometric determinations using

dibromamine-T and some further applications of dichloramine-T. *Talanta* **1976,** *23*, 239–241.

261. Nair, C. G. R.; Lalithakumari, R.; Senan, P. I., Bromamine-T as a new oxidimetric titrant. *Talanta* **1978,** *25*, 525–527.

262. Nicolle, S. M.; Moody, C. J., Potassium N-Iodo p-Toluenesulfonamide (TsNIK, Iodamine-T): A New Reagent for the Oxidation of Hydrazones to Diazo Compounds. *Chem. Eur. J.* **2014,** *20*, 4420–4425.

263. Harmand, L.; Lambert, R.; Scarpantonio, L.; McClenaghan, N. D.; Lastécouères, D.; Vincent, J.-M., A Photoreducible Copper(II)-Tren Complex of Practical Value: Generation of a Highly Reactive Click Catalyst. *Chem. Eur. J.* **2013,** *19*, 16231–16239.

264. Jochyms, Q.; Guillot, P.; Mignard, E.; Vincent, J.-M., A fluorosurfactant and photoreducible CuII-tren click catalyst: surfactant and catalytic properties at liquid/liquid interfaces. *Dalton Trans.* **2015,** *44*, 19700–19707.

265. Ross, M. O.; MacMillan, F.; Wang, J.; Nisthal, A.; Lawton, T. J.; Olafson, B. D.; Mayo, S. L.; Rosenzweig, A. C.; Hoffman, B. M., Particulate methane monooxygenase contains only mononuclear copper centers. *Science* **2019,** *364*, 566–570.

266. Davydov, R.; Herzog, A. E.; Jodts, R. J.; Karlin, K. D.; Hoffman, B. M., End-On Copper(I) Superoxo and Cu(II) Peroxo and Hydroperoxo Complexes Generated by Cryoreduction/Annealing and Characterized by EPR/ENDOR Spectroscopy. *J. Am. Chem. Soc.* **2022,** *144*, 377–389.

267. Cutsail, G. E.; Ross, M. O.; Rosenzweig, A. C.; DeBeer, S., Towards a unified understanding of the copper sites in particulate methane monooxygenase: an X-ray absorption spectroscopic investigation. *Chem. Sci.* **2021,** *12*, 6194–6209.

268. Peng, W.; Qu, X.; Shaik, S.; Wang, B., Deciphering the oxygen activation mechanism at the CuC site of particulate methane monooxygenase. *Nat. Catal.* **2021,** *4*, 266–273.

269. Jodts, R. J.; Ross, M. O.; Koo, C. W.; Doan, P. E.; Rosenzweig, A. C.; Hoffman, B. M., Coordination of the Copper Centers in Particulate Methane Monooxygenase: Comparison between Methanotrophs and Characterization of the CuC Site by EPR and ENDOR Spectroscopies. *J. Am. Chem. Soc.* **2021,** *143*, 15358–15368.

270. Elwell, C. E.; Gagnon, N. L.; Neisen, B. D.; Dhar, D.; Spaeth, A. D.; Yee, G. M.; Tolman, W. B., Copper–Oxygen Complexes Revisited: Structures, Spectroscopy, and Reactivity. *Chem. Rev.* **2017,** *117* (3), 2059-2107.

271. Shimoyama, Y.; Kojima, T., Metal-Oxyl Species and Their Possible Roles in Chemical Oxidations. *Inorg. Chem.* **2019,** *58* (15), 9517-9542.

272. Srnec, M.; Navrátil, R.; Andris, E.; Jašík, J.; Roithová, J., Experimentally Calibrated Analysis of the Electronic Structure of CuO+: Implications for Reactivity. *Angew. Chem. Int. Ed.* **2018,** *57*, 17053–17057.

273. de Kler, N. R. M.; Roithova, J., Copper arylnitrene intermediates: formation, structure and reactivity. *Chem. Commun.* **2020,** *56* (84), 12721-12724.

274. Maiti, D.; Lucas, H. R.; Narducci Sarjeant, A. A.; Karlin, K. D., Aryl Hydroxylation from a Mononuclear Copper-Hydroperoxo Species. *J. Am. Chem. Soc.* **2007,** *129* (22), 6998-6999.

275. Kunishita, A.; Kubo, M.; Ishimaru, H.; Ogura, T.; Sugimoto, H.; Itoh, S., H2O2-Reactivity of Copper(II) Complexes Supported by Tris[(pyridin-2-yl)methyl]amine Ligands with 6-Phenyl Substituents. *Inorg. Chem.* **2008,** *47* (24), 12032-12039.

276. Kunishita, A.; Ishimaru, H.; Nakashima, S.; Ogura, T.; Itoh, S., Reactivity of Mononuclear Alkylperoxo Copper(II) Complex. O-O Bond Cleavage and C-H Bond Activation. *J. Am. Chem. Soc.* **2008,** *130* (13), 4244-4245.

277. Hong, S.; Huber, S. M.; Gagliardi, L.; Cramer, C. C.; Tolman, W. B., Copper(I)-α-Ketocarboxylate Complexes: Characterization and O2 Reactions That Yield Copper-Oxygen Intermediates Capable of Hydroxylating Arenes. *J. Am. Chem. Soc.* **2007,** *129* (46), 14190-14192.

278. Maiti, D.; Lee, D.-H.; Gaoutchenova, K.; Wuertele, C.; Holthausen, M. C.; Narducci Sarjeant, A. A.; Sundermeyer, J.; Schindler, S.; Karlin, K. D., Reactions of a copper(II) superoxo complex lead to C-H and O-H substrate oxygenation: modeling copper-monooxygenase C-H hydroxylation. *Angew. Chem., Int. Ed.* **2008,** *47* (1), 82-85.

279. Blackman, A. G.; Tolman, W. B., Copper-Dioxygen and Copper-Oxo Species Relevant to Copper Oxygenases and Oxidases. In *Metal-Oxo and Metal-Peroxo Species in Catalytic Oxidations*, Meunier, B., Ed. Springer Berlin Heidelberg: Berlin, Heidelberg, 2000; pp 179–211.

280. Levanov, A. V.; Maksimov, I. B.; Isaikina, O. Y.; Antipenko, E. E.; Lunin, V. V., Interaction between gaseous ozone and crystalline potassium bromide. *Rus. J. Phys. Chem. A* **2016,** *90*, 1312–1318.

281. Addison, A. W.; Rao, T. N.; Reedijk, J.; van Rijn, J.; Verschoor, G. C., Synthesis, structure, and spectroscopic properties of copper(II) compounds containing nitrogen–sulphur donor ligands; the crystal and molecular structure of aqua[1,7-bis(N-methylbenzimidazol-2′-yl)-2,6-dithiaheptane]copper(II) perchlorate. *J. Chem. Soc. Dalton Trans* **1984**, 1349–1356.

282. Wurzenberger, M. H. H.; Szimhardt, N.; Stierstorfer, J., Nitrogen-Rich Copper(II) Bromate Complexes: an Exotic Class of Primary Explosives. *Inorg. Chem.* **2018,** *57* (13), 7940-7949.

283. Luo, Y.-r. In *Comprehensive handbook of chemical bond energies*, 2007.

284. Bu, L.; Ciesielski, P. N.; Robichaud, D. J.; Kim, S.; McCormick, R. L.; Foust, T. D.; Nimlos, M. R., Understanding Trends in Autoignition of Biofuels: Homologous Series of Oxygenated C5 Molecules. *J. Phys. Chem. A* **2017,** *121*, 5475–5486.

285. Zuo, Z.; Katsumura, Y., Formation of hydrated electron and BrO3 radical from laser photolysis of BrO3- aqueous solution. *J. Chem. Soc., Farady Trans.* **1998,** *94* (24), 3577-3580.

286. Koelm, J.; Engdahl, A.; Schrems, O.; Nelander, B., A spectroscopic and photoisomerization study of bromine dioxides in argon matrixes. *Chem. Phys.* **1997,** *214* (2,3), 313-319.

287. Das, A.; Reibenspies, J. H.; Chen, Y.-S.; Powers, D. C., Direct Characterization of a Reactive Lattice-Confined Ru2 Nitride by Photocrystallography. *J. Am. Chem. Soc.* **2017,** *139*, 2912–2915.

288. Baek, Y.; Das, A.; Zheng, S.-L.; Reibenspies, J. H.; Powers, D. C.; Betley, T. A., C–H Amination Mediated by Cobalt Organoazide Adducts and the Corresponding Cobalt Nitrenoid Intermediates. *J. Am. Chem. Soc.* **2020,** *142*, 11232–11243.

289. Schmidt-Räntsch, T.; Verplancke, H.; Lienert, J. N.; Demeshko, S.; Otte, M.; Van Trieste III, G. P.; Reid, K. A.; Reibenspies, J. H.; Powers, D. C.; Holthausen, M. C.; Schneider, S., Nitrogen Atom Transfer Catalysis by Metallonitrene C−H Insertion: Photocatalytic Amidation of Aldehydes. *Angew. Chem. Int. Ed.* **2022,** *61*.

290. Das, A.; Van Trieste, G. P.; Powers, D. C., Crystallography of Reactive Intermediates. *Comments Inorg. Chem.* **2020,** *40*, 116–158.

291. Armarego, W. L. F.; Chai, C., *Purification of Laboratory Chemicals, 5th Edition*. Butterworth-Heinemann: 2003.

292. Pangborn, A. B.; Giardello, M. A.; Grubbs, R. H.; Rosen, R. K.; Timmers, F. J., Safe and Convenient Procedure for Solvent Purification. *Organometallics* **1996,** *15* (5), 1518.

293. Ward, A. L.; Elbaz, L.; Kerr, J. B.; Arnold, J., Nonprecious Metal Catalysts for Fuel Cell Applications: Electrochemical Dioxygen Activation by a Series of First Row Transition Metal Tris(2-pyridylmethyl)amine Complexes. *Inorg. Chem.* **2012,** *51* (8), 4694-4706.

294. Song, L.; Li, T.; Zhang, S., Synthesis and characterization of Ag/AgBrO3 photocatalyst with high photocatalytic activity. *Mater. Chem. Phys.* **2016,** *182*, 119-124.

295. Maity, A.; Hyun, S.-M.; Powers, D. C., Oxidase catalysis via aerobically generated hypervalent iodine intermediates. *Nat. Chem.* **2018,** *10*, 200–204.

296. Adamo, C.; Barone, V., Toward reliable density functional methods without adjustable parameters: The PBE0 model. *J. Chem. Phys.* **1999,** *110*, 6158–6170.

297. Grimme, S., Semiempirical GGA-type density functional constructed with a long-range dispersion correction. *J. Comput. Chem.* **2006,** *27*, 1787–1799.

298. Grimme, S.; Ehrlich, S.; Goerigk, L., Effect of the damping function in dispersion corrected density functional theory. *J. Comput. Chem.* **2011,** *32*, 1456 01501465.

299. Couty, M.; Hall, M. B., Basis sets for transition metals: Optimized outer p functions. *J. Comput. Chem.* **1996,** *17*, 1359–1370.

300. Hay, P. J.; Wadt, W. R., Ab initio effective core potentials for molecular calculations. Potentials for K to Au including the outermost core orbitals. *J. Chem. Phys* **1985,** *82*, 299–310.

301. Hehre, W. J.; Ditchfield, R.; Pople, J. A., Self—Consistent Molecular Orbital Methods. XII. Further Extensions of Gaussian—Type Basis Sets for Use in Molecular Orbital Studies of Organic Molecules. *J. Chem. Phys.* **1972,** *56*, 2257–2261.

302. Eckenhoff, W. T.; Pintauer, T., Structural Comparison of Copper(I) and Copper(II) Complexes with Tris(2-pyridylmethyl)amine Ligand. *Inorg. Chem.* **2010,** *49* (22), 10617-10626.

303. Hematian, S.; Siegler, M. A.; Karlin, K. D., Heme/Copper Assembly Mediated Nitrite and Nitric Oxide Interconversion. *J. Am. Chem. Soc.* **2012,** *134*, 18912–18915.

304. Massoud, S. S.; Mautner, F. A.; Vicente, R.; Louka, F. R., μ-1,3- (trans) and μ-1,2- (cis) Bonding in Squarato-Bridged Dinuclear Copper(II) and Nickel(II) Complexes Derived from Polypyridyl Amines. *Eur. J. Inorg. Chem.* **2008,** *2008*, 3709–3717.

305. Massoud, S. S.; Deifik, P. J.; Bankole, P. K.; Lalancette, R.; Yee, G. T.; Tatum, D.; Bernal, I.; Mautner, F. A., Structural and magnetic characterization of a novel series of dinuclear Cu(II) complexes bridging by 2,5-pyrazine dicarboxylate. *Inorg. Chim. Acta.* **2010,** *363*, 1001–1007.

306. Wijeratne, G. B.; Hematian, S.; Siegler, M. A.; Karlin, K. D., Copper(I)/NO(g) Reductive Coupling Producing a trans-Hyponitrite Bridged Dicopper(II) Complex: Redox Reversal Giving Copper(I)/NO(g) Disproportionation. *J. Am. Chem. Soc.* **2017,** *139*, 13276–13279.

307. Mukhopadhyay, U.; Bernal, I.; Massoud, S. S.; Mautner, F. A., Syntheses, structures and some electrochemistry of Cu(II) complexes with tris[(2-pyridyl)methyl]amine: [Cu{N(CH2-py)3}(N3)]ClO4 (I), [Cu{N(CH2-py)3}(O–NO)]ClO4 (II) and [Cu{N(CH2-py)3}(NCS)]ClO4 (III). *Inorg. Chim. Acta.* **2004,** *357*, 3673–3682.

308. Zheng, H.; Que, L., Cu(II)-α-keto acid complexes as structural models of α-keto acid-dependent enzymes: syntheses, crystal structure and properties of [Cu(L)(benzoylformate)]X. *Inorg. Chim. Acta.* **1997,** *263*, 301–307.

309. Denisov, I. G.; Makris, T. M.; Sligar, S. G.; Schlichting, I., Structure and Chemistry of Cytochrome P450. *Chem. Rev.* **2005,** *105*, 2253–2278.

310. Podust, L. M.; Sherman, D. H., Diversity of P450 enzymes in the biosynthesis of natural products. *Nat. Prod. Rep.* **2012,** *29*, 1251–1266.

311. Svastits, E. W.; Dawson, J. H.; Breslow, R.; Gellman, S. H., Functionalized nitrogen atom transfer catalyzed by cytochrome P-450. *J. Am. Chem. Soc.* **1985,** *107*, 6427–6428.

312. McIntosh, J. A.; Coelho, P. S.; Farwell, C. C.; Wang, Z. J.; Lewis, J. C.; Brown, T. R.; Arnold, F. H., Enantioselective Intramolecular C□H Amination Catalyzed by Engineered Cytochrome P450 Enzymes In Vitro and In Vivo. *Angew. Chem. Int. Ed.* **2013,** *52*, 9309–9312.

313. Steck, V.; Kolev, J. N.; Ren, X.; Fasan, R., Mechanism-Guided Design and Discovery of Efficient Cytochrome P450-Derived C–H Amination Biocatalysts. *J. Am. Chem. Soc.* **2020,** *142*, 10343–10357.

314. Jia, Z.-J.; Gao, S.; Arnold, F. H., Enzymatic Primary Amination of Benzylic and Allylic C(sp3)–H Bonds. *J. Am. Chem. Soc.* **2020,** *142*, 10279–10283.

315. Athavale, S. V.; Gao, S.; Liu, Z.; Mallojjala, S. C.; Hirschi, J. S.; Arnold, F. H., Biocatalytic, Intermolecular C−H Bond Functionalization for the Synthesis of Enantioenriched Amides. *Angew. Chem. Int. Ed.* **2021,** *60*, 24864–24869.

316. Miller, D. C.; Athavale, S. V.; Arnold, F. H., Combining chemistry and protein engineering for new-to-nature biocatalysis. *Nat. Syn.* **2022,** *1*, 18–23.

317. Huang, X.; Groves, J. T., Beyond ferryl-mediated hydroxylation: 40 years of the rebound mechanism and C–H activation. *JBIC, J. Biol. Inorg. Chem.* **2017,** *22*, 185–207.

318. Groves, J. T.; Stern, M. K., Synthesis, characterization, and reactivity of oxomanganese(IV) porphyrin complexes. *J. Am. Chem. Soc.* **1988,** *110*, 8628–8638.

319. Groves, J. T.; Lee, J.; Marla, S. S., Detection and Characterization of an Oxomanganese(V) Porphyrin Complex by Rapid-Mixing Stopped-Flow Spectrophotometry. *J. Am. Chem. Soc.* **1997,** *119*, 6269–6273.

320. Mahy, J. P.; Battioni, P.; Bedi, G.; Mansuy, D.; Fischer, J.; Weiss, R.; Morgenstern-Badarau, I., Iron-porphyrin-nitrene complexes: preparation, properties, and crystal structure of porphyrin-iron(III) complexes with a tosylnitrene inserted into an iron-nitrogen bond. *Inorg. Chem.* **1988,** *27*, 353–359.

321. Groves, J. T.; Watanabe, Y., Preparation and characterization of an iron(III) porphyrin N-oxide. *J. Am. Chem. Soc.* **1986,** *108*, 7836–7837.

322. Callot, H. J.; Chevrier, B.; Weiss, R., N-aminoporphyrins. Preparation and metal complexes. Structure of N-tosylamino-5,10,15,20-tetraphenylporphinatonickel(II). *J. Am. Chem. Soc.* **1978,** *100*, 4733–4741.

323. Callot, H. J., Synthesis of n-aminoporphyrins. *Tetrahedron* **1979,** *35*, 1455–1456.

324. Callot, H. J.; Chevrier, B.; Weiss, R., Sitting-atop porphyrin complexes. The structure of the bischloromercury(II) complex of N-tosylaminooctaethylporphyrin. *J. Am. Chem. Soc.* **1979,** *101*, 7729–7730.

325. Chevrier, B.; Weiss, R.; Lange, M.; Chottard, J. C.; Mansuy, D., An iron(III)-porphyrin complex with a vinylidene group inserted into an iron-nitrogen bond: relevance

to the structure of the active oxygen complex of catalase. *J. Am. Chem. Soc.* **1981,** *103*, 2899–2901.

326. Latos-Grazynski, L.; Cheng, R.-J.; La Mar, G. N.; Balch, A. L., Reversible migration of an axial carbene ligand into an iron-nitrogen bond on a porphyrin. Implications for high oxidation states of heme enzymes and heme catabolism. *J. Am. Chem. Soc.* **1981,** *103*, 4270–4272.

327. Andrews, L. E.; Bonnett, R.; Ridge, R. J.; Appelman, E. H., The preparation and reactions of porphyrin N-oxides. *J. Chem. Soc., Perkin Trans. 1* **1983**, 103–107.

328. Balch, A. L.; Chan, Y. W.; Olmstead, M.; Renner, M. W., Structure of octaethylporphyrin N-oxide and the characterization of its nickel(II) and copper(II) complexes. *J. Am. Chem. Soc.* **1985,** *107*, 2393–2398.

329. Balch, A. L.; Chan, Y. W.; Olmstead, M. M., A complex containing a nickel-oxygen unit at the center of a porphyrin. The x-ray crystal and molecular structure of the nickel(II) complex of octaethylporphyrin N-oxide dianion. *J. Am. Chem. Soc.* **1985,** *107*, 6510–6514.

330. Joergensen, K. A., The mechanism of stereoselective epoxidation of alkenes by oxo-iron porphyrins. *J. Am. Chem. Soc.* **1987,** *109*, 698–705.

331. Tung, J.-Y.; Jang, J.-I.; Lin, C.-C.; Chen, J.-H.; Hwang, L.-P., Metal Complexes of N-Tosylamidoporphyrin: cis-Acetato-N-tosylimido-meso-tetraphenylporphyrinatothallium(III) and trans-Acetato-N-tosylimido-meso-tetraphenylporphyrinatogallium(III). *Inorg. Chem.* **2000,** *39*, 1106–1112.

332. Chang, C.-S.; Chen, C.-H.; Li, Y.-I.; Liau, B.-C.; Ko, B.-T.; Elango, S.; Chen, J.-H.; Hwang, L.-P., Metal Complexes of N-p-Nitrobenzoylamido- meso-tetraphenylporphyrin: cis-Acetato-N-p-nitrobenzoylimido-meso-tetraphenylporphyrinatothallium(III) and N-p-Nitrobenzoylimido-meso-tetraphenylporphyrinatonickel(II). *Inorg. Chem.* **2001,** *40*, 2905–2909.

333. Chen, C.-H.; Lee, Y.-Y.; Liau, B.-C.; Elango, S.; Chen, J.-H.; Hsieh, H.-Y.; Liao, F.-L.; Wang, S.-L.; Hwang, L.-P., Chloro(N-p-nitrobenzoylimido-meso-tetraphenylporphyrinato)iron(iii): a high-spin complex. *J. Chem. Soc., Dalton Trans.* **2002**, 3001–3006.

334. Yang, F.-A.; Chen, J.-H.; Hsieh, H.-Y.; Elango, S.; Hwang, L.-P., Metal Complexes of N-Benzamidoporphyrin: (N-Benzimido-meso-tetraphenylporphyrinato)(methanol)zinc(II) Methanol Solvate and (Acetato)(N-benzamido-meso-tetraphenylporphyrinato)cadmium(II) Benzene Solvate. *Inorg. Chem.* **2003,** *42*, 4603–4609.

335. Chen, C.-Y.; Hsieh, H.-Y.; Chen, J.-H.; Wang, S.-S.; Tung, J.-Y.; Hwang, L.-P., Two-stage formation of chloro (N-o-chlorobenzamido-meso-tetraphenylporphyrinato) zinc(II) methylene chloride solvate: Zn(N-NHCO(o-Cl)C6H4-tpp)Cl·CH2Cl2. *Polyhedron* **2007,** *26*, 4602–4608.

336. Tung, J.-Y.; Chen, J.-H., Electrostatic forces that determine O,O-trans versus O,S-cis conformers in the aminated porphyrin complexes of Cd(N-NHCO-2-C4H3O-tpp)(OAc) and Cd(N-NHCO-2-C4H3S-tpp)(OAc). *Polyhedron* **2007,** *26*, 589–599.

337. Chien, T.-Y.; Hsieh, H.-Y.; Chen, C.-Y.; Chen, J.-H.; Wang, S.-S.; Tung, J.-Y., Metal complexes of tetradentate and pentadentate N-o-hydroxybenzamido-meso-tetraphenylporphyrin ligand: M(N-NCO(o-OH)C6H4-tpp) (M=Zn2+, Ni2+, Cu2+) and M′(N-NCO(o-O) C6H4-tpp) (M′=Mn3+) (tpp=5, 10, 15, 20-tetraphenylporphyrinate). *Polyhedron* **2009,** *28*, 3907–3914.

338. Cho, C.-H.; Chien, T.-Y.; Chen, J.-H.; Wang, S.-S.; Tung, J.-Y., Intermediate (S = 1) spin state in five-coordinate cobalt(iii): Magnetic properties of N-o-hydroxy-benzamido-meso-tetraphenylporphyrin cobalt(iii), Co(N-NCO(o-O)C6H4-tpp). *Dalton Trans.* **2010,** *39*, 2609–2614.

339. Cho, C.-H.; Peng, C.-C.; Chen, J.-H.; Wang, S.-S.; Tung, J.-Y., Metal complexes of N-m-nitrobenzenesulfonylamido-meso-tetraphenyl porphyrin: M(N-NSO2(m-NO2)C6H4-tpp) (M=Zn2+, Ni2+, Cu2+) and Tl(N-NSO2(m-NO2)C6H4-tpp)(OAc) (tpp=5, 10, 15, 20-tetraphenyl porphyrinate). *Polyhedron* **2010,** *29*, 1116–1122.

340. Aguilar-Calderón, J. R.; Fehn, D.; Sorsche, D.; Miehlich, M.; Carroll, P. J.; Zars, E.; Meyer, K.; Mindiola, D. J., Redox-Controlled and Reversible N–N Bond Forming and Splitting with an IronIV Terminal Imido Ligand. *Inorg. Chem.* **2021,** *60*, 13091–13100.

341. Epping, R. F. J.; Hoeksma, M. M.; Bobylev, E. O.; Mathew, S.; de Bruin, B., Cobalt(II)–tetraphenylporphyrin-catalysed carbene transfer from acceptor–acceptor iodonium ylides via N-enolate–carbene radicals. *Nat. Chem.* **2022**, Just Accepted.

342. Wang, S. H.; Mandimutsira, B. S.; Todd, R.; Ramdhanie, B.; Fox, J. P.; Goldberg, D. P., Catalytic Sulfoxidation and Epoxidation with a Mn(III) Triazacorrole:

Evidence for A “Third Oxidant” in High-Valent Porphyrinoid Oxidations. *J. Am. Chem. Soc.* **2004,** *126*, 18–19.

343. Liu, Y.; Chen, G.-Q.; Tse, C.-W.; Guan, X.; Xu, Z.-J.; Huang, J.-S.; Che, C.-M., [Fe(F20TPP)Cl]-Catalyzed Amination with Arylamines and {[Fe(F20TPP)(NAr)](PhI□NAr)} Intermediate Assessed by High-Resolution ESI-MS and DFT Calculations. *Chem. Asian. J.* **2015,** *10*, 100–105.

344. Nguyen, T. N.; May, J. A., Branched Amine Synthesis via Aziridine or Azetidine Opening with Organotrifluoroborates by Cooperative Brønsted/Lewis Acid Catalysis: An Acid-Dependent Divergent Mechanism. *Org. Lett.* **2018,** *20*, 3618–3621.

345. Reed, S. A.; White, M. C., Catalytic Intermolecular Linear Allylic C−H Amination via Heterobimetallic Catalysis. *J. Am. Chem. Soc.* **2008,** *130*, 3316–3318.

346. Bhuyan, R.; Nicholas, K. M., Efficient Copper-Catalyzed Benzylic Amidation with Anhydrous Chloramine-T. *Org. Lett.* **2007,** *9*, 3957–3959.

347. Hamilton, C. W.; Laitar, D. S.; Sadighi, J. P., Oxidation-resistant, sterically demanding phenanthrolines as supporting ligands for copper(i) nitrene transfer catalysts. *Chem. Commun.* **2004**, 1628–1629.

348. Evans, D. A.; Faul, M. M.; Bilodeau, M. T.; Anderson, B. A.; Barnes, D. M., Bis(oxazoline)-copper complexes as chiral catalysts for the enantioselective aziridination of olefins. *J. Am. Chem. Soc.* **1993,** *115*, 5328–5329.

349. Dielmann, F.; Andrada, D. M.; Frenking, G.; Bertrand, G., Isolation of Bridging and Terminal Coinage Metal–Nitrene Complexes. *J. Am. Chem. Soc.* **2014,** *136*, 3800–3802.

350. Corona, T.; Ribas, L.; Rovira, M.; Farquhar, E. R.; Ribas, X.; Ray, K.; Company, A., Characterization and Reactivity Studies of a Terminal Copper–Nitrene Species. *Angew. Chem. Int. Ed.* **2016,** *55*, 14005–14008.

351. Kundu, S.; Miceli, E.; Farquhar, E.; Pfaff, F. F.; Kuhlmann, U.; Hildebrandt, P.; Braun, B.; Greco, C.; Ray, K., Lewis Acid Trapping of an Elusive Copper–Tosylnitrene Intermediate Using Scandium Triflate. *J. Am. Chem. Soc.* **2012,** *134*, 14710–14713.

352. Badiei, Y. M.; Krishnaswamy, A.; Melzer, M. M.; Warren, T. H., Transient Terminal Cu−Nitrene Intermediates from Discrete Dicopper Nitrenes. *J. Am. Chem. Soc.* **2006,** *128*, 15056–15057.

353. Aguila, M. J. B.; Badiei, Y. M.; Warren, T. H., Mechanistic Insights into C–H Amination via Dicopper Nitrenes. *J. Am. Chem. Soc.* **2013,** *135*, 9399–9406.

354. Bakhoda, A.; Jiang, Q.; Bertke, J. A.; Cundari, T. R.; Warren, T. H., Elusive Terminal Copper Arylnitrene Intermediates. *Angew. Chem. Int. Ed.* **2017,** *56*, 6426–6430.

355. Brotherton, W. S.; Guha, P. M.; Phan, H.; Clark, R. J.; Shatruk, M.; Zhu, L., Tridentate complexes of 2,6-bis(4-substituted-1,2,3-triazol-1-ylmethyl)pyridine and its organic azide precursors: an application of the copper(ii) acetate-accelerated azide–alkyne cycloaddition. *Dalton Trans.* **2011,** *40*, 3655–3665.

356. Kuang, G.-C.; Michaels, H. A.; Simmons, J. T.; Clark, R. J.; Zhu, L., Chelation-Assisted, Copper(II)-Acetate-Accelerated Azide−Alkyne Cycloaddition. *J. Org. Chem.* **2010,** *75*, 6540–6548.

357. Allão, R. A.; Jordão, A. K.; Resende, J. A. L. C.; Cunha, A. C.; Ferreira, V. F.; Novak, M. A.; Sangregorio, C.; Sorace, L.; Vaz, M. G. F., Determination of the relevant magnetic interactions in low-dimensional molecular materials: the fundamental role of single crystal high frequency EPR. *Dalton Trans.* **2011,** *40*, 10843–10850.

358. Barz, M.; Herdtweck, E.; Thiel, W. R., Transition Metal Complexes with Organoazide Ligands: Synthesis, Structural Chemistry, and Reactivity. *Angew. Chem. Int. Ed.* **1998,** *37*, 2262–2265.

359. Escobar, L. B. L.; Guedes, G. P.; Soriano, S.; Speziali, N. L.; Jordão, A. K.; Cunha, A. C.; Ferreira, V. F.; Maxim, C.; Novak, M. A.; Andruh, M.; Vaz, M. G. F., New Families of Hetero-tri-spin 2p−3d−4f Complexes: Synthesis, Crystal Structures, and Magnetic Properties. *Inorg. Chem.* **2014,** *53*, 7508–7517.

360. Kuang, G.-C.; Guha, P. M.; Brotherton, W. S.; Simmons, J. T.; Stankee, L. A.; Nguyen, B. T.; Clark, R. J.; Zhu, L., Experimental Investigation on the Mechanism of Chelation-Assisted, Copper(II) Acetate-Accelerated Azide–Alkyne Cycloaddition. *J. Am. Chem. Soc.* **2011,** *133*, 13984–14001.

361. Singh, P. N. D.; Mandel, S. M.; Sankaranarayanan, J.; Muthukrishnan, S.; Chang, M.; Robinson, R. M.; Lahti, P. M.; Ault, B. S.; Gudmundsdóttir, A. D., Selective Formation of Triplet Alkyl Nitrenes from Photolysis of β-Azido-Propiophenone and Their Reactivity. *J. Am. Chem. Soc.* **2007,** *129*, 16263–16272.

362. Ritschel, J.; Sasse, F.; Maier, M. E., Synthesis of a Benzolactone Collection using Click Chemistry. *Eur. J. Org. Chem.* **2007,** *2007*, 78–87.

363. Check, C. E.; Faust, T. O.; Bailey, J. M.; Wright, B. J.; Gilbert, T. M.; Sunderlin, L. S., Addition of Polarization and Diffuse Functions to the LANL2DZ Basis Set for P-Block Elements. *J. Phys. Chem. A* **2001,** *105*, 8111–8116.

364. Wadt, W. R.; Hay, P. J., Ab initio effective core potentials for molecular calculations. Potentials for main group elements Na to Bi. *J. Chem. Phys.* **1985,** *82*, 284–298.

365. Chavez, T. A.; Liu, Y.; Toscano, J. P., Time-Resolved Infrared (TRIR) Studies of Oxycarbonylnitrenes. *J. Org. Chem.* **2016,** *81*, 6320–6328.

366. Morita, H.; Tatami, A.; Maeda, T.; Ju Kim, B.; Kawashima, W.; Yoshimura, T.; Abe, H.; Akasaka, T., Generation of Nitrene by the Photolysis of N-Substituted Iminodibenzothiophene. *J. Org. Chem.* **2008,** *73*, 7159–7163.

367. Antoni, P. W.; Mackenroth, A. V.; Mulks, F. F.; Rudolph, M.; Helmchen, G.; Hashmi, A. S. K., Dibenzothiophenesulfilimines: A Convenient Approach to Intermolecular Rhodium-Catalysed C−H Amidation. *Chem. Eur. J.* **2020,** *26*, 8235–8238.

368. Greulich, T. W.; Daniliuc, C. G.; Studer, A., N-Aminopyridinium Salts as Precursors for N-Centered Radicals – Direct Amidation of Arenes and Heteroarenes. *Org. Lett.* **2015,** *17*, 254–257.

369. Miyazawa, K.; Koike, T.; Akita, M., Regiospecific Intermolecular Aminohydroxylation of Olefins by Photoredox Catalysis. *Chem. Eur. J.* **2015,** *21*, 11677–11680.

370. Miyazawa, K.; Koike, T.; Akita, M., Aminohydroxylation of olefins with iminopyridinium ylides by dual Ir photocatalysis and Sc(OTf)3 catalysis. *Tetrahedron* **2016,** *72*, 7813–7820.

371. Mo, J.-N.; Yu, W.-L.; Chen, J.-Q.; Hu, X.-Q.; Xu, P.-F., Regiospecific Three-Component Aminofluorination of Olefins via Photoredox Catalysis. *Org. Lett.* **2018,** *20*, 4471–4474.

372. Yu, W.-L.; Chen, J.-Q.; Wei, Y.-L.; Wang, Z.-Y.; Xu, P.-F., Alkene functionalization for the stereospecific synthesis of substituted aziridines by visible-light photoredox catalysis. *Chem. Commun.* **2018,** *54*, 1948–1951.

373. Gallagher, A. T.; Kelty, M. L.; Park, J. G.; Anderson, J. S.; Mason, J. A.; Walsh, J. P. S.; Collins, S. L.; Harris, T. D., Dioxygen binding at a four-coordinate cobaltous porphyrin site in a metal–organic framework: structural, EPR, and O2 adsorption analysis. *Inorg. Chem. Front.* **2016,** *3*, 536–540.

374. Gallagher, A. T.; Lee, J. Y.; Kathiresan, V.; Anderson, J. S.; Hoffman, B. M.; Harris, T. D., A structurally-characterized peroxomanganese(iv) porphyrin from reversible O2 binding within a metal–organic framework. *Chem. Sci.* **2018,** *9*, 1596–1603.

375. Anderson, J. S.; Gallagher, A. T.; Mason, J. A.; Harris, T. D., A Five-Coordinate Heme Dioxygen Adduct Isolated within a Metal–Organic Framework. *J. Am. Chem. Soc.* **2014,** *136*, 16489–16492.

376. Reid, K. A.; Powers, D. C., In crystallo organometallic chemistry. *Chem. Commun.* **2021,** *57*, 4993–5003.

377. Xiao, D. J.; Bloch, E. D.; Mason, J. A.; Queen, W. L.; Hudson, M. R.; Planas, N.; Borycz, J.; Dzubak, A. L.; Verma, P.; Lee, K.; Bonino, F.; Crocellà, V.; Yano, J.; Bordiga, S.; Truhlar, D. G.; Gagliardi, L.; Brown, C. M.; Long, J. R., Oxidation of ethane to ethanol by N2O in a metal–organic framework with coordinatively unsaturated iron(II) sites. *Nat. Chem.* **2014,** *6*, 590–595.

378. Winslow, C.; Lee, H. B.; Field, M. J.; Teat, S. J.; Rittle, J., Structure and Reactivity of a High-Spin, Nonheme Iron(III)- Superoxo Complex Supported by Phosphinimide Ligands. *J. Am. Chem. Soc.* **2021,** *143*, 13686–13693.

379. Huang, Z.; White, P. S.; Brookhart, M., Ligand exchanges and selective catalytic hydrogenation in molecular single crystals. *Nature* **2010,** *465*, 598–601.

380. Pike, S. D.; Chadwick, F. M.; Rees, N. H.; Scott, M. P.; Weller, A. S.; Krämer, T.; Macgregor, S. A., Solid-State Synthesis and Characterization of σ-Alkane Complexes, [Rh(L2)(η2,η2-C7H12)][BArF4] (L2 = Bidentate Chelating Phosphine). *J. Am. Chem. Soc.* **2015,** *137*, 820–833.

381. McKay, A. I.; Krämer, T.; Rees, N. H.; Thompson, A. L.; Christensen, K. E.; Macgregor, S. A.; Weller, A. S., Formation of a σ-alkane Complex and a Molecular Rearrangement in the Solid-State: [Rh(Cyp2PCH2CH2PCyp2)(η2:η2-C7H12)][BArF4]. *Organometallics* **2017,** *36*, 22–25.

382. Buswell, A. M.; McMillan, G. W.; Rodebush, W. H.; Wall, F. T., Infrared Absorption Studies. VIII. Hydrazoic Acid. *J. Am. Chem. Soc.* **1939,** *61*, 2809–2812.

383. Bläsing, K.; Bresien, J.; Labbow, R.; Michalik, D.; Schulz, A.; Thomas, M.; Villinger, A., Borane Adducts of Hydrazoic Acid and Organic Azides: Intermediates for the Formation of Aminoboranes. *Angew. Chem. Int. Ed.* **2019,** *58*, 6540–6544.

384. Sun, J.; Abbenseth, J.; Verplancke, H.; Diefenbach, M.; de Bruin, B.; Hunger, D.; Würtele, C.; van Slageren, J.; Holthausen, M. C.; Schneider, S., A platinum(ii) metallonitrene with a triplet ground state. *Nat. Chem.* **2020,** *12*, 1054–1059.

385. Abbenseth, J.; Goicoechea, J. M., A phosphorus analog of a bimetallic dinitrogen complex. *Chem* **2021,** *7*, 1698–1700.

386. Varava, P.; Dong, Z.; Scopelliti, R.; Fadaei-Tirani, F.; Severin, K., Isolation and characterization of diazoolefins. *Nat. Chem.* **2021,** *13*, 1055–1060.

387. Soleilhavoup, M.; Bertrand, G., Stable Carbenes, Nitrenes, Phosphinidenes, and Borylenes: Past and Future. *Chem* **2020,** *6*, 1275–1282.

388. Platz, M. S., Nitrenes. In *Reactive Intermediate Chemistry*, 2003; pp 501–559.

389. Braunschweig, H.; Krummenacher, I.; Légaré, M.-A.; Matler, A.; Radacki, K.; Ye, Q., Main-Group Metallomimetics: Transition Metal-like Photolytic CO Substitution at Boron. *J. Am. Chem. Soc.* **2017,** *139*, 1802–1805.

390. Ledet, A. D.; Hudnall, T. W., Reduction of a diamidocarbene-supported borenium cation: isolation of a neutral boryl-substituted radical and a carbene-stabilized aminoborylene. *Dalton Trans.* **2016,** *45*, 9820–9826.

391. Dahcheh, F.; Martin, D.; Stephan, D. W.; Bertrand, G., Synthesis and Reactivity of a CAAC–Aminoborylene Adduct: A Hetero-Allene or an Organoboron Isoelectronic with Singlet Carbenes. *Angew. Chem. Int. Ed.* **2014,** *53*, 13159–13163.

392. Drew, M. G. B.; Mitchell, P. C. H.; Scott, C. E., Crystal and molecular structure of three oxovanadium(IV) porphyrins: oxovanadium tetraphenylporphyrin(I), oxovanadium(IV) etioporphyrin(II) and the 1:2 adduct of (II) with 1,4-dihydroxybenzene(III). Hydrogen bonding involving the VO group. Relevance to catalytic demetallisation. *Inorg. Chim. Acta* **1984,** *82*, 63–68.

393. Yamabayashi, T.; Atzori, M.; Tesi, L.; Cosquer, G.; Santanni, F.; Boulon, M.-E.; Morra, E.; Benci, S.; Torre, R.; Chiesa, M.; Sorace, L.; Sessoli, R.; Yamashita, M., Scaling Up Electronic Spin Qubits into a Three-Dimensional Metal–Organic Framework. *J. Am. Chem. Soc.* **2018,** *140*, 12090–12101.

394. Budge, J. R.; Gatehouse, B. M. K.; Nesbit, M. C.; West, B. O., The autoxidation of a chromium (II) porphyrin: synthesis and structural characterisation by X-ray crystallography of αβγδ-tetraphenyl-porphinato-oxochromium(IV). *J. Chem. Soc,. Chem. Commun.* **1981**, 370–371.

395. Groves, J. T.; Takahashi, T.; Butler, W. M., Synthesis and molecular structure of a nitrido(porphyrinato)chromium(V) complex. *Inorg. Chem.* **1983,** *22*, 884–887.

396. Mahy, J. P.; Battioni, P.; Mansuy, D.; Fisher, J.; Weiss, R.; Mispelter, J.; Morgenstern-Badarau, I.; Gans, P., Iron porphyrin-nitrene complexes: preparation from 1,1-dialkylhydrazines. Electronic structure from NMR, Moessbauer, and magnetic susceptibility studies and crystal structure of the [tetrakis(p-chlorophenyl)porphyrinato][(2,2,6,6-tetramethyl-1-piperidyl)nitrene]iron complex. *J. Am. Chem. Soc.* **1984,** *106*, 1699–1706.

397. Fantauzzi, S.; Gallo, E.; Caselli, A.; Ragaini, F.; Casati, N.; Macchi, P.; Cenini, S., The key intermediate in the amination of saturated C–H bonds: synthesis, X-ray characterization and catalytic activity of Ru(TPP)(NAr)2 (Ar = 3,5-(CF3)2C6H3). *Chem. Commun.* **2009**, 3952–3954.

398. Berreau, L. M.; Young, V. G.; Woo, L. K., Synthesis and Characterization of (Imido)titanium(IV) Porphyrin Complexes. X-ray Structure of (Phenylimido)(tetratolylporphyrinato)titanium(IV). *Inorg. Chem.* **1995,** *34*, 527–529.

399. Wang, H.-X.; Wan, Q.; Low, K.-H.; Zhou, C.-Y.; Huang, J.-S.; Zhang, J.-L.; Che, C.-M., Stable group 8 metal porphyrin mono- and bis(dialkylcarbene) complexes: synthesis, characterization, and catalytic activity. *Chem. Sci.* **2020,** *11*, 2243–2259.

400. Li, Y.; Huang, J.-S.; Zhou, Z.-Y.; Che, C.-M.; You, X.-Z., Remarkably Stable Iron Porphyrins Bearing Nonheteroatom-Stabilized Carbene or (Alkoxycarbonyl)carbenes: Isolation, X-ray Crystal Structures, and Carbon Atom Transfer Reactions with Hydrocarbons. *J. Am. Chem. Soc.* **2002,** *124*, 13185–13193.

401. Liu, Y.; Xu, W.; Zhang, J.; Fuller, W.; Schulz, C. E.; Li, J., Electronic Configuration and Ligand Nature of Five-Coordinate Iron Porphyrin Carbene Complexes: An Experimental Study. *J. Am. Chem. Soc.* **2017,** *139*, 5023–5026.

402. Camp, C.; Settineri, N.; Lefèvre, J.; Jupp, A. R.; Goicoechea, J. M.; Maron, L.; Arnold, J., Uranium and thorium complexes of the phosphaethynolate ion. *Chem. Sci.* **2015,** *6*, 6379–6384.

403. Goicoechea, J. M.; Grützmacher, H., The Chemistry of the 2-Phosphaethynolate Anion. *Angew. Chem. Int. Ed.* **2018,** *57*, 16968–16994.

404. Grant, L. N.; Krzystek, J.; Pinter, B.; Telser, J.; Grützmacher, H.; Mindiola, D. J., Finding a soft spot for vanadium: a P-bound OCP ligand. *Chem. Commun.* **2019,** *55*, 5966–5969.

405. Grant, L. N.; Pinter, B.; Manor, B. C.; Suter, R.; Grützmacher, H.; Mindiola, D. J., A Planar Ti2P2 Core Assembled by Reductive Decarbonylation of −O−C≡P and P−P Radical Coupling. *Chem. Eur. J.* **2017,** *23*, 6272–6276.

406. Grant, L. N.; Pinter, B.; Manor, B. C.; Grützmacher, H.; Mindiola, D. J., A Scandium-Stabilized Diisophosphaethynolate Ligand: [OCPPCO]4−. *Angew. Chem. Int. Ed.* **2018,** *57*, 1049–1052.

407. Reinholdt, A.; Jafari, M. G.; Sandoval-Pauker, C.; Ballestero-Martínez, E.; Gau, M. R.; Driess, M.; Pinter, B.; Mindiola, D. J., Phosphorus and Arsenic Atom Transfer to Isocyanides to Form π-Backbonding Cyanophosphide and Cyanoarsenide Titanium Complexes. *Angew. Chem. Int. Ed.* **2021,** *60*, 17595–17600.

408. Jafari, M. G.; Park, Y.; Pudasaini, B.; Kurogi, T.; Carroll, P. J.; Kaphan, D. M.; Kropf, J.; Delferro, M.; Baik, M.-H.; Mindiola, D. J., Phosphorus-Atom Transfer from Phosphaethynolate to an Alkylidyne. *Angew. Chem. Int. Ed.* **2021,** *60*, 24411–24417.